PREPARATION AND PROPERTIES OF SPECTRALLY SELECTIVE, ELECTROCHROMIC AND PHOTOCATALYTIC COATINGS FROM DISPERSIONS OF NANOPARTICLES

Mohor Mihelčič

Doctoral Dissertation
Jožef Stefan International Postgraduate School
Ljubljana, Slovenia

Supervisor: Prof. Dr. Boris Orel, National Institute of Chemistry, Ljubljana, Slovenia

Evaluation Board:
Asst. Prof. Janez Kovač, Chairman, Jožef Stefan International Postgraduate School & Jožef Stefan Institute, Ljubljana, Slovenia
Prof. Dr. Saša Novak, Member, Jožef Stefan International Postgraduate School & Jožef Stefan Institute, Ljubljana, Slovenia
Prof. Dr. Urška Lavrenčič Štangar, Member, University of Nova Gorica, Nova Gorica, Slovenia

MEDNARODNA PODIPLOMSKA ŠOLA JOŽEFA STEFANA
JOŽEF STEFAN INTERNATIONAL POSTGRADUATE SCHOOL



Mohor Mihelčič

PREPARATION AND PROPERTIES OF SPECTRALLY SELECTIVE, ELECTROCHROMIC AND PHOTOCATALYTIC COATINGS FROM DISPERSIONS OF NANOPARTICLES

Doctoral Dissertation

PRIPRAVA IN LASTNOSTI SPEKTRALNO SELEKTIVNIH, ELEKTROKROMNIH IN FOTOKATALITSKIH PREVLEK IZ DISPERZIJ NANODELCEV

Doktorska disertacija

Supervisor: Prof. Dr. Boris Orel

Ljubljana, Slovenia, October 2015

To Nina, Lara & Mija

Acknowledgments

I would first like sincerely to thank Prof. Dr. Boris Orel, who gave me the opportunity to work at the Laboratory for Spectroscopy of Materials at the National Institute of Chemistry in Ljubljana. He guided me during both my undergraduate and postgraduate studies and gave me valuable advice in the field of solar energy and energy harnessing related materials.

I would also like to express my gratitude to Dr. Ivan Jerman for his help and support with experimental work. I wish to thank Dr. Angela Šurca Vuk and Dr. Franc Švegl for sharing their experience in the field of electrochromism; Dr. Lidija Slemenik Perše I thank for rheological measurements and SEM analysis of samples; Prof. Dr. Urška Lavrenčič Štangar for photocatalytic (PCA) and photosuperhydrophilic (PSH) measurements, Dr. Dejan Verhovšek for TEM measurements and Prof. Dr. Janez Kovač for XPS and AFM measurements.

I am grateful to all other employees of the Laboratory for Spectroscopy of Materials for selfless help and advice.

I would also like to thank my family: father Drago, mother Silva and sister Monika for their encouragement during the years of study.

At the end, my great thanks go to Nina for all the inspiration, support, assistance and patience during my study time and also my wonderful twin daughters, Lara and Mija, for all the happy moments.

Abstract

Within the scope of this thesis, various topics were studied related to harnessing solar energy, i.e., thickness sensitive spectrally selective (TSSS) coatings for solar absorbers, thin optically transparent electrochromic coatings prepared from pigment dispersions and photocatalytic coatings. The key problem common to all the studied systems was to prepare pigment particle dispersion enabling deposition of functional optical coatings exhibiting low haze (no scattering of visible light), high hiding power, fast and strong electrochromic effect and photocatalytic and super-hydrophilic properties. Black manganese spinel oxide (PK 3060), nickel oxide ($Ni_{1-x}O$) and titanium dioxide (TiO_2) pigments were used for making TSSS, electrochromic and photocatalytic coatings. Polyhedral oligomeric silsesquioxanes (POSS) served as material of choice because of their organic–inorganic nature and a combination of hydrophobic and hydrophilic properties.

The rheological properties of PK 3060 pigment modified with differently functionalized (isobutyl, isooctyl and phenyl) trisilanol POSS dispersants were first studied. The rheological studies revealed that trisilanol POSS molecules acted as super dispersants, enabling the preparation of pigment dispersions with pigment loadings (pigment to volume concentration ratio, PVC) that were higher than the PVC values obtained with ordinary organic pigment coatings, confirming their "super dispersant" properties. The results provided a suitable platform for making TSSS pigment coatings with appropriately high pigment loadings, which were essential in order to make solar coatings with high covering efficiency and high solar absorptance, i.e., spectral selectivity (a_S/e_T ratio).

Sol-gel based TSSS pigment coatings for solar absorbers were next studied. Pigment dispersions were made of black manganese spinel oxide (PK 3060) pigment, which was surface modified with isobutyl trisilanol POSS dispersant. Pigment dispersions were prepared by a two-step process; first, the pigment particles were equilibrated in trisilanol POSS mixture in order to make the pigment surface hydrophobic, then dried and, in the final step, dispersed by milling with zirconia beads. Sol-gel based TSSS pigment coatings were made by adding 3-glycidoxypropyltrimethoxy silane (Glymo) binder to the corresponding pigment dispersion. Before the application of spectrally selective coatings on an industrial coil coating line, the thickness and spectral selectivity was optimized for coatings deposited on a smaller scale by the spin coating process. The spectral selectivity of coatings deposited via coil coating exhibit $a_S = 0.90$ and $e_T = 0.12$.

The fact that the sol-gel based coatings decomposed to silica at higher temperatures (560-600 °C) was exploited for the preparation of high power (HIPO) solar absorber

coatings with improved spectral selectivity. Thermal degradation was studied with the aid of isoconversion kinetics and the degradation products were correlated with infrared spectra measurements, providing clear evidence of the formation of a silica network with embedded PK 3060 particles. The sol-gel TSSS pigment coatings exhibit exceptional high temperature (400 °C) and long-term (1216 h) stability, stemming from their inorganic (silica) nature. The spectral selectivity of HIPO coatings did not change significantly; e_T rose only by 3%, while as values remained practically unchanged.

Further investigations of the dispersant effect of trisilanol POSS dispersant were performed for TiO_2 pigment particles, which served for the deposition of electrochromic coatings. The interaction between TiO_2 (anatase and rutile made from metatitanic acid, mTiA and mTiR) and trisilanol POSS was characterized by infrared spectroscopy, TEM, XRD, TG and EDAX measurements combined with electrochemical and electrochromic measurements. The results confirmed the successful surface modification of TiO_2 particles, which we concluded from their good optical properties: haze was low (below 6%), transmittance of the pigment coatings in the visible range was above 80%, which dropped in the coloured state ($\Delta T = T_{bleached} - T_{coloured} = 55.7\%$, $\lambda = 634$ nm). The neutral colour EC foil based device was constructed from $Ni_{1-x}O$ and TiO_2 thin films, glued together with gel electrolyte.

For electrochromic coatings, pigment particle dispersions of electrochromic $Ni_{1-x}O$ pigment were used and dispersed in an aqueous suspension of nickel oxyhydroxide (NiO_xH_y) compound, serving in this case for surface modification of the $Ni_{1-x}O$. Pigment suspensions were used for the deposition of electrochromic coatings at low temperatures (150 °C, 30 minutes) on FTO and also on flexible conducting polymeric ITO-PET foils. The electrochromic properties of the corresponding $Ni_{1-x}O$ pigment coatings were tested in lithium and lithium-free electrolytes. We demonstrated that the coatings change colours from transparent to dark brown when charged in a liquid lithium based and, importantly, also in a lithium-free electrolyte (i.e., TBA^+ triflate/PC). This was taken as proof that only electrons enter the Ni-O semiconducting particles, not that the inserted lithium ions are needed to stabilize the Ni^{+3} states in the coloured (oxidized) $Ni_{1-x}O$ layer. For demonstration of the application potential of the ensuing coatings, flexible EC devices were constructed; either PEDOT (self-standing) or WO_3 on one side and $Ni_{1-x}O$ pigment coating on conductive FTO glass or flexible ITO-PET substrates on the other side. They were glued together with semi-solid electrolyte containing or not lithium ions.

The final part of the thesis was devoted to investigation of the surface modification of TiO_2 P25 through the photocatalytic (PCA) and photosuperhydrophilic (PSH) properties of coatings. Fabrication of the corresponding coatings was a major challenge because most of the dispersants negatively affected the photocatalytic effect. It was shown that both NiO_xH_y and titanium isopropoxide (TiP) sol-gel precursor acted as efficient dispersants for making homogeneous and stable pigment TiO_2 dispersions, which were suitable for the deposition of optically transparent TiO_2 coatings with low haze (2%) and high PCA and PSH effects. Importantly, the PCA and PSH effects were stronger than those of commercial Pilkington Activ™ Glass.

Finally, modification of cotton fibres was performed by deposition of coatings made of titanium isopropoxide (TiP) and titanium isopropoxide/(3-aminopropyl)triethoxysilane

(TiP/APTES) organic-inorganic hybrids. Despite the apparent differences in size and type of these two organic-inorganic hybrid dispersants with respect to trisilanol POSS and pigment particles, interactions between cotton surface and TiP and TiP/APTES hybrids were also studied with IR spectroscopy. The IR ATR technique was applied, subtraction spectra were constructed and interactive sites on cellulose molecules with the hybrids were identified from the measured IR ATR spectra. The main purpose of this work was to provide information about the distinguishable long-term washing stability of coatings and their prolonged antibacterial effects, which we attributed to the formation of the substrate-C-O/-Si- O- bonding.

Povzetek

V okviru doktorske naloge smo preučevali različna področja, povezana z izkoriščanjem sončne energije. To so debelinsko odvisne spektralno selektivne tanke (TSSS) plasti za sončne absorberje, optično prepustne elektrokromne tanke plasti, pripravljene iz pigmentnih disperzij, in fotokatalitske tanke plasti. Ključen problem, skupen vsem proučevanim sistemom, je bila priprava pigmentne disperzije, ki omogoča nanos funkcionalnih optičnih tankih plasti z nizko motnostjo (brez sipanja vidne svetlobe), visoko pokrivnostjo, hitrim in močnim elektrokromnim učinkom ter fotokatalitskimi in superhidrofilnimi lastnostmi.

V okviru doktorske naloge smo preučevali različna področja, povezana z izkoriščanjem sončne energije. To so debelinsko odvisne spektralno selektivne tanke (TSSS) plasti za sončne absorberje, optično prepustne elektrokromne tanke plasti, pripravljene iz pigmentnih disperzij, in fotokatalitske tanke plasti. Ključen problem, skupen vsem proučevanim sistemom, je bila priprava pigmentne disperzije, ki omogoča nanos funkcionalnih optičnih tankih plasti z nizko motnostjo (brez sipanja vidne svetlobe), visoko pokrivnostjo, hitrim in močnim elektrokromnim učinkom ter fotokatalitskimi in superhidrofilnimi lastnostmi.

Pigmente črnega spinel manganovega oksida (PK 3060), nikljevega oksida ($Ni_{1-x}O$) in titanovega dioksida (TiO_2) smo uporabili za pripravo TSSS, elektrokromnih in fotokatalitskih tankih plasti. Poliedrične oligomerne silseskvioksane (POSS) smo uporabili kot izbrani material zaradi njegove organske-anorganske narave in kombinacije hidrofobnih in hidrofilnih lastnosti.

Najprej smo preučevali reološke lastnosti PK 3060 pigmenta, oplaščenega z različno funkcionaliziranim (izobutil, izooktil in fenil) trisilanol POSS kot površinskim oplaščevalcem. Reološke raziskave so pokazale, da trisilanol POSS molekule delujejo kot super omakala, ki omogočajo pripravo pigmentnih disperzij z visoko vsebnostjo pigmenta (razmerje med koncentracijo pigmenta na volumen, PVK), višjega kot PVK vrednosti običajnih organskih pigmentnih premazov, kar potrjuje njegove "super oplaščevalske" lastnosti. Rezultati dajejo ustrezno osnovo za pripravo TSSS pigmentnih tankih plasti z ustrezno visokimi PVK razmerji, ki so potrebne za pripravo selektivnih tankih plasti z visoko pokrivnostjo in visoko sončno absorpcijo, tj. spektralna selektivnost (razmerje a_S/e_T).

V nadaljevanju smo preučevali tanke TSSS plasti na osnovi sol-gel veziva za sončne absorberje. Pigmentne disperzije smo pripravili iz črnega manganovega spinel pigmenta (PK 3060), ki smo ga površinsko oplaščili z izobutil trisilanol POSS-om površinskim omakalom. Pigmentne disperzije smo pripravili po dvostopenjskem postopku; v prvi stopnji smo pigmentne delce zmleli s trisilanol POSS površinskim omakalom, da smo dobili hidrofobno površino pigmenta, nato smo ga posušili in v zadnjem koraku ponovno zmleli s cirkonijevimi kroglicami. Tanke TSSS plasti na osnovi sol-gel veziva smo pripravili z dodatkom 3-glicidoksipropil trimetoksi silan (Glymo) veziva v ustrezno pigmentno disperzijo. Pred nanosom pigmentnih disperzij na industrijsko linijo s tehniko nanašanje iz svitka (*coil coating*) smo z metodo nanašanja na rotirajočo se podlago (*spin-coating*) predhodno optimizirali debelino in spektralno selektivnost tankih plasti. Spektralna

selektivnost tankih plasti, nanesenih s tehniko nanašanje iz svitka, je bila $a_S = 0{,}90$ in $e_T = 0{,}12$.

Dejstvo, da se tanke plasti na osnovi sol-gel veziva razgradijo v siliko pri višjih temperaturah (560–600 °C), smo uporabili z namenom izboljšanja spektralne selektivnosti tankih plasti za sončne absorberje (High Power coatings HIPO). Temperaturno degradacijo tankih plasti smo preučevali s pomočjo izokonverzijske kinetike in razpadnih produktov, ki smo jih korelirali z meritvami infrardečih spektrov, kar daje jasen dokaz za nastanek silikatne matrike z vgrajenimi PK 3060 delci. Sol-gel TSSS tanke plasti izkazujejo izjemno visoko temperaturno (400 °C) in dolgotrajno (1216 h) stabilnost, ki izhaja iz anorganske (silikatne) narave. Spektralna selektivnost HIPO tankih plasti se ni bistveno spremenila; e_T vrednost je zrastla le za 3 %, medtem ko a_S vrednosti ostanejo praktično nespremenjene.

Nadaljnje raziskave vpliva izobutil trisilanol POSS-om površinskega omakala smo naredili s TiO_2 pigmentnimi delci, ki so služili za pripravo elektrokromnih tankih plasti. Interakcije med TiO_2 (anatas in rutil sta bila pripravljena iz meta titanove kisline, mTiA in mTiR) in izobutil trisilanol POSS-om smo okarakterizirali z meritvami infrardeče spektroskopije, TEM, TG, XRD and EDAX, združene z elektrokemijskimi in elektrokromnimi meritvami. Rezultati so potrdili uspešno oplaščenje površine TiO_2 pigmentnih delcev, kar lahko sklepamo iz dobrih optičnih lastnosti: nizko motnostjo (pod 6 %), prepustnost v vidnem območju je bila nad 80 %, ki pa se zmanjša v obarvanem stanju ($\Delta T = T_{razbarvano} - T_{obarvano} = 55{,}7$ %, $\lambda = 634$ nm). Pripravili smo elektrokromni sklop na foliji z nevtralnim obarvanjem, sestavljen iz $Ni_{1-x}O$ in TiO_2 tankih plasti ter zlepljen s pol-trdim (gel) elektrolitom.

Elektrokromne tanke plasti smo pripravili iz pigmentne disperzije z elektrokromnim $Ni_{1-x}O$ pigmentom, dispergiranim v vodni suspenziji nikljevega oksohidroksida (NiO_xH_y), ki je bil uporabljen kot površinski oplaščevalec za $Ni_{1-x}O$. Pigmentno suspenzijo smo uporabili za nanos elektrokromnih tankih plasti, pripravljenih pri nizki temperaturi (150 °C, 30 minut), nanesenih na prevodno FTO in fleksibilno ITO PET podlago. Elektrokromne lastnosti $Ni_{1-x}O$ pigmentnih tankih plasti smo testirali v elektrolitu z in brez prisotnosti litijevih ionov. Predstavili smo tanke plasti, ki spremenijo barvo iz prepustne v temno rjavo ob nabijanju v tekočem elektrolitu. Pomembno je, da to deluje tudi v elektrolitu brez prisotnosti litijevih ionov (TBA^+ triflat/PC). To kaže, da le elektroni vstopijo v Ni-O polprevodni delec, ne pa tudi da so vstavljeni litijevi ioni potrebni za stabilizacijo Ni^{+3} stanja v obarvano (oksidirano) v $Ni_{1-x}O$ tanko plast. Za predstavitev aplikacijskega potenciala uporabljenih tankih plasti smo pripravili plastičen EC sklop, kjer smo uporabili bodisi PEDOT (samostoječ) bodisi WO_3 tanke plasti na eni ter $Ni_{1-x}O$ tanke plasti na prevodnem FTO steklu ali fleksibilnih polimernih ITO-PET na drugi strani. Tanke plasti so bile zlepljene s pol-trdim elektrolitom, ki vsebuje ali pa ne vsebuje litijevih ionov.

Zadnji del te naloge smo namenili preiskavam modifikacije površine TiO_2 – P25 s fotokatalitskimi (PCA) in fotosuperhidrofobnimi (PSH) lastnostmi tankih plasti. Izdelava ustreznih tankih plasti predstavlja velik izziv, saj večina omakal negativno vpliva na fotokatalitski učinek. Izkazalo se je, da tako NiO_xH_y kot tudi titanov izopropoksid (TIP) sol-gel prekurzor delujeta kot učinkoviti omakali pri izdelavi homogenih in stabilnih pigmentnih TiO_2 disperzij, ki so primerne za nanos optično prepustnih TiO_2 tankih plasti z nizko motnostjo (2 %) in visokim PCA in PSH učinkom. Pomembno je, da sta bila PCA in PSH učinka močnejša v primerjavi s komercialnim Pilkington Activ™ steklom.

Nazadnje smo naredili modifikacijo bombažnih vlaken z nanosom tankih plasti titanijevega izopropoksida (TIP) in titanovega izopropoksida/(3-aminopropil)trietoksisilana (TIP/APTES) organsko-anorganskega hibrida. Kljub razliki v velikosti in vrsti teh dveh organsko-anorganskih hibridnih omakalnih sredstev glede na trisilanol POSS in pigmentne delce, interakcije med bombažno površino in TiP ter TiP/APTES hibrida smo preučevali z infrardečo spektroskopijo. Uporabili smo IR ATR tehniko ter naredili odštete spektre. Z IR ATR tehniko smo določili interakcijska mesta na celuloznih molekulah s hibridno tanko plastjo. Glavni namen tega dela je bil objava informacij med dolgotrajno pralno

stabilnostjo tankih plasti in njihovih daljših antibakterijskih učinkov, ki jih pripisujemo nastanku vezi podlaga - C-O/ -Si-O.

Contents

List of Figures **xix**

Abbreviations **xxi**

1 Introduction **23**
1.1 Solar Energy 24
1.1.1 Types of solar collectors 25
1.1.1.1 Non-concentrating solar collectors 25
1.1.1.2 Concentrating solar collectors 28
1.2 Electrochromism 30
1.3 Photocatalysis 32
1.4 Spectroscopy 34
1.4.1 Infrared spectroscopy 34
1.4.2 Attenuated total reflection spectroscopy 35
1.4.3 Reflection-absorption spectroscopy 36
1.5 Optical Properties 38
1.6 Deposition Techniques 41
1.6.1 Spin coating 41
1.6.2 Dip coating 43
1.6.3 Coil coating 44
1.6.4 Spray coating 46

2 Aims of This Work **47**

3 Rheological and Optical Properties of Solar Absorbing Paints with POSS-Treated Pigments **49**

4 Novel Sol–Gel Based Selective Coatings: from Coil Absorber Coating to High Power Coating **65**

5 Electrochromic Coatings Made of Surface Modified Rutile and Anatase Pigments: Influence of Trisilanol POSS Dispersant on the Electrochromic Effect **85**

6 Foil-Based TiO_2/Gel Electrolyte/$Ni_{1-x}O$ Electrochromic Device Made of Electrochromic Pigment Coatings **103**

7 Comparison of the Electrochromic Properties of $Ni_{1-x}O$ in Lithium and Lithium-Free Aprotic Electrolytes: From $Ni_{1-x}O$ Pigment Coatings to Flexible Electrochromic Devices **119**

8 Preparation of Photocatalytic Optically Transparent Coatings from Pigment Dispersions **137**

9 Photocatalytic Cotton Modified with TiO_2 and TiO_2/APTES – Spectroscopic Analysis **149**

10 Conclusions **175**

References **179**

Bibliography **187**

Biography **191**

List of Figures

Figure 1.1: A flat plate solar absorber collector installation [6]. 26
Figure 1.2: Schematic diagram of an evacuated tube collector [15]. 27
Figure 1.3: Efficiency of different non-concentrating solar collectors at various stagnation temperatures [16]. 27
Figure 1.4: Schematic presentation of parabolic dish collector [18]. 28
Figure 1.5: Schematic presentation of parabolic trough collector [19]. 28
Figure 1.6: Schematic presentation of the solar-thermal tower system [24]. 29
Figure 1.7: Schematic presentation of electrochromic device. 31
Figure 1.8: Electrochromic behaviour of colour change of Gasimet EC windows [40]. 32
Figure 1.9: Schematic presentation of photocatalytic process. 33
Figure 1.10: Schematic presentation of total internal reflection with single reflection (left) and multiple reflections IRE (internal reflection element) (right). 36
Figure 1.11: The normalized solar radiation spectrum, black body radiation spectra at three different temperatures, and the ideal selective reflectance spectrum [61]. 39
Figure 1.12: The four stages of the spin coating process [69] 42
Figure 1.13: Dip coating process [69]. 43
Figure 1.14: Schematic presentation of a coil coating line [78]. 45
Figure 3.1: The structure of A) isobutyl (Ib_7), B) isooctyl (IO_7), C) phenyl (Ph_7) trisilanol POSS molecules [80]. 50
Figure 3.2: IR transmission spectra of a) $IO_7T_8(OH)_3$ POSS, b) PK 3060 pigment modified with $IO_7T_8(OH)_3$ POSS and c) PK 3060 pigment modified with $IO_7T_8(OH)_3$ POSS 3x washed in THF. 51
Figure 3.3: IR transmission spectra of a) $Ph_7T_8(OH)_3$ POSS, b) PK 3060 pigment modified with $Ph_7T_8(OH)_3$ POSS and c) PK 3060 pigment modified with $Ph_7T_8(OH)_3$ POSS 3x washed in THF. 52
Figure 3.4: Viscosity dependence of PVC ratio for dispersions of untreated and POSS modified pigment in silicon oil. 53
Figure 4.1: Deposition of sol-gel based TSSS on a coil coating line. 66
Figure 4.2: IR transmission spectra of various coatings exposed to different temperatures (A-a) 130 °C, 30 min, (A-b) 230 °C, 30 min, (A-c) 290 °C, 6 min and (A-d) 400 °C, 30 min. Formation of PEO chain at 130 °C (B) and direct conversion to Si-O-Si of coating heat treated at 400 °C, 30 min (C). 67
Figure 5.1: TEM micrograph of mTiA dispersion made with trisilanol POSS dispersant. 85
Figure 5.2: Adsorption (A) and infrared spectra (B) of washed mTiA/trisilanol POSS dispersions obtained from the intensity band variations of C-H stretching modes after equilibrating mTiA in hexane/trisilanol POSS solutions with concentrations (A) base line, (B) 0.01, (C) 0.025, (D) 0.05, (E) 0.1 and (F) 0.2 w/w%. 86
Figure 5.3: mTiA02 pigment coatings deposited on ITO PET foil (A) and FTO glass (B). 86

Figure 6.1: Cyclic voltammograms of mTiA, TiInfr (for both: with and without dispersant) and P25 pigment coatings without dispersant. 103
Figure 6.2: UV-Vis spectra of mTiA02/sol-gel electrolyte/$Ni_{1-x}O$ flexible EC device A) and a* and b* colour coordinates for single coatings and EC device B). 104
Figure 7.1: *Ex situ* IR RA spectroelectrochemical measurements of $Ni_{1-x}O/NiO_xH_y$ pigment coating (3x, 150 °C, 0.4 mm beads) in 1 M $LiClO_4$/PC electrolyte. 120
Figure 7.2: *Ex situ* IR RA spectroelectrochemical measurements of $Ni_{1-x}O/NiO_xH_y$ pigment coating (3x, 150 °C, 0.4 mm beads) in 0.1 M TBA^+ triflate/PC electrolyte. 120
Figure 7.3: Schematic presentation of four different plastic based EC device compositions. 121
Figure 8.1: Water contact angles on the different coatings as a function of irradiation time. The reference used was Pilkington Activ™ glass [95]. 138
Figure 8.2: Evolution of the concentration of HTPA with irradiation time on the different coatings. Lines represent the fitting of the obtained data to the kinetic model; $k1$ values obtained from these fittings are included in the legend. 138
Figure 9.1: ATR spectra of cotton as-received (a), cotton treated in EtOH and boiling water (EtOH/cotton) and (b) the subtraction spectrum of (EtOH/cotton—cotton as-received) (c) in the spectral region from 4000 to 500 cm^{-1}. 150
Figure 9.2: Subtraction spectra of TiP/cotton—EtOH/cotton (a), TiP/APTES/cotton—EtOH/cotton (b) and TiP/APTES/cotton—TiP/cotton (c) samples in the spectral region from 4000 to 500 cm^{-1}. 150
Figure 9.3: SEM images of TiP – coated cotton (A) and TiP/APTES coated cotton (B) fibres. 151

Abbreviations

POSS	... Polyhedral oligomeric silsesquioxane
CVD	... Chemical vapour deposition
TSSS	... Thickness sensitive spectrally selective coatings
TISS	... Thickness insensitive spectrally selective coatings
EC	... Electrochromic
TCO	... Transparent conductive oxide
SPD	... Suspended particle device
PDLC	... Phase dispersed liquid crystal
ChLC	... Cholesteric liquid crystal
IR	... Infrared spectroscopy
ATR	... Attenuated total reflection spectroscopy
IR RA	... Infrared reflection-absorption spectroscopy
NGIA	... Near grazing incidence angle
LO	... Longitudinal optical mode
TO	... Transversal optical mode
e_T	... Thermal emittance
a_S	... Solar absorbance
T	... Transmittance
R	... Reflectance
A	... Absorbance
I	... Incident light
PSH	... Photosuperhydrophylicity
PCA	... Photocatalytic effect
PVC	... Pigment to volume concentration
$PVC_{critical}$	... Critical pigment to volume concentration
CIE	... International commission on illumination
SEM	... Scanning electron microscopy
TEM	... Transmission electron microscopy
AFM	... Atomic force microscopy
XRD	... X-ray powder diffraction
XPS	... X-ray photoelectron spectroscopy
TG	... Thermogravimetric analysis
DLS	... Dynamic light scattering
UV-Vis-NIR	... Ultraviolet-Visible-Near infrared
THF	... Tetrahydrofurane
ITO PET	... Indium doped tin oxide coated polyethylene terephthalate
FTO	... Fluorine doped tin oxide
PEDOT	... Poly(3,4-ethylenedioxythiophene)
TiP	... Titanium (IV) isopropoxide
GLYMO	... 3-glycidoxypropyltrimethoxy silane
APTES	... 3-aminopropyltriethoxy silane

Chapter 1

Introduction

This thesis relates to the preparation of coatings with multifunctional properties that enable their use in various optical systems, especially those that are used for the production of energy from non-conventional sources of energy, among which heat recovery from sunlight certainly occupies the first place. I chose the proposed topic because of the need to accelerate the use of solar energy, in particular by making spectrally selective coatings for solar absorbers using wet deposition techniques on a metal substrate. It is also necessary to expand their usefulness on solar receivers operating at higher temperatures. These use solar heat for solar cooling, and if the coatings are stable at temperatures of around 500 °C, they are usable in solar towers that produce steam and solar thermal electricity.

Extensive use of solar radiation could also be linked to passive solar systems. Among the best known are windows fitted with glasses with different optical properties. They can either repel radiant heat of the sun to prevent overheating and glare, but allow reheating of facilities by not impeding access to the nearby thermal radiation from the sun. Windows equipped with such glasses have static optical properties, which means that they function optimally only for relatively narrow climatic conditions. At the end of the eighties, this led to the production of electrochromic systems with a dynamic optical response (smart windows). EC glazing systems have a significant advantage over static glazing. At the same time, they prevent glare and thus ensure a certain level of illumination in the facilities, and directly reduce energy demand, which is otherwise used for air-conditioning.

Given the wide range of applications, it is understandable that there is a variety of materials and techniques for the production of passive and active systems. The coatings of the solar absorbers, as well as coatings that are used in electrochromic systems are thus prepared by vacuum deposition techniques, which is the leading technology in the world. Vacuum techniques allow the preparation of materials - mainly in the form of thin coatings - that have different optical functional properties. Coatings of high solar absorbance and low thermal emissivity are suitable for solar absorbers (active solar systems). On the other hand, coatings used for electrochromic devices allow intercalation of small ions and are in part electrically conductive (the intercalation mechanism is similar as in the case of lithium batteries).

Photocatalysis is a process included in sustainable, non-hazardous and economically viable technologies, whereby the suns' energy can be harnessed. A photocatalytic material uses UV energy to break down various substances, such as organic materials - volatile organic compounds (VOCs), microbes (including viruses) and inorganic molecules such as nitrous oxides (NO_x). These reactions of molecules in the presence of a

photocatalyst make photocatalysis extensively applicable. TiO_2 is widely used in a variety of applications and products in the environmental and energy fields. Due to the variety of TiO_2 usage, my research was also focused on the photocatalytic and super hydrophilic properties of TiO_2.

The common feature of all the presented functional coatings, used as coatings in solar absorbers, electrochromic and photocatalytic coatings, is that the particles that impart the functional properties are of nanometer size. Coatings prepared from such particle sizes provide small scattering of visible light (optical coatings) and a thickness of less than 1 µm. Functionalization of the surface of the particles was achieved with the use of different dispersants.

The main challenge in the preparation of coatings for energy harnessing applications is to achieve a combination of several properties at the same time. The ideal coating should have a small thickness, together with negligible haze and an appropriate functionality, such as abrasion resistance, visual appearance, adhesion to the substrate (glass, metal, plastic), electrochromic properties, low thermal emissivity etc. To the characteristics mentioned above can still be added technological requirements; preparation should be inexpensive, mild conditions of deposition and the quality of the coatings must correspond to the devices for which the coatings are produced.

1.1 Solar Energy

Fast industrial development and continuously growing energy demands have brought us to the point at which the pollution of our planet is an increasing environmental concern. Our goal should be to reduce non-renewable and polluting fossil fuels (coal, oil and gas), which are the most frequently used sources of energy but their quantities are limited. Increasing use of these fuels will cause major environmental problems, which are already appearing in the form of an increasing CO content in the atmosphere and acid rain. It would therefore be beneficial to use alternative green energy resources and prevent increasing damage to our planet. One option is to make direct use of incoming solar energy. The sun is a natural power source, driving numerous natural processes, such as the circulation of global wind and ocean currents, the cycle of water evaporation and condensation that creates rivers and lakes, and the biological cycles of photosynthesis and life. Solar energy is free, renewable and non-polluting, and is thus one of the most promising alternative energy sources for the future [1].

The sun deposits far more energy on the surface of the Earth with its radiation than we need for our consumption. The main problem is that the solar radiation reaching the Earth's surface is very diluted (only about 1 KW/m^2) and is not constant. It varies depending upon the location, time of day, time of year and weather conditions). Solar thermal collectors and absorbers made from highly spectrally selective materials deposited on a metallic substrate, most effectively exploit this power. Materials for the exploitation of solar radiation must exhibit strong absorption of solar light, which is electromagnetic radiation in the UV-Vis-NIR regions, with wavelengths from 0.2 to 2.5 µm, and the lowest possible absorption in IR, with wavelengths above 2.5 µm. The measures for these properties are solar thermal emittance e_T and solar absorptance a_S values [2].

Investigation of solar selective coating was first performed by Tabor in 1955 [3]. Since then, many different design principles and physical mechanisms of solar selective coatings and surfaces have been researched. These have served as a basis for various kinds of thin coatings deposited on metallic substrates. Selective absorber surface coatings can be categorized into five distinct types [4]:

- Intrinsic
- Multilayer absorbers
- Textured surface
- Tandem absorber coatings
    - Semiconductor - metal tandems
    - Metal - dielectric composite coatings
- Spectrally solar - transmitting coating on a blackbody-like absorber

1.1.1 Types of solar collectors

The use of solar panels is already well widespread, especially in places where there is an appropriate climate. Although the technology has moved forward, there is still confusion between terms such as photothermal (PT) and photovoltaic (PV) or "solar cells". The difference between a photothermal solar collector and a photovoltaic solar cell is that a photothermal solar collector converts solar radiation into heat while a solar cell converts sunlight directly into electricity. In a collector, the black surface is the central part, which converts solar energy into heat. Water or air is the most common heat transfer substance [1].

Solar energy is converted into thermal energy using a particular kind of heat exchanger known as a solar collector, which is the major component of any solar system. Solar collectors can be classified into two general categories: concentrating and non-concentrating. The collector area (area intercepting solar radiation) and the absorber area (area absorbing radiation) are the same for the non-concentrating type of solar collectors. Flat plate collectors and evacuated tube collectors are non-concentrating types of collector. Photothermal collectors are mainly designed for space heating and cooling, and for heat application used in industrial processes that depend on energy delivery at temperatures between 60 and 250 °C. These collectors use both diffuse and direct solar radiation and do not require tracking of the sun [5].

There are also many types of concentrating collectors but, in general, three types are distinguished:

- Parabolic dish collectors,
- Parabolic trough collectors,
- Solar thermal towers.

These collectors use only direct sunlight for their operation, which is concentrated by mirrors or heliostats and focused into a single point. Operating temperatures are between 300 and 1000 °C. For optimal application, these types of collector require tracking of the sun (must be steered throughout the day). All these systems are also called active systems for harnessing solar heat.

1.1.1.1 Non-concentrating solar collectors

Flat plate collectors are very simple solar thermal energy systems and are the most commonly used type of photothermal collector today (Figure 1.1). They consist of a metal plate that is painted black and serves as an excellent heat collector. Water runs in pipes (mostly copper pipes) that are attached to the metal sheet for heat exchange. The whole system is mounted in the form of solar panels that are installed on rooftops. The heated water is then consumed for domestic purposes. The metal plate is well insulated and has a glass or transparent sheet in front, through which sunlight can easily pass.



Figure 1.1: A flat plate solar absorber collector installation [6].

In photothermal systems, the optical properties of the absorbers used for exploitation of solar energy are crucial. Research is carried out aimed at creating surfaces that absorb as much solar energy and emit as little heat as possible back into the environment.

The solar thermal market is dominated by highly spectrally selective surfaces ($a_S > 0.93$ and $e_T < 0.1$) made from various cermet materials deposited on aluminium or copper via vacuum deposition techniques. The chemical vapour deposition (CVD) method has good potential in large-scale industrial production but there are difficulties associated with ensuring the stoichiometry of the produced metal oxides. An alternative deposition technique is sol-gel processing, with great potential to combine high spectral selectivity and long-term stability of the coating with the cost-effectiveness of production. The advantages of these materials are especially in the extremely low emissivity ($< 0.1\%$), which is maintained if the coating thickness is from 800 nm up to 1 μm. A black coating greatly increases the absorptivity. A series of thickness sensitive (TSSS) [7-9] and thickness insensitive selective (TISS) coatings have therefore been made [10-12]. The development of spectrally selective coatings produced by the wet deposition technique (coil coating or roll-to-roll) has several advantages over older procedures prepared by electroplating or vacuum deposition techniques. The latter coatings have high cost, which is partially compensated by their high spectral selectivity and low consumption of materials. Their disadvantage is in rather poor corrosion resistance ($<$ 1 week in a salt spray chamber). The wet deposition technique is much cheaper and allows the preparation of harder and more corrosion-resistant coatings, with comparable optical properties to cermet coatings produced by vacuum deposition.

The emissivity of substrates for solar absorbers that do not have their own low-emissivity (plastic, steel or various alloys) could be decreased by a thickness insensitive spectrally selective (TISS) coating, with a thickness up to 20 μm. Unlike cheaper flat plate panels, evacuated tube collectors do not heat the water directly within the vacuum tubes. Instead, a sealed copper 'heat pipe' transfers the heat via convection of its internal heat transfer fluid to a 'hot bulb', which indirectly heats a copper manifold within the header. The heat pipes are inserted into curved absorbers, forming an assembly that is inserted into the glass tubes (Figure 1.2). The tubes are made of borosilicate glass, which is strong and has high transmittance for solar irradiation. To reduce the convection heat loss, the glass tubes are evacuated to a vacuum pressure of less than 10^{-3} Pa. The heat-transfer liquid contains a small amount of water, glycol, ammonia, methanol, ethanol, or other suitable volatile fluid [13], which undergoes an evaporating-condensing cycle.

Because no evaporation or condensation above the phase-change temperature is possible, the heat pipe offers inherent protection from freezing and overheating. This temperature self-control is an unparalleled advantage of an evacuated heat pipe collector. The outer side of the inner tube is coated with a sputtered solar selective coating that exhibits excellent solar absorptance ($a_S > 92\%$) and low thermal emittance ($e_T < 5\%$) [14].

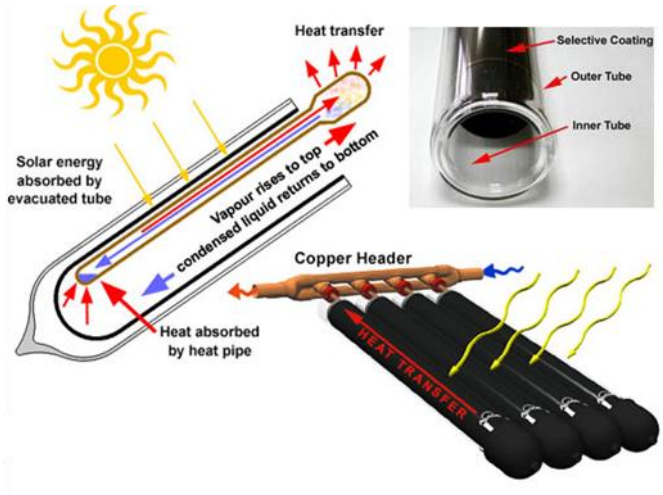


Figure 1.2: Schematic diagram of an evacuated tube collector [15].

Solar collector efficiency varies depending on the temperature at the collector inlet compared to the ambient air temperature. Figure 1.3 shows typical efficiency curves of three different collector types.

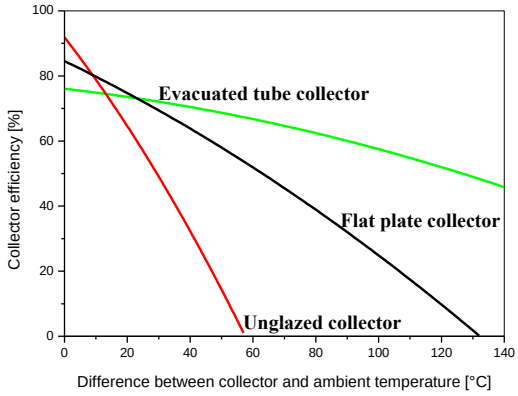


Figure 1.3: Efficiency of different non-concentrating solar collectors at various stagnation temperatures [16].

Unglazed collectors are inexpensive and very effective at low temperatures; when the temperature rises their efficiency diminishes. These collectors achieve their best performance in applications based on low temperature. Glazed collectors, on the other hand, need higher temperatures to obtain their highest efficiency. The glazing on a flat plate collector is subject to relatively high heat loss, and therefore the collector itself will not reach a temperature much above 200 °C, even if the heat transfer liquid is immobile stagnant [17]. Such temperatures are too low for efficient conversion to electricity. Energy losses in a glazed photothermal collector can be thermal (convection, radiation) or optical (reflection of light from the surface of the glass). Higher water temperatures

are required in cooling and heat applications in some industrial processes, for which evacuated tubes are unavoidable.

1.1.1.2 Concentrating solar collectors

Concentrating solar thermal collectors are a group of collectors used for energy conversion and power generation. This group consists of parabolic dish collectors, parabolic trough collectors and solar thermal towers. A parabolic dish collector (Figure 1.4) uses the principle of tracking the sun on two axes. It is always pointed at the sun and it concentrates the sun's energy at the focal point of the dish. The receiver converts the absorbed radiant solar energy into thermal energy, received by the circulating fluid. This thermal energy is subsequently converted into electricity by an engine-generator on the receiver, or transported through pipes to the central system of power-conversion. A thermal receiver has incorporated tubes, in which fluid (usually hydrogen or helium) circulates and transfers heat to the electricity producing generator.



Figure 1.4: Schematic presentation of parabolic dish collector [18].

A parabolic trough collector is the next type of concentrating solar collector. It focuses sunlight with the help of highly reflective mirrors onto a receiver tube, containing a working fluid such as oil, which is positioned along the focal line of the trough collector (Figure 1.5). The receiver tube is an evacuated tube collector with a spectrally selective coating inside.



Figure 1.5: Schematic presentation of parabolic trough collector [19].

Temperatures at the receiver can reach from 400 to 500 °C. The materials used in such applications must therefore withstand these temperatures. Cermet coatings (Mo-

SiO_2, W or Mo, Al_2O_3) are mainly used for this purpose. There are some commercially available cermet based coatings on the market, suitable for the receiver tube in parabolic trough collectors. These collectors exhibit high solar absorbance 0.93–0.96 and low thermal emittance 0.1–0.16, but these coatings are only stable in a vacuum [20].

Parabolic trough collectors use only direct radiation and even though they use tracking systems to keep them always facing the sun, they are most effective where there are excellent solar resources. For their efficient use, large areas of such collectors are necessary. The main problem is that the weather conditions are not always perfect and, therefore, their expected output is about 50-80%. The Solar Energy Generating Station (SEGS), located in California's Mojave Desert, is one of the largest parabolic trough power plants ever built. It was developed in the 1980s by the Israeli company BrightSource Energy. It consists of nine solar power plants that have a combined capacity of 354 MW.

The last high-temperature concept is a solar thermal tower (Figure 1.6). Solar-energy concentration and collection is based on a field of individually sun-tracking mirrors (heliostats) that reflect the solar radiation to a receiver (boiler) at the top of a centrally located tower. When the boiler absorbs the radiant solar energy, the heated heat transfer fluid creates a high-temperature flow. Typical heat transfer fluids are water, liquid sodium or molten salts – Hitec, which is a ternary molten salt composed of 53% KNO_3 + 40% $NaNO_2$ + 7% $NaNO_3$. Once the flow is produced, it feeds a conventional turbine to produce electricity, or it is used in thermal storage.

The heat-transfer fluid, which is pumped up the tower into the receiver, usually absorbs 80 to 95 percent of the reflected energy. To maximize the absorption, it is paramount that the receiver is coated with a material that enables the maximum absorption of solar radiation ($a_S > 0.95$). Solar receivers do not operate under a vacuum, as do most trough systems; these coatings must also be resistant to oxidation that may occur over long periods of operation in air. Due to the high operating temperature of the central receiver (> 650 °C) and oxidation of materials at such high temperatures, there is currently only one spectrally selective coating available (Pyromark 2500) on the market. This coating has a_s ~0.97, but e_T is above 0.8 [21], so there are large thermal losses at high temperatures. Ideal absorbers must exhibit high absorbance in the solar spectrum and low e_T (< 0.05) in the IR region. It is essential that they are stable in air (no oxidation), that they are low-cost and are readily manufactured [22].

Moon et al. [23] recently published results showing stable coatings based on cobalt oxide nanoparticles with high thermal efficiency of 88.2%. The coating showed no degradation after 1000 hour at 750 °C in air, while Pyromark 2500 degrades after 300 h at 750 °C for ~3%.

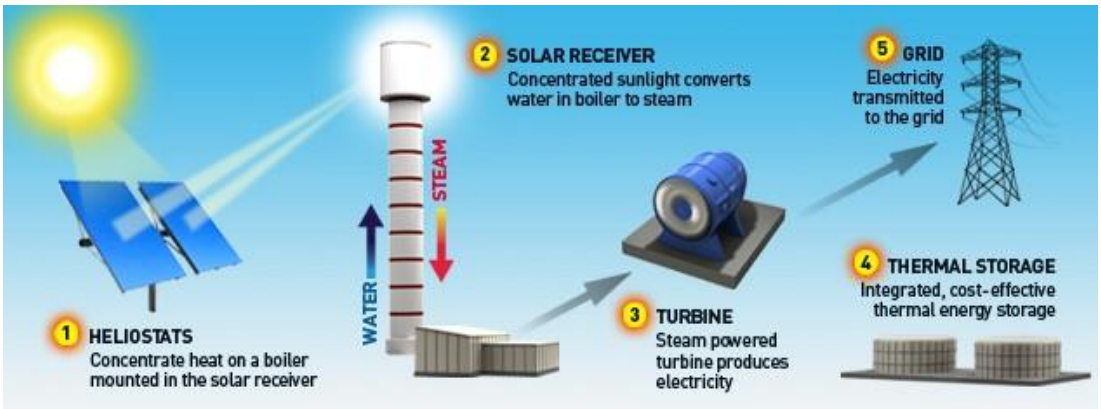


Figure 1.6: Schematic presentation of the solar-thermal tower system [24].

The largest solar electric generating system (ISEGS) based on a solar concentration tower built in California's Mojave Desert started to operate in 2013. It was produced by the Israeli company BrightSource Energy. It consists of 170,000 heliostats (mirrors) which are oriented towards three solar towers and give a combined capacity of 377 MW.

1.2 Electrochromism

Chromism covers the whole field of technologies, in which color changes occur in the visible spectral range. Chromic materials exhibit an ability to change optical properties, such as transmission, reflectance, emittance and/or absorption, under physicochemical changes. Nowadays, several different types of chromism exist: electrochromism (change of colour due to electrical charge or voltage), thermochromism (change of colour due to temperature change) and photochromism (change of colour under UV irradiation) [25] are the most studied ones. Electrochromism in inorganic materials is based on a reversible transmittance modulation that occurs by electrically controlling the oxidation states of the transition metal.

Deb first described the mechanism of electrochromic coloration in WO_3 thin films in 1969 [26]. Later, in 1973, he also described the basic principles of an EC (Electrochromic) device [27]. The main contribution in the field of electrochromism was from C.G. Granqvist, who introduced in his research many organic and inorganic materials that exhibit an EC effect [28]. The idea of developing a thin film on a glass substrate, whereby variation of optical properties is possible, was presented in 1985 [29]. This concept is called a 'smart window'. Since then, research in the field of electrochromic (EC) materials and EC devices has become more and more intense [30-32].

Many materials that exhibit an electrochromic effect have already been researched. Due to the nature of colouration of inorganic EC materials, they can be divided into three groups [28]:

- Materials that exhibit anodic electrochromism – become coloured under charge insertion (reduction process): NiO, IrO_2, Cr_2O_5, MnO_2, FeO_2 and CoO_2
- Materials that exhibit cathodic electrochromism – coloured under charge extraction (oxidation process): WO_3, TiO_2, Nb_2O_5, MoO_3 and Ta_2O_5;
- Materials that exhibit both anodic and cathodic electrochromism - colouration depends on the oxidation state (V_2O_5 in γ-Fe_2O_3).

In addition to inorganic compounds (metal oxides of transition), organic compounds are also known that exhibit an EC response. These are viologens, pyrazoline and conductive polymers [33]. Organic compounds have high potential in the preparation of variously coloured EC devices, due to the different oxidation and reduction state of the molecule – multichromism [34].

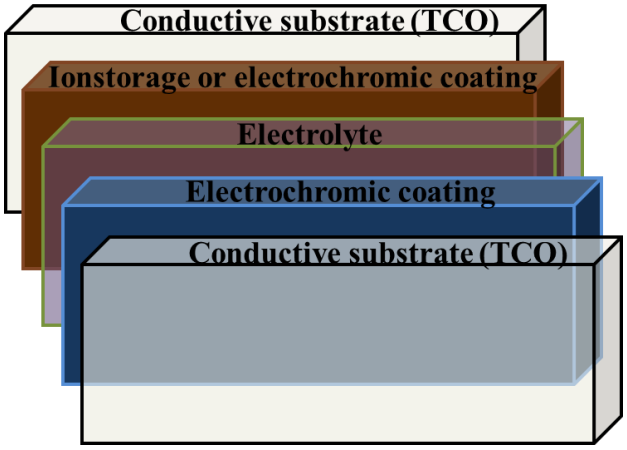


Figure 1.7: Schematic presentation of electrochromic device.

The working principle of an electrochromic device is ion exchange between two electrochromic (EC) layers. The ion resides in one of the EC layers, which can supply the ions during the coloration process. This layer will remain colourless or will have a complementary colour, i.e., the primary EC film gets coloured cathodically while the other EC layer, the ion storage thin film layer gets coloured anodically. The complementary colouring effect will enhance the optical modulation by simultaneously changing the colour of both EC layers.

Most EC devices have a battery-like structure consisting of five layers (Figure 1.7). It consists of two electronically conductive optically transparent layers (TCO) on glass or plastic substrate, an optically active thin layer (working electrode), a counter electrode and an electrolyte in between. The counter electrode can be ″active″, which means that it colours at the same time as the working electrode, or ″passive″, whereby no coloration of the material is present. The electrolyte between the two electrodes serves as the electrical contact and balances the charge on the electrodes by intercalation/deintercalation of ions. Due to the transport of ions, the electrolyte must have ion conductivity ($\geq 10^{-5}$ Ω^{-1} cm^{-1}) and low electrical conductivity ($< 10^{-12}$ Ω^{-1} cm^{-1}). The most commonly used liquid electrolyte is $LiClO_4$ in propylene carbonate.

Due to sealing problems in EC devices, (semi) solid polymer and inorganic solid electrolytes are used. The optical properties of an EC device can be changed by application of a low switching voltage (1 to 5 V) and it reverts to its original state when the polarity of the voltage is reversed. The electric potential during the coloration or bleaching can be controlled at any intermediate stage, which is a great advantage of electrochromism.

Research in the field of electrochromic (EC) materials is becoming more intense, with the goal of producing different prototypes and also commercial products [35]. Beatens et al. [36] wrote a review article in 2010 that presents EC devices and their properties, depending on whether the EC device contains WO_3 or not. WO_3 is the most studied EC material. It is also very durable. One of its most important applications is energy-efficient windows, often called smart windows, used as architectural glazing or skylights, whereby the amount of light and solar-energy passing through can be controlled. The solar heat that enters through such glazing can save energy for air-conditioning in summer and heating in winter. Commercial use of EC devices as smart windows in architecture is still far from reaching its potential, the main reasons being their high cost and relatively low durability (~10 years). In addition to electrochromic devices, there are various devices

that are electrically powered, such as suspended particle devices (SPD), phase dispersed liquid crystals (PDLC) and cholesteric liquid crystals (ChLC)[37, 38].

Most commercially available established EC large area windows are produced by Sage Electrochromics, Inc., EControl-Glass GmBH and Co. KG and Gasimet GmbH [36, 39]. Figure 1.8 shows the colouration and bleaching changes of Gasimet EC windows.



Figure 1.8: Electrochromic behaviour of colour change of Gasimet EC windows [40].

Other applications of EC devices are electrochromic mirrors and sunroofs in cars, motorcycle helmet visors, paper-like displays (e-paper), as well as EC windows in airplanes. The potential for new applications is very broad and promising.

1.3 Photocatalysis

Research of photocatalysis is mainly related to the development of harvesting solar energy. The common point is that all employ technology of converting solar energy into chemical energy to oxidize or reduce materials in order to obtain useful materials.

Photocatalysis is a process that occurs under exposure to light of energies higher than or equal to the bandgap of the material. Highly reactive temporary species are formed on the surfaces of a semiconductor material. The high oxidizing power of these species can induce degradation of many refractory organic and inorganic pollutants on wall surfaces and in water and air. Most of the organic compounds are degraded to CO_2 and H_2O. A photocatalytic effect has been observed in some semiconductor oxides of Ce, Cd, Fe, Nb, Sb, Sn, Ti, W, Zn and Zr. The most common and also most researched material used as a photocatalytic material is titanium dioxide (TiO_2) [41-45]. TiO_2 can be found in different phases, as anatase, rutile or brookite. Brookite, which also exhibits some photocatalytic response, is the least researched phase of TiO_2 [46-48]. TiO_2 in the anatase phase, due to its larger band gap and different surface properties, expresses better photocatalytic activity [49, 50]. Anatase, which is the most photocatalytically active phase, has a band gap ~3.2 eV. The absorption edge lies in the near UV range at 386 nm. Rutile has a band gap ~3.0 eV while the absorption edge is in the visible range at 410 nm.

The best commercially available TiO_2 photocatalyst is undoubtedly P25 from Degussa, which contains a mixture of approximately 70% anatase and 30% rutile phase. TiO_2 has some crucial advantages over other materials that also express a photocatalytic effect: good chemical stability, low price, non-toxic, transparent to visible light, and high reactivity.

Nevertheless, for more extensive application of TiO_2, as a catalyst for the removal of organic pollutants it has relatively low efficiency and a lack of absorption in the visible spectrum. Modification of TiO_2 is therefore necessary and also an important field of research [51].

The beginnings of research into the photocatalytic effect date back to 1972, when Fujishima and Honda [52] discovered that illumination of TiO_2 caused the splitting of water. This was the beginning of a new era in heterogeneous photocatalysis; an area that has attracted significant attention from scientists from a wide range of areas. Since then, many environmental applications showing great promise have been developed, such as photo-electrocatalytic production of hydrogen and renewable energy to disinfect water [53]. Absorbing only 5% of the solar light that falls on the surface of the earth, TiO_2 is still the most investigated semi-conductor; best for storing and converting solar energy. TiO_2 has been applied in recent years to solving environmental problems such as detoxification of water and air.

For solar harnessing applications, photocatalytic TiO_2 is widely used in a variety of applications and products in the environmental and energy fields. In general, these processes can be used in various applications:

- self-cleaning surfaces,
- air purification and deodorizing,
- anti-fogging
- water purification
- hydrogen evolution
- sterilization (anti-bacterial)
- corrosion protection

One of the advantages of TiO_2 is that it shows two distinct photo-induced phenomena. The first is a photocatalytic phenomenon and the second a super hydrophilic phenomenon. Photocatalysis and PSH are intrinsically different processes; they can and in fact must take place at the same time on the TiO_2 surface. In general, it can express a more photocatalytic character and a less superhydrophilic character, or vice versa.

The basic mechanism of TiO_2 photocatalysis is shown in Figure 1.9.

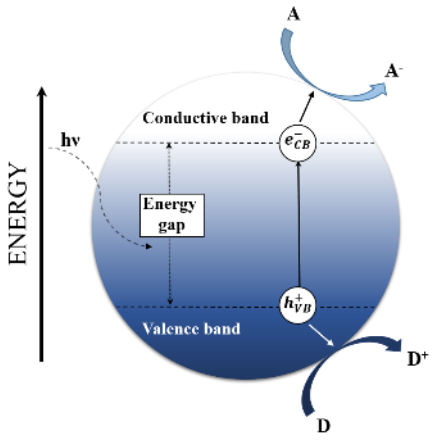


Figure 1.9: Schematic presentation of photocatalytic process.

The primary photocatalytic events are given by reactions (1.1)-(1.4):

$$TiO_2 + h\nu \rightarrow e^-_{CB} + h^+_{VB} \tag{1.1}$$

$$h^+_{VB} + D \rightarrow D^+ \tag{1.2}$$

$$e_{CB}^{-} + A \rightarrow A^{-} \tag{1.3}$$

$$e_{CB}^{-} + h_{VB}^{+} \rightarrow h\nu \; and/or \; \Delta \tag{1.4}$$

The second phenomenon, photo-induced super hydrophilicity (PSH), involves the formation of a highly wettable TiO_2 surface under exposure to ultraviolet (UV) irradiation. This means that the contact angle for water is below 10°. PSH, and consequently high wettability, is caused by photogeneration of electron/hole pairs and their migration to the surface. An increase in the adsorbed hydroxyl group density is caused by oxygen vacancies and leads to the formation of hydrophilic regions. Storage of TiO_2 coatings in the dark, in the presence of oxygen, recovers the surface to its original hydrophobic state, whereby defects, chemisorbed hydroxyl groups, are replaced with oxygen groups [41]. In equation (1.5), a simple surface reorganisation mechanism for PSH is presented:

$$\equiv Ti - O - Ti \equiv \; + H_2O \; \underset{dark}{\overset{O_2, h\nu \geq E_{BG}}{\rightleftarrows}} \; \equiv Ti - OH \; HO - Ti \equiv \tag{1.5}$$

1.4 Spectroscopy

1.4.1 Infrared spectroscopy

Infrared spectroscopy is an analytical technique that allows determination and identification of chemical compounds, or monitoring changes occurring in the course of a chemical reaction. This method is therefore widely used by inorganic and organic chemists. The infrared range of the electromagnetic spectrum is divided into three regions: the near-, mid- and far-infrared. The far-infrared region (400-10 cm^{-1}) has low energy and is mainly used in inorganic studies, due to the stretching and bending vibrations of bonds between the metal atoms and ligands. The most important part of the analytical observation of rotational-vibrational structures is the middle part of the IR-area, between 4000 and 400 cm^{-1}. In the near-IR region (12800-4000 cm^{-1}), absorption bands are weak because they arise from vibrational overtones and combination bands. Combination bands occur when two molecular vibrations are excited simultaneously.

Infrared spectroscopy is based on absorption of infrared radiation into the energy of molecular vibration. The molecule absorbs electromagnetic radiation in the IR range only when the dipole moment of the molecule vibration changes. IR active molecules are therefore heteronuclear diatomic, by which the bond contracts and expands. Symmetrical bonds (O_2, N_2, CH_3-$CH_{3,...}$) do not have a dipole moment and are therefore IR-inactive (homonuclear diatomic molecule).

The probability of absorption of light and, consequently, vibrational frequency, depend on the strength and polarity of the vibrating bonds, which are affected by intra- and intermolecular changes in the structure. The approximate position of an infrared absorption band is determined by the type of bond (single, double, triple), exact position by electron withdrawing or donating effects of the intra- and intermolecular environment, vibrating masses and by coupling with other vibrations. The strength of absorption increases with increasing polarity of the vibrating bonds. The number of possible

vibrations increases with the size of the molecules; infrared spectra of molecules are thus very complex.

Equation (1.6) shows that, in infrared spectra, band positions are presented as wavenumbers ($\bar{\nu}$), which are reciprocal to wavelength (λ).

$$\bar{\nu} = \nu c = \frac{1}{\lambda}[cm^{-1}] \tag{1.6}$$

where $\bar{\nu}$ is vibrational frequency (cm^{-1}), ν frequency of light, c velocity of light (cm/s) and λ wavelength (nm).

The stretching frequency of a bond can be approximated by Hooke's Law, which proposes that two atoms that are joined by a spring are treated as a simple harmonic oscillator. The vibration frequency of the bond $\bar{\nu}$ is related to the reduced mass (μ) and the stiffness of the bond, characterized by a force constant (k), and can be described by the equation (1.7):

$$\bar{\nu} = \frac{1}{2\pi c}\sqrt{\frac{k}{\mu}} \tag{1.7}$$

where $\bar{\nu}$ is vibrational frequency (cm^{-1}), c velocity of light (cm/s), μ reduced mass and k force constant.

Force constant k gives information about the bond strength, whereby the stronger the bond the greater the vibration frequency. The two masses (m_1 and m_2) of the atoms at the ends of the bond give the opposite dependence on the vibration frequency.

$$\mu = \frac{m_1 m_2}{m_1 + m_2} \tag{1.8}$$

where m_1 and m_2 are the masses of the atoms at the ends of the bond.

1.4.2 Attenuated total reflection spectroscopy

Attenuated Total Reflectance (ATR) was developed independently in the 1960´s by Harrick [54] and Fahrenfort [55]. It is nowadays one of the most commonly used FT-IR analysis techniques. Its application covers a broad range of materials for analysis, since it can be used for analysis of solids, thin films and liquids, which cannot be analysed with the traditional FT-IR transmission technique. ATR analysis is therefore used in chemistry (compositional changes), biology, forensic (drug analysis) and pharmacological (imaging to pharmaceutical formulations) research. Its biggest advantage compared to FT-IR sampling by transmission is that there is no need for sample preparation, which speeds up the analysis process. The ATR technique is a non-destructive method.

Basically, two different reflectance measurements can be distinguished: internal or external. ATR uses the property of total internal reflection, resulting in an evanescent wave, whereby the beam of infrared light is passed through the ATR crystal. At the contact surface between the ATR crystal and the sample, the beam reflects at least once off the internal surface, which is in close contact with the sample (Figure 1.10 left). If there are multiple reflections of the infrared light beam in the ATR crystal, the signal intensity is higher than with only one reflection (Figure 1.10 right).

Crystals that are mainly used in ATR analysis exhibit a high refractive index. Typically they are made from zinc selenide (ZnSe, n_1=2.4), zinc sulfide (ZnS, n_1=2.2), germanium (Ge, n_1=4), silicon (Si, n_1=3.4) and diamond (n_1=2.4). Germanium crystal, which has the highest refraction of all the ATR materials is preferentially used for analysis of highly absorbent materials (dark polymers or materials with a high refractive index). Diamond is mostly used as ATR crystal material, because of its hardness, chemical resistance and durability [56].

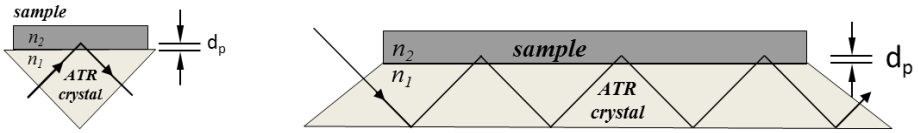


Figure 1.10: Schematic presentation of total internal reflection with single reflection (left) and multiple reflections IRE (internal reflection element) (right).

When electromagnetic radiation travels from an optically denser medium (ATR crystal with n_1) toward an optically rarer medium (sample with n_2), total internal reflection will occur at the interface of the two media, where $n_1 > n_2$. To achieve total reflection, the angle of incidence (θ) must be larger than the critical angle (θ_c), which is given by equation (1.9):

$$\Theta_c = sin^{-1}(\frac{n_2}{n_1}) \tag{1.9}$$

where n_1 is the refractive index of the ATR crystal and n_2 the refractive index from the sample.

The penetration depth d_p of the reflected beam into the sample depends on the wavelength of light and is typically between 0.5 and 5 µm.

The penetration depth (d_p) depends on several factors, such as the wavelength λ, the angle of incidence θ, the refractive index of the ATR crystal n_1, and of the sample n_2. The penetration depth d_p of the reflected beam is described in equation (1.10) as:

$$d_p = \frac{\lambda}{2\pi n_1 \sqrt{sin^2\Theta - \left(\frac{n_2}{n_1}\right)^2}} \tag{1.10}$$

where λ is the wavelength of the incident radiation, θ is the angle of incidence, and n_1 and n_2 are the refractive indices.

Deeper penetration into a sample can be achieved with either a smaller incident angle or a lower refractive index of the ATR crystal. The penetration depth of radiation increases with increasing wavelength of the infrared light [57].

1.4.3 Reflection-absorption spectroscopy

Infrared reflection-absorption (IR-RA) spectroscopy is an instrumental technique mainly used for the study of the chemical composition of thin films, especially the absorption of impurities or degradation processes of the thin film.

The interaction between electromagnetic waves and analysed material describes $\tilde{\varepsilon}(\omega)$ complex dielectric function [58], or complex refractive index $\tilde{n}(\omega)$.We can divide

the real and imaginary part, which can be described by the following equations (1.11) - (1.14):

$$\tilde{\varepsilon}\,(\omega) = \varepsilon'(\omega) - \varepsilon''(\omega) = (\tilde{n}\,(\omega))^2 \tag{1.11}$$

$$Re\,(\tilde{\varepsilon}\,) = \varepsilon'(\omega) = n^2(\omega) - k^2(\omega) \tag{1.12}$$

$$Im\,(\tilde{\varepsilon}\,) = \varepsilon''(\omega) = 2n(\omega)k(\nu) \tag{1.13}$$

$$\tilde{n}\,(\omega) = (\tilde{\varepsilon}\,(\omega))^{1/2} = n(\omega) - ik(\omega) \tag{1.14}$$

where $\tilde{n}(\omega)$ expresses the complex refractive index, $n(\omega)$ *the* refractive index, $k(\omega)$ the extinction coefficient and ω is the frequency.

The IR-RA technique is used for determination of longitudinal optical (LO) modes in spectra, which become visible by using p-polarized radiation. Changes in dipole moments that are detected by the reflection-absorption technique under a high angle of incidence (NGIA – near grazing incidence angle), which is perpendicular to the surface of the thin film (LO modes) are shifted to higher frequencies than the TO vibrational modes parallel to the surface. The angle of incidence α is 70-80°, where LO phonons would be expected to be dominant. Polarised radiation interacts distinctly with LO and TO modes. While normal incidence radiation can only interact with TO vibrations, the p-polarized component of oblique incident radiation has subcomponents parallel and perpendicular to the film surface, which in addition to exciting the TO phonons, can also interact with LO vibrations. The difference between the positions of the LO modes and TO modes in the spectra depends on the polarity of the bond. With organic molecules, this difference is small, while with the characterisation of inorganic material these changes in LO-TO modes can be up to 500 cm^{-1} (TiO_2).

Strong reflectivity from the conductive substrate (metals, glass or semiconductors) decreases at the frequency of the LO mode, which is known as the Berreman effect. This effect was first discovered in 1963 in a study of vibrational spectra of 300 nm thick LiF films [59]. Harbecke, Heinz and Grosse [58] quantitatively described the Berreman effect for films deposited on a metal substrate.

The Berreman effect is maximally expressed at a thickness of the thin layer called the Berreman thickness d_B [58]:

$$d_B = \frac{\lambda}{2\pi}\frac{\cos\alpha}{\sin^2\alpha}\left(Im\left(-\frac{1}{\varepsilon}\right)\right)^{-1}_{max} \tag{1.15}$$

For the Berreman thickness, absorption is nearly one with the LO mode and almost no absorption at the frequency of the TO mode. The Berreman effect enables the detection of spectra and also the characterization of very thin layers on a conductive substrate (below 10 nm). With thicker films ($d > d_B$), in addition to LO, TO modes are also present in the spectra.

The spectral structures (absorption and reflection bands) contribute to the frequency-dependent dielectric properties of the material, the thickness, homogeneity, dielectric and geometric properties of the surface, the angle of incidence and p-polarization of light [57].

The most significant feature of the near-grazing incidence angle (NGIA) spectra are the frequency shifts and the intensity dependence of the observed LO resonance modes, which these modes exhibit as a function of the coating thickness.

1.5 Optical Properties

The solar energy that comes from the sun is actually energy generated by nuclear fusion in the sun's core. The pressures and temperatures in the sun's core are high enough to force atoms of hydrogen to come together in a nuclear fusion reaction; hydrogen fuses into helium. It is the ongoing production of a constant amount of energy, which is sent to Earth in the form of electromagnetic radiation. The solar spectrum consists of a UV region (λ = 0.25 to 0.38 µm), with ~5% of the sun's emission being in this wavelength region. The visible light is a form of electromagnetic radiation that can be perceived by our eyes. Light has a wavelength of between 0.38 to 0.78 µm and 46% of the radiation of the sun is in this zone. Another ~49% of the sun's radiation falls in the region between 0.71 to 4.0 µm.

While all matter emits thermal electromagnetic radiation, the intensity and wavelength distribution is strongly dependent on its absolute temperature, T. Thermal emission (e_T), is the ratio between the infrared light emitted from a surface and that emitted from a perfect black body at the same wavelength and same temperature. According to Kirschoff's law, the emittance is equal to the absorbance. The radiation power, P, from a *black body* increases as the fourth power of the absolute temperature of the same body and it is given by Stefan's law as:

$$P = \sigma T^4 \tag{1.16}$$

$\sigma = 5.67\times10^{-8}\,\mathrm{W/m^2\,K^4}$ is Stefan's constant.

The amount of emission varies with the temperature and the spectroscopic composition of the object, leading to the appearance of coloured temperature and emission lines (Figure 1.11).

For the characterization of spectral selectivity of different coating surfaces, two fundamental parameters are used: solar absorptance (a_S) and thermal emittance (e_T).

Solar absorbance a_S (equation (1.17)) is described as the weighted fraction of absorbed radiation and incoming solar radiation. It is calculated according to [60]:

$$a_s = \frac{\int_{0.3}^{2.5} S(\lambda)(1 - R(\lambda)d\lambda)}{\int_{0.3}^{2.5} S(\lambda)d\lambda} \tag{1.17}$$

where λ is wavelength, $R(\lambda)$ reflectance in the solar spectral region and $S(\lambda)$ is the solar spectrum with an air mass 1.5 (ISO standard 9845-1 (1992)).

Thermal emittance e_T (equation (1.18)) is described as the weighted fraction of emitted radiation and the Planck black body radiation $r(\lambda, T)$ at absolute temperature T [60]:

$$e_T = \frac{\int_{2.5}^{15} r(\lambda,T)\big(1 - R(\lambda)\big)d\lambda}{\int_{2.5}^{15} r(\lambda,T)d\lambda} \tag{1.18}$$

e_T values were calculated for 350 K, being close to the operating temperature of solar collectors.

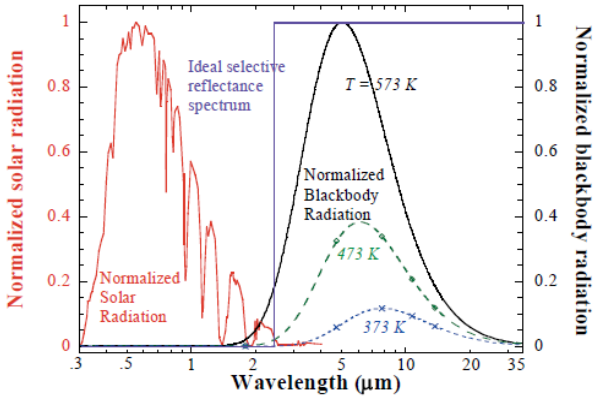


Figure 1.11: The normalized solar radiation spectrum, black body radiation spectra at three different temperatures, and the ideal selective reflectance spectrum [61].

An ideal absorber surface should have zero reflectance (R (λ) = 0) at 0.2 < λ < 3 μm of the solar spectral range in order to maximize the capture of solar energy. In the infrared wavelength range (3 < λ < 100 μm), the coating surface should exhibit reflectance equal to one (R (λ) = 1) in order to minimize radiation losses (Figure 1.11). Various design principles and physical mechanisms can be used to obtain a spectrally selective solar absorbing surface, where in reality the spectral selectivity of a good spectral solar absorber has an absorption edge at about 2 μm [4].

A material is called spectrally "selective" when the optical properties of the material vary with wavelength. This phenomenon is called "spectral selectivity". Surfaces with spectrally selective properties, which are used in solar energy applications, exhibit optical properties such as transmittance (T), reflectance (R), absorbance (A) and thermal emittance (e_T). These values are different at different parts of the electromagnetic spectrum of solar radiation. According to the law of conservation of energy, where for each wavelength (λ), the sum of the intensity of the light that is reflected (I_R), transmitted (I_T) and absorbed (I_A) must equal the intensity of the incident light (I_0):

$$I_T + I_R + I_A = I_0 \tag{1.19}$$

where I_0 is the intensity of the incident light, I_T is the intensity of the transmitted light, I_R is the intensity of the reflected light and I_A is the intensity of the absorbed light.

Whenever an object absorbs energy, its energy rises, and we say that the object has become heated. All components of solar radiation, including visible light, will cause heating when absorbed. IR is readily absorbed into most materials and is, therefore, the component most responsible for heating.

Materials that are transparent are defined by negligible loss in intensity of transmitted light. Surface reflection, absorption and scattering have an effect on the reduction of transmittance.

The reflectance of a coating is determined only by the refractive index, independent of the particle size or coating thickness. The reflectance, R, of a given material can be calculated from equation (1.20):

$$R = \left(\frac{\bar{n} - 1}{\bar{n} + 1}\right)^2 \tag{1.20}$$

where $\bar{n}$ is the complex refractive index ($\bar{n}$ =n+iκ), n the refractive index and κ the extinction coefficient. When κ= 0, no absorption is present, and the reflectance is described by equation (1.21):

$$R = \left(\frac{n - 1}{n + 1}\right)^2 \tag{1.21}$$

If there is no scattering, the transmittance is lowered only by the reflection at the sample's front and back surfaces. It can be described by equation (1.22):

$$T = (1 - R)^2 \tag{1.22}$$

Scattering of light has a large impact on the optical properties of a surface, which is caused by the interaction of light with pigment particles. When particles are much smaller than the wavelength of the light (d << λ), scattering of light is called Rayleigh scattering. It is inversely proportional to the fourth power of the wavelength of light. The scattering produced by such small particles is equal in all directions (isotropic). This type of scattering is also responsible for the blue colour of the sky on a sunny day. The sky is blue because it is the shortest wavelength that we are capable of perceiving with our eyes. Another type of scattering is Mie Scattering, which appears when the diameter of the scattering particle is similar to the wavelength of light (d = λ); scattering is dominated by diffraction. Clouds consist of small droplets, similar to the size of the visible wavelengths of light; when these droplets scatter white light, the clouds themselves appear diffuse and white.

Mie scattering describes the strength of the interactions, which depends on four factors:

- Refractive index of the particle,
- Refractive index of the surrounding medium,
- Size and shape of the particle,
- Wavelength of light striking the particle.

Scattering is the strongest when the difference in refractive indices of the particle and the surrounding medium is large, and the particle size and wavelength of light are similar to one another. The Mie model is an important refractive index of both the sample and the medium. For example, based on Mie's equations, the most efficient scatterer of visible light is a 250 nm large TiO_2 particle [62].

Haze often refers to the visual quality of a material, which is an important parameter in the characterization of materials. It is described as scattering of light that passes through transparent material [63, 64]. It can be caused by material inhomogeneities: scattering from the surface topography, surface contamination, density differences etc. Haze (H %)) of thin films is described as the ratio between diffuse total transmittance DT (λ) and total transmittance TT (λ) (equation (1.23)) in the visible spectral range between 380 and 780 nm [65].

$$H\ (\%) = \frac{DT(\lambda)}{TT(\lambda)} * 100 \tag{1.23}$$

Luminous transmittance (T_{lum}) is defined as the transmission weighted and integrated with the sensitivity curve of the human eye in the visible region of the spectrum (from λ = 380 nm to λ = 780 nm). T_{lum} can be calculated according to equation (1.24):

$$T_{lum} = \frac{\int f(\lambda)T(\lambda)d\lambda}{\int f(\lambda)\,d\lambda} \tag{1.24}$$

where $f(\lambda)$ is the relative sensitivity of the human eye in a photopic condition and T (λ) is the measured transmission spectrum of the thin layer, which is the sum of total contributions of total (TT (λ)) and diffuse transmittance (DT (λ)).

The procedure for measuring haze in transparent materials was developed by ASTM and is described in the ASTM Test Method D1003: "Standard Method for Haze and Luminous Transmittance of Transparent Plastics" [65]. This testing procedure is adequate for laboratory measurements of relatively small samples. Some experimental data on the characterisation of TCO films for solar cells on a large glass sheet have also been obtained [66].

Optical quality (haze) measurements are mainly done with a spectrophotometer equipped with an integration sphere. Sumpner introduced the concept of an integration sphere in 1892 [67]. An integration sphere, also known as an "Edwards Sphere", is a hollow ball, the interior of which is coated with a highly reflective and diffuse substance – polytetrafluoroethylene (PTFE) or barium sulphate ($BaSO_4$) and the detector is in the wall of the sphere. Spheres used for analyzation in the mid-IR region have an interior covered with diffuse gold (InfraGold) [68]. Haze measurements are especially important for optical diffuser manufacturers, who require highly uniform diffusing samples, or in the production of windows and lenses, where very low haze is required in order to minimize scattering of light passing through.

1.6 Deposition Techniques

In my thesis, I will present various application methods that are suitable for the deposition of pigment dispersions onto various substrates. In this work, almost all coatings were deposited by the spin-coating technique. However, spectrally selective coatings have also been deposited on an industrial coil coating line in Alanod (Germany).

1.6.1 Spin coating

Spin coating is an efficient method for the preparation of uniform thin coatings from a solution, dispersion or suspension, which are deposited onto a flat substrate. This technique has been used in various applications, such as optical coatings, antireflective coatings, protective coatings, polymer electronics, photovoltaic cells and membranes.

The spin coating process can be divided into four stages presented in Figure 1.12:
a) deposition,
b) spin-up,
c) spin-off,
d) evaporation.

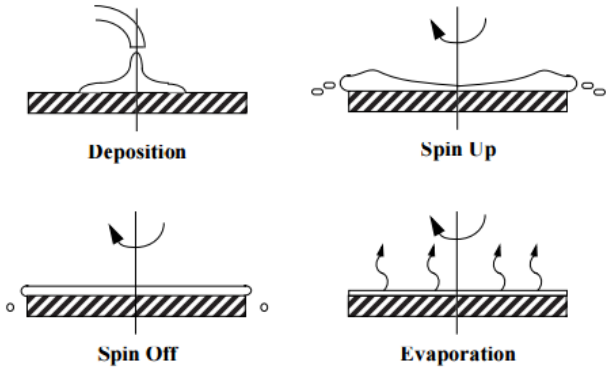


Figure 1.12: The four stages of the spin coating process [69].

In the first phase, the liquid is deposited in an excessive amount through a nozzle onto the centre of a stationary or slowly rotating substrate. An excessive amount of liquid is used to prevent coating discontinuities, which are caused by the liquid front drying prior to it reaching the wafer edge.

In the spin-up stage, the substrate is accelerated to the final spin speed. As rotational forces are transferred upward through the liquid, a wave front forms and flows to the substrate edge by centrifugal force, leaving a fairly uniform layer on the substrate. At low rotating speeds, the layer thickness is higher due to low centrifugal force and viscosity increase due to spin-off [70].

Evaporation is a complex process by which a portion of the excess solvent is absorbed into the atmosphere. It occurs during all stages. At the beginning of the spin-up stage, the layer of the liquid thins due to high centrifugal forces balancing with shear stresses, by which convection of the liquid dominates and evaporation is almost negligible. Changes in the solvent concentration occur only in the narrow boundary layer near the surface. Evaporation of the solvent controlled by diffusion becomes dominant on a longer time scale of spinning, by which the solvent also evaporates from the inner layer of the coating [71, 72].

The film thickness is roughly inversely proportional to the square root of the spin speed. A variety of film thicknesses can therefore be deposited by spin coating. The final film thickness and other properties also depend on the nature of the liquid that is applied to the substrate. For example, the solvent evaporation rate, viscosity of the liquid, liquid density, percentage of solids in the dispersion, surface tension, vapour pressure, temperature and local humidity etc., which cannot always be controlled. On the other hand, acceleration, rotational speed and time of rotation can be controlled.

The thickness of a uniform film during spin-off can be evaluated by the use of the following equation [69].

$$h(t) = \frac{h_0}{\sqrt{1 + \frac{4\rho\omega^2 h_0^2 t}{3\eta}}} \tag{1.25}$$

where h_0 is the initial thickness, η is the viscosity, ρ is the density, t is the time, and ω is the angular velocity.

Equation (1.25) is very useful for Newtonian liquids that do not exhibit shear rate dependence of the viscosity during the spin-off stage. If the liquid is non-Newtonian, i.e.

shear-thinning, the shear rate near the centre of the substrate is lower and, consequently, the viscosity in this area is higher, resulting in higher film thickness. This phenomenon is frequent in sol-gel systems.

The spin coating deposition technique has many advantages, such as easy and fast preparation of uniform films. Moreover, the film thickness can easily be changed by changing the spin speed or viscosity of the deposited liquid. This deposition technique is very fast and cost effective.

There are a few disadvantages of spin coating, and they become more important as the size of the substrate increases. For large substrates, the throughput of the spin coating process decreases because they cannot be spun at a sufficiently high rate for the film to thin and dry in a timely manner. Moreover, the liquid should be deposited on round and not bendable surfaces. Spin coating deposition is a batch deposition technique (only one sample can be coated at a time). Every sample must therefore be monitored for imperfections. Defects may also arise due to poor environmental conditions [73]. The biggest disadvantage of the spin coating method is the lack of material efficiency, because typically less than 5% of the material remains on the substrate.

1.6.2 Dip coating

Dip coating is the oldest and simplest method for the deposition of a thin film on a substrate. The dip coating process is mainly used in research laboratories and rarely in industry for the production of a high-quality thin coating. The deposition of silica coating onto a substrate by dip coating was first performed in 1939. The dip coating technique is mainly used for the deposition of sol-gel coatings, for the production or research of corrosion protective and optical coatings.

The application of a coating using the dip coating technique is usually performed by withdrawing the substrate vertically from the coating bath at a constant speed. It is sometimes very difficult to obtain a high-quality coating by this method. Much care must be taken while lifting the substrate out of the bath, in order to decrease surface defects. A non-constant speed can lead to air bubbles being trapped in the coating. A drip of the solution can remain at the tip of the substrate, leading to variable thickness of the deposited layer, i.e., higher thickness at the tip and lower thickness in the middle of the layer [74]. Dip coating can be performed either by lifting the substrate from the liquid (withdrawing) or by lowering the bath with liquid, i.e., a process in which the substrate remains at rest and the level of the solution is lowered by draining. The withdrawal process is economically more applicable.

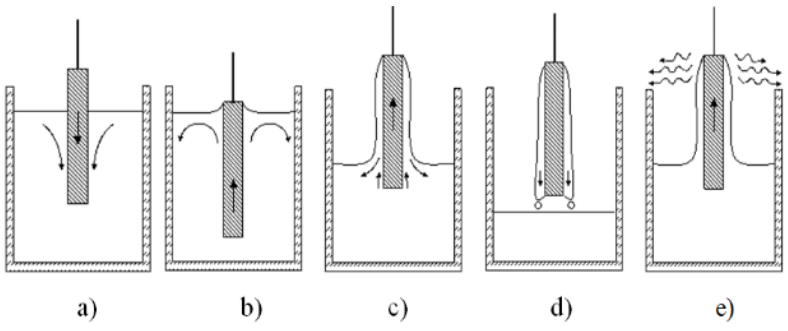


Figure 1.13: Dip coating process [69].

The dip coating process can be divided into five steps (Figure 1.13), proposed by Scriven [75]:

a) Sinking (immersion of the substrate into a bath filled with the deposition liquid)
b) Start of drawing (substrate is pulled-up from the deposition bath at a constant speed)
c) Deposition and drying (the coating thickness is controlled by the withdrawal speed; the coating is formed due to gravitational forces)
d) Drying (the excess liquid is drained from the substrate surface)
e) Evaporating (evaporation of volatile solvents – can be at the same time as drying).

During withdrawal of the coating from the deposition bath, there are six forces that act on the formation of the coating [76]:

- Viscous drag upward on the liquid by movement of the substrate
- Force of gravity
- Resultant force of surface tension in the concavely shaped meniscus
- Inertial force of the boundary layer liquid arriving at the deposition region
- Surface tension gradient
- Disjoining or conjoining pressure (critical for films less than 1 μm thick).

The coating thickness deposited onto a flat surface can be described by the Landau – Lewich equation:

$$h = 0.94 \cdot \frac{(\eta \cdot \nu_0)^{2/3}}{\gamma^{1/6}(\rho \cdot g)^{1/2}} \tag{1.26}$$

ν_0..... withdrawal velocity
γ ..... surface tension
η ..... viscosity
ρ ..... density
g ..... gravitational constant

Dip coating is a simple and cost-effective deposition process, which can easily be automated. This technique enables good coverage of the surface with a coating; moreover, thicknesses of the applied coating below 20 nm can be achieved. The viscosity of the liquid coating is very important and should be between 20–2000 mPa s, because high viscosity gives thicker final coatings. A dip coating technique has some disadvantages. The application is performed at a relatively slow deposition rate (typical withdrawal speeds on a laboratory scale are 0.01–10 mm/s, while for industrial use withdrawal speeds are a bit higher). Furthermore, a large amount of liquid coating is required, leading to the problem of possible contamination. The commonest defects by this deposition are flow lines of liquid around holes or a thicker coating on the lower part of the surface and thin films at the bottom ("wedge effect"). Especially with the deposition of water-based liquids, the presence of foam can cause craters or voids in the final coating.

1.6.3 Coil coating

Coil coating is a continuous and highly automated process, whereby the coating is applied to a metal sheet in a closed system. In this process, the most commonly used substrates are copper, aluminium and cold rolled steel. The field of application of the pre-coated substrate is very versatile. Coil-coating products are used in various areas, such as metal building panels, automotive parts, domestic appliances, heating and ventilation

panels, furniture and packaging etc. [77]. One of the advantages of the coil coating technique is the preparation of cost-efficient and homogeneous coatings on a large scale. The thickness of the applied coating depends on the liquid composition. A thickness of ~ 1-200 µm is usually achieved by depositing speeds ~ 3-250 m/min. The efficiency of coil coating is very high, typically more than 95%. Apart from the deposition, the coating line can also have the possibility of laminated, coined or embossed in-line material. Typical coating requirements are formability, scratch and corrosion resistance, appearance, printability etc.

In practice, two application techniques are commonly used: forward and reverse roll coating deposition. The forward coating deposition technique is used for the application of coatings with thickness 10-200 µm, achieved by the use of liquid with low viscosity (20-1000 mPa s) deposited at relatively low speeds, up to 2 m/s. The main problem of such deposition is that it is sensitive to speed, viscosity and the gap between the rollers. The second technique is reverse roll coating deposition, which allows a wider range of film thicknesses, from 5-400 µm, achieved with coating speeds up to 250 m/min and viscosities of the deposition liquid from 100-20,000 mPa s.

The main disadvantage of the coil coating technique is a high initial investment in the coil coating line. A problem also appears with coating curing (short curing times are required, < 5 minutes with temperatures up to 350 °C), which is insufficient for many coating systems.

A coil coating line can have several steps, which are different for each coating system. Many different coil coating lines are available on the market, by which a single coating can be applied on one or both sides of the substrate. Most aluminium coils can be coil coated with a thin primer coat followed by a two-coat topcoat. However, products with a multi-layer topcoat are also producible.

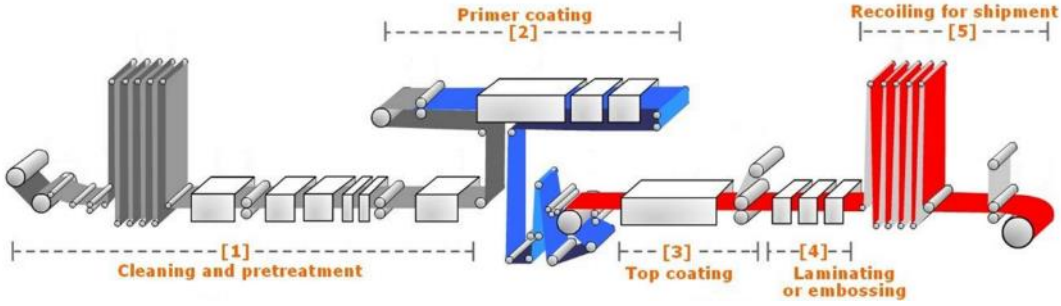


Figure 1.14: Schematic presentation of a coil coating line [78].

In the first step, the bare metal substrate is unwound and cleaned or pre-treated in several steps, whereby all dirt and grease is removed from the surface. A uniform layer is then deposited with the aid of a pickup roller from the pan to the applicator roll, which applies the wet coating liquid onto the substrate (Figure 1.14). Paint in the deposition bath should have a long pot life (the period of time for which the paint can be applied). The applied wet film should be stable enough to prevent surface irregularities before curing, which can occur due to incorrect dilution of the coating, rapid evaporation of the solvent etc.

The next step is curing, in which the coating deposited on the metal substrate passes through an oven, where it is exposed to high temperatures (> 300 °C) for a relatively short time, usually less than 1 minute. The last step of the coil coating deposition is quality control of the deposited coating followed by lamination with permanent plastic foil. The finished metal strip is either rewound into a coil or cut, depending on the customer's specification [74].

The coil coating method is also very useful in the production of thickness sensitive spectrally selective (TSSS) coatings for solar panels, where they should be applied to the aluminium surface with a uniform layer [8, 9].

1.6.4 Spray coating

The application of coatings by spraying is the most commonly used deposition technique in the coatings industry. It is broadly used in large-volume coating applications, such as appliances, automobiles, and wood and paper products. Deposition of the coating is easy, controllable, and very useful for application on non-even substrates, even though the method is very irrational, due to substantial overspray. The transfer efficiency of spray deposition is a significant factor with respect to productivity, cost and environmental savings [79]. It is defined as the amount of material that adheres to the substrate compared to the amount of material that was sprayed toward the substrate and is expressed as a percentage. Transfer efficiency is influenced by various factors, including the skill of the sprayer, size and geometry of the surface being coated, the type of spray gun, gun-target distance, speed of spray gun travel, liquid coating viscosity, liquid and atomizing air pressure etc. One of the disadvantages of spray deposition is environmentally polluting emissions, which are produced by the deposition of solvent-borne coatings with a high content of volatile solvents (VOC) at low transfer efficiency. Most research is nowadays therefore focused on the production of environmentally friendly water-based coatings, with a low VOC content.

Many different kinds of spraying techniques (conventional, airless, electrodeposition, rotary and electrostatic spraying) are available on the market. Transfer efficiency is lowest with conventional spray deposition (30-60%), while airless deposition gives 65-70%, electrostatic spray 65-95% and electrodeposition 90-99%.

Conventional spray application is based on the atomization of the liquid paint using compressed air. Atomization is the process of generating drops by forcing liquid through a nozzle. A cloud of very fine droplets (aerosol) is deposited onto the substrate surface. Velocity and average droplet size are the most important parameters in spray coating deposition. Prediction of the theoretical spray impact is therefore crucial.

The following equation can be used for the calculation of the theoretical spray impact:

$$I = K * Q * \sqrt{P} \tag{1.27}$$

where I is the total theoretical spray impact [kg], K is constant (0.028), Q the flow rate [l/min] and P the liquid pressure [kg/cm^2].

The actual spray impact values depend on the spray pattern distribution, nozzle type, and spray angle and are much lower than the theoretical values calculated from equation (1.27).

Chapter 2

Aims of This Work

The overall aim of this work is to contribute to understanding the influence of different dispersants used in the preparation of pigment dispersions applied to various end products:

1. Study of the influence of differently substituted trisilanol POSS dispersants in relation to the rheological and optical properties of the spectrally selective coating. (Paper I: L. Slemenik Perše, M. Mihelčič, and B. Orel, "Rheological and optical properties of solar absorbing paints with POSS-treated pigments," *Materials Chemistry and Physics,* vol. 149–150, pp. 368-377, 2015)

2. Preparation and characterisation of a novel spectrally selective coating based on sol-gel, in which a hybrid crosslinker was used to improve the thermal stability of coatings. (Paper II: M. Mihelčič, V. Francetič, J. Kovač, A. Šurca Vuk, B. Orel, R. Kunič, and D. Peros, "Novel sol–gel based selective coatings: From coil absorber coating to high power coating," *Solar Energy Materials and Solar Cells,* vol. 140, pp. 232-248, 2015)

3. Study of interactions between hepta-isobutyl trisilanol POSS dispersant and the TiO_2 surface and determination of the electrochromic properties of TiO_2/POSS thin films. (Paper III: M. Mihelčič, V. Francetič, P. Pori, H. Gradišar, J. Kovač, and B. Orel, "Electrochromic coatings made of surface modified rutile and anatase pigments: Influence of trisilanol POSS dispersant on electrochromic effect," *Applied Surface Science,* vol. 313, pp. 484-497, 2014)

4. Study of the optical and electrochromic behaviour on different commercial TiO_2 pigments, modified with and without hepta-isobutyl trisilanol POSS dispersant and preparation of foil based electrochromic device. (Paper IV: M. Mihelčič, A. Šurca Vuk, D. Vrhovšek, F. Švegl, M. Hajzeri, and B. Orel, "Foil-based TiO_2/gel electrolyte/$Ni_{1-x}O$ electrochromic device made of electrochromic pigment coatings," *Acta Chimica Slovenica*, vol. 61, pp. 517-529, 2014)

5. Characterisation of electrochromic properties of $Ni_{1-x}O$ in lithium and lithium-free aprotic electrolytes and characterisation of the influence on the presence of Li^+ ions in the electrolyte used for foil based electrochromic device. (Paper V: M. Mihelčič, A. Š. Vuk, I. Jerman, B. Orel, F. Švegl, H. Moulki, C. Faure, G. Campet, and A. Rougier, "Comparison of electrochromic properties of $Ni_{1-x}O$ in

lithium and lithium-free aprotic electrolytes: From $Ni_{1-x}O$ pigment coatings to flexible electrochromic devices," *Solar Energy Materials and Solar Cells,* vol. 120, pp. 116-130, 2014)

6. Study of the influence of different surface modifiers on TiO_2 – P25 pigment dispersion in terms of photosuperhydrophilicity (PSH) and photocatalytic (PCA) effect. (Paper VI: M. Mihelčič, B. Orel, F. Fresno, U. Štangar Lavrenčič, and R. Kunič, "Preparation of Photocatalytic Optically Transparent Coatings from Pigment Dispersions," *Journal of Surfaces and Interfaces of Materials,* vol. 2, pp. 280-287, 2014)

7. Study of the chemical interactions between cotton and titania/silica hybrid coating in relation to antimicrobial photocatalytic properties. (Paper VII: B. Tomšič, V. Jovanovski, B. Orel, M. Mihelčič, J. Kovač, V. Francetič, and B. Simončič, "Bacteriostatic photocatalytic properties of cotton modified with TiO_2 and TiO_2/aminopropyltriethoxysilane," *Cellulose,* vol. 22, pp. 3441-3463, 2015)

With respect to the aims explained above, we expected to verify that the trisilanol POSS and its derivatives were suitable compounds for dispersing different pigments and manufacturing of pigment dispersions enabling the deposition of pigment coatings with optical properties (low haze, high and/or low transmittance), high abrasion resistance, temperature stability and adequate electrochromic response. Such a variety of properties we expected to be achieved only when dispersant molecules was attached on the pigment surface in a form of thin layer, which modified the interactions between pigment/solvent/resin binder in a way that stable homogeneous pigment dispersion was obtained.

For the $Ni_{1-x}O$ based electrochromic coatings we expected that trisilanol POSS dispersant could not work because the trisilanol POSS blocked surface of the pigment particles and prevented their electrochromic effect. Accordingly, we wanted to verify that by using water based Ni oxyhydroxide (NiO_xH_y) dispersant and water medium for milling the $Ni_{1-x}O$ electrochromic particles, it was possible to make stable pigment dispersions with high optical transmittance and large colouring/bleaching changes and persistence electrochromic effect. The main challenge was to check that dispersant used enabled charging/discharging of the $Ni_{1-x}O$ particles merely by the insertion/extraction of electrons, but the insertion/extraction of lithium ions was not compulsory for achieving the electrochromic effect. In this case the electrochromic devices where the electrolytes did not contain lithium ions should also exhibit electrochromic effect.

Chapter 3

Rheological and Optical Properties of Solar Absorbing Paints with POSS-Treated Pigments

The challenge of this work is to find a common denominator of otherwise quite different systems. The main focus was on the use of a polyhedral oligomeric silsesquioxane (POSS) molecule as dispersant for pigment surface modification. The commercial use of POSS with the composition $(RSiO_{3/2})_n$ (R = organic group, n = 6, 8, 10, 12,...) has been developed in recent years [80], although the synthesis was already published in 1965 [81]. POSS molecules are the smallest silica in nature with dimensions of 0.8 to 1.5 nm. They are typical organic-inorganic hybrids and, in terms of their characteristics, they are similar to bridging polysilsesquioxanes (bridging POSS) but from which they differ by their well-defined polyhedron structure. They most often appear in the form of cubes with eight corners (hence the name octamer T_8 POSS) but there are other known polyhedron structures (T_{10}, T_{12},...) with organic groups (polifunctionalized POSS) attached at the corners. Various organic groups (acryloxy, epoxy, mercapto, amino, isobutyl, isooctyl, methyl, perfluorooctyl etc.) can be the same on all corners or a polyhedron can have corners with various functional groups attached. Among a host of different POSS compounds, the focus was on isobutyl trisilanol POSS (IB_7 $(OH)_3$ T_8 POSS) with an open structure (one of the vertices of the -$(SiO_{3/2})_7$ octahedron is missing) and three OH groups. There are many reasons for this choice: polarity of -OH groups is large and in contrast to non-polar isobutyl groups at the corners of the octahedron. A molecule that has a polar head and a hydrophobic tail (tadpole model) is in a condition for the orientation of interactions with polar groups, which are located on the surface of the pigments. Adsorption of trisilanol isobutyl POSS on the surface of the pigment from non-polar media occurs spontaneously. Trisilanol isobutyl POSS are known as "superdispersants", which means that they enable incorporation of a high concentration of the pigment (high pigment loading) in the dispersion, without an excessive increase in its viscosity.

For this study, it was also important that the analogues isooctyl trisilanol POSS and phenyl trisilanol POSS are known, allowing systematic research of the adsorption properties. This comparison was made because different substituent R-groups attached to the corner of an open cage-like structure with reactive silanol groups (trisilanol POSS), can cause different interactions with the pigment.

The preparation of thickness sensitive spectrally selective (TSSS) coatings with pigment dispersions is a very complex task. My first task within the framework of this thesis study was therefore to define the dispersion properties of selected POSS, which was done by means of rheological studies of three different functionalized (isobutyl, isooctyl or phenyl) trisilanol polyhedral oligomeric silsesquioxanes (POSS) (Figure 3.1) dispersant agents on black manganese spinel pigment (PK 3060 - $CuFeMnO_x$). The influence of the POSS structure on the rheological and spectral selective properties has previously been insufficiently investigated.

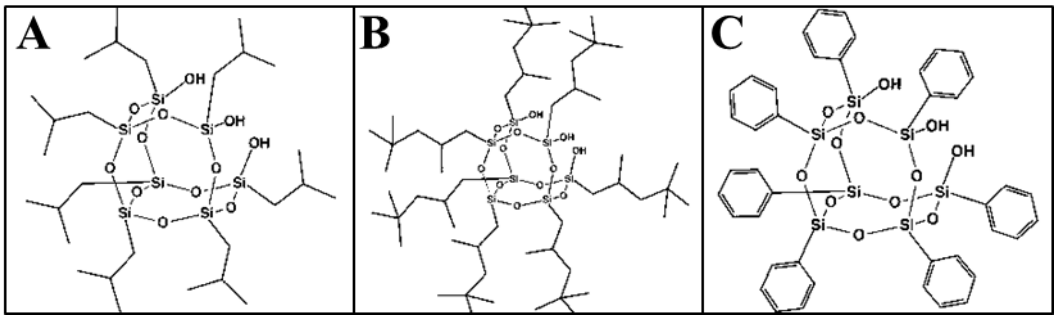


Figure 3.1: The structure of A) isobutyl (Ib_7), B) isooctyl (IO_7), C) phenyl (Ph_7) trisilanol POSS molecules [80].

The mechanism of chemical attachment of isobutyl trisilanol POSS onto the surface of black spinel pigment has already been described by Jerman et al [7]. The use of the other two dispersants for the preparation of spectrally selective coatings was new. The interactions of trisilanol POSS with pigment are typically observed by infrared spectroscopy. The results disclosed in this article enabled the conclusion that isooctyl and phenyl trisilanol POSS dispersants have a similar mechanism of attachment onto the black pigment surface.

Black pigments used for the preparation of spectrally selective coatings are mainly manganese spinels doped with Co, Fe and Cu, known by their distinctive solar absorptance, chemical inertness, and excellent UV, thermal (> 500 °C) and oxidation stability. Spinel oxide pigments have the general formula AB_2O_4, (A, B = Ni, Co, Fe, Cu). While cations can exist in a variety of oxidation states (+2, +3, +4), they allow us to adjust their optical properties chemically (doping with different transition metals). In our studies, $CuFeMnO_x$ spinel pigment was used but, due to its similar characteristics, $FeMnO_x$ spinel pigment can also be used.

IR spectroscopy provides information about the efficiency of the modification process, by which a change of characteristic functional groups can be evaluated. By analysis of trisilanol POSS dispersants, the disappearance of the silanol (Si-OH) bands was observed, as well as the concurrent presence of the Si-O…substrate [82] and the siloxane (Si-O-Si) modes. An asymmetric Si-O-Si mode band corresponding to the silsesquioxane cages in isobutyl trisilanol POSS can be observed at 1118 cm^{-1} [83]. Stretching bands include CH_2 (2927 and 2903 cm^{-1}) and CH_3 (2954 and 2871 and 2817 cm^{-1}) groups and corresponding deformational modes (1461, 1350, 1228, and 839 cm^{-1}). Infrared spectra of pigment modification with isobutyl trisilanol POSS revealed that the bands at 1228 and 2954 cm^{-1} (-CH_3 deformational mode) allow identification of the establishment of covalent interactions between the trisilanol POSS and the surface of the pigment. The intensity of these peaks increases with the concentration of isobutyl trisilanol POSS used as a dispersant, until the pigment surface is completely covered. The surplus trisilanol POSS dispersant that was not attached to the pigment surface can be washed with THF [7]. The surface modification of spinel pigment particles with isobutyl trisilanol POSS was

further confirmed by TEM, EDAX and XPS analyses. In addition, thermogravimetric (TG) measurements revealed that 5% of the POSS dispersant was covalently bonded to the pigment surface.

The infrared spectra of pigment modification with isooctyl trisilanol POSS showed that the intensity of the peak at 2906 cm^{-1} (-CH_3 deformational mode) decreases after three times washing in THF (Figure 3.2). Hydroxyl groups on the surface of black pigment are reactive sides for reaction with Si-OH groups from trisilanol POSS molecules. The -OH valence band shifts to a higher value, i.e., from 3367 to 3429 cm^{-1}. The peak at 1626 cm^{-1} (-OH stretching) is present in the modified pigment, which had been washed with THF three times. The Si-O-Si band at the 1116 cm^{-1} mode and Si-OH band at 890 cm^{-1} are less pronounced when the pigment is repeatedly washed.

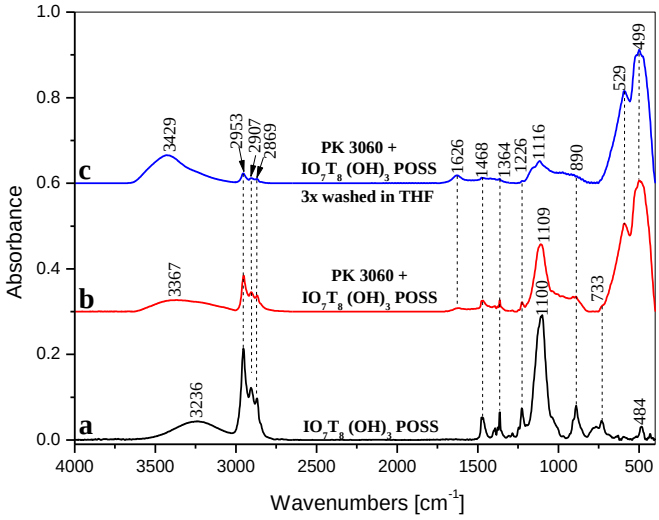


Figure 3.2: IR transmission spectra of a) $IO_7T_8(OH)_3$ POSS, b) PK 3060 pigment modified with $IO_7T_8(OH)_3$ POSS and c) PK 3060 pigment modified with $IO_7T_8(OH)_3$ POSS 3x washed in THF.

The mechanism of grafting phenyl trisilanol POSS onto the surface of TiO_2 was presented by Nowacka et al. [84].The preparation of dichlorotriazine dye functionalized with isobutyl and phenyl trisilanol POSS was presented by Spoljaric et al. [85]. In the infrared spectra of phenyl trisilanol POSS (Figure 3.3), Si-O-Si bands at 1134 and 1103 cm^{-1} and Si-OH stretching vibrations at 890 cm^{-1} were observed. Stretching bands in the trisilanol POSS open-corner cage include CH_3 (3072, 3051 and 3027 cm^{-1}) groups. Sharp deformational modes, found at 1595, 1570, 1490 and 1430 cm^{-1}, were ascribed to C=C bands in the phenyl ring and C–H bending vibrations at 740 and 696 cm^{-1}. Between 2000 and 1650 cm^{-1}, bands with weak intensities that also belong to stretching bands of the phenyl ring were observed. The intensity of bands at 1595, 1430 and 1103cm^{-1}, presenting on the surface of the pigment particle modified with phenyl trisilanol POSS by washing in THF, was reduced but the bands were still visible. This indicates that the surplus dispersant, unattached to the pigment surface was washed away, and there was only a monolayer of covalently bonded phenyl trisilanol POSS molecules present.

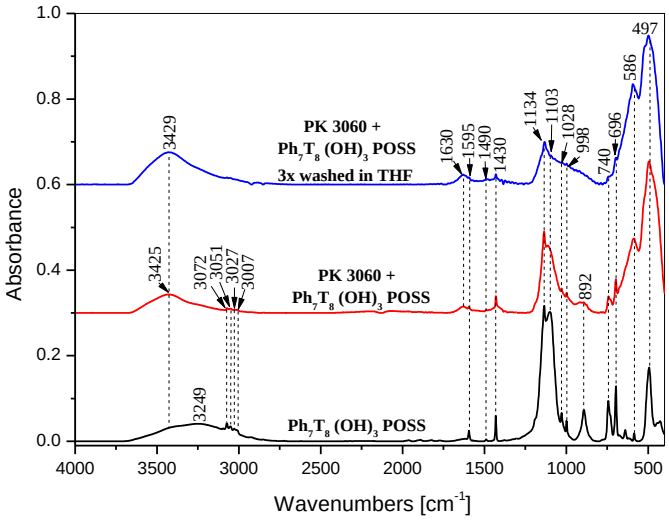


Figure 3.3: IR transmission spectra of a) $Ph_7T_8(OH)_3$ POSS, b) PK 3060 pigment modified with $Ph_7T_8(OH)_3$ POSS and c) PK 3060 pigment modified with $Ph_7T_8(OH)_3$ POSS 3x washed in THF.

Rheology is the science of the flow and deformation of matter caused by the influence of mechanical forces acting on the unit area. In general, the behaviour of fluids can be divided into two groups: Newtonian fluids (viscosity depends only on the temperature and pressure) and non-Newtonian fluids (viscosity is dependent on the temperature and pressure, but also on shear conditions). Except gasses and most liquids with a simple molecular formula and low molecular weight (e.g., argon, N_2 and hydrocarbons), many fluids (also pigment dispersions) exhibit non-Newtonian flow behaviour. The dispersion process is the entire procedure of embedding solid particles in the liquid medium, so that the final product consists of primary pigment particles that are equally distributed in a liquid medium. The result of the dispersion process depends on various factors, such as: shear forces, surface tension, viscosity, contact angle between the liquid medium and pigment, as well as various interactions that appear between solid particles and molecules in the liquid phase.

In the continuation of the article, the influence of the pigment volume fraction (PVC) on flow behaviour for modified and unmodified pigment in silicon oil is presented.

The addition of a higher concentration of particles into the system increases the viscosity of the liquid and can change the rheological behaviour of the pigment dispersion, i.e., shear rate dependent viscosity, elasticity and time-dependent behaviour, or even the occurrence of apparent yield stress [86]. The characterization of the microstructure and flow properties of pigment dispersions is therefore necessary for understanding and controlling their rheological behaviour. The purpose of these measurements was to increase the PVC to maximum packing volume with the desired fluidity, while maintaining sufficient stability against sedimentation, aggregation and agglomeration of the particles [87]. Two fundamental interactions exist between particles in pigment dispersion: one being attractive and the other repulsive. When the attraction forces dominate, the particles adhere to each other and, finally, the entire dispersion may flocculate when the system is diluted with solvent or solvent/resin binder solution. When repulsion forces dominate, the system is stable and remains in a dispersed state non-aggregated and dispersed. Van der Waals forces are the primary source of attraction

between colloidal particles and are always present between particles of similar composition. A pigment dispersion is therefore said to be stable only when a sufficiently strong repulsive force counteracts the van der Waals attraction. For many colloid systems, the range of Van der Waals attraction forces is between 5 and 10 nm.

High pigment loadings of the pigment dispersion in the coating can be achieved only through suitable modification of the surface of the pigment particles. The dispersant in the pigment dispersion thus allows a more homogenous distribution of the pigment and incorporation of higher pigment loadings into the binder. Trisilanol POSS dispersants, due to their regular structure, polarity and tadpole geometry, enable various functionalization of pigments and, therefore, the preparation of materials with multifunctional properties. In Figure 3.4, the influence of variously trisilanol POSS dispersant-modified black pigment in silicon oil on the viscosity versus PVC ratio is presented.

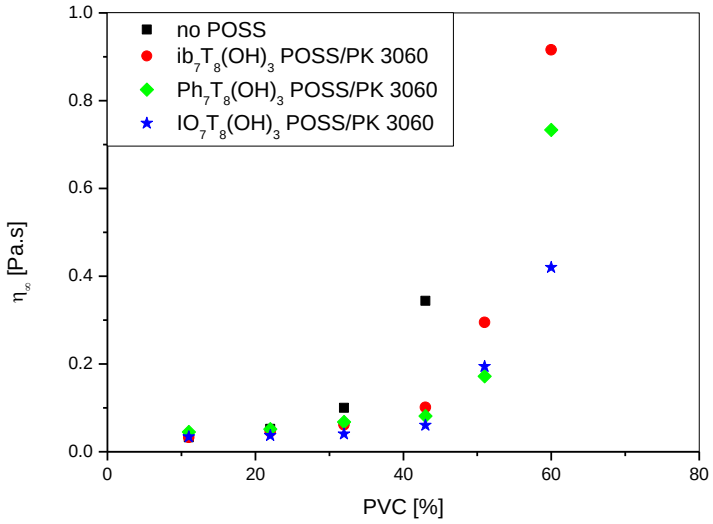


Figure 3.4: Viscosity dependence of PVC ratio for dispersions of untreated and POSS modified pigment in silicon oil.

The preparation of spectrally selective coatings is then shown. Different PVC ratios were prepared and tested in order to find the best physical and chemical coating characteristics (i.e., hardness, gloss, corrosion resistance, density of coating, hydrophobicity, oleophobicity and spectral selectivity) of the final dry coating.

In the final part of the study, the pigment dispersions were deposited on aluminium substrate by the spraying technique. The efficacy of the dispersant was checked by the deposition of various coatings and assessment of their spectral selectivity. It was surmised that the highest spectral selectivity is attained only when the pigment particles are uniform in size, well packed in a homogeneous paint coating and, as such, exhibit high solar absorptance. Since this is achieved only when the particles are well dispersed and form a compact, for solar light nearly opaque layer, the corresponding paint coating has low thermal emittance. Coatings with various thicknesses did not show visual defects. Spectral selectivity was assessed from a_S and e_T values, while the visual appearance of the same coatings was determined by CIELAB colour space measurements.

My contribution to this study was (i) the selection of three different POSS systems used for the modification of black PK 3060 pigment, (ii) the modification of the

PK 3060 pigment with various (isobutyl, isooctyl and phenyl) trisilanol POSS molecules, (iii) the preparation of pigment dispersions and measuring their spectral selectivity.

Materials Chemistry and Physics 149-150 (2015) 368–377

Contents lists available at ScienceDirect

Materials Chemistry and Physics

journal homepage: www.elsevier.com/locate/matchemphys

Rheological and optical properties of solar absorbing paints with POSS-treated pigments

Lidija Slemenik Perše*, Mohor Mihelčič, Boris Orel

National Institute of Chemistry, Ljubljana, Slovenia

HIGHLIGHTS

- POSS dispersants influence the rheological behavior of liquid paints.
- POSS improve solar absorptivity of dry solar absorbing coatings.
- Proper rheological properties are essential for uniform distribution of pigment.
- Rheological properties could be used to predict solar absorptivity of TSSS coatings.

ARTICLE INFO

Article history:
Received 4 October 2013
Received in revised form
26 September 2014
Accepted 16 October 2014
Available online 24 October 2014

Keywords:
Thin films
Coatings
Optical properties
Thermal properties

ABSTRACT

Thickness sensitive spectrally selective (TSSS) coatings should be capable of absorbing high amounts of solar energy, i.e. they should exhibit high solar absorptivity. However, due to their sensitivity to thickness, it is extremely difficult to prepare uniform, smooth and thin coatings with dense distribution. In our study, we prepared black TSSS paints at various PVC ratios by using a pigment that was treated with trisilanol POSS dispersants. Various POSS dispersants were used for pigment treatment in order to determine the influence of POSS structure on the rheological behavior of liquid paints and the solar absorptivity of applied coatings. Liquid paints were prepared at various PVC ratios in order to examine the effect of pigment loading on the rheological behavior of the paint. The rheological properties were correlated to the solar absorptivity of coatings applied on the substrate. The results revealed that POSS dispersants enable the preparation of dispersions with particularly high pigment loadings (above PVC = 51), which still exhibit liquid-like viscoelastic behavior and are sufficiently flowable to enable proper leveling, uniform distribution of pigment particles inside dry coating and, therefore, excellent solar absorptivity.

© 2014 Elsevier B.V. All rights reserved.

1. Introduction

Due to increasing interest in the exploitation of renewable energy sources, absorbers for solar thermal applications are becoming increasingly important. Paint coatings for solar absorbers that are capable of absorbing high amounts of solar energy and emitting low amounts of thermal energy back to the surroundings are called spectrally selective. Their spectral selectivity can be sensitive to thickness (these paints are called thickness sensitive spectrally selective: TSSS paints) or insensitive to thickness (thickness insensitive spectrally selective: TISS paints).

In general, TSSS paints are extraordinarily complex systems consisting of a binder, additives, solvent and pigment particles, which should be evenly distributed (dispersed) in a polymeric resin binder. Due to the variety of many compounds, the rheology of these paints is a complex function of physical properties and processes that occur at the scale of the suspended particles. Flow and leveling, viscosity and applied shear by application technique are typical parameters in the science of rheology, which are crucial in order to solve not only aesthetic but also functional problems (gloss, flow, leveling, application disadvantages, spectral selectivity) [1–4]. The factors influencing the rheological properties of paint and the quality of final coating are particle volume fraction (PVC), particle shape, interactions between particles, distribution of particles inside coating film, and the nature of the bulk flow field [5]. In order to meet different requirements, dispersion paints need to have high viscosities in the low shear rate range to avoid settling and instability during storage and transport of the paint. At the same time, the paints need to have low viscosities in the high shear rate region that corresponds to the application process [3]. Such

* Corresponding author.
E-mail address: lidija.slemenik.perse@ki.si (L. Slemenik Perše).

http://dx.doi.org/10.1016/j.matchemphys.2014.10.031
0254-0584/© 2014 Elsevier B.V. All rights reserved.

behavior, called shear-thinning or pseudoplastic behavior, should be upgraded with time-dependence, called thixotropy, which supports storage stability at zero shear and enables slower structure reformation, which results in better flow and leveling [6].

For the optimal performance of solar thermal systems with TSSS coatings, it is essential that they exhibit high solar absorptivity, while liquid paints should simultaneously exhibit rheological properties that assure easy application and stability against sedimentation at rest. The low emissivity of these coatings is closely related to the properties of the binder, which should be transparent in the infrared region. It has recently been shown that there is a significant relation between the infrared emissivity and binder viscosity [7]. More significant is solar absorptivity, which largely depends on the properties and distribution of pigment particles. High values of solar absorptivity could be attained by increasing the amount of high absorbing pigment particles, which should be evenly distributed inside the polymer binder. However, high amounts of pigment (solid) particles usually lead to high viscosity and rheologically extremely complex liquid paints that are impossible to apply, especially in the low thicknesses required for TSSS coatings. Furthermore, binder and pigment particles are not the only compounds influencing spectral selectivity. Dispersants are also important additives. Their use and selection in the course of paint preparation is considered to be the most crucial step in the production of any paint [8]. Dispersants are materials that are capable of providing the compatibility of the pigment particles with the polymeric phase by modifying their surface, which means altering it from hydrophilic to organophilic. The effect of the dispersant can be inferred from the optical properties of the coatings, as well as from the rheological behavior of the paint during its deposition and the formation of selective coatings.

In order to prepare thin TSSS paints with high pigment loading, we treated the pigment with Polyhedral Oligomeric Silsesquioxane (POSS) dispersants. We used POSS because they can act as efficient surface modifiers enabling the preparation of highly concentrated pigment dispersions in a binder. Incorporation of POSS cages into polymeric resin binder may result in dramatic improvements in final properties, can affect the morphology and may change the rheological and viscoelastic properties [9,10]. POSS dispersants could be used in highly filled resins due to their ability to decrease viscosity. They strongly bond to the surface of the pigments and break up particle–particle interactions. The result is increased productivity, improved mechanical properties and surface finish. Due to viscosity reduction, more pigment can be added to the binder while maintaining the desired viscosity. Consequently, a lower amount of solvent is needed, which reduces the amount of volatile organic components (VOC). The paint production and the paints themselves are therefore less harmful to the environment and to the health of the people producing the paints.

Many papers are published in the literature regarding solar paints and chemical structure of pigments and dispersants. However, only few papers, to our knowledge, are concerning rheological properties of solar paints and almost nothing has been reported about the synergistic effect of all together. In this paper, different commercially available POSS were used as dispersants for the treatment of the pigment. In the first step, pigments were dispersed in silicon oil at various pigment loadings in order to determine the influence of the PVC ratio, the pigment treatment with POSS, and the POSS structure on rheological behavior of dispersions. In the second step, TSSS paints were prepared with the same treated and untreated pigments as dispersions with silicon oil. A detailed rheological characterization of the paints with various pigment treatments presented the behavior of the paints during storage and drying (at rest) and application process (high shear). After the deposition of the paints on the substrate, solar absorptivity and colorimetric properties of dry coatings were investigated at different thicknesses. The rheological properties of liquid paints were correlated with the functionality of dry coatings.

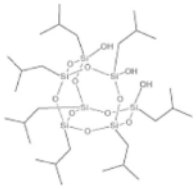
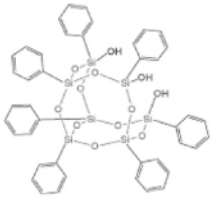
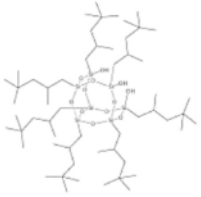
2. Experimental

2.1. Preparation of paints

Black Cu–Mn–Fe pigment with spinel crystal structure (Ferro, D) was used with and without treatment with POSS dispersants. 10 wt.% of trisilanol POSS dispersants: IBu POSS, Ph POSS and IO POSS (Hybrid Plastics) with different types of peripheral R groups on the cage core of the molecule (Table 1) were used for pigment treatment. Pigment dispersions based on Newtonian silicon oil as a model binder were used in order to examine the influence of pigment loading on rheological properties. TSSS paints were prepared with fluoropolymer resin binder (Lumiflon 200, Asahi Glass Co., Ltd., Japan) following the same procedure. The pigment was treated with POSS by dissolving trisilanol POSS in hexane to which the black pigment PK3060 was added and mixed with a high speed dissolver (Dispermat CNF2 (VMA-GETZMAN GMBH, D). Dispersion was then displaced to a ball mill (glass balls $\Phi = 3$ mm, 4000 rpm) and milled for 2 h. We repeated the same procedure for each of the trisilanol POSS. Different pigment-to-volume concentrations (PVC) of the pigment and binder examined, were calculated with the following formula [8]:

$$\mathrm{PVC}(\%) = \frac{V_p}{V_p + V_b} \times 100, \quad (1)$$

Table 1
Chemical structure and commercial names of POSS dispersants (Hybrid Plastics) used in the study.

Abbreviation	Commercial name	Chemical structure
IBu POSS	Trisilanol Isobuthyl POSS	$C_{28}H_{66}O_{12}Si_7$ 
Ph POSS	Trisilanol Phenyl POSS	$C_{42}H_{38}O_{12}Si_7$ 
IO POSS	Trisilanol Isooctyl POSS	$C_{56}H_{122}O_{12}Si_7$ 

where V_p is the volume of the pigment and V_b is the volume of the binder. In the study, the same PVC (PVC = 22, 32, 43 and 51) was used for TSSS paints with treated and untreated pigments (a total of 16 different TSSS paints).

2.2. Application of the paints

Liquid paints were deposited on aluminum substrates by a Walther Pilot WA 520 HVLP spray gun with an operating pressure of $2.5 \cdot 10^5$–$3 \cdot 10^5$ Pa.

The morphology of the dry coatings that were prepared from liquid TSSS paints was analyzed by SEM micrographs followed by EDX compositional analysis. Fig. 1 shows the differences between low and high values of the PVC ratio for pigment with dispersant IO POSS. At a low PVC ratio (PVC = 22, Fig. 1A), the pigment was sparsely distributed over the coating, which was heavily covered with flouropolymer binder hence the amount of fluorine, obtained by EDX analysis, was high, while the amounts of Mn, Fe and Cu – the elements of the pigment – were low. On the other hand, at higher values of the PVC ratio (PVC = 51, Fig. 1B), the distribution of the pigment was extremely dense and uniform resulting in high values of Fe, Mn and Cu and lower amount of fluorine F.

The thickness of dry coating was determined by measuring the mass and the area of the coating before and after the application on the substrate. Once the mass and area have been determined, the thickness was calculated by dividing the mass by the area and the results were presented in g/m^2.

2.3. Instrumental

Rheological measurements were performed with a rotational controlled rate rheometer (Physica MCR301, Anton Paar), equipped with a cone and plate sensor system (CP 50/2°). All rheological measurements were performed at a constant temperature $T = 23$ °C.

SEM micrographs and EDX compositional analysis were obtained via an FE-SEM Supra 35 VP (Carl Zeiss) electron scanning microscope.

Reflectance in the visible (VIS) and near infrared (NIR) ranges were measured using a Perkin Elmer Lambda 950 UV/VIS/NIR spectrometer with an integrating sphere (module 150 mm). The reflectivity spectra in the middle IR spectral range were obtained on a Bruker IFS66/S spectrometer equipped with an integrating sphere (OPTOSOL), using a gold plate as a standard for diffuse reflectance.

2.4. Determination of spectral selectivity and colorimetric parameters

Dry coatings were examined regarding their spectral selectivity and color. Spectral selective properties of paint coatings were determined from spectroscopic measurements. Solar absorptivity (a_s) and thermal emissivity (e_T) values were determined from the reflectance spectra with the use of a standard procedure [11]. The solar absorptivity a_s is theoretically defined as a weighted fraction between absorbed radiation and incoming solar radiation. It was calculated according to [11]:

$$a_s = \frac{\int_{0.3}^{2.5} S(\lambda)(1 - R(\lambda))\mathrm{d}\lambda}{\int_{0.3}^{2.5} S(\lambda)\mathrm{d}\lambda}, \quad (2)$$

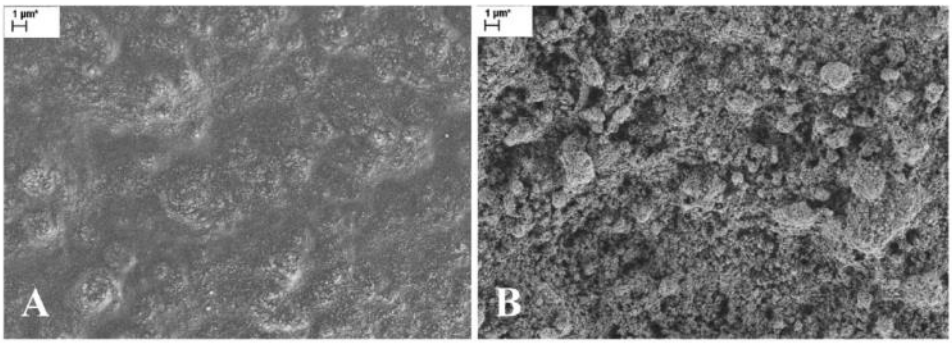
where λ is wavelength, $R(\lambda)$ reflectance in solar spectral region and $S(\lambda)$ is solar spectrum with air mass 1.5 (ISO standard 9845-1 (1992)). Thermal emissivity e_T is a weighted fraction between emitted radiation and the Planck black body radiation $r(\lambda,T)$ at absolute temperature T [11]:

$$e_T = \frac{\int_{2.5}^{15} r(\lambda, T)(1 - R(\lambda))\mathrm{d}\lambda}{\int_{2.5}^{15} r(\lambda, T)\mathrm{d}\lambda}. \quad (3)$$

e_T values were calculated for 350 K, being close to operating temperature of solar collectors. Spectral selectivity was determined as an average value for a set of five samples. The accuracy of e_T and a_s was within ±3%.

The colorimetric parameters were calculated from the reflectance data in visible spectral region using CIELAB color space, under D65 illumination and 10° standard observer. Color differences were calculated using the color difference formulas [12]. Chroma values C^* were calculated from:

$$C^*_{ab} = \sqrt{(a^*)^2 + (b^*)^2}, \quad (4)$$



C

IO POSS	C	O	F	Si	Mn	Fe	Cu	Total
PVC = 21 (A)	33.78	18.91	19.54	1.85	12.36	2.63	10.93	100.00
PVC = 51 (B)	18.59	24.04	7.51	1.33	23.17	4.56	20.81	100.00

All results are in weight %.

Fig. 1. SEM micrographs of coatings prepared with IO POSS at A) PVC = 21, B) PVC = 51 and C) results of EDX analysis.

while color differences, $\Delta E_{ab}{}^{*}$ (*CIELAB*), between color pair of coatings, were calculated as a Euclidean distance between the color of the two coatings [12]:

$$\Delta E^{*}_{ab} = \sqrt{(\Delta L)^2 + (\Delta a)^2 + (\Delta b)^2}. \quad (5)$$

3. Results and discussion

3.1. Rheological characterization of silicon oil dispersions with untreated and POSS-treated pigment

Flow curves of dispersions with pigment (with and without POSS treatment) in silicon oil are presented in Fig. 2. Due to the Newtonian behavior of silicon oil, the changes in non-Newtonian rheological behavior were solely attributed to the addition of pigment. The shapes of flow curves showed a systematic dependence of shear dependent viscosity on the PVC ratios for all dispersions. Lower PVC ratios indicated the clear leveling of the flow curve at high shear rates with no detectable time dependent effects, which resembled rheological properties typical for structured liquids or weak gels. However, higher concentrations of pigment (PVC = 51 and PVC = 60) resulted in more pronounced shear thinning behavior with detectable thixotropic time dependence. In order to quantify the changes in flow behavior due to increased PVC ratios, the experimental flow curves were fitted with rheological models. It was found out that among various models, the best fitting was obtained with the generalized Casson model (Fig. 2, solid lines). The model describes the flow of viscoplastic fluids that can be mathematically expressed as follows:

$$\tau^{n} = (\tau_y)^{n} + (\eta_{\infty}\dot{\gamma})^{n}, \quad (6)$$

where τ_y represents yield stress, while η_{∞} is the limiting viscosity in the range of high shear rates (infinite viscosity). When n equals 0.5, the generalized model becomes an original form of the model, introduced by Casson in 1959 [13]. The model was proposed for the prediction of flow behavior of pigment-oil suspensions and is based on a structure model of the interactive behavior of solid and liquid phases of a two-phase suspension and shows both yield stress and shear-thinning non-Newtonian viscosity.

The results showed that the parameters of the generalized Casson model depended on the PVC ratio as well as on POSS treatment of the pigment (Fig. 3). For all dispersions, the values of yield stress (Fig. 3A) and infinite viscosity (Fig. 3B) increased with increasing PVC ratios. Significant differences were observed, especially at higher PVC ratios, between dispersions prepared with untreated pigment and dispersions with POSS-treated pigment, while the values of the parameters only slightly depended on the type of POSS used for the pigment treatment. The results showed that when dispersions were prepared with POSS-treated pigment, the same yield stress and the same infinite viscosity were achieved

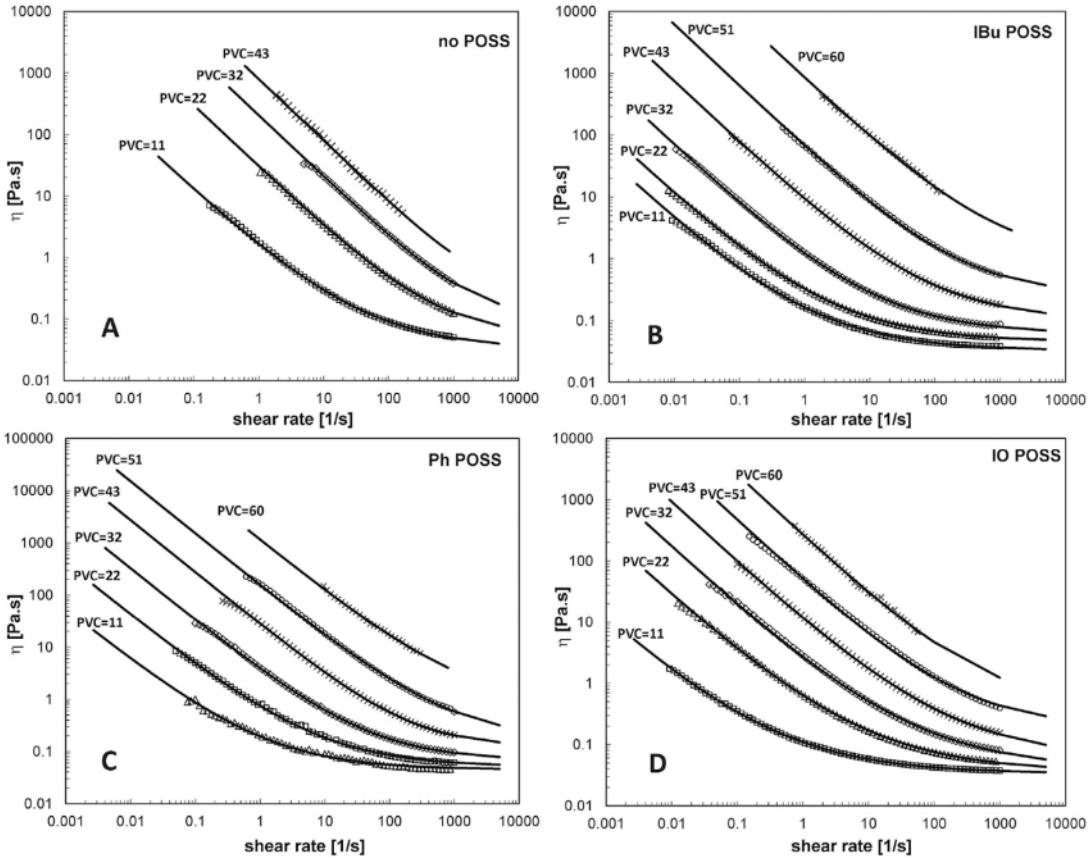


Fig. 2. Flow curves of pigment dispersed in silicon oil at different PVC ratios: A) no POSS treatment; B)–D) pigment treatment with IBu POSS; Ph POSS and IO POSS dispersant. Open symbols represent experimental values, while solid lines present correlated values according to Eq. (6).

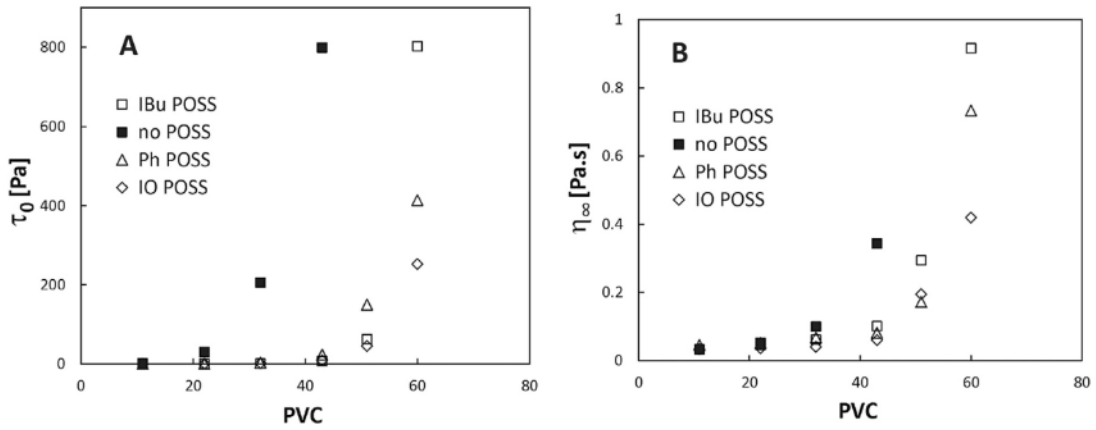


Fig. 3. Parameters (yield stress τ_y and infinite viscosity η_∞) of generalized Casson model (Eq. (6)) in dependence of PVC ratios for dispersions of untreated and POSS treated pigment dispersed in silicon oil.

at higher values of pigment loading compared to dispersions with untreated pigment. Increased values of yield stress usually illustrate stable dispersions in which sedimentation is prevented, but high yield stresses could also lead to decreased ability of good flow and leveling. The proper balance of these properties is therefore essential for good quality and functionality of dry coatings.

In order to determine the influence of PVC ratio and POSS treatment of the pigment on the viscoelastic nature of the dispersions, further rheological tests were performed under non-destructive oscillatory conditions. The viscous (liquid-like) and elastic (solid-like) contributions to the viscoelastic behavior of dispersions were determined in the linear viscoelastic range, i.e.

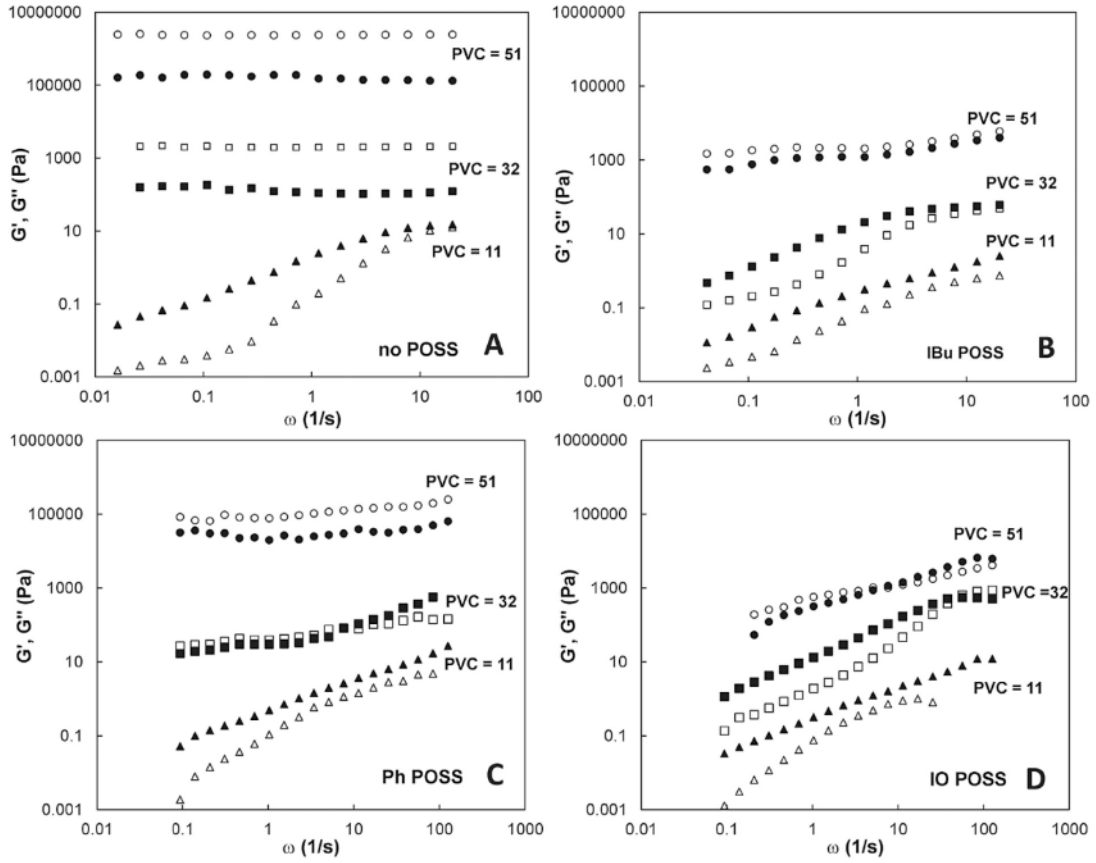


Fig. 4. The influence of PVC ratio on frequency dependence of dynamic moduli G' (open symbols), G'' (closed symbols) for dispersions examined. Silicon oil with pigment: A) without POSS treatment; pigment coated with B) IBu POSS; C) Ph POSS; D) IO POSS.

under the deformation that was sufficiently low so that no destruction of the basic structure might occur. Due to small deformations applied in these tests, the results can be correlated to the structure of the sample in the state of rest. Fig. 4 presents the frequency dependence of the viscoelastic moduli (elastic contribution G' and viscous contribution G'') for untreated pigment (Fig. 4A) and the same pigment, treated with the three above-mentioned POSS (Fig. 4B–D). For the sake of clarity, the results are presented only at three different PVC ratios. The comparison of viscoelastic moduli at the same PVC ratio showed that the values of G' and G'' for dispersions of untreated pigment exceeded the values of the moduli for dispersions with coated pigment, regardless of the POSS dispersant used. However, some similarities between POSS-treated pigment dispersions were observed. At the lower PVC ratios (PVC = 11, PVC = 22), dynamic moduli of all dispersions increased with the increasing frequency of oscillation with the domination of viscous modules ($G'' > G'$). Such behavior is typical for viscoelastic liquid, i.e. dispersions with viscoelastic liquid-like behavior. At these PVC ratios, dispersions are sufficiently movable to allow good flow and leveling. The increasing of pigment loading changed the viscoelastic liquid-like nature of the dispersions to solid-like behavior at different PVC ratios depending on pigment treatment. For dispersions without pigment treatment, the liquid-like behavior changed to solid-like when PVC = 32, while for dispersions of POSS-treated pigment, the changes from liquid-to solid-like behavior occurred at considerably higher PVC ratios (exceeding PVC = 51 for IO POSS). For higher pigment loadings, G' became predominant, and the elastic properties were the main part of contribution to viscoelastic properties. Such behavior is typical for systems that consist of extremely high interparticular interactions and behave in a strongly elastic manner, and could therefore cause problems during application and leveling.

In addition to all these observations, the frequency tests also revealed the influence of the type of POSS used for the treatment of black pigment, which was not so clearly detected with the flow tests. It can be seen from Fig. 4B–D that the viscoelastic properties also depended on the type of R groups on the peripheral organic groups attached on the cage core of POSS dispersants. Dispersions prepared with pigment treated with IO POSS, with isooctyl structure as the R group, exhibited viscoelastic liquid-like behavior to exceptionally high PVC ratio, i.e. PVC = 51. Such pigments would therefore enable the preparation of solar paints with an extremely high amount of pigment (which increase solar absorptivity) and appropriate viscoelastic properties to assure good application and proper leveling.

3.2. Rheological properties of TSSS paints, prepared with untreated and POSS-treated pigment

After the rheological study of the influence of PVC ratio and pigment treatment with different POSS dispersants on dispersions with silicon oil, a similar study was performed for black TSSS paints, which were developed in our group for application on solar thermal absorbers. Four sets of TSSS paints were prepared with an identical procedure and with the same binder, additives and solvents. The paints differed only in pigments, which were the same as in the previous study: untreated black pigment and black pigment treated with three above-mentioned POSS. The influence of POSS dispersants on the behavior of TSSS paints during deposition was monitored with rheological flow and frequency tests. The results of flow tests showed that all the paints exhibited shear thinning flow behavior which depended on the PVC ratio. The shear thinning behavior of the paints, prepared with untreated pigment and paints with pigment coated with IO POSS dispersant is presented in Fig. 5. The binder (PVC = 0) exhibited nearly Newtonian flow behavior, while shear thinning was more pronounced at higher values of the PVC ratio. Similar results were observed also for the paints prepared with pigment coated with IBu POSS and Ph POSS dispersants.

Model dispersions of pigment in silicon oil were best described with the Casson model (Eq. (6)), while flow curves of TSSS paints were the best presented with the Power Law equation [14]:

$$\eta = k\dot{\gamma}^{n-1} \tag{7}$$

where n presents power law index, while k is consistency index. Both parameters (n and k) depended on the PVC ratio as well as on the type of POSS dispersants used for pigment treatment. We focused on the dependence of shear thinning behavior (the parameter n) on the PVC ratio for different POSS treatments (Fig. 6). It was determined that n decreased with increasing PVC ratio for all the paints, showing the increasing shear thinning behavior as the amount of pigment in the paint increased (increased PVC ratio). The differences in the dependence of n on PVC ratio were observed especially when comparing paints prepared with untreated pigment and paints with pigment treated with POSS dispersants (Fig. 6). The paints with no pigment treatment exhibited the lowest values of flow behavior index n over the whole range of PVC ratio and the steepest decreasing of the parameter with an increasing PVC ratio. These paints exhibited the most pronounced shear thinning behavior at the highest PVC ratio. In contrast, the highest values of n and the smallest drop of n with increasing PVC (less

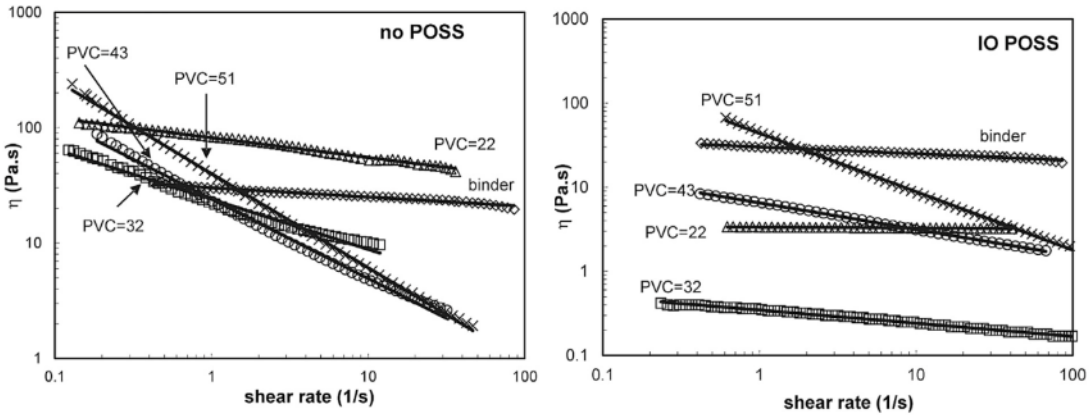


Fig. 5. Flow curves of binder and different PVC ratios of TSSS paints with pigment as prepared (left) and TSSS paints with pigment coated with IO POSS dispersant (right).

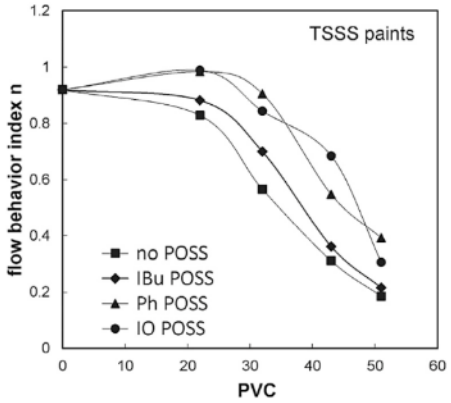


Fig. 6. Dependence of flow index n on PVC ratio for TSSS paints with pigment as received (no POSS) and pigment, coated with different POSS dispersants.

pronounced shear thinning) were observed for paints with Ph POSS-coated pigment, which also chemically differed (phenyl structure as the R groups of POSS molecule) from other two POSS (isobuthyl and isooctyl structure, respectively) dispersants.

In addition to flow behavior tests, oscillation tests were performed also for TSSS paints. Frequency tests, performed in the linear viscoelastic range, are presented in Fig. 7, where the influence of PVC ratio on dynamic moduli during the oscillation test is presented for the binder (Fig. 7A), the paints without pigment treatment (Fig. 7B) and the paints with pigment coated with IO POSS (Fig. 7C). Similar results were also obtained for the paints with IBu and Ph POSS-coated pigment. The influence of PVC ratio on the viscoelastic behavior of the paints was observed from the frequency dependence of dynamic moduli and the relation between G' and G'' (Fig. 7). For the paints with POSS-treated pigment, dynamic moduli increased with increasing frequencies of oscillation with $G'' > G'$ up to PVC = 43 with more pronounced prevalence of G'' at lower PVC ratios. At PVC = 51, the viscoelastic properties changed as the elastic modulus G' for this paint slightly dominated over G''; moreover, both moduli were almost independent of the frequency of oscillation. This indicates that up to PVC = 51 this paint exhibited liquid-like or weak gel behavior; therefore, this PVC could be the highest acceptable value for TSSS paints prepared with this dispersant (IO POSS). If the PVC ratio is increased over this value, the concentration of the pigment in the paint is too high while the amount of the binder is too low. The paint consequently loses its ability to flow, causing problems during the application and leveling. In contrast, the corresponding PVC values, whereby the dominating effect of the viscous modulus changed, were much lower for the paints prepared with untreated pigment (Fig. 6B), where at PVC = 43 the prevalence of elastic modules G' over the viscous one G'' was already much higher than similar prevalence of G'' at PVC = 51 for the paints with treated pigment (Fig. 6C). We can therefore conclude that the highest acceptable PVC ratio for the

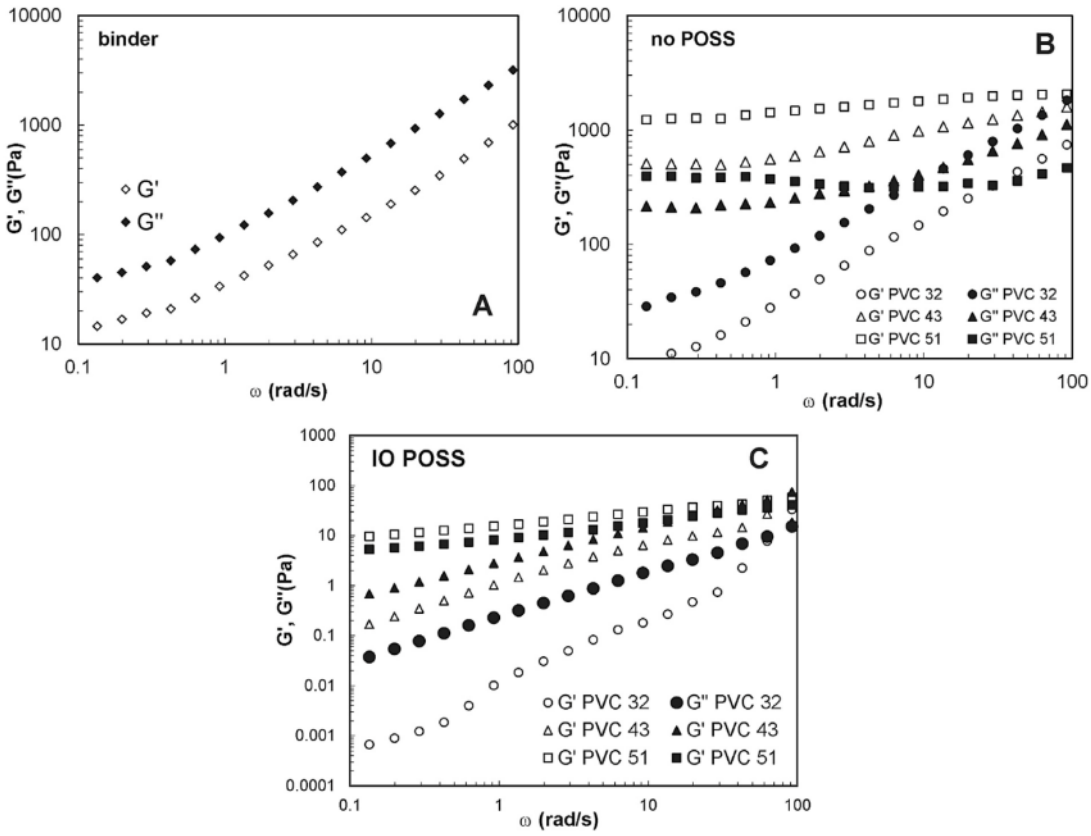


Fig. 7. Oscillation tests: frequency dependence of G' (open symbols) and G'' (closed symbols) for A) binder; B) TSSS paints with pigment without POSS treatment; C) TSSS paints with IO POSS treated pigment.

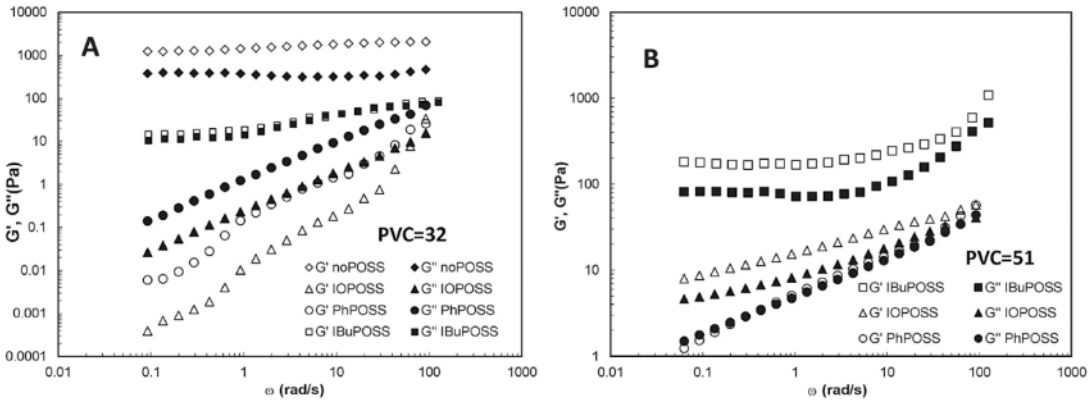


Fig. 8. Oscillation tests: frequency dependence of G' (open symbols) and G'' (closed symbols) for TSSS paints with treated and untreated pigment at PVC = 32 and PVC = 51.

paints with untreated pigment could be determined at much lower values, i.e. PVC < 32.

3.3. The influence of rheological properties on solar absorptivity of TSSS coatings

Viscoelastic properties of TSSS paints, determined during non-destructive oscillatory conditions (frequency tests, Fig. 8) were compared and correlated to the results of solar absorptivity a_s (Fig. 9) at two pigment loadings: PVC = 32 and PVC = 51. In the range of very low deformations simulating the conditions during the process of leveling, only the paint with untreated pigment exhibited strong gel-like structure ($G' > G''$) at PVC = 32, while paints with POSS-treated pigment (especially IO POSS and Ph POSS) exhibited more liquid-like structure ($G'' > G'$) (Fig. 8A). The domination of elastic modulus G' in paints with untreated pigment hindered the formation of smooth coating and prevented uniform distribution of pigment particles inside the binder. Consequently, the values of a_s obtained for these paints were the lowest for all thicknesses of dry coatings. In contrast, TSSS paints with Ph POSS and IO POSS-treated pigment with liquid-like structure at both pigment loadings enabled the formation of coatings with the best a_s values. The high prevalence of G'' enabled proper leveling and, due to the high steric properties of Ph POSS (phenyl structure), the distribution of the pigment inside the binder was the most homogeneous, leading to the best solar absorptivity.

At higher pigment loading (PVC = 51, Figs. 8B and 9B), TSSS paints with untreated pigment were, due to overly high pigment loading unable to prepare and could therefore not be presented in the figures. The values of dynamic moduli for the paints with IBu POSS at PVC = 51 were relatively high and independent of the frequency with $G' > G''$, while the paints with IO POSS and Ph POSS exhibited frequency-dependent moduli with smaller values and $G'' > G'$. Such structures of the paints were reflected in solar absorptivity, where again the more solid-like structure of the paints with IBu POSS-treated pigment resulted in coatings with lower values of solar absorptivity, regardless of the thickness of dry coatings. Smaller difference in viscoelastic properties of paints with IO POSS and Ph POSS-treated pigment reflected also in similar values of solar absorptivity (Fig. 9B).

Significant effects of POSS treatment were also detected from the thickness dependence of solar absorptivity for TSSS coatings with treated and untreated pigment at various PVC ratios (Fig. 10). For coatings prepared with pigment coated with either of three POSS dispersants, solar absorptivity a_s at the same thickness of the coating, irrespective of PVC ratio, exceeded a_s values of the coatings prepared with untreated pigment (Fig. 10). Moreover, for all three dispersants, solar absorptivity systematically increased with increasing PVC ratios, i.e. at the same thickness the values of a_s were the highest at the highest PVC ratio (PVC = 51). A detailed examination of the results showed slight differences in a_s values between various POSS dispersants (Fig. 10). The lowest values of a_s were

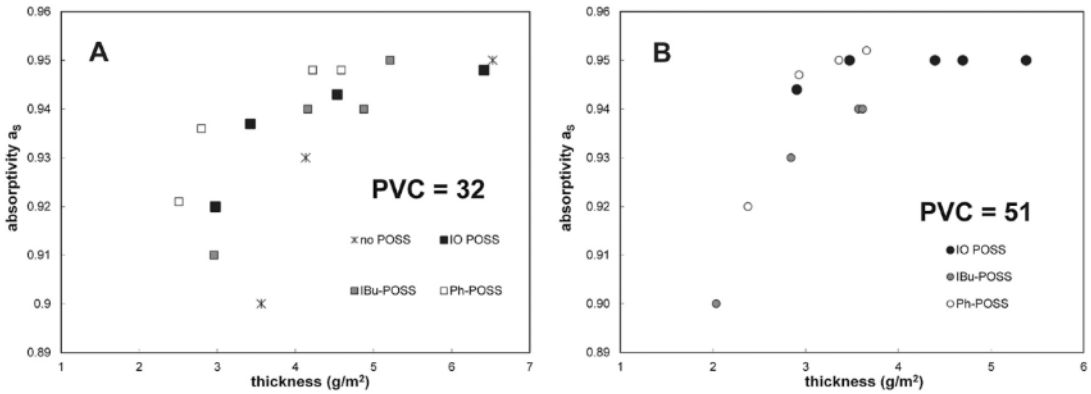


Fig. 9. Dependence of solar absorptivity on thickness at PVC = 32 and PVC = 51 for TSSS coatings with untreated pigment (no POSS) and POSS treated pigment (IBu POSS, Ph POSS; IO POSS).

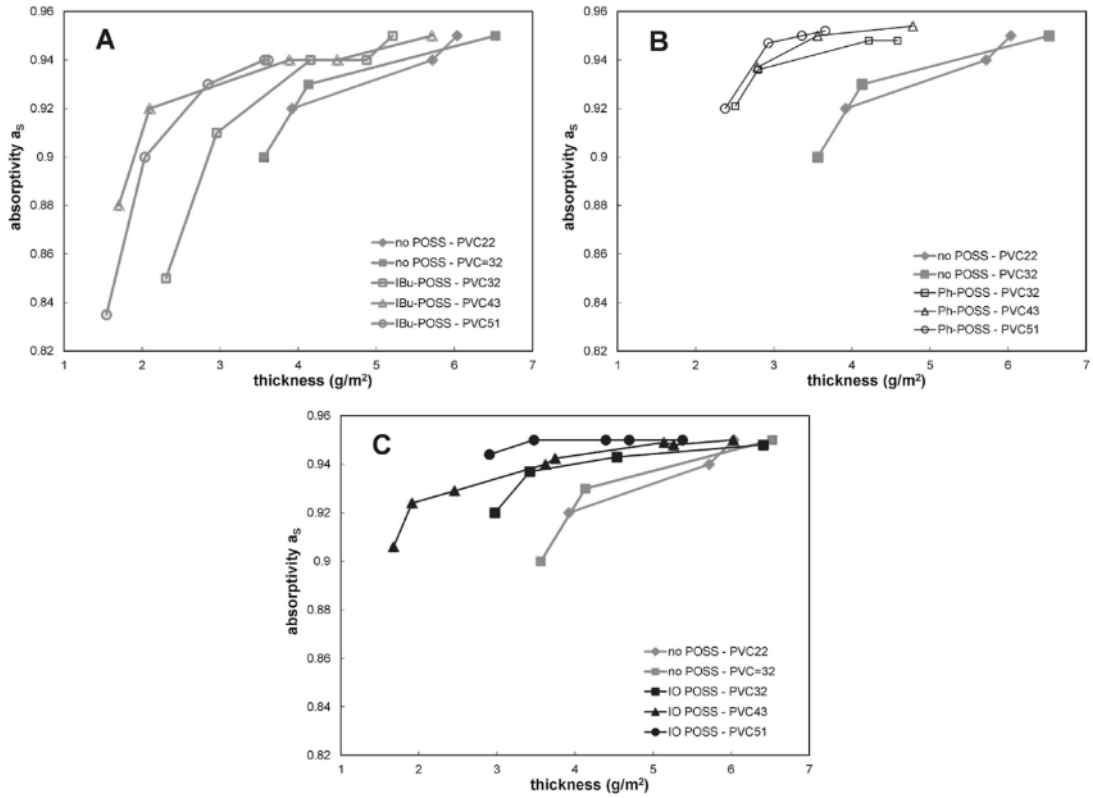


Fig. 10. Dependence of solar absorptivity on thickness at different PVC ratios for TSSS coatings with: A) untreated pigment – pigment with IBu POSS; B) untreated pigment – pigment with Ph POSS; C) untreated pigment – pigment with IO POSS.

obtained with IBu POSS, which exhibited solid-like viscoelastic behavior, while the differences in a_s values between Ph POSS and IO POSS with similar liquid-like viscoelastic properties were negligible.

To conclude, treatment of the pigment with POSS decreased the viscosity of the prepared TSSS paints and consequently for the same viscosity higher pigment loading was achieved. For untreated pigment the highest values of a_s were not higher than 0.94 with thermal emissivity e_T close to 0.4, while for POSS treated pigment the highest values of a_s approached 0.96 with e_T close to 0.3.

3.4. Colorimetric properties of TSSS coatings

Our study was expanded to the color of coatings in CIELAB color space (Fig. 11). The colors of the studied TSSS coatings were grouped in the (a^*, b^*) and (C^*, L^*) planes according to the treatment of the pigments (Fig. 11). The results showed that the coatings with untreated pigment had the most neutral color (a^*, b^*, C^* close to zero), while the color of the coatings with POSS-treated pigments was shifted to the red-yellow (IBu-POSS and Ph-POSS) or the blue-

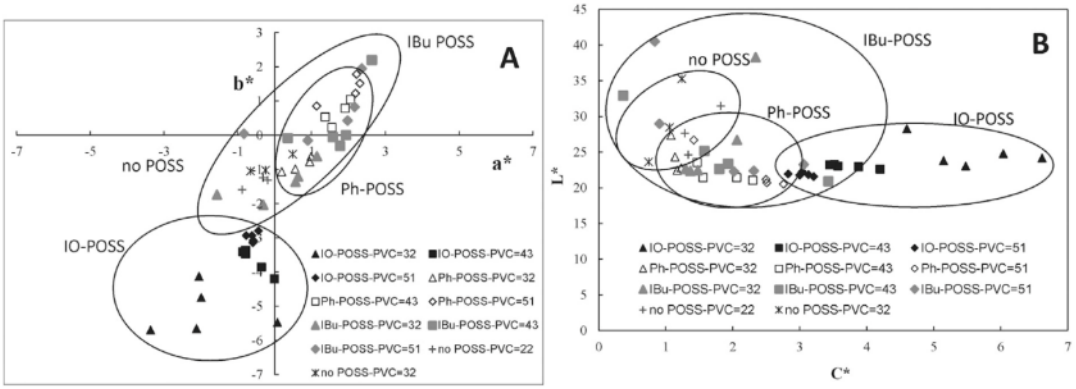


Fig. 11. Color parameters: A) b^* vs. a^* and B) C^* vs. L^* for TSSS coatings prepared with pigment as received (no POSS) or with pigment treated with various POSS (IBu POSS, Ph POSS, IO POSS).

Table 2
Spectral selectivity and color differences for selected pairs of TSSS coatings.

PVC = 32	Thickness (g/m^2)	a_s	e_T	$a_s - e_T$	ΔE
no-POSS	4.1	0.93	0.4	0.53	12.1
IO-POSS	4.5	0.94	0.39	0.55	
no-POSS	4.1	0.93	0.4	0.53	12.97
IBu-POSS	4.1	0.94	0.32	0.62	
no-POSS	4.1	0.93	0.4	0.53	12.95
Ph-POSS	4.2	0.95	0.38	0.57	
no-POSS	6.5	0.95	0.48	0.47	0.98
Ph-POSS	4.2	0.95	0.38	0.57	
PVC = 51					
IBu-POSS	3.6	0.94	0.37	0.57	4.9
IO-POSS	3.5	0.95	0.35	0.6	
Ph-POSS	3.7	0.95	0.36	0.59	5.74
IO-POSS	3.5	0.95	0.35	0.6	

green (IO-POSS) part of the color space (Fig. 11A). At lower values of PVC, the colors of coatings with IBu POSS and Ph POSS were similar to colors of coatings without pigment treatment, while higher PVC ratio for these coatings resulted in higher values of a^* and b^* (slight red-yellow shade). However, the values of a^* and b^* for IO POSS-coated pigment were negative with more pronounced (but still slight) blue-green shade at lower PVC ratio.

Interestingly, most samples exhibited similar lightness L^*, but the chroma C^* varied with PVC ratio and POSS treatment of the pigment (Fig. 11B). TSSS coatings prepared with untreated pigment and pigment coated with IBu POSS were slightly lighter than other coatings with highly similar values of lightness ($L \sim 22$), regardless of the PVC. This is in agreement with lower solar absorptivity of the coatings prepared with untreated pigment and pigment treated with IBu POSS (Fig. 10). The influence of POSS dispersants was more pronounced for chroma values C^* (Fig. 11B). The highest values of C^* were obtained for the coatings with IO POSS-coated pigment, for which C^* strongly depended on PVC. For these coatings, a systematic decrease of C^* was observed with increasing PVC.

Coatings with similar thickness were compared at two PVC ratios by the calculation of color difference ΔE^*. The values presented in Table 2 present the mean values of 5 samples with standard deviation of ±2%. The comparison showed that color difference between similarly coatings with untreated and POSS-treated pigments (at PVC = 32) are significant ($\Delta E^* > 12$), and such a difference could be freely observed by the naked eye (Table 2). The coatings at the same PVC ratio become indistinguishable ($\Delta E < 1$) only if a thick coating with untreated pigment is compared to the thin coating with POSS-treated pigment (e.g. no-POSS with Ph-POSS, Table 2). This means that when we want to prepare two coatings with untreated and POSS-treated pigment having the same color, the thickness of the coating with untreated pigment should be much higher compared to the coating with POSS-treated pigment. However, thicker coatings exhibit high thermal emissivity e_T and therefore poor spectral selectivity (lower values of $a_s - e_T$).

Color differences at PVC = 51 showed that the selection of POSS had modest influence on the color differences, as ΔE^* for coatings with treated pigment was at the same thickness similar, regardless of the selected POSS ($\Delta E^* \sim 5$). Moreover, also the spectral selectivity of these coatings ($a_s - e_T$) was similar (Table 2).

4. Conclusions

The performance of solar thermal absorbers depends on different properties of the coating applied on the surface. In order to achieve high spectral selectivity, the paints require high pigment loading, which increases the solar absorptivity of the coating. However, in heavily pigmented paints, the flocculation of pigments and consequently poor rheological properties become a serious problem. High quality dispersing additives are therefore required to assure appropriate rheological properties and distribution of pigments within the coating.

Our study shows that POSS materials are very valuable dispersants for black pigments in TSSS paint coatings. The rheological tests confirmed reduced viscosity and increased flowability of TSSS paints prepared with pigments treated with POSS. We showed that POSS enables the preparation of dispersions with extremely high pigment loadings with PVC ratios above 50, which is twice as much as with conventional additives. Moreover, rheological tests showed that the paints with POSS-treated pigment exhibit more liquid-like properties with high values of G'' that are necessary for uniform surface and proper leveling. Due to strong interfacial bonding between the binder and dispersant molecules on the pigment surfaces and good steric properties of peripheral R groups on the cage core of POSS molecules, pigments treated with IO and Ph POSS were uniformly distributed inside the coating during the application of TSSS paints as well as during the process of drying. Consequently the coatings, prepared with these two trisilanol POSS dispersants, enabled the preparation of thin, uniform coating with very high solar absorptivity.

The application of POSS dispersants also appreciably changed the color of TSSS coatings. In order to achieve similar color, the coatings with untreated pigment should be much thicker than the coatings prepared with POSS-treated pigment. Nevertheless, the thicker coatings exhibit high thermal emissivity leading to poor spectral selectivity.

We can conclude that treatment of black pigment with POSS dispersants heavily influences the rheological behavior of liquid TSSS paints and gives rise to improved solar absorptivity of dry TSSS coatings. At PVC = 32 TSSS paints without pigment treatment exhibited gel-like behavior with dynamic moduli G' and G'' close to 1000 Pa. Consequently solar absorptivity of these coatings hardly exceeded 0.9 and thermal emissivity was close to 0.4. On the other hand, at the same thickness and PVC ratio TSSS paints with POSS treated pigment exhibited liquid-like or weak-gel rheological behavior with dynamic moduli below 100 Pa resulting in a_s reaching the value of 0.94 and e_T below 0.3. These results clearly indicate that proper rheological properties of liquid TSSS paints are essential in order to achieve good leveling and uniform distribution of pigment particles inside dry coating leading to excellent functionality of dry coatings. Rheological properties can therefore be used to predict the performance, i.e. solar absorptivity of dry TSSS coatings.

References

[1] L. Slemenik Perše, A. Bizjak, B. Orel, Sol. Energy Mater. Sol. Cells 110 (2013) 115–125.
[2] R.R. Eley, Rheol. Rev. (2005) 173–240.
[3] U. Kästner, Coll. Surf. A 183–185 (2001) 805–821.
[4] T.F. Tadros, Colloids in Paints, Wiley-Interscience, Weinheim, 2010.
[5] S. Mueller, E.W. Llewellin, H.M. Mader, Proc. R. Soc. A 466 (2010) 1201–1228.
[6] O. Cohu, A. Magnin, Prog. Org. Coatings 28 (1996) 89–96.
[7] L. Yuan, X. Weng, L. Deng, Infrared Phy Tech. 56 (2013) 25–29.
[8] Z.W. Wicks, Organic Coatings: Science and Technology, Wiley-Interscience, Hoboken NJ, 2007.
[9] M. Joshi, B.S. Butola, G. Simon, N. Kukaleva, Macromolecules 39 (2006) 1839–1849.
[10] S.A. Madbouly, J.U. Otaigbe, Prog. Polym. Sci. (2009) 1283–1332.
[11] M.G. Hutchins, in: M. Santamouris (Ed.), Solar Thermal Technologies for Buildings, James & James, London, 2003.
[12] CIE Publication X015, Colorimetry, third ed., CIE Central Buerau, Vienna, 2004.
[13] N. Casson, Rheology of Disperse Systems, Pergamon Press, Oxford, 1959.
[14] T.G. Metzger, The Rheology Handbook, second ed., Vincentz Network, Hannover, 2006.

Chapter 4

Novel Sol–Gel Based Selective Coatings: from Coil Absorber Coating to High Power Coating

In the previous chapter, the modification of spinel pigment with isobutyl trisilanol POSS was presented. The modified pigment was afterwards embedded into fluoropolymer resin. The encouraging results obtained from these studies have led to more detailed research on pigment dispersions of black pigments ($CuFeMnO_x$ spinels) useful for making coatings for solar absorbers. Creating layers for solar absorbers is not new since the first attempts date back to the nineteen seventies; also, their development already has a long tradition. Special use of 3-aminopropyltriethoxy silane as a dispersant for black spinel pigment in polysiloxane binder has been effectively proven to enable stable pigment dispersions. These spectrally selective absorber coatings, deposited by coil coating, are currently mass produced for the global solar market [9]. However, the system is not energy efficient enough. Thermal emissivity is too high (20-22%), due to the excessive thickness of the coating and because of the intrinsic thermal emissivity of polysiloxane binder.

In this study, our purpose was to prepare sol-gel based spectrally selective coatings that exhibit better characteristics than the previous one. Typically, silanes are a better option because they have lower thermal emissivity and, after curing, silanes give hard and heat-resistant coatings.

Among many known silanes, 3-glycidoxypropyltrimethoxy silane (Glymo) has been used as a binder for coatings of black spinel pigment. The use of silanes as binders in practical (mainly commercial systems) is not very popular. They are more expensive than polymer binders, whose viscosity is hard to keep within the limits that still allow the deposition of pigment dispersions on the metal substrate (coil coating technique). It is also difficult to ensure compatibility between pigments dispersed with standard (organic) dispersants and alcohol media, for which mainly silane dispersants are used. It has been shown that surface modification of black spinel pigment with isobutyl trisilanol POSS is highly efficient and provides long-term stability of the dispersions. The challenge for basic research of this thesis was thus given. It has been shown that strong interactions (Si-O...pigment) occur between the surface of the pigment and isobutyl trisilanol POSS molecules. This has been proven both by infrared spectroscopy and by other analytical techniques (TEM, SEM, AFM, XPS and TG).

The interactions of pigment particles with isobutyl trisilanol POSS were determined by preparing a series of TSSS coatings. It was confirmed that the coatings offer high solar absorption and low thermal emissivity; the coatings are spectrally selective, which means that they prevent the release of heat back to the atmosphere by far-infrared radiation.

Optimisation of the thickness and spectrally selective characteristics of sol-gel based TSSS coatings was first done by spin coating deposition. The final optimised pigment dispersions were also deposited by the coil coating technique in the German company Alanod (Figure 4.1).



Figure 4.1: Deposition of sol-gel based TSSS on a coil coating line.

Sol-gel pigment dispersions have also made it possible to produce spectrally selective absorber coatings that are stable at high temperatures (up to 500 °C). At such high temperatures, isobutyl trisilanol POSS thermally converts into silica and binds into the silicate matrix of the nanocomposite based on 3-glicidoxypropyltrimetoxy silane, which served in this case as the binder phase for the pigment dispersion.

This finding led us to research of the interaction with pigments and isobutyl trisilanol POSS dispersants on the one hand, and to show that the dispersant has an active part in the thermal conversion in which the formation of compact silicate nanocomposite structure occurs (modified pigment particles) on the other. It is sensible to talk of such particles (core-shell nanoparticles), since there is a strong connection with the surface of the pigment and dispersant and evidence is provided in this thesis. The results obtained by IR spectroscopy revealed that a GlyBP coating forms a compact coating after deposition. When the coating is exposed to temperatures below 130 °C, the polyethylene (PEO) chains are still present in the matrix (Figure 4.2A-a) and a proposed mechanism of TSSS coating is given in Figure 4.2B. The infrared spectra of GLYBP coating exposed to 400 °C show that the Si–O–Si modes of the nanocomposite and the coating at 1060 and 1105 cm^{-1} converted to the modes of silica (SiO_2) (band at 1061 cm^{-1} and a shoulder band at 1134 cm^{-1}). The bands of the organic compounds (–CH groups) in the coating exposed to 400 °C disappeared (Figure 4.2A-d). Ae coating exposed to high temperatures undergoes a formation mechanism presented in Figure 4.2C.

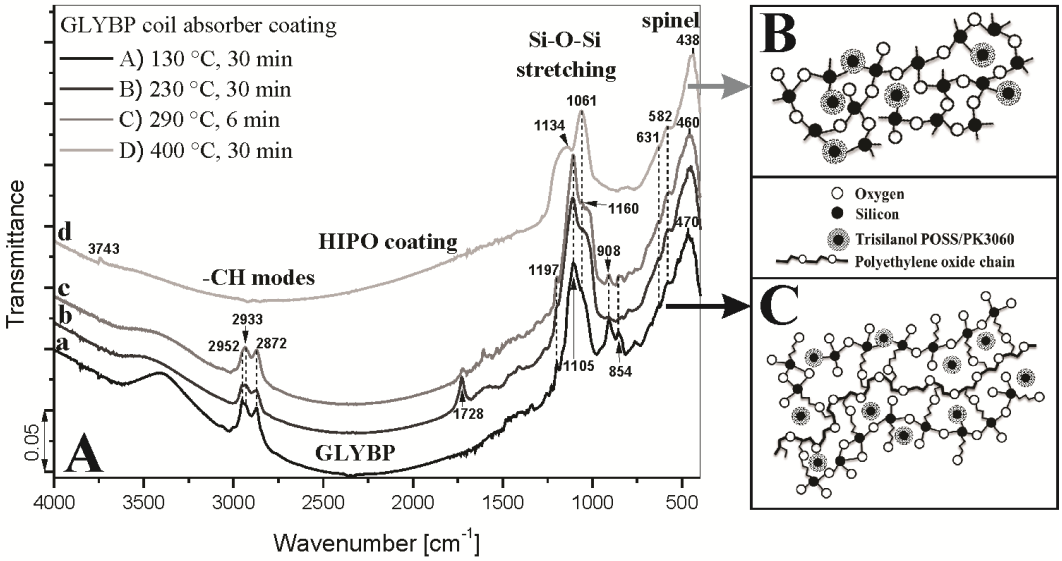


Figure 4.2: IR transmission spectra of various coatings exposed to different temperatures (A-a) 130 °C, 30 min, (A-b) 230 °C, 30 min, (A-c) 290 °C, 6 min and (A-d) 400 °C, 30 min. Formation of PEO chain at 130 °C (B) and direct conversion to Si-O-Si of coating heat treated at 400 °C, 30 min (C).

The procedure for preparation of sol-gel based TSSS coating has been patented [88]. We also won 1st prize, which was shared equally between the two participants for best inventive/innovative projects from PRO's for the economy, with innovation called »Go solar, go future« - a sol-gel based spectrally selective solar absorber coating.

My contribution to this study was (i) the preparation of the pigment dispersion, in which isobutyl trisilanol POSS was used as dispersant, (ii) the preparation of pigment dispersions and measuring their spectral selectivity (iv) and some of the writing.

Solar Energy Materials & Solar Cells 140 (2015) 232–248

Contents lists available at ScienceDirect

Solar Energy Materials & Solar Cells

journal homepage: www.elsevier.com/locate/solmat

Novel sol–gel based selective coatings: From coil absorber coating to high power coating

M. Mihelčič [a,b], V. Francetič [c], J. Kovač [d], A. Šurca Vuk [a], B. Orel [a,*], R. Kunič [e], D. Peros [f]

[a] National Institute of Chemistry, Hajdrihova 19, 1000 Ljubljana, Slovenia
[b] Jozef Stefan International Postgraduate School, Jamova cesta 39, 1000 Ljubljana, Slovenia
[c] Faculty of Chemistry and Chemical Technology, University of Ljubljana, Aškerčeva cesta 5, 1000 Ljubljana, Slovenia
[d] Jozef Stefan Institute, Jamova cesta 39, 1000 Ljubljana, Slovenia
[e] Faculty of Civil and Geodetic Engineering, University of Ljubljana, Jamova cesta 2, p.p. 3422, 1000 Ljubljana, Slovenia
[f] Alanod GmbH & CO. KG, Egerstraße 12, DE-58256 Ennepetal, Germany

ARTICLE INFO

Article history:
Received 5 November 2014
Received in revised form
20 March 2015
Accepted 4 April 2015

Keywords:
Spectral selectivity
Solar absorbers
Sol-gel coatings
Thermal stability
Advanced isoconversion kinetics
High-power coatings

ABSTRACT

Single layer black selective coatings for solar thermal energy conversion were produced by low cost sol–gel dip-coating, spin-coating and coil-coating methods, the last made on the industrial line of the Alanod company (DE). For the deposition, pigment dispersion was prepared by milling a mixture of a black spinel ($FeMnO_4$) pigment, whose surface was modified with trisilanol heptaisobutyl POSS dispersant, dried and re-milled with (3-glycidoxypropyl)trimethoxysilane (GLYMO) and $Ti(i\text{-}OPr)_4$ acting as binders. The corresponding organic–inorganic hybrid consisted of silica clusters linked together with poly(ethyleneoxide) chains acting as a network former. The as-prepared nanocomposite dispersion served for the deposition of coil absorber coatings (~800 m) on aluminium coil in an industrial plant in the Alanod factory. They gave solar absorptance of 0.905 and thermal emittance of 0.12 and excellent homogeneity. The stability of the coatings at 400 °C was excellent but corrosion resistance was moderate (5 days in salt spray).

The coil absorber coating was then used for making a High Power (HIPO) solar coating with solar absorptance of 0.92 and thermal emittance of 0.075, which was achieved by exposure of the as-prepared coil to 400 °C. The isoconversion kinetics approach was used for assessing the thermal loading (time and temperature of heat treatment) required to provide a HIPO coating from the coil absorber. The improvement of selectivity was investigated by infrared spectroscopy and XPS measurements, revealing that HIPO coatings deposited on stainless steel (AISI 316) survived 1216 h at 460 °C and 400 h at 500 °C without any change of selectivity, while after exposure to 500 °C for 1216 h, thermal emittance increased to 5–7% but solar absorptance remained unchanged. Thermal emittance changes observed at thermal loading were explained with the help of infrared spectra analysis, revealing the formation of iron oxide on the surface of the HIPO coating. The deposited HIPO coating is an interesting option for temperature and corrosion stable coatings for applications in concentrated solar power (CSP) plants for solar processing heat generation.

© 2015 Elsevier B.V. All rights reserved.

1. Introduction

Solar energy is the cleanest (does not produce air pollutants or CO_2) renewable natural resource available. The world's energy demands are growing rapidly and the development of surfaces with high absorption of solar radiation (a_s) and low thermal emittance (e_T) is thus a driving force for the development of absorber coatings with spectral selectivity, i.e., high a_s/e_T ratio. Since the amount of sunlight that arrives at the Earth's surface is not constant, varying depending on location, time of day, time of year and weather conditions, a large surface area of solar absorbers with high spectral selectivity is required to collect the energy at a useful rate. Absorber coatings made by a coil-coating technique seem to be the best solution.

Thickness Sensitive Spectrally Selective (TSSS) paint coatings made by the deposition of black paints with controlled thickness on metallic substrates [1–5] are a cheap alternative to vacuum based coatings, even though such coatings have attracted only sporadic interest for almost forty years, mainly due to the predominant role of electrodeposited black chrome based coatings [6,7] on the market. Because toxic Cr(VI) compounds are used in

* Corresponding author.
E-mail address: boris.orel@ki.si (B. Orel).

http://dx.doi.org/10.1016/j.solmat.2015.04.010
0927-0248/© 2015 Elsevier B.V. All rights reserved.

the electroplating process, with a significant impact on the environment, interest shifted between 1990 and 1995 onto vacuum deposited coatings [8,9]. Despite the high cost of vacuum deposition equipment, the solar thermal market is currently dominated by highly spectrally selective surfaces made of various cermet materials deposited on aluminium or copper via vacuum deposition techniques [10–12]. Vacuum deposition, which is automatic and is performed on coils (roll-to-roll, R2R), enables the formation of coatings with multiple film structures and high a_s/e_T ratios (> 20) (a_s ~0.95 and e_T ~0.05).

The development of TSSS paint coatings is a multifaceted problem, since selectivity strongly depends on mutually dependent parameters: thickness of the paint layer, composition of paint, which in turn depends on the pigment type and thermal emittance properties of the binder and dispersant, all affecting the pigment loading, curing and deposition conditions of the paint dispersions. Only the harmonization of all issues makes it possible to prepare paints that enable the deposition of TSSS coatings from paints with a high selectivity ratio.

A TSSS paint coating was prepared in our laboratory using a paint made of black manganese spinel pigment dispersed in polysiloxane (TEGO, Non-stick 60) resin binder with the help of (3-aminopropyl)trimethoxy silane (APTMS) [13], which served as dispersant. The use of APTMS dispersant has been found to be a major breakthrough; it has enabled the deposition of coatings with high pigment loading (33–35%), which have consequently given improved spectral selectivity (a_s ~0.90 to 0.91 and e_T ~0.20 to 0.22) and imparted excellent corrosion resistance (10 days in salt spray) and adequate abrasion resistance (H3) and temperature stability (650 h at 240 °C). Following the IEA Task 10 protocol, the last named promised a lifetime of more than 25 years. Selective absorber coils with this paint are currently manufactured by the Alanod factory (DE) on an industrial coil-coating line under the trade name Mirosol TS.

The central aim of this study was first to make a selective TSSS coil absorber coating from sol–gel precursor/pigment dispersions with solar absorptance of about 0.90–0.91 but lower thermal emittance (e_T ~0.12 to 0.14) than polysiloxane based coatings [13] and, second, to use this coil absorber coating as a starting material for the production of high power (HIPO) coatings with higher a_s/e_T ratios, i.e. $a_s > 0.91$ and e_T ~0.075. Heat treatment ($T > 400$ °C) was used for this purpose.

There were several reasons for choosing sol–gel precursors instead of polymeric siloxanes [13]. Surprisingly, there are no commercial selective absorber coatings prepared from sol–gel based pigment dispersions, even though sol–gel coatings are used in practice in many applications [14–17]. Tetraethoxysilane (TEOS) seems to work well, as reported by Morales et al. [18], as antireflective and protection coatings for solar absorbers, while Rincon et al. [19] made sol–gel based TSSS absorber coatings from titanium(IV) isopropoxide (TIP) with added carbon soot and carbon nanotubes as pigments. Selective absorber cermets (33% Au/67% TiO_2) have been made by inexpensive sol–gel techniques, with good optical selectivity a_s/e_T (400 °C)=0.80/0.01 and high thermal durability (> 500 °C in air) [20,21]. However, such sol–gel pigment dispersions have low viscosity and seem to be more suitable for dip and spin-coating depositions than for much faster coil coating and other less sophisticated but more common paint deposition methods.

Basically, two different wet deposition preparation routes exist: in situ preparation of a black sol–gel coating from a mixture of silanes or titaniumalkoxyde and metal salt precursors followed by heat treatment and a *standard route* used for the preparation of paints, in which the pigment particles are milled in the presence of silanes serving as binders. By following the first route, Kaluza et al. and later Vince et al. [22,23] demonstrated that it is possible to make black $CuCoMnO_x$ and $CuTiMnO_x$ spinel crystalline thin films (300 nm) with a solar absorptance of 0.86 and thermal emissivity of 0.11. The added Ti-alkoxide acted as a binding phase, which connects the black spinel pigment particles formed after heat treatment at 400–500 °C (few h). Using sol–gel and spin-coating deposition, Bostroem et al. [24] obtained similar black spinel based coatings with thermal emittance below 0.05, which absorbed 97% of the incoming solar energy. Bayon et al. [25–27] obtained highly selective coatings based on Cu–Mn–Si oxides that show excellent optical performance. A solar absorptance of 0.95 combined with thermal emittance of 0.035 was achieved for coatings on aluminium substrates. Recently, Joly et al. [28] reported sol–gel based Cu–Co–Mn–Si–O nanocrystalline multilayer thin films, in which TEOS acted as a binding phase and depositing the precursor solution on steel by the dip-coating technique and application of inductive heating considerably shortened duration of heat treatment. Multi-layered coatings showed high spectral selectivity (a_s ~0.94 and e_T ~0.12) but single layer films exhibit much smaller a_s values (a_s ~0.81), due to the inherent high reflection of the formed spinel/silica coating. Temperature stability was checked at 400 °C and was adequate, but corrosion resistance (acid drop test) was about 3 times worse than for electrodeposited black chrome coating. Despite the use a special heat treatment procedure [28], the in situ fabrication of black crystalline manganese spinel films seems to be time consuming, especially because an additional layer(s) is/are needed in order to decrease the inherently high reflection of the crystalline material. Sol-gel based cermets [29,30] could also be ranked among coatings in which the absorbing phase forms in situ during the preparation. In situ preparation of the sol–gel black TSSS coatings from sol–gel solutions is undoubtedly time consuming and wet deposition of TSSS coatings the sol–gel dispersions is a better option.

In general, alkyltrialkoxysilanes (R-(Si-OR′)$_3$, where R= mercapto, glycido, methyl, acryl, vinyl,… and R′ – alkoxy groups) are promising alternative to existing tetraalkoxysilane binders because the viscosity of the pigment dispersions and compatibility of the dispersed pigment particles can be relatively easily adjusted by choosing the appropriate alkyl (R) groups. Namely, alkyltrialkoxysilanes, during the course of condensation, form organic–inorganic hybrid materials with highly condensed and cross-linked silica organic–inorganic networks with a nanocomposite structure (ORMOCER) [31–33]. Organic–inorganic hybrids have already been used for making Thickness Insensitive Spectrally Selective (TISS) paint coatings with added aluminium flakes [34,35] but the spectral selectivity was much lower than for TSSS paint coatings, even though selective paint coatings with different colors have also been produced [36].

In this study, (3-glycidoxypropyl)trimethoxysilane (GLY for short) was selected as a binder because this popular precursor has already been used as precursor for many organic–inorganic hybrid coatings [14,16]: hard coatings for plastic ophthalmic lenses [37], low temperature coatings for glass coloration [38,39], organic dye-doped hybrid sol–gel coatings [40], planarization layers for microelectronics [41] and generally for multifunctional coatings [42]. However, it has not been used for selective coatings yet.

An additional reason for choosing GLY as a binder for the sol–gel TSSS coatings in this study was that GLY has lower thermal emittance per coating thickness than polysiloxanes and other organic binders [43–45]. GLY is actually one of the simplest organic–inorganic hybrid precursors, which consists after polymerization of silica clusters (short linear, cyclic, ladder and partially octameric silsesquioxanes), covalently linked into polyether (poly(ethylene oxide), PEO) chains formed by direct reactions between the epoxy rings (Fig. 1) [46]. Ring opening is achieved by the presence of a metal (Zr, Ti, Al, and Sn) alkoxyde, such as titanium tetraethylate ($Ti(OEt)_4$), Al sec$(OBu)_3$ [47] or AlO(OH) boehmite nanoparticles [37]. The boehmite nanoparticles thus have a

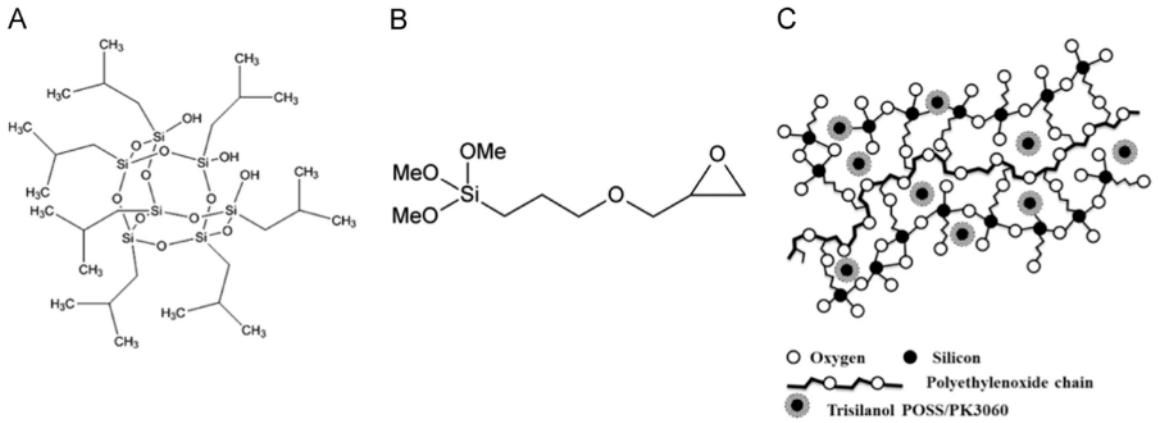


Fig. 1. Trisilanol POSS (A), GLY (B) and schematic structure of nanocomposite coating based on GLY/PEO with trisilanol POSS dispersed black spinel (C).

double role: acting as catalyst for the epoxy ring opening and also contributing to enhanced surface hardness [48]. We deliberately used ($Ti(OEt)_4$) here, enabling curing of GLY at 290 °C in the short time typical of a coil-coating line (6 min).

For making coatings from paints, the selection of the dispersant is of equally important to the selection of binders. Trisilanol POSS dispersant, which was used in this study, belongs to a large family of POSS compounds, characterized by a $[RSiO_{3/2}]_n$ structure [49–51], organized in the form of various polyhedra (T_n, $n=3, 6, 8, 10, 12, \ldots$). Various organic pendant groups (R) are attached on the corners of the $(RSiO_{3/2})_8$ cubes, providing flexibility in their structure and composition and imparting them multifunctionality [44,45]. POSS materials have been used for various applications in our laboratory [43,52–59] and—important for this study—also as pigment surface modifiers for black PK 3060 spinel pigment (FERRO, USA) in spectrally selective coatings [44,45]. It has already been shown that the trisilanol POSS covalently bonded on the PK 3060 pigment surface; infrared spectra analysis combined with TEM, EDAX and TG measurements was used for this purpose [45].

In the framework of this study, trisilanol POSS played a dual role; it acted as dispersant, which provided compatibility of the pigment with the GLY sol–gel binder and thus enabled the deposition of TSSS coil absorber coating. At the same time, it also acted as a source of the silica binding phase in the high power sol–gel coating (HIPO, for short), made by thermal treatment of the as deposited GLY/trisilanol POSS/PK3060 (GLYBP, for short) coil absorber coating. Trisilanol POSS dispersant, being covalently bonded on the pigment surface, also stays attached to the pigment surface during the heat treatment when it changed to silica. The silica provided the necessary particle-to-particle contact and mechanical integrity of the HIPO coating because at higher temperatures ($T > 440$ °C) trisilanol POSS transformed into the silica wrapping spinel pigment (core–shell particles). It is important to note that since the amount of trisilanol POSS was just 7% [44,45], we expected that the corresponding trisilanol POSS/PK3060 system would exhibit $e_T < 10\%$. The preparation of the HIPO coatings was thus reduced to an assessment of the thermal loading (T of heat treatment and time (t)) that should be applied on the GLYBP coating in order to convert the GLYBP coil absorber coating to the HIPO coating with the desired higher selectivity ratio ($R=a_s/e_T=0.92/0.07$). Chemical kinetics based on an isoconversion model free approach was used here for the prediction of the thermal treatment protocol that had to be applied in order to make the desired HIPO coatings by GLYBP coil-coating.

This work is organized as follows: a brief overview of the preparation procedure of the sol–gel paints and GLYBP coil absorber coating briefly reported in our patent [60] is provided in the first part, followed by a description of the properties of the pigment dispersions obtained from the dynamic light scattering (DLS) coatings' properties and viscosity measurements reported in [61]. Preparation of the sol–gel coatings was extended to the fabrication of the TSSS coatings made of various sol–gel silane precursors and preparation of a two-layered selective sol–gel coating with the GLYBP coil absorber coating acting as a base.

The main part of this study represents the preparation of HIPO coatings from the GLYBP coil absorber coating. The GLYBP coil absorber coating is described and its surface properties established from the AFM and SEM measurements. Conversion of the GLYPB coatings to the HIPO coatings was studied with the help of isoconversion kinetics developed by Vyazovkin [62–67], providing thermal loading, i.e. time and temperature of heat treatment, which is needed to change solar absorptance and thermal emittance values of the initial coil absorber coating to the desired selective HIPO coating.

Spectral selectivity changes accompanying the formation of the HIPO coating were correlated to the vibrational bands observed in both spectra before and after the heat treatment, thus also providing evidence of the formation of a black spinel pigment core with a silica shell. The structure of the HIPO coating was studied with the help of XPS spectra measurements and its morphology was obtained from SEM and AFM studies. Finally, the thermal stability of the sol–gel GLYBP selective coatings is discussed and compared with the Mirosol TS coil absorber coatings produced by Alanod (DE).

2. Experimental

2.1. Instrumental

Determination of the particle size distribution in dispersions was obtained by dynamic light scattering (DLS) measurements, using a Malvern Zetasizer Nano ZS laser particle size analyzer. The instrument was equipped with an He–Ne laser source ($\lambda=633$ nm) at a scattering angle of 173°. The dispersion concentration was around 0.1 g/l. The suspension was prepared by dispersing the powder in butanol and treating for 2 min in an ultrasonic bath to obtain a well-dispersed suspension.

IR spectra were taken on a Bruker IFS66/S spectrophotometer with a resolution of 4 cm^{-1}, equipped with an integrating sphere (OPTOSOL), using a gold plate as a standard for diffuse reflectance.

The infrared reflection–absorption (IR RA) spectra of the GLYBP coatings and AISI 316 were recorded on a Bruker IFS66/S

spectrometer using a Monolayer Grazing Angle Specular Reflectance Accessory at a near-grazing incidence angle (NGIA) of 80° and with P-polarized light.

UV–vis spectra of the sol–gel pigment coatings were measured by a PerkinElmer Lambda 950 UV–vis spectrometer equipped with an integrating sphere.

SEM micrographs were obtained on a FE-SEM Supra 35 VP electron scanning microscope.

Atomic force microscopy (AFM) was carried out on the TSSS paint coatings using an AFM microscope Solver PRO produced by the NT-MDT company.

X-ray photoelectron spectroscopy (XPS or ESCA) was applied to investigate the chemical status of the elements on the surface of the sol–gel pigment coatings. The analysis was performed in an XPS spectrometer produced by Physical Electronics Inc., model TFA XPS. An Al Kα monochromatized source of X-ray light, with a power of 200 W, was used. The energy of the X-ray beam was 1486.7 eV. The analyzed area was 0.4 mm in diameter and the signal during the XPS analysis came from the surface layer up to 6 nm in thickness. Sample charging during XPS analysis was compensated by a low-energy electron gun-neutralizer. Depth profile analysis of the sol–gel pigment coatings was obtained by Ar^+ ion beam etching with an energy of 1 keV over a region of 5×5 mm^2 of the sample surface. The corresponding etching rate was 1 nm/min. The XPS depth profile was measured in order to reveal in-depth concentration variations. The survey spectra were taken every 2 nm, from which we determined the profiles representing the concentration of elements over the analyzed depth of 20 nm.

Thermogravimetric analysis (TGA) was performed on a Mettler Toledo TGA/SDTA 851^e instrument. TGA curves were measured from 30 °C to 500 °C in an air atmosphere, using a heating rate of 10 °C/min.

Contact angles for GLYBP coatings for water were determined using a manual goniometer (Krüss) with 20 μL liquid drops. The GLYBP coatings were cut into small pieces in order to adapt their size to the goniometer sample compartment.

2.2. Materials and preparation of pigment dispersions, paints and their deposition

As explained in our patent [60], the sol–gel GLYBP coatings (GLY/trisiloanol POSS/PK 3060 pigment) were prepared by the execution of the following interrelated steps. In the first step, the black spinel pigment particles (PK 3060, FERRO, USA) were functionalized with trisilanol isobutyl POSS (www.hybridplastics.com). Trisilanol POSS (7 wt%) was dissolved in a petrolether and mixed with spinel pigment using a high speed dissolver. The dispersion was then milled in a Dyno-mill Research Laboratory agitator bead mill (WAB, Willy A. Bachofen AG Maschinenfabrik) with zirconia beads with dimensions of 0.4 mm. The functionalized spinel pigment was dried and re-milled in 1-butanol (Sigma Aldrich). The homogeneous trisilanol POSS/PK 3060 dispersion was characterized by particles of a size of ~150 nm, as shown in Fig. 2. The dispersion is stable for more than a year and no re-milling is necessary before deposition of the coatings. No sedimentation of pigment was observed, because of the effective modification of the pigment particles with trisilanol POSS.

In the second step, (3-glycidoxypropyl) trimethoxysilane (GLY) (Sigma-Aldrich) sol–gel binder was prepared separately. Hydrolysis was achieved by the addition of diluted 0.1 M HCl, while the sol–gel precursors were added in concentrations up to 50%. Before the application, the pigment dispersion and sol–gel binder were mixed in a high speed mixer (Dispermat) for ½ h in order to obtain a homogeneous mixture. The addition of sol–gel binder to the dispersion was performed in mass ratios 1:0.08, 1:0.095 and 1:0.11.

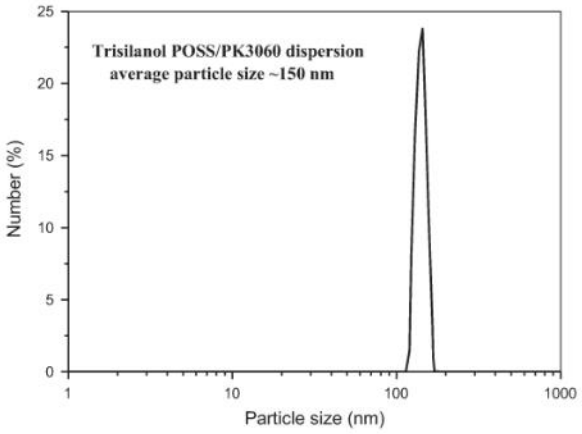


Fig. 2. Average particle size of trisilanol POSS/PK 3060 dispersion.

The typical concentration of the functionalized pigment in the final sol–gel paint was from 10% to 25% by weight.

In the final step, the sol–gel paint was used for the deposition of spectrally selective GLYBP paint coatings. On the laboratory scale, the coatings were made by a spin-coater at various rotation speeds (600, 800 and 1000 rpm for 60 s) in order to adjust the thickness of the coatings for a coil-coating system application (Alanod, DE). On an industrial line, ~800 m coil absorber coatings (1.25 m wide Al strip) were produced by a heating temperature of 290 °C for 6 min.

GLYBP coatings were prepared on an aluminium substrate for testing up to 400 °C. In the last part, the behavior of the GLYBP at 460 and 500 °C was examined, so the coatings had to be deposited on stainless steel AISI 316.

3. Results

3.1. Spectral selectivity of GLYBP coil absorber coatings

A few general remarks about the properties of crystalline $CoCuMnO_x$ [22,23,28] and TSSS coatings prepared from pigment dispersions should be made before discussing the results. The two coatings differ in pigment loadings, which to a large extent influence the selectivity. For $CoCuMnO_x$ coatings made by in situ crystallization of metal salt precursors, the pigment loading is up to 95%, contrasting the much lower pigment loadings (from 24% [4] to 38% [13]) encountered with polysiloxane based paint coatings. Despite the higher pigment loadings of the former coatings, the solar absorptance values were fairly low (a_s ~0.82 to 0.86), which is due to their inherently high reflection losses (> 10–12%) in the solar spectral region. These coatings inevitably need anti-reflecting coatings in order to increase a_s values above 0.92. In contrast, the main advantage of the crystalline in situ made black spinel coatings is their low thermal emittance; coatings are thin (300–500 nm) and the Mn–O vibrational modes [22,23], which appear outside the thermal spectral region (640 and 460 cm^{-1}) [22,28], do not contribute to e_T values, and the amount of the silica (or titania) binding phase was also low (a few%). In situ preparation of the black spinel coating is slow but seems to be enhanced by using inductive heating [28]. Coil-coating deposition of the black spinel coating using pigment dispersions is obviously faster and cheaper.

Even though the pigment loading was only 75–85% for the GLYBP coil absorber coating, a_s values above 0.90 were easily achieved. This was done by controlling the milling process, by influencing the

pigment particle size, affecting the surface roughness of the GLYBP coating and, consequently, the solar absorptance. Such effects are not new; they were reported by Etherden et al. [68], who showed by calculations that the optimal ratio between the solar absorption and extinction cross section is reached for particles of a size of ~300 nm and coating thickness ~1 μm. Taking these facts into an account, the pigment was intensively milled until the particle size ranged from 140 to 160 nm (Fig. 2) and the coating thickness was adjusted to 700–1300 nm.

Apart from the pigment loadings, the size of the pigment particles and their distribution within the coating, a_s/e_T ratios depend to the largest extent [1–5,13,69,70] on the coating thickness. Coating thickness, expressed by weight of dry paint per area (g/m^2), was changed for the GLYBP coatings by various means: by changing the speed of the coil-coating line (not shown here), spinning time and spinning speeds in case of laboratory samples, quantity of deposited wet paint and pigment loading expressed by the paint/GLY (hydrolyzed) mass ratio (1:0.08, 1:0.095. and 1:0.11) (Fig. 3). Examination of the results (Fig. 3) confirmed that a_s of the coatings increased with pigment loading and thickness of the coating. Thermal emittance also increased with the coating thickness but the pigment loading had a smaller effect. This meant that much thicker coatings could be deposited in order to achieve the desired spectral selectivity, with $a_s > 0.90$ and $e_T \sim 0.12$.

For example, spin-coated GLYBP with thicknesses of 2.3 g/m^2 provided selectivity with $a_s=0.928$ and $e_T=0.18$, while $a_s=0.91$ and $e_T=0.08$ for thinner coatings (1.7 g/m^2). For TSSS paint coatings shown in Ref. [13], for which silicone resin binder in combination with aminosilane dispersant was used, the corresponding selectivity values a_s/e_T were $a_s=0.913/e_T=0.25$ (for a thickness of 2.3 g/m^2) and $a_s=0.893/e_T=0.163$ (for a thickness of 1.7 g/m^2).

According to the results shown in Fig. 3, the absorber coating was made from paint with a paint/GLY ratio 1:0.095 (medium curve in Fig. 3A and B). The amount of applied paint was adjusted to give grammage of about 1.8 g/m^2, which corresponded to a coating thickness of about 800 nm, as explained above (Fig. 4B). The GLYBP coating that was deposited on the Alanod coil-coating line had $a_s=0.90$ and $e_T=0.12$.

Spin-coated GLYBP coatings exhibited abrasion resistance H2 and H3 (pencil hardness test – ISO 15184) and corrosion resistance in a salt spray chamber up to 100 h (microclimate ISO CD 12952-2).

To conclude, the dispersion of black spinel particles functionalized with trisilanol POSS and the added GLY binder provided stable sol–gel pigment dispersions in alcohol solutions. The resultant dispersion was compatible with many other silicon, titanium and zirconium alkoxydes (Table 1), enabling the fabrication of a plethora of sol–gel coatings with a_s ~0.90 to 0.92 and e_T up to 0.15. Some of the coatings exhibited even higher selectivity but had worse corrosion stability or adherence on the aluminium substrate. GLYBP coatings provided a good compromise (excellent adhesion, corrosion protection for 1 week in salt spray), which led us to improve their properties by applying an additional sol–gel over-coating. Before showing the properties of the two-layered coating, SEM, AFM measurements and optical properties of the GLYBP coil absorber coating are briefly presented below.

3.2. *Surface properties of GLYBP coil absorber coatings: SEM, AFM and optical properties*

SEM micrographs (Fig. 4A and B) of the coil absorber coatings revealed that the coatings consisted of well packed pigment particles of nearly equal size and without larger voids and holes. This meant that, after the deposition of wet paint, the solvent evaporated and the pigment particles sunk on the substrate and folded down, forming a compact pigment particle layer. The surface of the GLYBP coil absorber coatings was quite smooth, which we inferred from the AFM images (Fig. 4C), showing individual pigment particles with a surface roughness of about 31 nm and a particle size from 100 to 130 nm, which agreed well with the pigment particle size determined from the DLS measurement of the pigment dispersions (Fig. 2). Coil absorber coatings fulfill the basic requirement for high solar absorptance coatings, since they consist of small de-agglomerated pigment particles, as shown in Fig. 4.

The de-agglomeration of particles could be inferred from the total transmittance (TT (λ)), diffuse transmittance (DT(λ)) and the corresponding haze (in%) of the GLYBP pigment dispersion applied on FTO glass (Fig. 5). The results revealed that the haze was small (from 4% to 7%) [71], enabling clear sight through the coating, while the total transmittance could easily be modulated by changing the coating thickness. Coatings also adhered excellently on glass and were difficult to scratch. In this regard, the GLYBP coatings showed similar properties to those of electrochromic pigment coatings (NiO_{1-x} [72] and TiO_2 [73]) made with the deposition of the corresponding pigment dispersions on glass and plastic foils. Eventually, the GLYBP coatings on glass could be used as solar absorber coatings on glass with antiglare properties.

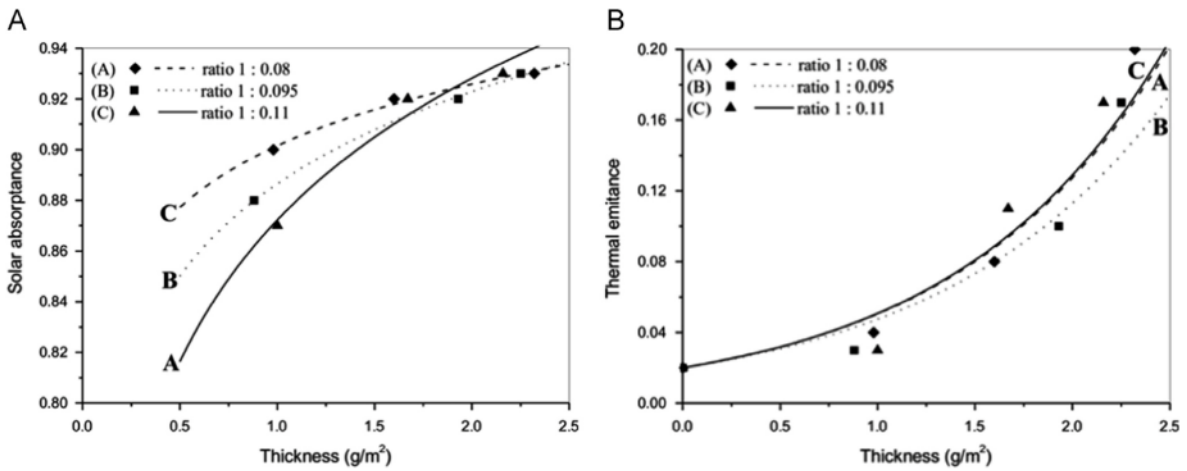


Fig. 3. Spectral selectivity parameters (a_s (A) and e_T (B)) for spin-coated GLYBP coatings deposited from different pigment dispersion vs. sol–gel binder ratios: 1:0.08, 1:0.095 and 1:0.11 and thickness of coatings in g/m^2 varied by the spin-coating speeds.

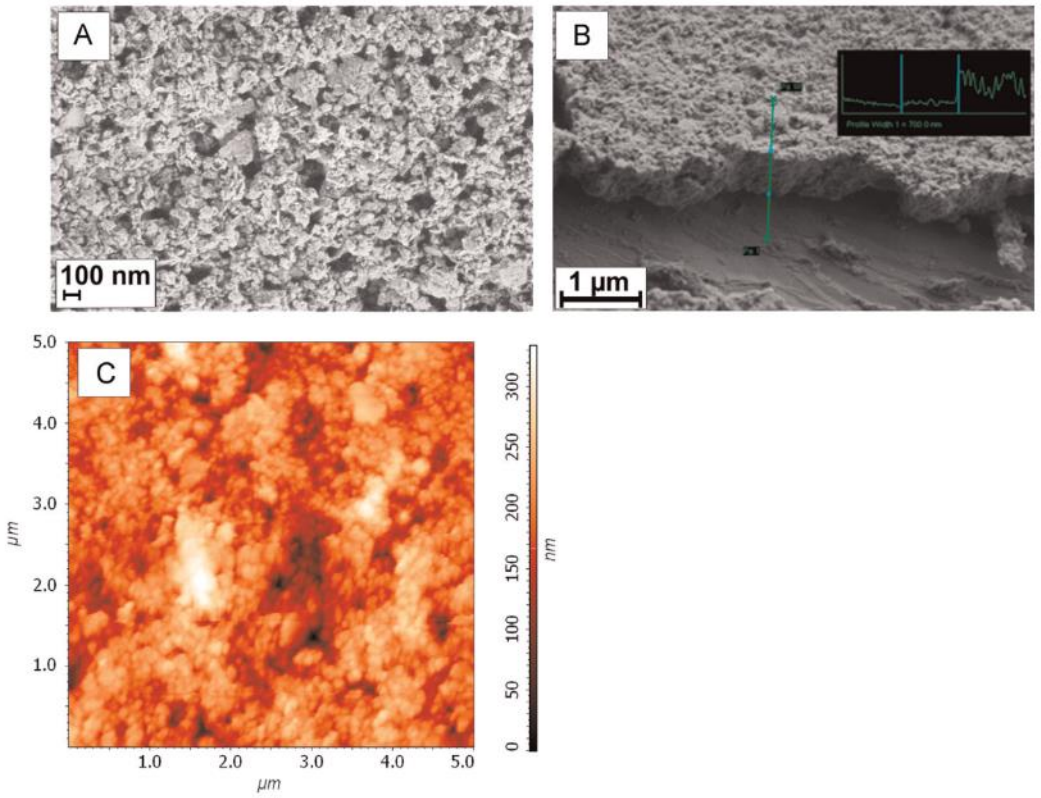


Fig. 4. Surface morphology of the GLYBP coil absorber coatings deposited on the coil-coating line (A), thickness measurements (B) and AFM images of coil absorber coating (C).

Table 1
Composition of spin-coated (1000 rpm, 60 s) sol–gel coatings made from various precursors, solar absorptance (a_s) and thermal emittance (e_T) and heat treated at 290 °C for 6 min.

Coating	a_S	e_T	Sol–gel former	Solvent	Catalyst
1	0.91	0.04	Tyzor TE	1-BuOH	AcOH glacial + EAA
2	0.91	0.11	TIP	2-Methoxyethanol	AcOH glacial
3	0.92	0.12	Zr butoxide polymer	1-BuOH	
4	0.92	0.1	DMDES	1-BuOH	
5	0.93	0.2	DMDES	1-BuOH	

EAA – ethyl acetoacetate, TIP – titanium(IV) isopropoxide, Tyzor TE – triethanolamine titanium complex, zirconium (IV) butoxide polymer, DMDES – dimethyldiethoxysilane (ABCR), 1-BuOH – 1-butanol, 2-methoxyethanol (FLUKA), AcOH glacial – acetic acid glacial (MERCK). All other chemicals were purchased at Sigma-Aldrich.

3.3. *Two-layered coating: morphology and spectral selectivity*

There were two reasons for the deposition of the second layer on top of the GLYBP coil absorber coating: to improve corrosion stability and to increase solar absorptance. It is difficult to satisfy both requirements because thick and dense coatings are needed for good corrosion protection, which is just the opposite to porous and relatively thin coatings performing as anti-reflecting coatings.

Despite the limited possibility of improving the GLYBP coil absorber coatings, two-layered GLYBP coatings were made with the aim of demonstrating the general use of the GLYBP coating. Various non-pigmented sol–gel coatings were thus applied on top of GLYBP coil absorber coatings with a_s=0.90 and e_T=0.12 (d=560–860 nm) (Table 2), i.e., GLY/diisopropoxy-bis(ethylacetoacetato) titanate (GLY/TiAcac), GLY/methyltrimethoxysilane (GLY/MTMS), GLY/tetraethoxysilane (GLY/TEOS) and GLY/tetramethyl orthosilicate (GLY/TMOS). Precursors were hydrolyzed with acidified water and diluted in ethanol, stirred for 24 h and deposited by spin- and/or dip-coating on top of the GLYBP coil absorber coatings. All coatings were cured by additional heat treatment at 290 °C for 6 min in order to mimic conditions on the coil-coating line [13].

The thickness of the over-coats was determined by making cross-cuts and using SEM analysis (Fig. 6). The results revealed that the GLYBP base coil absorber coatings consisted of individual and non-agglomerated pigment particles covered with a homogeneous layer of the sol–gel coating. The thickness of the latter varied from 40 to 50 nm (GLY/TEOS and GLY/MTMS) (Fig. 6A and B) and reached 180 nm for the GLY/TiAcAc coating (not shown).

Spectral selectivity measurements revealed (Table 2) that some of the two-layered coatings actually showed smaller e_T values and higher a_s values than those of the initial GLYBP coil absorber coatings. We attributed this to the partial degradation of the two-layered coatings and restructuring of the organic–inorganic silica network. Namely, organic–inorganic hybrids tend to condense in a wide temperature range by forming various incompletely condensed linear (T^1), branched and cyclic (T^2), open (ladder) and closed silsesquioxanes (T^3), while silica (T^4) species are formed at higher temperatures (T > 430 °C) [14]. Transformation of the sol–gel network when exposed to thermal loading at higher temperatures (i.e., 400 °C) was thus exploited in order to convert the as-prepared GLYBP coil absorber coatings into HIPO coatings with higher spectral selectivity. An isoconversion kinetics approach was used for this purpose.

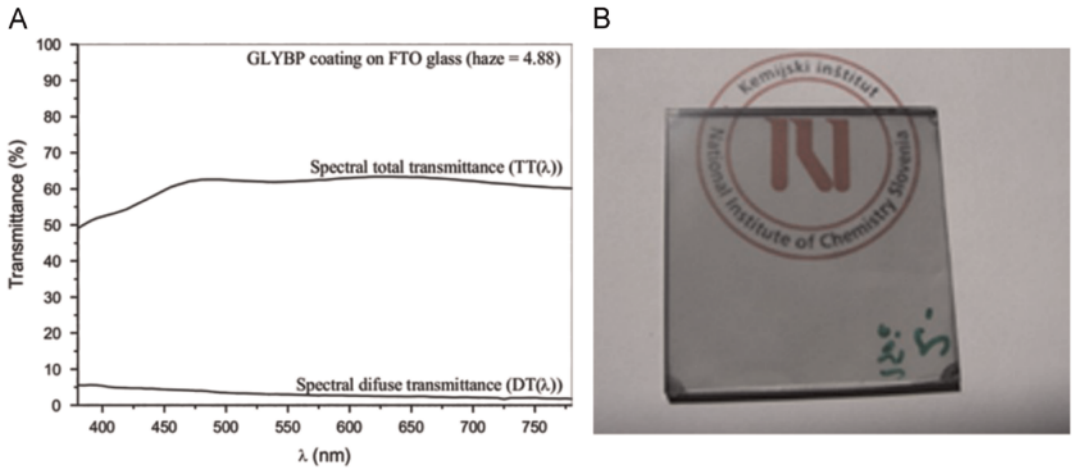


Fig. 5. Total (TT(λ)) and diffuse (DT(λ)) transmittance spectra of spin-coated GLYBP (GLY/trisilanol POSS/PK3060) coatings on FTO glass made of GLYBP dispersions after milling with 0.4 mm zirconia beads and spin-coated for 60 s at a rotation speed of 1500 s^{-1} (A) and photograph of the correspondent coating (B).

Table 2
Solar absorptance and thermal emittance of over-coats on GLYBP coating.

Over-coat	a_s	e_T	$d_{overcoat}$ (nm)
As prepared coil absorber coating (base)	0.905	0.12	~800
GLY/MTMS	0.88	0.08	50
GLY/TMOS	0.9	0.15	90
GLY/TiAcAc	0.92	0.1	180
GLY/TEOS	0.93	0.12	40

3.4. HIPO coating: isoconversion kinetics

3.4.1. Preparation of HIPO coating

An isoconversion kinetics approach was applied here for assessment of the thermal loadings, i.e., time of heat treatment and temperature that should be applied in order to transform the GLYPB coil absorber coating (a_s=0.90 and e_T=0.12) into an HIPO coating characterized by higher spectral selectivity. The proposed approach, based on the heat treatment decreasing e_T values, is not new. A drop of e_T values of TSSS paint coatings has already been noted during thermal stability studies of polysiloxane [13] and polyurethane resin based TSSS coatings [74,75] (up to 3 weeks). The mechanical integrity of the polysiloxane based TSSS coatings remained unchanged [13] but polyurethane based TSSS paint coatings deteriorated [75]. At higher thermal loading (400 °C, a few weeks), the polysiloxane based TSSS paint coatings [13] deteriorated mechanically but the e_T values dropped from an initial ~0.20–0.22 to 0.15–0.16 final values. However, this approach has not been identified as an alternative way of making paint coatings with higher spectral selectivity, mainly because thermal degradation of polysiloxane binders is fairly complex and the end products are difficult to control. In this regard, sol–gel GLYBP coatings are a better option because the PEO groups in the GLY hybrid have poor thermal stability, which was exploited here for fast and easy conversion of the coatings into the more spectrally selective HIPO coatings.

In order to get an insight into the structural changes that took place during the heat treatment of the GLYBP coatings, the corresponding pigment dispersions were deposited on Si wafers and the infrared spectra measured (Fig. 7).

GLY/PEO hybrids were not designed as temperature stable coatings and complete curing could already be achieved after 30 min at 130 °C [16,37] (Fig. 7A). This meant that the coil-coating conditions (290 °C, 6 min) were too severe and the PEO groups already to certain extent broken (Fig. 7C). This was also noted for a coating exposed to longer (30 min) but milder conditions (230 °C), whose infrared spectra revealed the C=O mode at 1728 cm^{-1} (Fig. 7B). As expected, significant changes were already observed in the infrared spectra of coatings exposed to 400 °C after 30 min (Fig. 7D). The Si–O–Si modes of the nanocomposite and the GLYBP coating at 1060 and 1105 cm^{-1} converted to the modes of silica, characterized by a band at 1061 cm^{-1} and a shoulder band at ~1148 cm^{-1}. At the same time, the –CH bands disappeared. As expected, the bands of spinel at 631, 582 and 438 cm^{-1} remained unaffected [22].

Heat treatment of the GLYBP coil absorber coating (Fig. 8) at 400 °C increased the a_s values by ~2% (a_s=0.92) and e_T dropped by ~5% (e_T ~0.075). The spectral selectivity of the corresponding HIPO coating remained unchanged for 26 days, as can be seen from the IR reflectance spectra depicted, together with a_s and e_T values, in Fig. 8. The rate of transformation of the GLYBP nanocomposite into the structure of the HIPO coating was studied with the help of isoconversion kinetics, as described below.

3.4.2. Isoconversion kinetics of GLYBP coil absorber coating

Thermal treatment is a complex process, which can induce a variety of physical and chemical changes in coatings; melting, sublimation and polymorphic transitions, partial degradation, oxidation, condensation, etc. By using heat treatment, the coatings become denser and more compact, which can beneficially affect solar absorptance. On the other hand, e_T values were expected to decrease due to the partial or complete loss of highly absorbing organic groups. However, longer exposure times (2 weeks or more) at temperature of 500 °C and higher inevitably led to the increase of e_T values due to the oxidation of the metallic substrates (AISI 316, Inconel, Mo, Cr, etc.). This we consider as a serious problem common to cermet coating nowadays employed in vacuum solar absorbers, since a loss of vacuum can have a disastrous effect on spectral selectivity.

During the heat treatment, a_s and e_T values changed simultaneously with time and temperature and at different conversion rates $\frac{d\alpha}{dt}$, the rate being dependent on temperature. We expressed the change of thermal emittance with a conversion indicator α ($0<\alpha<1$)=((e_T (initial)/(e_T(initial))−$e_T(t)$), which, depending on time and temperature, can be described [76] by the following

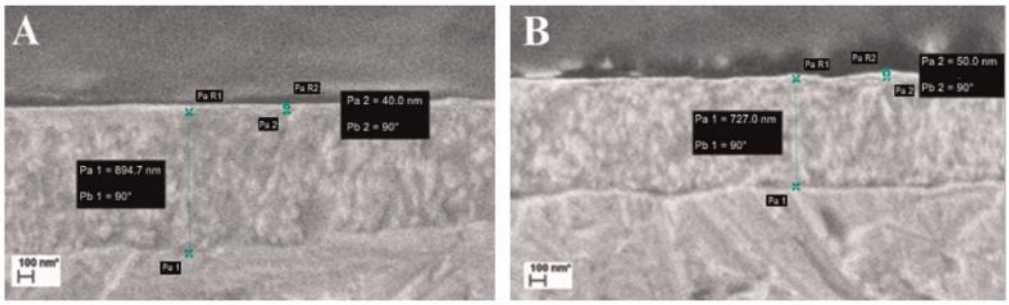


Fig. 6. SEM of cross-cuts of: (A) GLY/TEOS and (B) GLY/MTMS coatings deposited on GLYBP coating.

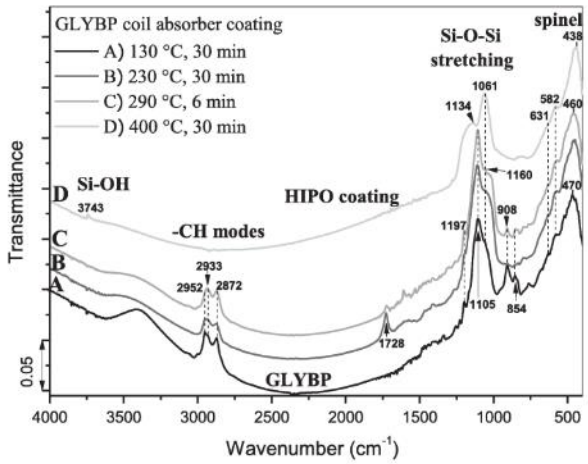


Fig. 7. IR transmission spectra of various coatings exposed to different temperatures (A) and (B) the corresponding changes of the Si–O–Si stretching and –CH valence modes. Initial: wet dispersion dried at 130 °C (1/2 h).

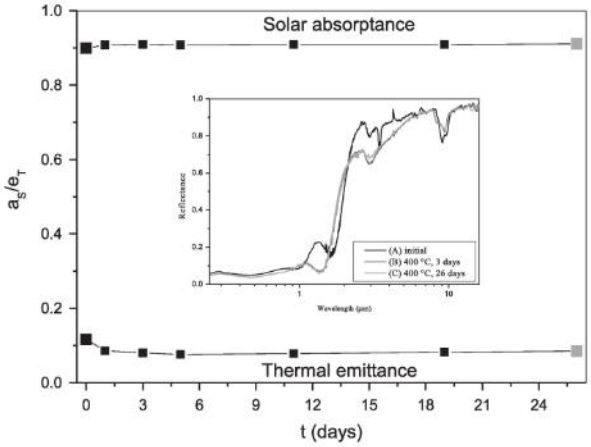


Fig. 8. Changes of the solar absorptance and thermal emittance of the GLYBP coil absorber coating during exposure to 400 °C for 26 days. The inset shows the reflectivity spectra of the initial GLYBP coil absorber coating (A) and coil absorber coating after exposure to 400 °C for 3 days (B) and 26 days (C).

general Arrhenious equation [66]:

$$\frac{d\alpha}{dt} = k_{(T)} f_{(\alpha)} \tag{1}$$

where $(d\alpha/dt)$ is the reaction rate, $k_{(T)}$ is the rate constant, t is the time, T is the temperature, α is the conversion factor attributed to the specific degradation indicators (change of mass, solar absorptance and thermal emittance changes, vibrational mode intensity variations etc.) and $f_{(\alpha)}$ is the reaction model. By knowing the values of $f_{(\alpha)}$, A and E (known as the kinetic triplet), it is possible to predict the rate of the conversion $(d\alpha/dt)$ (i.e., e_T values) of the selective coating.

For assessment of the thermal loadings, i.e., time and temperature, which brought about the selective HIPO coating, the GLYBP coating was exposed to isothermal loadings for 7 days at temperatures T_i=230, 250 and 270 °C and the corresponding e_T values were measured every second day (Fig. 9). The time of heat treatment was limited to 7 days because the e_T values no longer changed after that. The e_T values served as a conversion indicator expressed by the conversion factor α $(0<\alpha<1)$, as defined above. From Eq. (1) and with the help of the advanced isoconversion (model free) kinetics approach [62,64,66], we calculated time t_α at the selected temperature (T_0) that was needed to reach the desired value of conversion α:

$$t_\alpha = \frac{J\left[E_\alpha T(t_\alpha)\right]}{\exp\left(\frac{-E_\alpha}{RT_0}\right)} \tag{2}$$

E_α in Eq. (2) represents the activation energy, which was calculated as a minimized function Φ (E_α) [77] from Eq. (3)

$$\Phi(E_\alpha) = \sum_{i=1}^{n} \sum_{j\neq i}^{n} \frac{J\left[E_\alpha, T_i(t_\alpha)\right]}{J\left[E_\alpha, T_j(t_\alpha)\right]} \tag{3}$$

where the value of the integral J in the equation (Eq. (4))

$$J\left[E_\alpha, (t_\alpha)\right] \equiv \int_{t_\alpha-\Delta\alpha}^{t_\alpha} \exp\left[\frac{E_\alpha}{RT_i(t)}\right] dt \tag{4}$$

was calculated numerically using the trapezoidal rule for a series of different α values obtained from the results depicted in Fig. 10. Integration was performed within a narrow time interval, thus reducing the systematic error that is due to a possible change of the activation energy in a broad temperature interval. Activation energy E_α, which is the same for specific degradation α, but—as shown in Fig. 10A—was different for the different conversion indicators α. In other words, the advanced isoconversional method [62] thus takes into an account changes in the activation energy at various stages of conversion α. Examination of α vs. t curves showed the predicted time t_α needed to reach the specific desired conversion α at selected temperatures T_0 (Fig. 10B).

Examination of the curves shown in Fig. 10B shows that—as expected—high values of conversion α can be attained much faster at higher temperatures T_0, e.g., e_T values dropped below α=0.08 in less than 2 days but at 180 °C, which corresponded to the stagnation temperature [74] of the solar collector with coil-coating absorber (a_s=0.905 and e_T=0.12), the time τ_α (or t_α) needed to convert the coil absorber coating to the HIPO coating was 5.3 days.

Interestingly, the coil absorber coating could also change under working conditions (100 °C) in a relatively short time (11.5 days). This indicated that the coil absorber coating possessed inherent instability and thus a tendency for spontaneous but steady curing even at lower temperatures. This can be explained by the low activation energy at small conversion values (Fig. 10A), agreeing also with the concept of isoconversion kinetics, which considers the activation energy to depend on the conversion factor α and temperature.

3.4.3. TG, DTG and DSC measurements

The explanation for the observed tendency of the coil absorber coatings to change to HIPO coatings was obtained from TG, DTG and DSC measurements (Fig. 11). TG measurements of the GLYBP paint showed that the mass already started to decrease below 200 °C and the decrease in mass became strongest at ~360 °C. The coating stabilized at ~470 °C. Total mass loss was ~17.11% (Fig. 11A). Interesting information was obtained from the DSC measurement (Fig. 11C), revealing the existence of exothermic processes, which started at 240 °C and terminated at 470 °C.

Not only with the coil absorber coating but also the GLYBP paint itself, which was dried (24 h) in air, TG showed a continuous loss of mass up to high temperatures ($T > 410$ °C) (Fig. 11B). Air-dried GLYBP paint also exhibited an exothermic process with the peak of heat release shifted to lower temperatures (Fig. 11C).

The exothermic processes noted from the DSC measurements (Fig. 11C) were in agreement with the general tendency of sol–gel organic–inorganic hybrids to condense in a wide temperature range into various forms of open (ladder) and/or closed silsesquioxanes (T^3), while silica (T^4) species prevail at higher temperatures ($T > 430$ °C) [78]. The identification of all possible intermediates is a formidable task that is beyond the scope of this study. However, as inferred from infrared spectra analysis (Figs. 7 and 8), the condensation reactions of the Si–O–Si groups were the prevailing process, being energetically more intense than the endothermic loss of the –CH groups that took place simultaneously (Figs. 8 and 9). The loss of the –CH groups was the main cause of the decrease of e_T values and formation of the HIPO coating, agreeing with the e_T changes observed for other spectrally selective paint coatings prepared from other resin binders [75] and for the polysiloxane based TSSS paint coatings mentioned above.

To conclude, advanced isoconversion kinetics calculations predicted that the sol–gel GLYBP hybrid coil absorber coatings would change e_T values during the course of heat treatment, the conversion rate to HIPO coating depending on temperature. This enabled us to predict that the as-deposited coil absorber coating

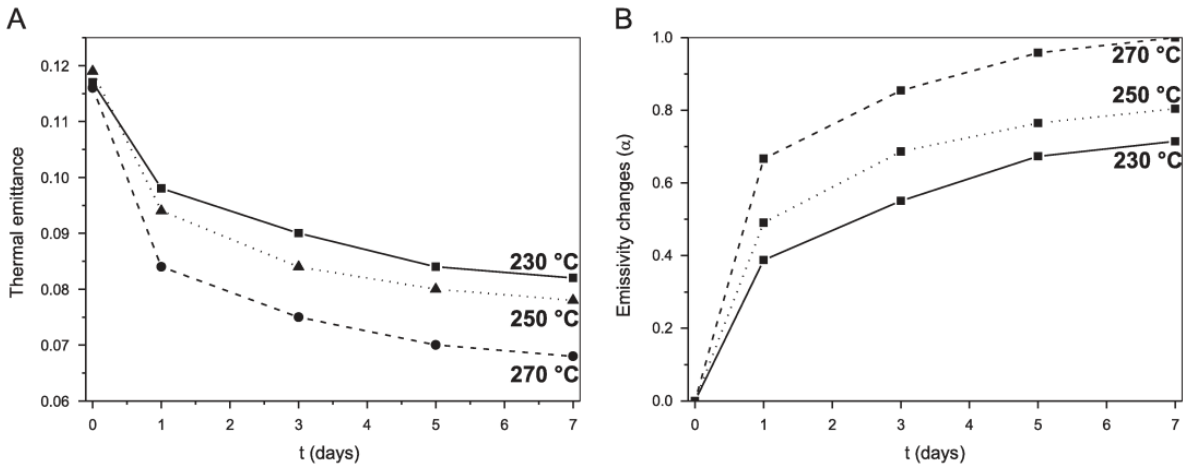


Fig. 9. e_T values (A) and the corresponding conversion indicators α (B).

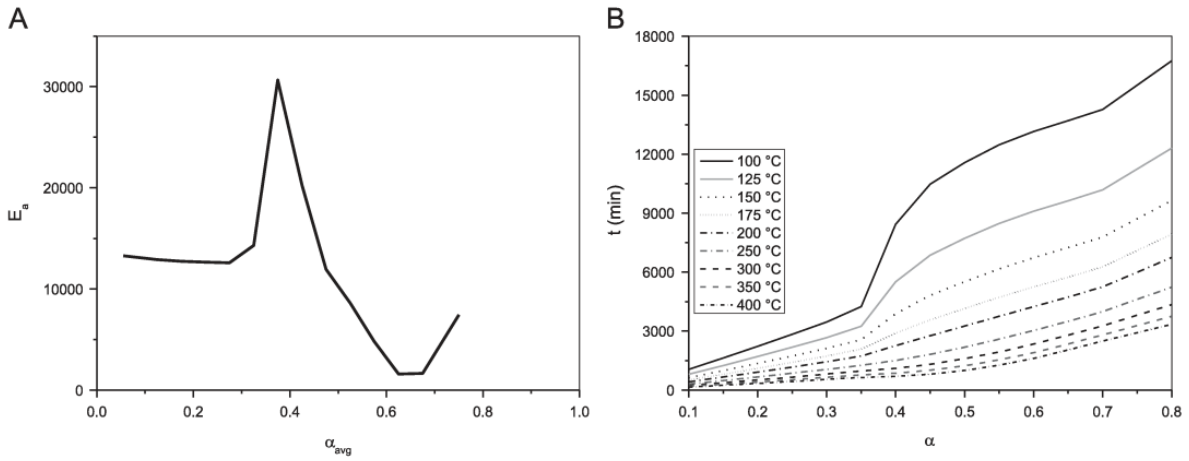


Fig. 10. The variation of the activation energy (E_α) as a function of degradation (α) (A) and predicted times (t) as a function of degradation (α) for various temperatures.

cured at 290 °C (6 min) would inevitably start to change its structure and its spectral selectivity when the coating was exposed to working and, more intensively, under stagnation conditions (~180 °C) in the solar system. However, the coil absorber coatings retained their surface morphology and surface roughness, which changed from 31 nm to 28 nm, as inferred from the SEM and AFM measurements (Fig. 12). It should be noted that outgassing of the degradation products could not be detected in solar collector simulation tests and further TG MS experiments are planned for the future to reveal the corresponding phenomenon.

In order to establish the composition of the sol–gel HIPO coatings, XPS spectra were studied in detail, as shown below.

4. XPS analyses of coil absorber coatings and HIPO coatings

4.1. Survey spectra

The main purpose of XPS studies was to obtain additional information about the surface structure and composition of the TSSS coil absorber GLYBP and HIPO coatings, in relation to their hydrophobic properties, stemming from the presence of trisilanol POSS dispersant as the main source of water repellence. The XPS survey spectra of selected coatings, i.e., as-prepared GLYBP coil absorber coating, and the same coating heat treated for 26 days at 230 and 400 °C, are depicted in Fig. 13. The spectra exhibited C 1s, O 1s, Si 2p, Mn 2p, Cu 2p and Fe 2p peaks, confirming the coatings'

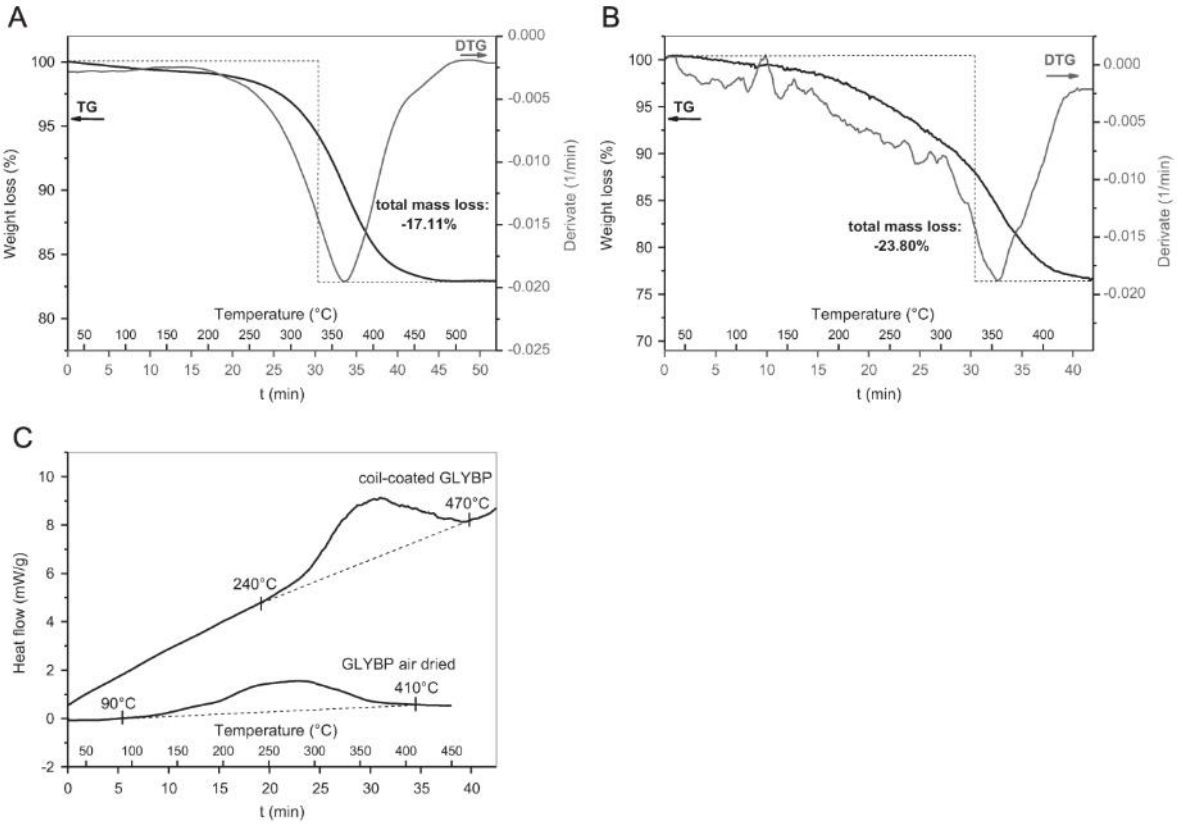


Fig. 11. TG (A, B) and DSC (C) measurements of the as-prepared GLYBP coil absorber paint (A and C-a) and air-dried paint (B and C-b).

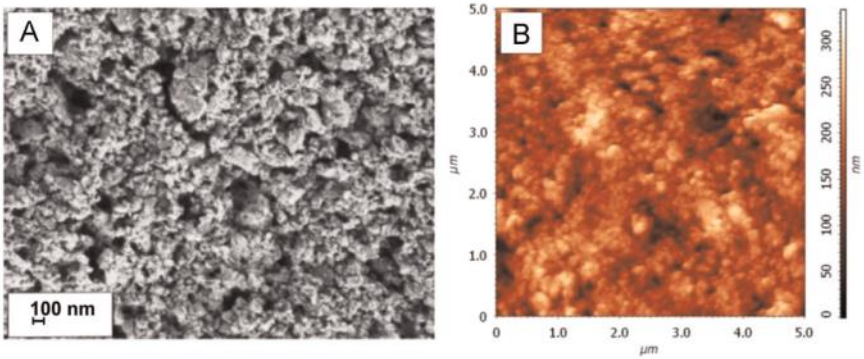


Fig. 12. SEM (A) and AFM (B) measurements of the HIPO coating.

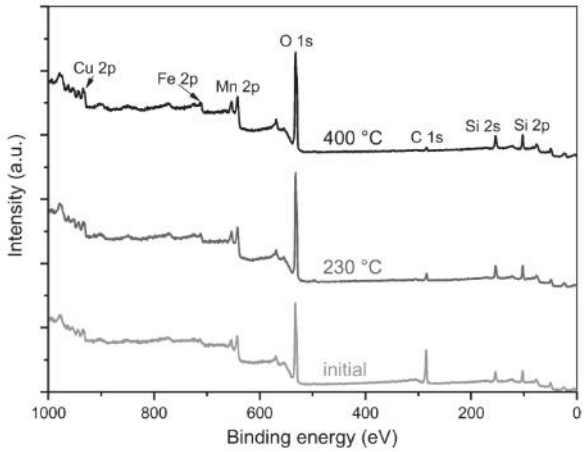


Fig. 13. XPS survey spectra of GLYBP coil absorber coating and coatings exposed to 230 and 400 °C for 26 days presenting the Mn 2p, Cu 2p, Fe 2p, C 1s, Si 2p and O 1s peaks.

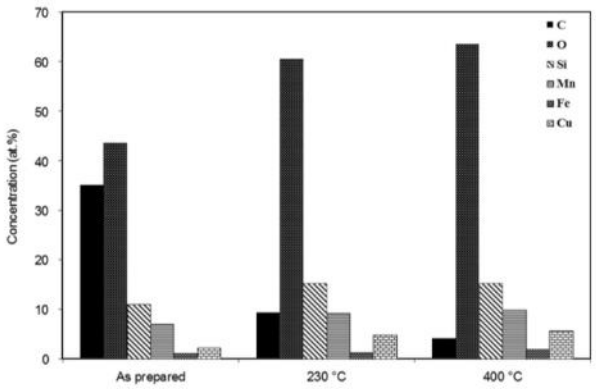


Fig. 14. Surface elemental composition obtained by the XPS method of GLYBP coil absorber coating and the same coatings exposed to 230 and 400 °C for 26 days.

composition; trisilanol POSS and GLY were the source of Si, O and C, while the remaining elements belonged to the BP pigment ($FeMnO_4$). The presence of Cu was considered to be an impurity related to the pigment synthesis. From the intensities of XPS peaks, the surface composition was calculated and is presented in Fig. 14. The surface of the as-prepared GLYBP coating was achieved with carbon-based species, which were gradually removed during the course of heat treatment.

4.2. High-energy resolution XPS spectra

High-energy resolution XPS spectra gave information about the concentration and chemical structure of elements. The results confirmed (Fig. 15) the expectation that the black spinel pigment was thermally stable under the applied thermal loadings, which we inferred from the Mn $2p_{3/2}$ and Mn $2p_{1/2}$ peaks at 653.7 and 642.0 eV respectively [79,80], which remained unchanged during the heat treatment. On the basis of the literature data, we assigned the corresponding binding energies to different MnO_2 or Mn_2O_3 phases attributed to the Mn(3+) and Mn(4+) valence states. The intensity of the Mn $2p_{3/2}$ peak did not change significantly at higher thermal loading, which indicated the stability of the Mn oxidation state in the pigment.

Fe $2p_{3/2}$ spectra (Fig. 16) were less expressive than the Mn 2p spectra, which is related to the low concentration of Fe in all samples, because Fe was used as a dopant of Mn. An Fe $2p_{3/2}$ peak was found at 711.0 eV and it was related to one of the Fe-oxide phases [81].

The XPS spectra of O 1s were more expressive (Fig. 17). Spectrum O 1s consisted of two peaks at energies 530.0 and 532.5 eV. The peak at 530.0 eV was assigned to metal oxides in the matrix, while the peak at 532.5 eV was ascribed to Si–O. Progressive oxidation of the coatings with thermal treatment was conceived from the gradual energy shift of the two peaks to higher binding energies.

Spectrum C 1s (Fig. 18) showed two peaks with binding energy 284.4 and 286.5 eV. The peak at 284.4 eV indicated the presence of CH_2 and CH_3 moieties, stemming from the formation of the PEO chains (C–H and C–C) and the pendant groups of trisilanol POSS. The peak at 286.5 eV (C–O and C=O), presented in the initial GLYBP coil absorber coating, disappeared after the coatings were exposed for 26 days at 400 °C. This peak could probably be assigned to Si–C bonds that remained in the structure after the heat treatment [82].

The spectrum of the as-prepared GLYBP coil absorber showed just a single Si 2p peak (Fig. 19) at 102.5 eV, which can undoubtedly be

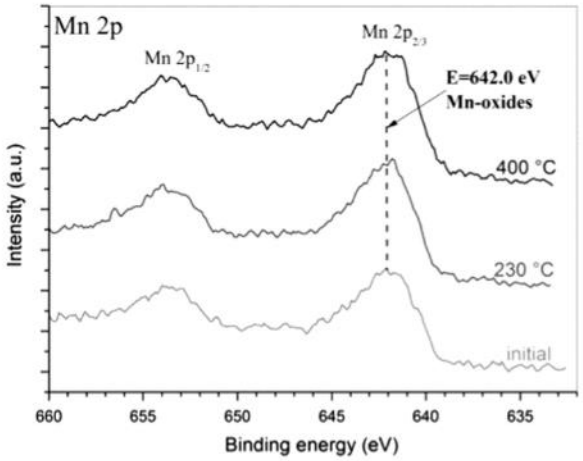


Fig. 15. Mn 2p XPS spectra: initial GLYBP coil absorber coating and the coatings thermally treated at 230 and 400 °C for 26 days.

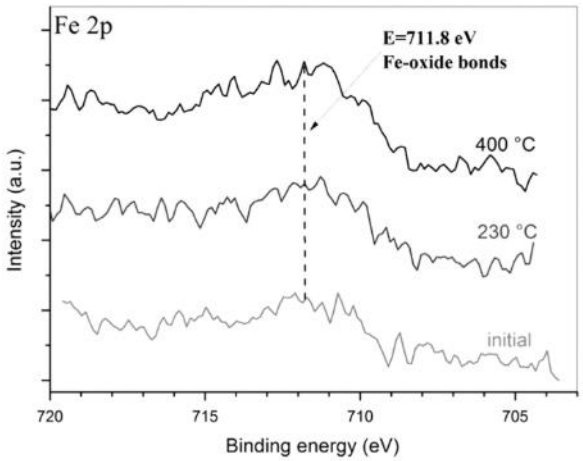


Fig. 16. Fe $2p_{3/2}$ XPS spectra of initial GLYBP coil absorber coating and coatings thermally treated at 230 and 400 °C for 26 days.

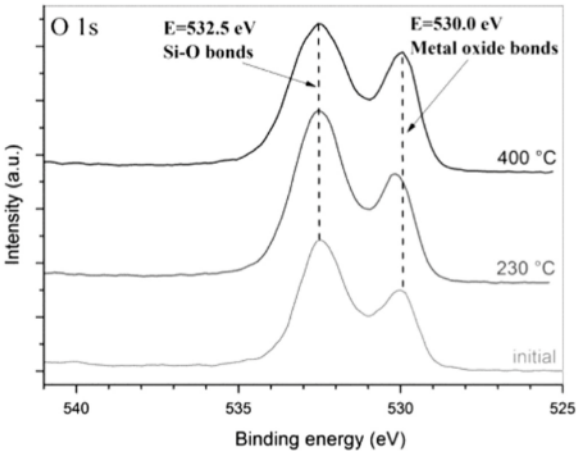


Fig. 17. O 1s XPS spectra of initial GLYBP coil absorber coating and coatings thermally treated at 230 and 400 °C for 26 days.

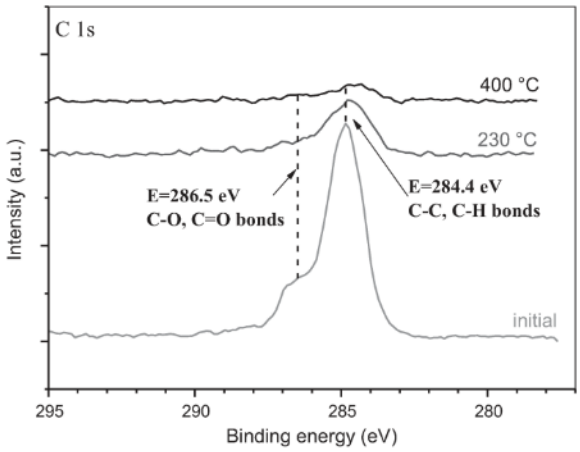


Fig. 18. C 1s XPS spectra of initial GLYBP coil absorber coating and coatings thermally treated at 230 and 400 °C for 26 days.

assigned to SiO_3–C [82]. As expected, heat treatment shifted the peak to higher energy (i.e., 103.0 eV).

4.3. Depth profile analysis of coatings

XPS depth profile analysis enabled us to get an insight into the depth distribution of elements and the nature of the hydrophobicity of the coatings. The XPS depth profile analysis was performed by Ar ion beam etching of the coatings over an area of 5×5 mm^2, with energy of 1 keV. The corresponding etching rate was 1 nm/min, measured on a reference sample of Ni. In order to reveal in-depth concentration variations, XPS spectra were taken every 2 min (2 nm). The variations of concentration of elements to a depth of 20 nm are shown in Fig. 20. The changes in concentration of elements before (on surface) and at the end of etching corresponding to a depth of about 20 nm are shown in Fig. 21.

Examination of Fig. 20A shows that the as-prepared GLYBP coil absorber coating contained more carbon but a lower concentration of oxygen than the heat treated coatings. The latter coatings consequently showed lower C/O ratios (Fig. 21). As expected, the concentration of Si was higher for the heat treated samples, before and after etching, compared to the GLYBP coil absorber coatings.

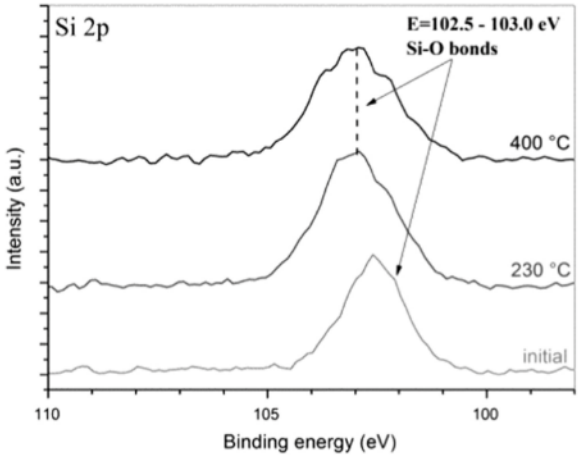


Fig. 19. Si 2p XPS spectra of initial GLYBP coil absorber coating and coatings thermally treated at 230 and 400 °C for 26 days.

The results of XPS analysis could explain the loss of hydrophobicity of the GLYBP coil absorber coating noted for heat treated coatings. As-prepared GLYBP coatings exhibited a fairly high contact angle (~124°) but this dropped to 14.7° and 8.7° after the coil absorber coatings were thermally treated at 230 and 400 °C, respectively, for 26 days. The corresponding process was much faster for the coatings exposed to 400 °C (Fig. 21). In both cases, the end result of the degradation process was a drop of thermal emittance as a result of conversion of the initial Si–O–Si bands typical of the GLYBP nanocomposite (1105 and 1060 cm^{-1}) to the silica bands (1061 and 1148 cm^{-1}) characteristic of heat treated coatings (Fig. 7). We attributed the hydrophobicity noted for the as-prepared GLYBP coil absorber coating to the free and/or bonded trisilanol POSS dispersant molecules (Fig. 20A); of a total 7% of the trisilanol POSS present, 4.3% is covalently attached to the pigment surface [44,45], while the remaining trisilanol POSS (~3%) is free to move inside the coating, as we have shown for perfluoro POSS functionalized cotton fabrics regaining their hydrophobicity after ironing (180 °C) [83]. To conclude, long exposure (26 days) of the GLYBP coatings to 230 °C (Fig. 20B) led to the depletion of dispersant in the outer part of the coating, the C/O ratios decreased and the coatings became hydrophilic (Fig. 21).

5. Long-term stability of coatings deposited on stainless steel (SS) at high temperatures

5.1. Oxidation of SS substrate and coatings

For solar absorbers operating at high temperatures (> 450 °C), oxidation of the substrates may be one of the most important mechanisms of degradation. In order to check the long term temperature stability of the HIPO coatings and to establish the role of oxidation of the substrate in the long-term thermal stability of the coatings, the GLYBP pigment dispersion was applied on stainless steel (AISI 316), exposed to 460 and 500 °C for 1216 h, and the a_s and e_T values determined at various time intervals (Fig. 22). Two HIPO coatings were made by heat treatment (290 °C, 6 min) of GLYBP coatings, made by spin-coating deposition with slightly different thicknesses: HIPO-SS-460 (e_T=0.28 and a_s=0.90) (thicker) and HIPO-SS-500 (e_T=0.25 and a_s=0.90) (thinner) coatings. Higher e_T

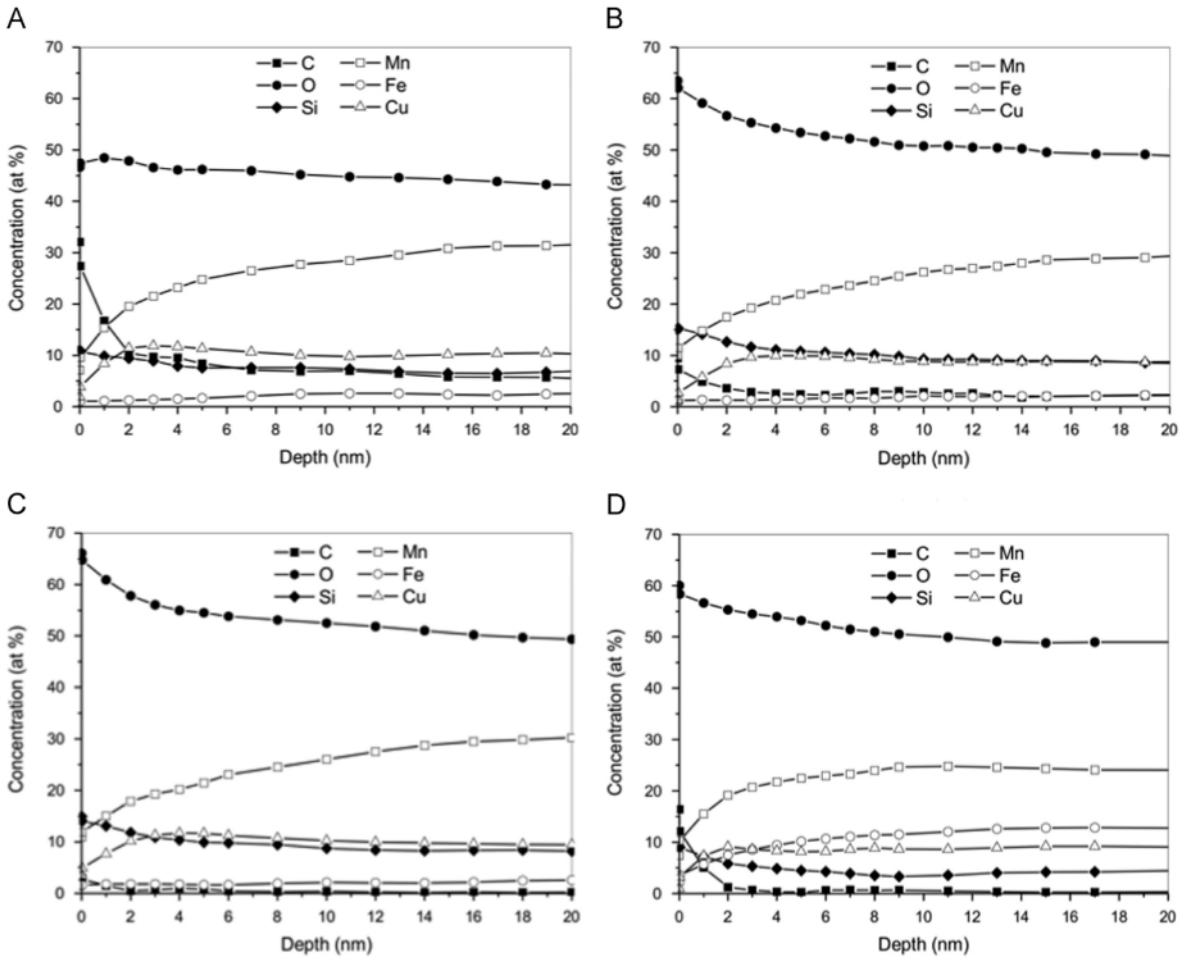


Fig. 20. XPS depth profiles of elemental composition across 20 nm thick surface layer of the as-prepared GLYBP coil absorber coating (A) and coatings thermally treated at 230 °C (B) and 400 °C (C) for 26 days. GLYBP absorber coating on AISI 316 thermally treated at 500 °C for 1216 h (D).

values were expected compared to the GLYBP coil absorber coating, due to the high thermal emittance of the SS substrate (~0.12).

Examination of the results (Fig. 22) shows that the selectivity of the HIPO coatings changed during the first few days (see above) but did not change significantly over the course of later heat treatment ($t > 76$ h), confirming their long-term thermal stability. As expected, thicker HIPO coatings ($e_{Tinitial}$=0.29) that were exposed to a lower temperature, i.e. 460 °C, changed e_T values to a smaller extent (~3% to 4%) compared to the thinner coatings ($e_{Tinitial}$= 0.25) exposed to 500 °C, which showed the e_T increase of about 7–8%. Both coatings started to show enhancement of the e_T values after ~250 h of heat treatment. The SS substrates only changed e_T values by about 2–3% (Fig. 22), which was less than the e_T changes of the HIPO coating (7–8%). Unfortunately, because of the poor spectral resolution of the hemispherical infrared reflectivity spectra, which served for the determination of the corresponding e_T values, vibrational bands that we could attribute to the e_T changes could not be established. Surprisingly, solar absorptance values remained practically unchanged.

In order to obtain an insight into the nature of the changes and the oxidation mechanisms that led to the increase of the e_T values of the HIPO coatings, the corresponding longitudinal optical modes (LO modes) were determined from the NGIA reflection–absorption spectra measured with a P-polarized infrared light (NGIA RA) and the intensity of the LO modes correlated to the e_T values.

One of the problems in the interpretation of the NGIA IR spectra was the splitting between the frequencies of the LO and transversal optical (TO) modes, the former being blue shifted compared to the TO modes obtained from the infrared transmission spectra of thin coatings (Berreman effect) [84]. Once the LO modes were assigned, the intensity variations could be directly correlated to the thickness of the formed oxide layer, as has been demonstrated by Wackelgard [85,86] for Ni/Al_2O_3 cermets.

We first studied the oxidation of the SS substrate (AISI 316) (Fig. 23). The oxidation of SS has been thoroughly studied. With the help of reflection–absorption (RA) spectroscopy, Mertens [87], Guillamet et al. [88] and Kotenov et al. [89] studied the formation of oxide layers on AISI 316 steel, while Schruebl and Thomas [90] performed similar studies on SC16 alloy. For the assignment of the TO modes of the oxide layers formed, diffuse reflection spectra of oxide layers [89] were also measured, enabling the establishment of correlations between the LO and TO modes.

Reflection absorption infrared spectra of AISI 316 [87,88] and diffuse reflectance spectra [88] provide reliable information about the LO vibrational modes of various oxide species formed up to 500 °C, enabling the type of oxides formed to be established: α-Fe_2O_3

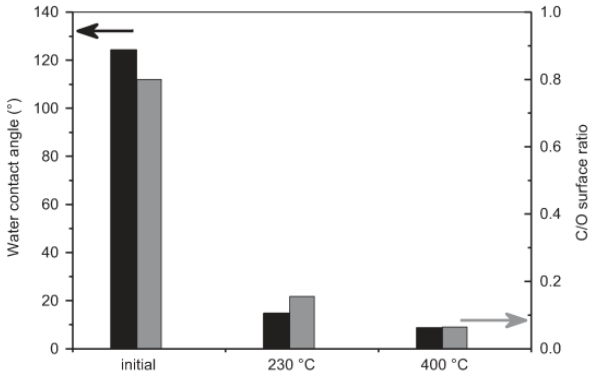


Fig. 21. Water contact angle and C/O surface atomic concentration ratio for the GLYBP coil absorber coating and the same coating exposed to 230 and 400 °C for 26 days.

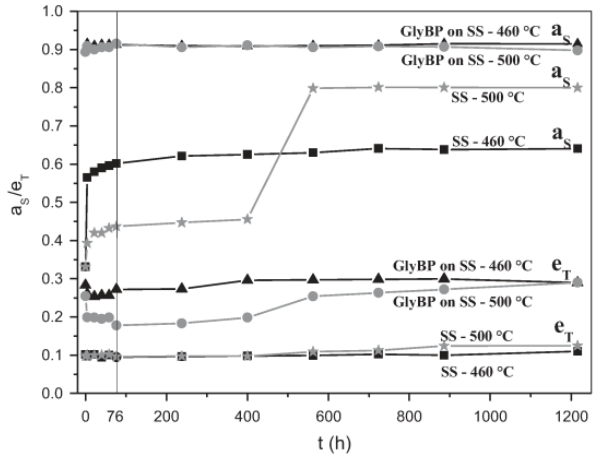


Fig. 22. Variations of a_s and e_T values of the HIPO coatings deposited on the SS substrate (AISI 316) and for the SS substrate itself over the course of heat treatment (460 and 500 °C) at various time intervals up to 1216 h.

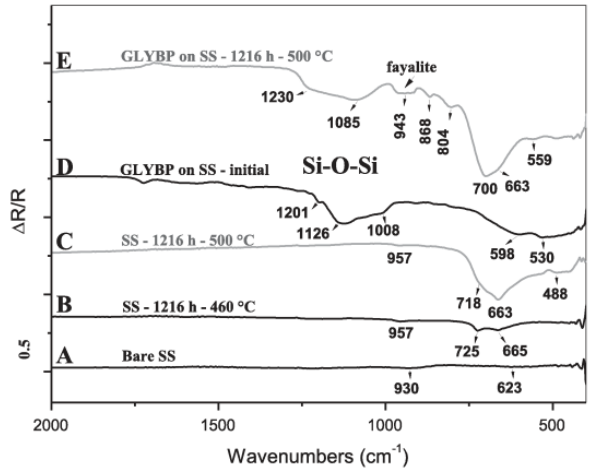


Fig. 23. NGIA IR spectra of SS substrates exposed to thermal loadings at 460 and 500 °C for various times: bare stainless steel (A), exposed to 460 °C (B) and 500 °C (C) for 1216 h and initial GLYBP coating on stainless steel (D) and after 1216 h at 500 °C (E).

(LO: 665–635, 522, and 495 cm^{-1}), α-Cr_2O_3 (LO: 765–715, 610, and 410 cm^{-1}), Fe_2O_4 (TO: 690–685, 550–525, and 395–380 cm^{-1}), NiO (LO: 620–580 cm^{-1}) and $NiCr_2O_4$ (LO: 700–690 cm^{-1}). At higher temperatures (650 and 850 °C [87]), $FeO \cdot Cr_2O_3$ spinels form (665, 710 shoulder band); the content of Fe and Cr influences the frequencies of the Fe–O and Cr–O LO modes; spinels rich in iron shift the LO mode to lower frequencies and chromium rich spinels to higher frequencies.

Examination of the LO spectra of SS AISI 316 substrate exposed to 460 °C for 1216 h (Fig. 23A and B) revealed the formation of the bands ~725 cm^{-1} belonging to Cr_2O_3 and at 665 cm^{-1} attributed to α-Fe_2O_3. The corresponding oxide phases formed already after ~100 h but the intensity of the vibrational bands did not change significantly, even after 1216 h. It seems that the growth of Cr_2O_3 at 460 °C was faster than that of Fe_2O_3, which was inferred from the gradual domination of the Cr–O band at 725 cm^{-1}.

During the first 400 h of heating at 500 °C, the spectra of the SS substrate showed similar LO bands as noted for the substrate heat treated at 460 °C (not shown here). But at longer exposures to 500 °C (Fig. 23C), the increase of the e_T values, as shown in Fig. 22, attributed to a massive enhancement of the band at 663 cm^{-1}, signaling the formation of Fe_2O_3, accompanied by a shoulder band at 718 cm^{-1}, which belonged to Cr_2O_3 [87] (Fig. 23C). Heat treatment of the HIPO coating at 500 °C showed the same LO bands (700 and 663 cm^{-1}) in the corresponding LO spectra (Fig. 23E), which meant that the coatings were permeable for air oxygen causing growth of the oxide layer of the SS beneath. The formation of some silicon-metal oxidation products, e.g. glassy fayalite (Fe_2SiO_4) showing absorption bands at 933 and 508 cm^{-1} [91], could not be excluded.

Formation of iron oxides on the heat treated HIPO coating deposited on the SS substrate was noted from the XPS profiles (Fig. 20), showing a high content of Fe, beyond the Fe recorded in the XPS profile analysis of the heat treated GLYBP coating deposited on Al substrate (Fig. 20A–C). The presence of Cr in the XPS spectra of the heat treated HIPO coating was not observed, due to the interference of other signals, even though they undoubtedly formed during the heat treatment, as inferred from the infrared spectra (Fig. 20C).

Prolonged exposure of the SS substrate and HIPO coating to 500 °C changed their texture and surface roughness, which increased for the SS substrate from 7 nm to 45 nm (Fig. 24A and B) and for the HIPO coating from 24 nm (Fig. 4C) to 98 nm (Fig. 24C).

To conclude, the HIPO coating did not protect the SS substrate against oxidation at 500 °C; however, the stability of the a_s values was quite remarkable (~1.5% drop). It seems that the oxidation of metallic substrates (Mo, Cr, Inconel, etc.) used for the TSSS paint coatings and metallic particles in cermets represents a serious problem for high temperatures (> 500 °C) solar thermal systems [92]. We plan to test other types of metal substrates (Mo, Inconel) as an alternative for SS AISI 316 reflecting mirrors for TSSS paint coatings.

6. Conclusions

One of the main reasons for this study was to show that it is possible with the aid of wet deposition techniques to make a solar coating with solar absorptance above 0.90 and thermal emittance from 0.75 to 0.12, which is an essentially greater spectral selectivity than that of selective coatings [13] made by Alanod company using a coil-coating procedure, the selectivity of which is 0.90–0.92 and e_T from 0.20 to 0. 22. In this study, therefore, instead of polysiloxane binder (commercial silicon resin) we used a GLY/PEO binder that has a nanocomposite composition and the structure of an organic–inorganic hybrid material. Trisilanol POSS dispersant (5–7%) was found to be crucial for obtaining homogeneous black spinel pigment dispersion,

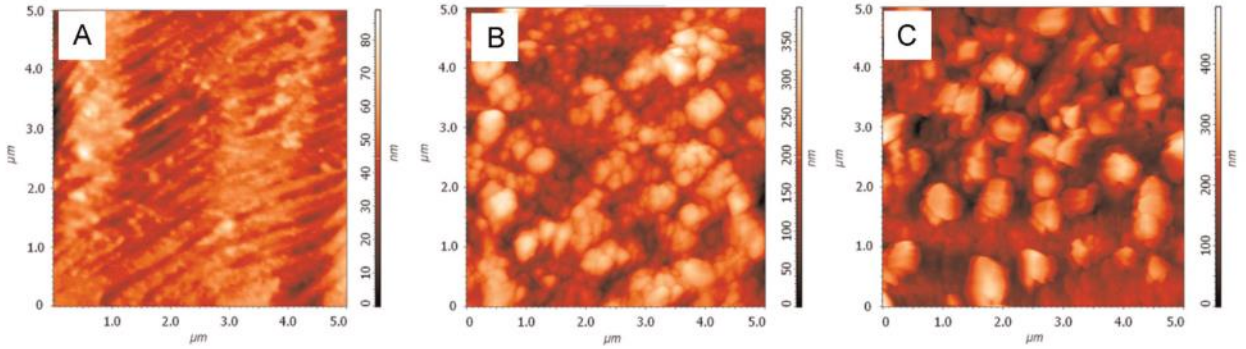


Fig. 24. AFM images of SS substrates: (A) untreated, (B) heat treated for 1216 h at 500 °C and (C) HIPO coating exposed to 500 °C for 1216 h.

small pigment particle size (~100 to 120 nm) and compatibility with GLY binder. The corresponding pigment dispersion was successfully deposited on coil-coating line on 800 m of aluminium coil with thickness ~700 to 800 m and good spectral selectivity (a_s=0.905 and e_T=0.12) and homogeneity.

The main accent of this study was to make by heat treatment High Power (HIPO) coating where the as-prepared coil absorber coating served as starting material. Namely, GLY precursor, otherwise popular for the production of organic–inorganic hybrids for the preparation of hard coatings, is not the most suitable for solar absorbers, since its thermal durability is limited to temperatures below 150–160 °C, because of the presence of the temperature labile PEO chains, which are an integral part of the hybrid. In view of this, we directed this research into seeking conditions that enabled exploitation of the temperature instability of the GLY/PEO sol–gel nanocomposite, expecting that its structure could change into being predominantly inorganic by the removal of the organic groups, under relatively mild conditions and fairly fast. For determining the conditions (time of curing and temperature) at which removal of the organic parts of the hybrid occurs, we used the advanced isoconversion kinetics approach [64]. Through recognition of the activation energy, this method enables prediction of the structural changes that take place with thermal treatment of a material, at arbitrary temperatures, and how much time is needed to achieve these changes. We thus exposed the coil-absorber coating for several days to three test temperatures (230, 250 and 270 °C), long enough for the thermal emittance of the coil-absorber coating to change to the desired (low) value (e_T=0.075). From the measured isothermal changes of the e_T values the activation energy was determined enabling the calculation of conditions, i.e., temperature and time of exposure of the coating that lead to the HIPO coating.

Using infrared spectroscopy, we showed that the lowering of thermal emittance at high temperatures can be ascribed to the formation of a predominantly inorganic (silica) skeleton and the decomposition of organic groups in the hybrid. The isoconversion kinetics method, as a universal method, is also suitable for the study of the long-term stability of solar absorbers (IEA Task 19), which we are currently working on for the study of the stability and lifespan of vacuum coatings within the framework of a NECSO project (Grant Agreement no. 310344, NECSO).

We established also the durability of the HIPO coatings from the temporal changes of thermal emittance of the HIPO coating on SS substrate (AISI 316) exposed to temperatures of 460–500 °C for 1216 h. The results of measurements of thermal emittance confirmed that the HIPO coating is stable up to 460 °C, while at 500 °C, the thermal emittance of the HIPO coating starts to rise after 400 h but does not rise by more than 5–7% even after 1216 h. We studied the rise of thermal emittance in more detail with the aid of NGIA RA spectra and found that the rise in thermal emittance can be ascribed to oxidation of the AISI 316 substrate. With HIPO coatings that were exposed to a temperature of 500 °C, oxidation led predominantly to the formation of Fe-oxide and not Cr-oxide, which, to a prevailing but lesser extent, is created on AISI 316 at 460 °C. After 1216 h at 500 °C, a sintering of particles occurs, their spontaneous growth and agglomeration, which is finally also seen from the measured AFM recordings. However, all the collected data lead to the conclusion that the HIPO coating on Al substrate is also stable for the temperature region up to 400 °C and, when the HIPO coating is deposited on AISI 316 substrate, it is durable at least to 460 °C for 1216 h.

The results thus showed that, in terms of their temperature resistance, HIPO coatings can compete with coatings recently made by sol–gel processes, whereby the spinel pigment was made in situ by thermal treatment of suitable inorganic precursors with the addition of silanes [22,23,28]. In addition to the HIPO coating, on both Al and AISI 316 substrates, having high solar adsorption and low thermal emittance 0.075 (on Al), its essential advantage is that it is made as a single layer coating. This enables pigment dispersions, the deposition of which leads to coarse coatings (RMS ~98 nm) that have inherently low reflection for solar radiation and thus solar adsorption of 0.92, while solar adsorption with coatings made from crystalline spinel [22] is at least 6–8% less because of reflection losses.

Finally, it should be mentioned that the essential component of the GLYBP coil absorber coating and HIPO coatings is a trisilanol POSS, which has been used as a dispersant for spinel pigment. Its advantage has been shown to be that it ensures the proper balance of the interaction between the surface of the milled spinel particles, the solution and the sol–gel binding. The effect of this is a thin optical coating with haze not higher than a few%, deposited from diluted solutions. This property is of crucial importance for the production of TSSS paint coatings, since it ensures balancing the thickness of the coatings for the purpose of obtained the lowest possible thermal emittance. The intensively milled pigment particles in synergy with a stable dispersion, also ensures high covering efficiency of the base and thus high solar absorption. With drying, the deposited layer of pigment dispersion collapses into a dense coating consisting of the core shell pigment particles that homogeneously cover the substrate.

The use of POSS dispersants with various functionalities, which we have established to act as superdispersants [61] in combination with black pigment, certainly opens further possibilities for the preparation of TSSS coatings, since the POSS molecules also function at high temperatures as a sol–gel silica network formers and thus enable the production of a TSSS coating for high temperature solar absorbers.

Acknowledgment

This work has received funding from the Slovenian Research Agency (Program P1-0030) and the European Community's Seventh Framework Program (Grant Agreement no. 310344, NECSO). Authors are thanks to Prof. Dr. Vojmir Francetič for the application of an advanced isoconversion method. Thanks to Dr. Ivan Jerman for help in production of coil absorber coating.

References

[1] O.P. Agnihotri, B.K. Gupta, Solar Selective Surfaces, Wiley, New York, 1981.
[2] S.W. Moore, Solar-absorber selective paint research, Sol. Energy Mater. 12 (1985) 435–447.
[3] H.Y.B. Mar, R.E. Peterson, P.B. Zimmer, Low-cost coatings for flat-plate solar collectors, Thin Solid Films 39 (1976) 95–103.
[4] B. Orel, Z.C. Orel, I. Radoczy, Thickness sensitive spectrally selective (TSSS) paint for solar collectors-optical-properties, surface characterization and application properties, Sol. Energy Mater. 18 (1988) 97–107.
[5] R.C. Agarwal, P.K.C. Pillai, Chemically sprayed PbS coatings for photothermal solar-energy conversion, Appl. Energy 11 (1982) 61–68.
[6] H. Tabor, Selective radiation, in: Proceedings of the Transactions of the Conference on the Use of Solar Energy, Bulletin of the Research Council of Israel, Israel, 1956, pp. 119–128.
[7] T.H. Zvi, Receiver for Solar Energy Collectors, 1959.
[8] C.G. Granqvist, Materials Science for Solar Energy Conversion Systems, 1st ed., Pergamon Press, Oxford, England, New York, 1991.
[9] C.G. Granqvist, J.C. Cutler, Materials for Solar Energy, Encyclopedia of Energy, Elsevier, New York, 2004.
[10] F. Cao, K. McEnaney, G. Chen, Z. Ren, A review of cermet-based spectrally selective solar absorbers, Energy Environ. Sci. 7 (2014) 1615–1627.
[11] C.E. Kennedy, Review of Mid- to High-Temperature Solar Selective Absorber Materialsm, NREL/TP-520-31267, 2002.
[12] N. Selvakumar, H.C. Barshilia, Review of physical vapor deposited (PVD) spectrally selective coatings for mid- and high-temperature solar thermal applications, Sol. Energy Mater. Sol. Cells 98 (2012) 1–23.
[13] M. Kozelj, B. Orel, M. Steinbuecher, I. Jerman, M. Vodlan, Aminosilane Modified Pigments for Spectrally Selective Coatings, Method for Preparation and Their Use in Coatings, EP2261288 A1, 2010.
[14] K.H. Hass, Crosslinked heteropolysiloxanes as inorganic–organic polymers: precursors, synthesis, properties and application, in: H.S. Nalwa (Ed.), Handbook of Organic–Inorganic Hybrid Materials and Nanocomposites, American Scientific Publishers, Stevenson Ranch, CA, 2003, pp. 207–230.
[15] G. Schottner, J. Kron, A. Deichmann, Industrial application of hybrid sol–gel coatings for the decoration of crystal glassware, J. Sol–Gel Sci. Technol. 13 (1998) 183–187.
[16] G. Schottner, Hybrid sol-gel derived polymers: applications of multifunctional materials, Chem. Mater. 13 (2001) 3422–3435.
[17] S. Hofacker, M. Mechtel, M. Mager, H. Kraus, Sol–gel: a new tool for coatings chemistry, Prog. Org. Coat. 45 (2002) 159–164.
[18] A. Morales, Protection Coatings Produced by Sol–Gel on Silver Reflectors, EP 0818561 A1, 1998.
[19] M.E. Rincón, J.D. Molina, M. Sánchez, C. Arancibia, E. García, Optical characterization of tandem absorber/reflector systems based on titanium oxide–carbon coatings, Sol. Energy Mater. Sol. Cells 91 (2007) 1421–1425.
[20] A. Morales, J.I. Ajona, Durability, performance and scalability of sol–gel front surface mirrors and selective absorbers, J. Phys. IV 9 (1999) 513–518.
[21] E. Barrera-Calva, J. Mendez-Vivar, M. Ortega-Lopez, L. Huerta-Arcos, J. Morales-Corona, R. Olayo-Gonzalez, Silica-copper oxide composite thin films as solar selective coatings prepared by dipping sol gel, Res. Lett. Mater. Sci. 2008 (2008) 190920(1)–190920(5).
[22] L. Kaluža, B. Orel, G. Dražič, M. Kohl, Sol–gel derived $CuCoMnO_x$ spinel coatings for solar absorbers: structural and optical properties, Sol. Energy Mater. Sol. Cells 70 (2001) 187–201.
[23] J. Vince, A. Šurca Vuk, U.O. Krašovec, B. Orel, M. Köhl, M. Heck, Solar absorber coatings based on $CoCuMnO_x$ spinels prepared via the sol–gel process: structural and optical properties, Sol. Energy Mater. Sol. Cells 79 (2003) 313–330.
[24] T. Bostrom, G. Westin, E. Wackelgard, Optimization of a solution-chemically derived solar absorbing spectrally selective surface, Sol. Energy Mater. Sol. Cells 91 (2007) 38–43.
[25] R. Bayon, G. San Vicente, A. Morales, Durability tests and up-scaling of selective absorbers based on copper-manganese oxide deposited by dip-coating, Sol. Energy Mater. Sol. Cells 94 (2010) 998–1004.
[26] R. Bayon, G. San Vicente, C. Maffiotte, A. Morales, Preparation of selective absorbers based on CuMn spinels by dip-coating method, Renew. Energy 33 (2008) 348–353.
[27] R. Bayon, G.S. Vicente, C. Maffiotte, A. Morales, Characterization of copper-manganese-oxide thin films deposited by dip-coating, Sol. Energy Mater. Sol. Cells 92 (2008) 1211–1216.
[28] M. Joly, Y. Antonetti, M. Python, M. Gonzalez, T. Gascou, J.L. Scartezzini, A. Schuler, Novel black selective coating for tubular solar absorbers based on a sol–gel method, Sol. Energy 94 (2013) 233–239.
[29] T. Bostrom, E. Wackelgard, G. Westin, Solution-chemical derived nickel–alumina coatings for thermal solar absorbers, Sol. Energy 74 (2003) 497–503.
[30] Z.X. Li, J.X. Zhao, L.H. Ren, Aqueous solution-chemical derived $Ni–Al_2O_3$ solar selective absorbing coatings, Sol. Energy Mater. Sol. Cells 105 (2012) 90–95.
[31] C. Sanchez, F. Ribot, Design of hybrid organic–inorganic materials synthesized via sol–gel chemistry, New J. Chem. 18 (1994) 1007–1047.
[32] U. Schubert, N. Husing, A. Lorenz, Hybrid inorganic–organic materials by sol–gel processing of organofunctional metal alkoxides, Chem. Mater. 7 (1995) 2010–2027.
[33] P. Judeinstein, C. Sanchez, Hybrid organic–inorganic materials: a land of multidisciplinarity, J. Mater. Chem. 6 (1996) 511–525.
[34] V. Posset, K. Rose, Innovative Hybrid Coatings for Facades, Organosilicon Chemistry V, Wiley-VCH Verlag GmbH, Weinheim, Germany (2008) 645–649.
[35] K. Rose, U. Posset, K.-H. Haas, M. Koehl, Farbe Lack 108 (2002) 29.
[36] B. Japelj, A. Šurca Vuk, B. Orel, L. Slemenik Perše, I. Jerman, J. Kovač, Preparation of a TiMEMO nanocomposite by the sol–gel method and its application in coloured thickness insensitive spectrally selective (TISS) coatings, Sol. Energy Mater. Sol. Cells 92 (2008) 1149–1161.
[37] R. Kasemann, H. Schmidt, Coatings for mechanical and chemical protection based on organic–inorganic sol–gel nanocomposites, New J. Chem. 18 (1994) 1117–1123.
[38] J. Kron, G. Schottner, K.J. Deichmann, Colouration of crystal glass through the application of decorative, coloured coatings based on organic-inorganic hybrid materials, in: Proceedings of the Fundamentals of Glass Science and Technology 3rd Conference, German Society of Glass Technology, Frankfurt am Main, 1995, pp. 378–385.
[39] J. Kron, S. Amberg-Schwab, G. Schottner, Functional coatings on glass using ORMOCER-systems, J. Sol–Gel Sci. Technol. 2 (1994) 189–192.
[40] G. Schottner, S. Hofacker, J. Sandrock, Organic dye-doped hybrid sol–gel coatings and pigments-synthesis, structural elucidation and application, in: Materials Research Society Simposia Proceedings, Materials Research Society, 1998, pp. 251–256.
[41] M. Popall, J. Kappel, M. Pilz, J. Schulz, G. Feyder, A new inorganic–organic polymer for the passivation of thin film capacitors, J. Sol–Gel Sci. Technol. 2 (1994) 157–160.
[42] Y. Sorek, M. Zevin, R. Reisfeld, T. Hurvits, S. Ruschin, Zirconia and zirconia-ORMOSIL planar waveguides prepared at room temperature, Chem. Mater. 9 (1997) 670–676.
[43] I. Jerman, A. Surca Vuk, M. Kozelj, F. Svegl, B. Orel, Influence of amino functionalised POSS additive on the corrosion properties of (3-glycidoxypropyl) trimethoxysilane coatings on AA 2024 alloy, Prog. Org. Coat. 72 (2011) 334–342.
[44] I. Jerman, M. Kozelj, B. Orel, The effect of polyhedral oligomeric silsesquioxane dispersant and low surface energy additives on spectrally selective paint coatings with self-cleaning properties, Sol. Energy Mater. Sol. Cells 94 (2010) 232–245.
[45] I. Jerman, M. Mihelcic, D. Verhovsek, J. Kovac, B. Orel, Polyhedral oligomeric silsesquioxane trisilanols as pigment surface modifiers for fluoropolymer based thickness sensitive spectrally selective (TSSS) paint coatings, Sol. Energy Mater. Sol. Cells 95 (2011) 423–431.
[46] P. Innocenzi, G. Brusatin, F. Babonneau, Competitive polymerization between organic and inorganic networks in hybrid materials, Chem. Mater. 12 (2000) 3726–3732.
[47] D. Hoebbel, M. Nacken, H. Schmidt, The effect of nanoscaled metal oxide sols on the structure and properties of glycidoxypropyltrimethoxysilane derived sols and gels, J. Sol–Gel Sci. Technol. 19 (2000) 305–309.
[48] G. Philipp, H. Schmidt, The reactivity of TiO_2 and ZrO_2 in organically modified silicates, J. Non-Cryst. Solids 82 (1986) 31–36.
[49] S. Craig, G.L. Harding, Effect of argon pressure on the optical properties of sputtered solar selective surfaces, Appl. Opt. 22 (1983) 583–586.
[50] D.A. Loy, K. Tahimian, Hybrid Materials, Chapter 3: Building Hybrid Organic–Inorganic Materials Using Silsesquioxanes, in: H.S. Nalwa (Ed.), Handbook of organic–inorganic hybrid materials and nanocomposites, vol. 1, American Scientific Publishers, Stevenson Ranch, CA, 2003, pp. 125–163.
[51] P.G. Harrison, Silicate cages: precursors to new materials, J. Organomet. Chem. 542 (1997) 141–183.
[52] M. Kozelj, B. Orel, Synthesis of polyhedral phenylsilsesquioxanes with KF as the source of the fluoride ion, Dalton Trans. (2008) 5072–5075.
[53] M. Kozelj, B. Orel, N-heterocyclic carbenes-catalysts for the preparation of polyhedral silsesquioxanes, Dalton Trans. 42 (2013) 9432–9436.
[54] I. Jerman, B. Orel, A. Surca Vuk, M. Kozelj, J. Kovac, A structural and corrosion study of triethoxysilyl and perfluorooctyl functionalized polyhedral silsesquioxane nanocomposite films on AA 2024 alloy, Thin Solid Films 518 (2010) 2710–2721.
[55] I. Jerman, A. Surca Vuk, M. Kozelj, B. Orel, J. Kovac, A structural and corrosion study of triethoxysilyl functionalized POSS coatings on AA 2024 alloy, Langmuir 24 (2008) 5029–5037.
[56] M. Colovic, I. Jerman, M. Gaberscek, B. Orel, POSS based ionic liquid as an electrolyte for hybrid electrochromic devices, Sol. Energy Mater. Sol. Cells 95 (2011) 3472–3481.
[57] S. Kraus-Ophir, I. Jerman, B. Orel, D. Mandler, Symmetrical thiol functionalized polyhedral oligomeric silsesquioxanes as building blocks for LB films, Soft Matter 7 (2011) 8862–8869.

[58] E. Stathatos, V. Jovanovski, B. Orel, I. Jerman, P. Lianos, Dye-sensitized solar cells made by using a polysilsesquioxane polymeric ionic fluid as redox electrolyte, J. Phys. Chem. C 111 (2007) 6528–6532.
[59] I. Jerman, B. Tomšič, B. Simončič, B. Orel, Tailoring of cotton fabrics surface properties by silsesquioxane molecules, in: Proceedings of the 41st International Symposium on Novelties in Textiles and 5th International Symposium on Novelties in Graphics and 45th International Congress IFKT, Ljubljana: Faculty of Natural Sciences and Engineering, Department of Textiles, 27–29 May 2010, Ljubljana, Slovenia, 2010, pp. 96–103.
[60] I. Jerman, M. Mihelčič, M. Koželj, B. Orel, Sol–Gel Based Spectrally Selective Solar Absorber Coatings and the Process for Producing Said Coatings, WO 2013/158049, 2012.
[61] L. Slemenik Perše, M. Mihelčič, B. Orel, The influence of the PVC ratio of various dispersing agents on the rheological properties of specially selective paint coatings for solar thermal application, in: M. Sjödqvist (Ed.), Papers Presented at the Nordic Rheology Conference, Helsinki, Finland, June 8–10, 2011: General Papers and Papers From the Special Session on Polymer solution, Suspensions and Melts, vol. 19, Nordic Rheology Society, Brabrand, 2011, pp. 253–261, Annual Transactions, ISSN 1601-4057.
[62] S. Vyazovkin, A unified approach to kinetic processing of nonisothermal data, Int. J. Chem. Kinet. 28 (1996) 95–101.
[63] S. Vyazovkin, Evaluation of activation energy of thermally stimulated solid-state reactions under arbitrary variation of temperature, J. Comput. Chem. 18 (1997) 393–402.
[64] S. Vyazovkin, Advanced isoconversional method, J. Therm. Anal. 49 (1997) 1493–1499.
[65] S. Vyazovkin, Modification of the integral isoconversional method to account for variation in the activation energy, J. Comput. Chem. 22 (2001) 178–183.
[66] S. Vyazovkin, A.K. Burnham, J.M. Criado, L.A. Pérez-Maqueda, C. Popescu, N. Sbirrazzuoli, ICTAC kinetics committee recommendations for performing kinetic computations on thermal analysis data, Thermochim. Acta 520 (2011) 1–19.
[67] S. Vyazovkin, C.A. Wight, Model-free and model-fitting approaches to kinetic analysis of isothermal and nonisothermal data, Thermochim. Acta 340–341 (1999) 53–68.
[68] N. Etherden, T. Tesfamichael, G.A. Niklasson, E. Wäckelgård, A theoretical feasibility study of pigments for thickness-sensitive spectrally selective paints, J. Phys. D: Appl. Phys. 37 (2004) 1115.
[69] Z. Crnjak Orel, B. Orel, Thermal stability and cross-linking studies of diiso-cyanate cured solar absorptance low-emittance paint coatings prepared via coil-coating process, Sol. Energy Mater. Sol. Cells 36 (1995) 11–27.
[70] B. Orel, Z.C. Orel, A. Krainer, M.G. Hutchins, Ftir spectroscopic investigations and the thermal-stability of thickness sensitive spectrally selective (TSSS) paint coatings, Sol. Energy Mater. 22 (1991) 259–279.
[71] A. Jonsson, A. Roos, E.K. Jonson, The effect on transparency and light scattering of dip coated antireflection coatings on window glass and electrochromic foil, Sol. Energy Mater. Sol. Cells 94 (2010) 992–997.
[72] M. Mihelcic, I. Jerman, F. Svegl, A. Surca Vuk, L.S. Perse, J. Kovac, B. Orel, U. Posset, Electrochromic Ni1−xO pigment coatings and plastic film-based $Ni_{1-x}O/TiO_2$ device with transmissive light modulation, Sol. Energy Mater. Sol. Cells 107 (2012) 175–187.
[73] M. Mihelčič, V. Francetič, P. Pori, H. Gradišar, J. Kovač, B. Orel, Electrochromic coatings made of surface modified rutile and anatase pigments; influence of trisilanol POSS dispersant on electrochromic effect, Appl. Surf. Sci. 313 (2014) 484–497.
[74] R. Kunič, M. Koželj, B. Orel, A. Šurca Vuk, A. Vilčnik, L. Slemenik Perše, D. Merlini, S. Brunold, Adhesion and thermal stability of thickness insensitive spectrally selective (TISS) polyurethane-based paint coatings on copper substrates, Sol. Energy Mater. Sol. Cells 93 (2009) 630–640.
[75] R. Kunič, M. Mihelčič, B. Orel, L. Slemenik Perše, B. Bizjak, J. Kovač, S. Brunold, Life expectancy prediction and application properties of novel polyurethane based thickness sensitive and thickness insensitive spectrally selective paint coatings for solar absorbers, Sol. Energy Mater. Sol. Cells 95 (2011) 2965–2975.
[76] M. Köhl, M. Heck, S. Brunold, U. Frei, B. Carlsson, K. Möller, Advanced procedure for the assessment of the lifetime of solar absorber coatings, Sol. Energy Mater. Sol. Cells 84 (2004) 275–289.
[77] N. Sbirrazzuoli, L. Vincent, A. Mija, N. Guigo, Integral, differential and advanced isoconversional methods: complex mechanisms and isothermal predicted conversion–time curves, Chemom. Intell. Lab. Syst. 96 (2009) 219–226.
[78] H.S. Nalwa, Handbook of Organic–Inorganic Hybrid Materials and Nano-composites, American Scientific Publishers, Stevenson Ranch, CA, 2003.
[79] T. Grzybek, H. Papp, M. Baerns, Fe/Mn oxide catalysts for fischer-tropsch synthesis: Part 5 Xps surface characterization of calcined and reduced samples, Appl. Catal. 29 (1987) 335–350.
[80] C.D. Wagner, M.G. E., Handbook of X-ray Photoelectron Spectroscopy: A Reference Book of Standard Data for Use in X-ray Photoelectron Spectroscopy, Physical Electronics Division, Perkin-Elmer Corp., Eden Prairie, MN, 1979.
[81] A.P. Grosvenor, B.A. Kobe, M.C. Biesinger, N.S. McIntyre, Investigation of multiplet splitting of Fe 2p XPS spectra and bonding in iron compounds, Surf. Interface Anal. 36 (2004) 1564–1574.
[82] R. Navamathavan, C.Y. Kim, A.S. Jung, C.K. Choi, H.J. Lee, Deposition and characterization of porous low-dielectric-constant SiOC(-H) thin films deposited from TES/O-2 precursors by using plasma-enhanced chemical vapor deposition, J. Korean Phys. Soc. 53 (2008) 351–356.
[83] A. Vilčnik, I. Jerman, A. Šurca Vuk, M. Koželj, B. Orel, B. Tomšič, B. Simončič, J. Kovač, Structural properties and antibacterial effects of hydrophobic and oleophobic sol–gel coatings for cotton fabrics, Langmuir 25 (2009) 5869–5880.
[84] D.W. Berreman, Infrared absorption at longitudinal optic frequency in cubic crystal films, Phys. Rev. 130 (1963) 2193–2198.
[85] E. Wäckelgård, A comparative study of the optical properties of nickel pigmented alumina films of different thicknesses exposed to elevated temperature and humidity, Sol. Energy Mater. Sol. Cells 54 (1998) 171–179.
[86] T. Tesfamichael, S.K. Andersson, T. Chibuye, E. Wackelgard, Oxidation kinetics for metal-dielectric films using IR optical measurements, in: Proceedings of the SPIE 3138, Optical Materials Technology for Energy Efficiency and Solar Energy Conversion XV, 1997, pp. 146–153.
[87] F.P. Mertens, Reflectance infrared study of the oxidation of stainless steels and component metals, Corrosion 34 (1978) 359–364.
[88] R. Guillamet, J. Lopitaux, B. Hannoyer, M. Lenglet, Oxidation of stainless steels (AISI 304 and 316) at high temperature. Influence on the metallic substratum, J. Phys. IV 03 (1993) 349–356.
[89] V.A. Kotenev, N.P. Sokolova, A.M. Gorbunov, Fourier-transform diffuse reflection IR-spectroscopy in studies of thermal oxidation of X18H10T steel, Prot. Met. 40 (2004) 587–590.
[90] T. Scherübl, L.K. Thomas, Investigation of high-temperature-oxidation of metals by infrared-reflection-absorption spectroscopy (IRAS), Fresenius J. Anal. Chem. 353 (1995) 589–593.
[91] K. Kusabiraki, Y. Shiraishi, The infrared spectrum of vitreous fayalite, J. Non-Cryst. Solids 44 (1981) 365–368.
[92] M. Kotilainen, K. Mizohata, M. Honkanen, P. Vuoristo, Influence of microstructure on temperature-induced ageing mechanisms of different solar absorber coatings, Sol. Energy Mater. Sol. Cells 120, Part B (2014) 462–472.

Chapter 5

Electrochromic Coatings Made of Surface Modified Rutile and Anatase Pigments: Influence of Trisilanol POSS Dispersant on the Electrochromic Effect

The idea of producing electrochromic coatings based on pigment particles seems to be trivial but many factors need to be considered during development in order to demonstrate the advantages of the production of pigment EC coatings for practical applications. Given the importance of isobutyl trisilanol POSS for practical preparation of spectrally selective coatings (Chapters II and III), further investigation of the interactions between the trisilanol POSS dispersant and the surface of the TiO_2 (anatase) pigment was demonstrated from TEM (Figure 5.1) and SEM and the effect of milling was obtained from DLS measurements.

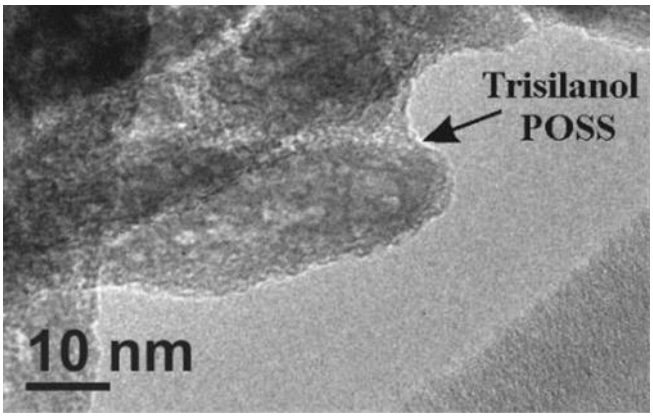


Figure 5.1: TEM micrograph of mTiA dispersion made with trisilanol POSS dispersant.

The attachment of isobutyl trisilanol POSS onto the surface of TiO_2 was studied with infrared spectroscopy and the results combined with TG measurements. In Figure 5.2, the adsorption of trisilanol POSS on accessible sites on the mTiA pigment surface is presented. We also showed that new vibrational bands belonging to trisilanol POSS were

observed in the IR spectra after thorough washing of surface modified TiO_2 pigment particles with THF.

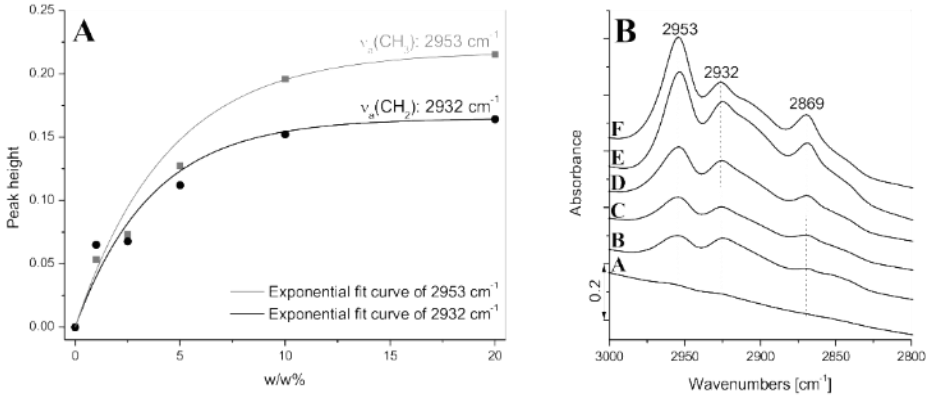


Figure 5.2: Adsorption (A) and infrared spectra (B) of washed mTiA/trisilanol POSS dispersions obtained from the intensity band variations of C-H stretching modes after equilibrating mTiA in hexane/trisilanol POSS solutions with concentrations (A) base line, (B) 0.01, (C) 0.025, (D) 0.05, (E) 0.1 and (F) 0.2 w/w%.

An additional aim was to demonstrate that merely by mechanical ball milling it was possible to make coatings that exhibited optical properties, similar to thin optical coatings prepared by the sol-gel process. They have low haze and high visible light throughput, whereby the scattering of the light passing the coating was minimal (Figure 5.3).



Figure 5.3: mTiA02 pigment coatings deposited on ITO PET foil (A) and FTO glass (B).

For the preparation of TiO_2 dispersions, similar procedures were used as for making dispersions based on black spinel pigments and used for the development of a spectrally selective coating. The effect of mechanical ball milling was demonstrated by varying the ball milling conditions, i.e., by using different sizes of zirconia beads (0.4, 0.2 and 0.1 mm) as grinding media. As expected, longer grinding times and smaller zirconia beads beneficially affected haze, being small for more thoroughly ground pigment particle dispersions. The as-prepared TiO_2 coatings were checked in terms of their EC properties, revealing that the EC effect ($\Delta T = T_{charged} - T_{discharged}$) was high (55.7% at λ=634 nm) and comparable to the EC effect and EC efficiency of TiO_2 coatings prepared from titania sol-gel precursors [89]. Two main benefits were established. First, the coatings could be prepared at low temperatures ($T < 150$ °C), since the post-heat-treatment, which is compulsory for titania coatings made via the sol-gel processing, can be omitted. Secondly,

the EC coatings could be applied on flexible plastic foils (i.e., ITO PET) which could lead to the production of flexible EC devices [32]. This aspect of EC device applications is frequently forgotten, since EC devices on glass substrates prevail on the market.

My contribution consisted of sample and dispersion preparation, most of the measurements and part of the writing.

Applied Surface Science 313 (2014) 484–497

Contents lists available at ScienceDirect

Applied Surface Science

journal homepage: www.elsevier.com/locate/apsusc

Electrochromic coatings made of surface modified rutile and anatase pigments: Influence of trisilanol POSS dispersant on electrochromic effect

Mohor Mihelčič[a], Vojmir Francetič[c], Pavli Pori[d], Helena Gradišar[a], Janez Kovač[e], Boris Orel[a,b,*]

[a] National Institute of Chemistry, Hajdrihova 19, 1000 Ljubljana, Slovenia
[b] CO-NOT, Hajdrihova 19, Ljubljana, Slovenia
[c] Faculty of Chemistry and Chemical Technology, University of Ljubljani, Aškerčeva cesta 5, 1000 Ljubljana, Slovenia
[d] Chemcolor Sevnica d.o.o., Dolenje Brezovo 35, 8290 Sevnica, Slovenia
[e] Jožef Stefan Institute., Jamova 39, SI-1000 Ljubljana, Slovenia

ARTICLE INFO

Article history:
Received 28 February 2014
Received in revised form 28 May 2014
Accepted 3 June 2014
Available online 10 June 2014

Keywords:
Trisilanol POSS
Dispersant/pigment interactions
Pigment dispersion
Vibrational spectra
Optical coatings
Electrochromism

ABSTRACT

Polyhedral oligomeric silsesqioxanes (POSS) compounds consisting of $[RSiO_{3/2}]_n$ groups organized in the form of various polyhedra (T_n, $n = 3, 6, 8, 10, 12, \ldots$) have not often been used as pigment surface modifiers. Their interactions with pigments are not known in detail and coatings deposited from pigments modified by POSS dispersants are rare. Identification of interactions between a dispersant and the surface of pigments is important from the point of view of obtaining stable pigment dispersions enabling the deposition of optical coatings with high pigment loading, low haze and mechanical integrity.

Thin TiO_2 (anatase) pigment coatings (70–260 nm) were deposited from pigment dispersions prepared by milling metatitanic acid (mTiA) powder agglomerates with trisilanol heptaisobutyl silsesquioxane dispersant (trisilanol POSS) in butanol and hexane. The results of TEM, EDAX and TG measurements confirmed the influence of trisilanol POSS dispersant on the formation of a dispersion with a uniform distribution of mTiA and rutile (mTiR) nanoparticles with a size of about 30 ± 5.0 nm and 90 ± 5.0 nm, respectively, as determined from dynamic light scattering (DLS) measurements. The mTiA/trisilanol POSS dispersions with added titanium tetraisopropoxide were deposited on fluorine-doped tin oxide (FTO) coated glass (spin-coating) and indium tin oxide coated polymeric substrate (ITO PET) (coil-coating) and thermally treated at 150 °C. UV–vis spectra, AFM and SEM results showed that the pigment coatings exhibited low haze (up to 6%), low surface roughness (up to 20 nm) and uniform morphology.

mTiA/trisilanol POSS interactions were assessed from the frequency shifts of the Si—O—Si stretching modes of trisilanol POSS, while the adsorption of the dispersant was followed from the intensity changes of the corresponding $-CH_3$ and $-CH_2$ stretching modes, confirming the gradual occupation of the mTiA crystalline sites by trisilanol POSS dispersant. Examination of IR vibrational spectra showed that trisilanol POSS interacted with the mTiA surface by establishing hydrogen bonding. The advantage of using trisilanol POSS dispersant was demonstrated by the enhanced electrochromic effect of the mTiA pigment coatings.

© 2014 Elsevier B.V. All rights reserved.

1. Introduction

Polyhedral oligomeric silsesquioxanes (POSS) [1] are an interesting class of compounds, attracting attention as precursors for the preparation of various materials [2,3] with multifunctional properties. Several excellent reviews on the synthesis, properties and application of a variety of POSS compounds have been published over the years [4,5]. POSS compounds consist of $[RSiO_{3/2}]_n$ groups organized in the form of various polyhedra (T_n, $n = 3, 6, 8, 10, 12, \ldots$), octahedral ($T_8$) POSS being the most frequently used. Various organic pendant groups (R) are attached on the corners of the $(RSiO_{3/2})_8$ cubes, providing flexibility in their structure and composition and imparting them multifunctionality. POSS are attracting greatest interest as nanocomposite structure modifiers for polymers [6,7], improving their mechanical properties, flame retardancy, reactivity and functionality, opening

* Corresponding author. Tel.: +386 0 1 4760 276; fax: +386 0 1 4760 300.
E-mail address: boris.orel@ki.si (B. Orel).

http://dx.doi.org/10.1016/j.apsusc.2014.06.010
0169-4332/© 2014 Elsevier B.V. All rights reserved.

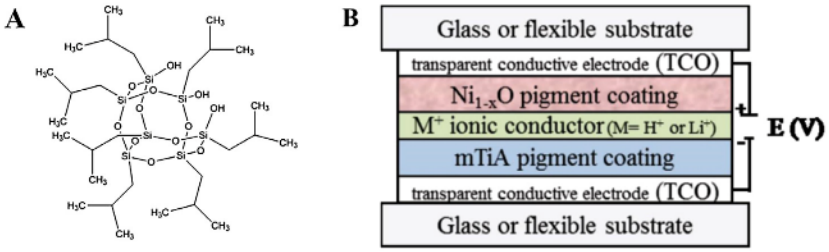


Fig. 1. Schematic representation of the dispersant trisilanol heptaisobutyl silsesquioxane (T_8 $1B_7$ $(OH)_3$ POSS) (A) and cross section of electrochromic device (B).

the possibility of the construction of various organic/inorganic nanocomposite materials. In our laboratory, we have worked on improvements in their synthesis by using different catalysts [8,9] and have used synthesized POSS for making corrosion protective coatings for aluminium (AA 2024) [10–12], for the deposition of Langmuir–Blodgett films with selective ionic conductivity [13], as structural modifiers for ionic liquids in order to make them semi-solid lithium conducting electrolytes [14,15], hydrophobic and oleophobic surface finishes for textile fabrics [16] and as pigment surface modifiers for spectrally selective coatings [17,18].

Studies of dispersant/pigment interactions are part of our long-term development of solar absorber coatings for thermal collectors, in which spectrally selective coatings [19–21] have been made from paints. Solar absorbing black manganese pigments [22,23] have been treated with alkyltrialkoxysilanes [24] in the appropriate paints and incorporated in various types of resin binders (polysiloxanes, perfluoropolymers [17,18,21,22] and polyurethanes [25]). Recently, spectrally selective coatings with high solar absorptance and low thermal emittance have been prepared [26], in which, as in [17,18], black spinel pigment was dispersed with the help of an open-corner heptaisobutyl POSS-triol (T_8 $1B_7$ $(OH)_3$ POSS, trisilanol POSS, for short) (Fig. 1A), while a sol–gel precursor, i.e., glycidoxypropyltriethoxy silane (GLYMO), served as binder. It has been noted that on glass, FTO glass and ITO PET foils, transparent coatings with low haze (a few %) can be deposited, which we attribute to the presence of small and well dispersed pigment particles, which form due to the efficacy of milling the pigment with trisilanol POSS. This opened the possibility of depositing coatings from other pigments; mTiA pigment was selected because, in the form of thin films, it exhibits an electrochromic effect [27] (Fig. 1B).

Electrochromism has attracted interest for many decades, mainly for the fabrication of "smart" windows, preventing overheating and ensuring adequate light levels for the occupants [27] due to the possibility of modulating the intensity of light entering the buildings with a potential pulse. EC "smart" windows represent a multi-coating system, consisting of two coatings usually based on electrochromic transition metal oxides glued together with an electrolyte doped with lithium ions (Fig. 1B). After the application of the potential, electrons from the electrode and Li^+ ions from the electrolyte become inserted in cathodic material such as TiO_2 [28–30], leading to a change of the oxidation state of the Ti^{+4} ions, schematically shown below:

$$TiO_2(\text{transparent}) + xe^- + xLi^+ = Li_xTiO_2(\text{blue colouration}) \quad (1)$$

The insertion/extraction reactions are reversible and the transparent initial state of TiO_2 can be restored by the application of anodic potentials. By combining TiO_2 or some other cathodic electrochromics (WO_3 [31], Nb_2O_5 [32]) with another EC material like Co oxide [33] and Ni oxide [34], which colours at anodic potentials, an EC device is constructed that enables reversible modulation of transmitting light by switching potentials at both parts of the device. In order to demonstrate the quality of the EC properties of the mTiA coatings developed within the frame of this study, coatings consisting of mTiA pigment particles dispersed with trisilanol POSS were made by wet deposition of the corresponding pigment dispersions on FTO glass and ITO PET foils and used to construct the EC device with anodic NiO pigment coatings reported in [27,35–38].

For wet deposition of coatings [39], the pigment particle/solvent/binder interaction should be known in details in order to make coatings that could be competitive with vacuum based coatings. High transparency, low haze (no scattering) and high EC effect are necessary for the application of EC coatings made of pigment particles in EC devices. The advantages are obvious; coatings made of EC pigment particle dispersions could be deposited on flexible polymeric (ITO PET) foils by roll-to-roll (R2R) application techniques, providing much cheaper fabrication of EC windows than standard glass-based EC windows [40,41] (~50 $/m^2 for a whole EC stack [9]).

Pigment/dispersant interactions are fairly elusive to study but have already been established for various alkyltrialkoxysilanes as surface modifiers for nanocrystalline titania, demonstrating their grafting from the presence of the Si—O—(TiO_2) stretching mode observed at 910–930 cm^{-1} in the infrared spectra of surface modified TiO_2 [42,43]. Godnjavec et al. [42] reported the infrared spectra of rutile pigment, first functionalized with alumina to make TiO_2–Al_2O_3 pigment and then with trisilanol POSS in order to incorporate the TiO_2–Al_2O_3 in a water borne acrylic lacquer but the expected Si—O—(TiO_2) mode in the spectral region 900–930 cm^{-1} has not been reported.

Accordingly, in this work we re-examined [44,45] the infrared spectra of the trisilanol POSS alone in order to provide a suitable platform for establishing dispersant/pigment interactions. The effect of trisilanol POSS on the surface modification of mTiA and mTiR pigments was further supported by performing TEM, EDAX and TG measurements of surface modified and unmodified pigments and the pigment coating's properties, i.e., SEM, AFM and UV–vis spectra, were established. The results were conclusive, confirming that trisilanol POSS is an effective pigment surface modifier, proven by the deposition of highly transmissive mTiA pigment sol–gel based coatings, enabling high EC effect to be obtained and the construction of a flexible EC device consisting of mTiA (cathodic) and $Ni_{1-x}O$ (anodic) pigment coatings glued together with semi-solid lithium conducting polymeric electrolyte.

2. Experimental

2.1. Materials and preparation of coatings

2.1.1. Metatitanic acid powder (mTiA)

mTiA powder was prepared by the so-called "sulphate route" [46], which is currently used in the Cinkarna d.d. factory [47] for

its industrial manufacturing. In brief, white precipitate mTiA is obtained after dissolution of ilmenite in concentrated sulphuric acid (98%, Cinkarna Celje) hydrolysed in the presence of anatase seeds. The anatase seeds are prepared separately by hydrolysing a titanyl sulphate solution at 80 °C and are added to the dissolved ilmenite solution. By varying the concentration of this solution (from 0.1% to 1.8%), various mTiA types are easily produced, differing in the size of the anatase powder.

mTiA agglomerates (size up to a few μm) consist of aggregates, of a size from 30 to 50 nm [48,49]. The aggregates are formed of nanocrystallites (5–7 nm in size) strongly linked together via crystalline bridges. In order to obtain at least partially dispersed aggregates of mTiA powder, a small amount of barium chloride was added to the metatitanic acid agglomerates [46]. Since barium has a high affinity to sulphate ions, the added barium salt drew together the sulphate ions, which were removed from the metatitanic acid by centrifugation, freeing the agglomerates and forming separated aggregates. Before the as-prepared mTiA aggregates were used for making pigment dispersions, the mTiA pigment was thoroughly washed with distilled water and then dried at 100 °C. The as-prepared dry mTiA powder aggregates were used for preparation of pigment dispersions.

Raw rutile pigment (mTiR, for short), which was characterized by an unmodified surface free of any additional layer such as Al_2O_3 [42], was prepared from rutile acidic suspension (90 g/L). After the addition of NaOH (180 g/L in mass), a pH = 7 was reached, which led to the agglomeration of rutile particles. The agglomerate was washed with water until no white powder was observed in the precipitate, indicating the absence of sulphate ions. The washed white precipitate was then dried at 80 °C and used for the preparation of pigment dispersions.

2.1.2. Preparation of pigment dispersion

Ten wt% of as-prepared mTiA and mTiR powders were first dispersed in butanol and hexane (Sigma-Aldrich) in the presence of trisilanol POSS dispersant [1] (0.1 w/w% vs. powder). The synthesis of trisilanol POSS has been previously reported [17,18]. mTiA was milled in a Dyno-mill Research Laboratory agitator bead mill (WAB, Willy A. Bachofen AG Maschinenfabrik) for 1.5 h at 3600 rpm. Zirconia beads with dimensions of 0.4, 0.2 and 0.1 mm were used as grinding media, providing pigment dispersions mTiA04, mTiA02 and mTiA01, respectively. mTiR pigment was also milled; however the dimension of the zirconia beads was only 0.4 mm. The zirconia beads to modified titania powder ratio was 2:1 for all dispersions. In order to improve the adhesion of the coatings to the substrates, $Ti(iOPr)_4$ was added together with glacial acetic acid ($AcOH_{gl}$) at the end of the milling process, the latter enabling its hydrolysis and long-term stability [50].

2.1.3. Deposition of pigment coatings

Pigment coatings were deposited on FTO glass plates (Pilkington, 14 Ω/□), fused quartz plates and conductive polymeric substrate (Solaronix, ITO PET 175-60) by spin-coating techniques. By repeating the spinning deposition cycles (1 cycle: spinning frequency = 1500 rpm, time = 40 s), the thickness of the deposited mTiA coatings was varied from 100 nm (1× spinning) up to 400 nm (4× spinning). A dip-coating deposition technique was also used, giving reproducible results in terms of coating thickness, morphology and pigment particle distribution. Based on our experience with the deposition of $Ni_{1-x}O$ [36,51] WO_3 and copper manganese spinel sol–gel based pigment dispersions [26], the corresponding mTiA dispersions are also suitable for continuous deposition via the coil-coating technique.

2.2. Instrumental

IR spectra were taken on a Bruker IFS 66/S spectrophotometer with a resolution of 4 cm^{-1}. For IR transmission spectra, the titania powder was prepared as a KBr pellet and the trisilanol POSS was deposited on partly IR transmissive silicon wafers. Near-grazing incidence angle reflection absorption (NGIA RA) spectra were recorded using a Bruker IFS 66/S spectrophotometer at P type polarization, equipped with a nitrogen-cooled mercury cadmium telluride detector at a resolution of 4 cm^{-1}. Typically, 64 scans were collected vs. a reference, which was a bare FTO glass surface, pretreated with the different solvents.

UV–vis spectra of the pigment coatings on FTO glass and ITO PET foils were measured by a Perkin Elmer Lambda 900 UV–vis spectrometer equipped with an integrating sphere, giving spectral total reflectance ($R(\lambda)$), spectral total transmittance ($TT(\lambda)$) and spectral diffuse transmittance ($DT(\lambda)$) spectra. The optical quality of the coatings was estimated by determining transmission haze numbers (H in %), defined as the ratio of diffuse to total transmittance (DT/TT %) of coatings in the spectral range 380–780 nm following the American Society for Testing and Materials (ASTM) test method D1003 [52], as described previously [51].

SEM micrographs were obtained on a FE-SEM Supra 35 VP electron scanning microscope.

Transmission electron microscopy (TEM) micrographs were obtained on a JEOL JEM-2100 high resolution transmission electron microscope (HR-TEM) operating at 200 keV. Energy dispersive X-ray spectroscopy (EDAX) measurements were performed on a JEOL JED-2300T EDS system with high energy resolution and high sensitivity.

X-ray diffraction (XRD) analyses were done by means of a Siemens 5000D X-ray powder diffractometer equipped with graphite monochromatized Cu-Kα radiation (λ = 1.54178 Å). The scan speed was 10°/min, with a scan step of 0.02° of 2Θ.

Atomic force microscopy (AFM) was carried out on nanocrystalline mTiA coatings deposited on FTO glass using an AFM microscope Solver PRO produced by the NT-MDT company. Contact mode acquisition was used to acquire images over the range of 2 × 2 μm^2.

Coating thickness was determined by scratching the coating with a hard tip, in order to remove the coating from the FTO glass substrate, and the region was then used for Talystep measurements.

Dynamic light scattering (DLS) measurement was used for determination of the particle size distribution of the powders, using a Malvern Zetasizer Nano ZS laser particle size analyzer. The instrument was equipped with a He–Ne laser source (λ = 633 nm) at a scattering angle of 173°. The dispersion concentration was around 0.1 g/l. The suspension was prepared by dispersing the powder in butanol and treating for 2 min in an ultrasonic bath to obtain a well-dispersed suspension.

Thermogravimetric analysis (TGA) was performed on a Mettler Toledo TGA/SDTA 851^e instrument. TGA curves were measured from 30 °C to 600 °C in an air atmosphere, using a heating rate of 10 °C/min.

UV–vis spectroelectrochemical properties of the coatings were characterized *in situ* during chronocoulommetry (CC) measurements on an Autolab PGSTAT 302N potentiostat–galvanostat. The coatings were examined in a 1 M $LiClO_4$/propylene carbonate (PC) electrolyte in a standard three electrode configuration consisting of the nanocrystalline TiO_2 coating on FTO glass (working electrode), a modified Ag/AgCl reference electrode and a platinum rod (counter electrode). The home-made spectroelectrochemical cell was mounted in an HP 8453A diode array spectrophotometer and the optical modulation of the coatings in the spectral range of 300 to 1100 nm was recorded. CCs were used for coloration of coatings at −1.7 V (60 s) and bleaching at 0 V (60 s).

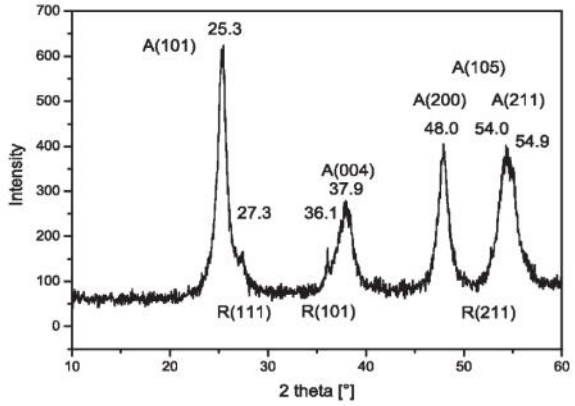


Fig. 2. XRD of as-prepared mTiA powder.

3. Results and Discussion

3.1. Characterization of mTiA powder

3.1.1. XRD analysis of mTiA

XRD analysis of the mTiA powder (Fig. 2) showed that it consisted predominantly of an anatase phase [46] with a small amount of rutile phase (estimated ~15%) and, in this regard, resembled other commercial titania powders, such as Inframat and P25 powders (not shown here). Based on a consideration of the normal peak distribution of polycrystalline anatase, the powder consisted of randomly oriented anatase nanoparticles. The crystallite size obtained from the Scherrer relation, which was estimated from the various (hkl) peaks (A(1 0 1), A(0 0 4), A(2 0 0) and A(1 0 5)), gave the nanocrystals a size of 5–7 nm, from which larger aggregates (up to 20–50 nm in size) were formed.

3.1.2. Characterization of mTiA (anatase) and mTiR (rutile) dispersions with TEM

TEM micrographs can provide the most direct evidence of the trisilanol POSS layer wrapping around the pigment particles. In order to demonstrate this, mTiA and mTiR pigments were first milled with 0.1 mm zirconia beads, without any trisilanol POSS and, in the next stage, the same procedure was applied for both the pigments milled in solutions containing 10% of trisilanol POSS. The structure of the mTiA pigment aggregates obtained from TEM measurements is shown in Fig. 3A.

As the TEM micrographs show, completely dispersed pigment aggregates were not obtained by milling either mTiA or mTiR powders with 0.1 mm zirconia beads (mTiA01, for short) without the added dispersant, but when the mTiA was milled with trisilanol POSS dispersant, separated aggregates formed, with an average size up to 50 ± 5.0 nm (Fig. 4Aand B), agreeing well with the particle size of 50 nm provided by DLS measurements (Fig. 4C). EDAX measurements clearly demonstrated the presence of trisilanol POSS, as shown on Fig. 4D.

TEM micrographs of mTiR pigment dispersions with pigment particle dimension ~100 nm (Fig. 3B), characterized by mTiR aggregates with an average size of ~250–300 nm, after milling with trisilanol POSS showed a diffuse layer of dispersant wrapping around the mTiR aggregates (Fig. 5A). Due to milling, the size of the aggregates decreased, reaching an average size of about 80 nm, as noted from the DLS results (Fig. 5B). The trisilanol POSS dispersant on the mTiR pigment surface confirmed from TEM micrographs (Fig. 5A), was also substantiated from the corresponding EDAX results (Fig. 5C) and further proved from the infrared spectra shown below.

3.2. Transmission IR spectra of surface modified pigment: pigment/dispersant interactions

3.2.1. Vibrational spectra of mTiA

Vibrational spectra of TiO_2 in various polycrystalline forms [53] are well documented and a number of vibrational spectra studies have been devoted to the surface modification of titania particles by various dispersants, including alkoxysilanes [54–61]. Infrared spectra studies have been less frequent than those on Raman spectra [53] because the infrared spectra of titania powders measured in transmission are complex, due to the presence of Froelich modes [62] stemming from the polarizability of the titania particles, depending on their size and shape. Vibrational bands in transmission spectra of titania powders are broad and extend between the longitudinal optical (LO) and transversal optical (TO) modes, appearing in the spectral region from ~850 cm^{-1} (LO) to as low as 400 cm^{-1} (TO), leaving a transmission window for vibrational bands in the spectral region above ~900 cm^{-1}, which allowed us to observe the skeletal (Si—O—Si) bands of trisilanol POSS dispersant in the corresponding transmission spectra (Fig. 6).

3.2.2. Vibrational bands of trisilanol POSS

Detailed assignment of vibrational modes of trisilanol POSS should be known in order to conceive the interactions between trisilanol POSS with mTiA surface from the vibrational band shifts and intensity changes. The assignment of the main asymmetric stretching ν_{as} Si—O—Si mode of the octahedral (T_8) silsesquioxane cage $(RSiO_{3/2})_8$, is not problematic, since it was expected to appear in the relatively narrow region from 1200 to 1000 cm^{-1} [4]. As expected, the octaisobutyl POSS (T_8 IB_8 POSS) (Fig. 6A) [45] showed a single band at 1113 cm^{-1} [17] but for the trisilanol POSS, a splitting of the corresponding mode was envisaged in view of

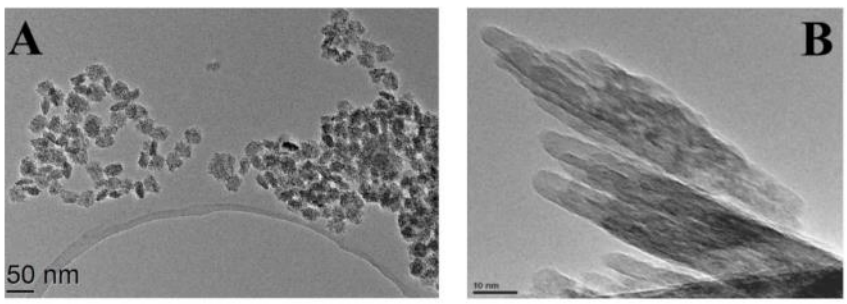


Fig. 3. TEM micrograph of starting material: (A) as-prepared mTiA (anatase) powder with aggregates forming larger agglomerates and (B) mTiR (rutile) aggregates consisting of needle-like particles.

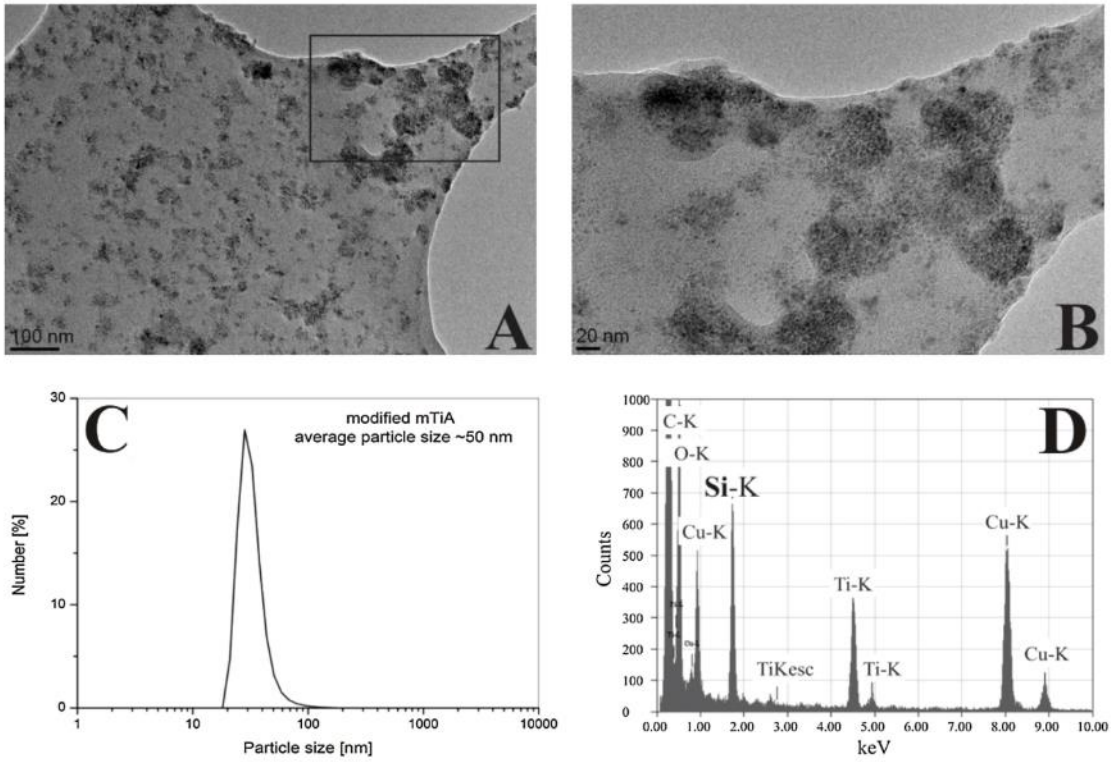


Fig. 4. TEM micrographs of mTiA01 dispersion, modified with trisilanol POSS, milled with 0.1 mm zirconia beads at two different magnifications (A, B), the corresponding DLS measurement (C) and EDAX spectrum (D).

its monoclinic structure and the formation of dimers in crystalline form [44]. In our previous study of trisilanol POSS/black spinel pigment interactions [17], the corresponding ν_{as} Si—O—Si mode at 1119 cm^{-1} was observed but the splitting of this band, stemming from the lower symmetry of the trisilanol POSS dimers, was not detected due to the modes of the alumina layer. Godnjavec et al. [42] reported two bands in the infrared spectra of trisilanol POSS/TiO_2–alumina pigment dispersed in KBr, at 1118 and 1130 cm^{-1}, but only the first was explicitly assigned to the ν_{as} Si—O—Si mode.

Examination of the infrared spectra of trisilanol POSS having an open-cage structure in a KBr pellet (Fig. 6B), revealed a ν_{as} Si—O—Si mode band at 1108 cm^{-1}, which was accompanied by two shoulder bands at 1126 cm^{-1} (strong) and 1096 cm^{-1} (weak). A thin film of trisilanol POSS (Fig. 6C) deposited on silicon wafer from hexane solution also exhibited three bands but at slightly different wavenumbers, i.e., 1122, 1102 and 1092 cm^{-1} (shoulder). More than just a single ν_{as} Si—O—Si band, which was observed in transmission spectra in Fig. 6B and C, suggested the decrease of molecular symmetry stemming from the POSS–POSS interactions in trisilanol POSS dimers [44]. An exact matching of frequencies of the corresponding bands in transmission spectra of thin film (TO modes) and KBr pellet was not expected, because the bands in the KBr matrix could be shifted due to optical effects (refractive index matching) and to the polarization effects of trisilanol POSS crystallites present in the KBr matrix (Froelich modes [48]).

In contrast, when trisilanol POSS was deposited on the FTO glass substrate, in the NGIA RA spectra measured in P-polarized light, a strong band was noted at 1143 cm^{-1}, assigned to the ν_{as} Si—O—Si LO counterpart mode [13,63,64] (Fig. 7A(a) and B(a)), agreeing with reflection–absorption spectra of other POSS molecules, which formed Langmuir–Blodgett monolayers on water [13,63]. The most persuasive proof of the orientation of trisilanol POSS on FTO glass surface being perpendicular to the substrate was inferred from the ν_{as} O—H band, which shifted from 3201 cm^{-1} (TO spectra) to 3258 cm^{-1} (Fig. 7A(c) and C(c)). In the NGIA RA spectra of thick multi-layered films (Fig. 7A(b) and C(b)), the corresponding OH stretching band was not observed but in the spectral region from 1200 to 800 cm^{-1}, in addition to the ν_{as} Si—O—Si LO mode at 1143 cm^{-1} (Fig. 7B(a)), additional bands at 1120, 1104 and 1087 cm^{-1} (Fig. 7B(c)) were noted. The presence of more than just a single ν_{as} Si—O—Si LO mode at 1143 cm^{-1} in the spectra of thick coatings (Fig. 7B(b)) indicated the presence of TO modes, stemming from the randomly orientation trisilanol POSS molecules and the deviation from the surface selection rule.

To conclude, the finding of the LO modes confirming the formation of oriented trisilanol layers on FTO glass, providing additional evidence that the SiOH groups of trisilanol POSS were sufficiently reactive to form a bonding with FTO glass, supporting the assumption of bonding to other polar surfaces such as mTiA. NGIA RA spectra of trisilanol POSS on mTiA could obviously not be measured and transmission spectra of mTiA/trisilanol POSS were employed for assessment of the corresponding interactions.

3.2.3. *Vibrational bands of mTiA/trisilanol POSS*

mTiA pigment, in contrast to TiO_2 and black spinel pigment [17,18] the surface of which has been modified with a thin layer of alumina pigment [42], provides a suitable means of identifying vibrational mode changes stemming from the interactions of the trisilanol POSS with the mTiA pigment surface (Fig. 8). Accordingly, the infrared spectra of mTiA and mTiA/trisilanol POSS were first examined and the latter spectra were then compared with the spectra of the surface modified mTiA before being washed (Fig. 8A)

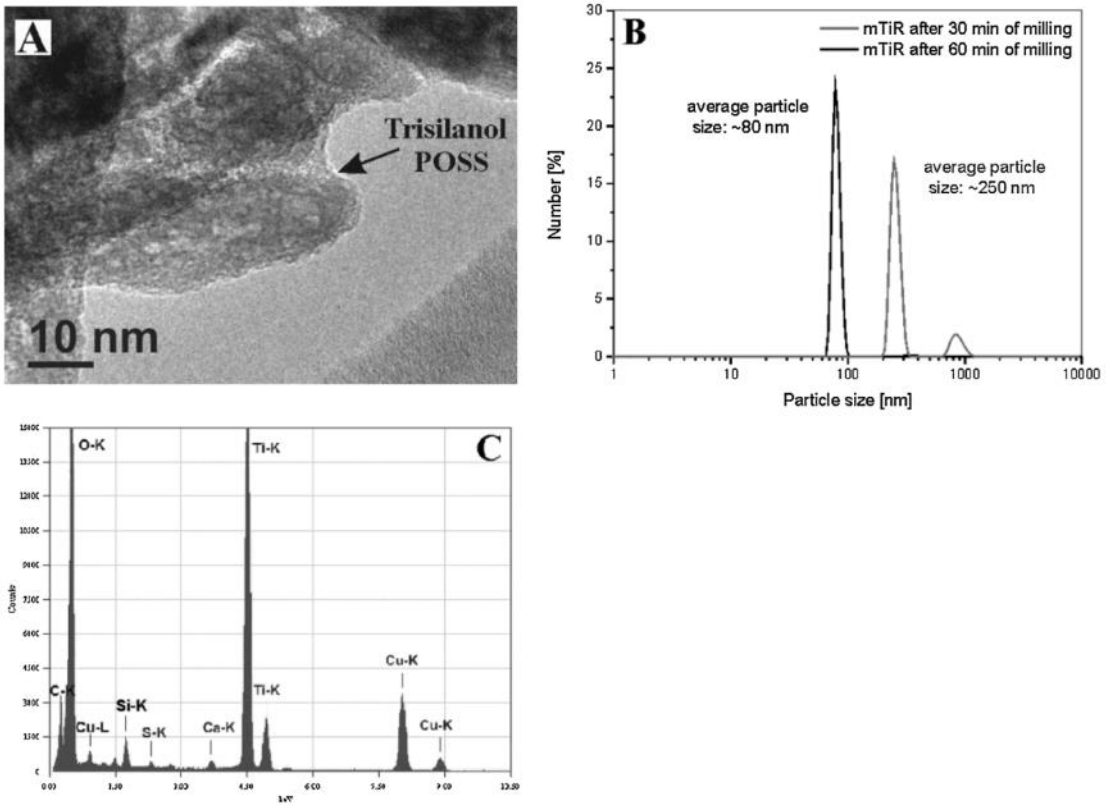


Fig. 5. TEM micrographs of mTiR (rutile) dispersion made with trisilanol POSS dispersant (A), milled with 0.1 mm zirconia beads and the corresponding DLS measurements (B) and EDAX spectrum (C).

and after washing with tetrahydrofuran (THF) solvent (Fig. 8B). In addition, in order to change the amount of bonded trisilanol POSS molecules on the mTiA, the pigment was milled with larger and smaller beads (0.4 and 0.2 mm in size) and the spectra compared with each other (see below).

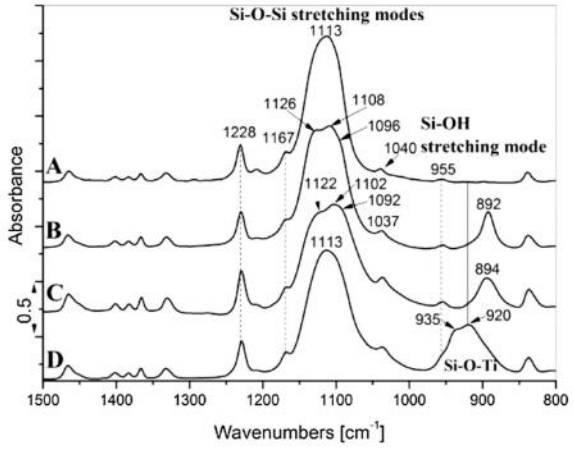


Fig. 6. Infrared transmission spectra of octaisobutyl POSS (T_8IB_8 POSS) (A), trisilanol POSS in a KBr pellet (B), as thin pigment film deposited on a silicon wafer (C) and trisilanol POSS-titanium isopropoxide metal silsesquioxane prepared by an end-capping reaction (D).

3.2.3.1. Si—O—Si stretching modes (spectral region 1500–800 cm^{-1}). With respect to the infrared spectra of trisilanol POSS (Fig. 6B, C and Fig. 9A), the spectra of unwashed mTiA/trisilanol POSS dispersion made by milling mTiA pigment with 0.4 mm beads (Fig. 9B) showed bands at 1115, 1095 and 1082 cm^{-1}, which indicated fairly strong frequency shifts and changes of band intensities. In the infrared spectra of unwashed mTiA/trisilanol POSS dispersions prepared with the smaller beads (0.2 mm) (Fig. 9C), the band at 1115 cm^{-1} shifted to 1119 cm^{-1} and the bands at 1095 and 1082 cm^{-1} merged to a single strong band at 1080 cm^{-1} (Fig. 9B). In the spectra of washed mTiA/trisilanol POSS dispersions (Fig. 9D), the latter band became dominant and appeared together with the band at 1116 cm^{-1}. The corresponding bands could obviously not be seen in the spectra of bare mTiA (Fig. 9E).

To conclude, the Lewis acidity of the co-ordinatively unsaturated (cus) Ti^{4+} surface sites [43,65] was high enough to disturb the trisilanol POSS. The interactions were strong, as was inferred from the large red-frequency shifts of the Si—O—Si modes and their dependence on the mTiA particle size. This substantiated the need for investigation of the isobutyl modes (Fig. 8), expected to be also disturbed by interactions of the corner SiOH groups with the surface of the mTiA.

3.2.3.2. Isobutyl stretching modes (spectral region 3000–2800 cm^{-1}). The methyl stretching modes of the isobutyl pendant groups of the POSS cage and the corresponding methylene modes of the trisilanol POSS (Fig. 10A) appeared at 2949–2954 cm^{-1} (ν_a (CH_3)), 2866–2870 cm^{-1} (ν_s (CH_3)) and 2928–2932 cm^{-1} (ν_a (CH_2)). This assignment agreed with the bands listed by Godnjavec et al. [42],

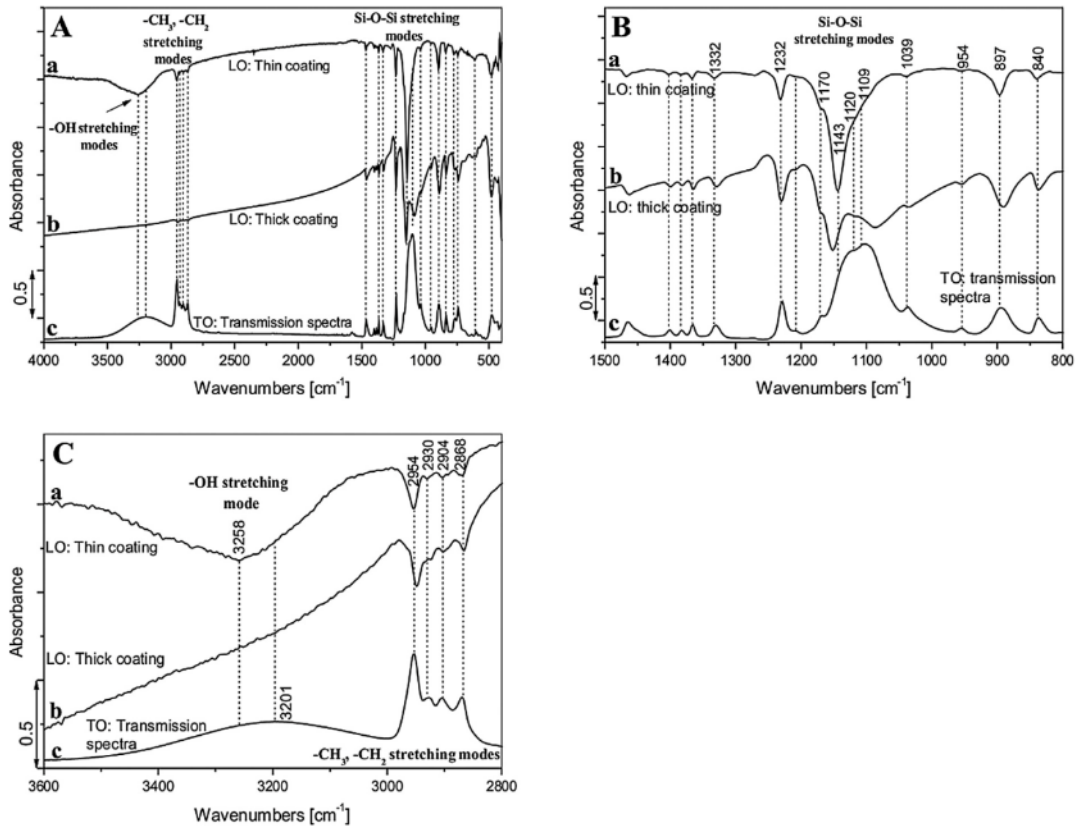


Fig. 7. NGIA RA spectra of thin (A(a), B(a) and C(a)) and thick ((A(b), B(b) and C(b)) layers of trisilanol POSS on FTO glass substrate (P-polarized light) and the corresponding transmission spectra ((A(c), B(c) and C(c)) in various spectral regions.

with the exception of the band at 2904 cm^{-1}, which we assigned to the Fermi resonance band of the overtone of $-CH_2$ deformational mode at 1478 cm^{-1} coupled with the $-CH_2$ stretching mode. Examination of the infrared spectra of trisilanol POSS and mTiA/trisilanol POSS dispersion made with larger (Fig. 10B) and smaller beads (Fig. 10C), the latter also washed with THF (Fig. 10D), revealed that, due to the adsorption of dispersant on the surface of the mTiA, their frequencies changed slightly but their relative intensities were modified to a considerable extent. As expected, the bare mTiA (Fig. 10E) did not show any bands in this spectral region. The

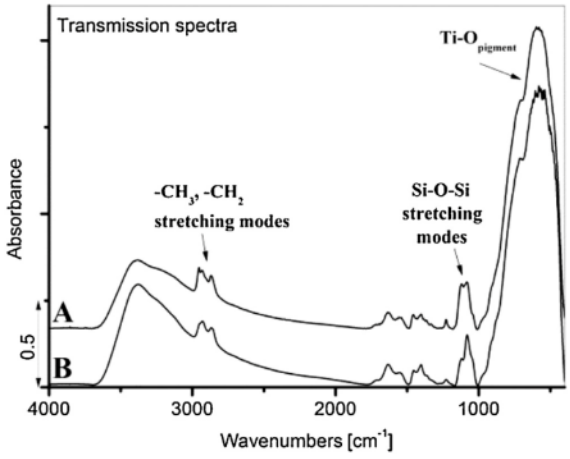


Fig. 8. Infrared spectra of mTiA/trisilanol POSS in KBr pellets (unwashed) prepared with milling beads of 0.2 mm (A) and washed (3×) with THF (B).

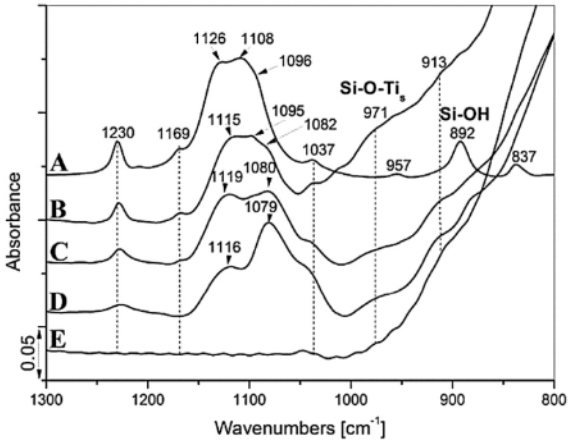


Fig. 9. ν_{as} Si-O-Si mode stretching modes of trisilanol POSS (A) in KBr pellets, mTiA/trisilanol POSS dispersions (unwashed) prepared with milling beads of 0.4 mm (B) and 0.2 mm (unwashed) (C) and washed (3×) with THF (D) and as-prepared mTiA (E).

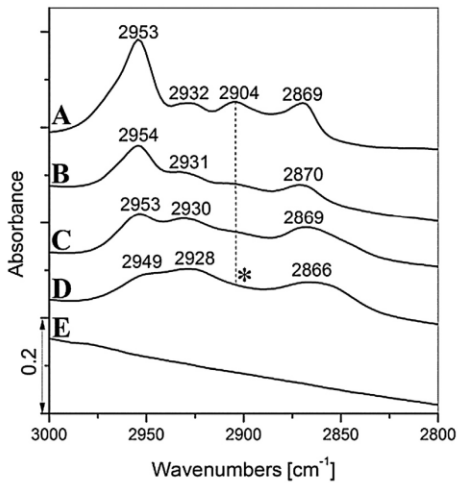


Fig. 10. Methyl and methylene stretching modes of trisilanol POSS (A) in KBr pellets, mTiA/trisilanol POSS dispersions (unwashed) prepared with milling beads of 0.4 mm (B) and 0.2 mm (unwashed) (C) and washed (3×) with THF (D) and as-prepared mTiA (E).* indicates Fermi resonance mode (see text).

intensity ratios of the methyl vs. methylene bands (2953 cm^{-1} (ν_a (CH_3))/2932 cm^{-1} (ν_a (CH_2)) increased steadily with a decreasing concentration of trisilanol POSS equilibrated in mTiA/trisilanol POSS/butanol solutions; in the case of the washed mTiA/trisilanol POSS (Fig. 10D) reaching an intensity ratio greater than 1. The intensity increase of the methylene (ν_a (CH_2)) band at 2932 cm^{-1} could reasonably be expected due to the kinematic coupling with the nearby open-cage silicon groups, disturbed to the greatest extent after the dispersant had interacted with the mTiA surface. A closer look at the band at 2932 cm^{-1} also revealed that the width of the band increased, indicating that the band broadening could be due to the different orientations of the trisilanol POSS with respect to the mTiA surface inferred from the Si—O—Si modes splitting. Nevertheless, the interactions of the trisilanol POSS with the pigment surface was strong, of which the large red-frequency shifts of the Si—O—Si stretching modes (Fig. 9) provided the most convincing evidence.

It should be noted that similar vibrational band broadening and red-frequency shifts of bands has been reported for the Si—H modes of octahydrido T_8 POSS encapsulated within carbon nanotubes [66]. The effect was stronger for MWNT-1 (diameter 1.0–3.0 nm) than for SWNT-1 (diameter 1.3–1.5 nm) because, in the case of the former nanotubes, a higher degree of disorder inside the nanotubes could be expected, which created a distribution of different local environments for the positioning of the ocathydrido T_8 POSS. This situation could not be directly compared to the adsorption of trisilanol POSS on the surface of the mTiA, even though the red-frequency shift of the Si—O—Si modes and the broadening of the (ν_a (CH_2)) mode at 2929 cm^{-1} suggested a variety of interactions with the mTiA surface sites.

3.2.3.3. Trisilanol POSS adsorption on mTiA pigment. mTiA pigment was next milled with zirconia beads of 0.4 mm size in trisilanol POSS/hexane, instead of mTiA/trisilanol POSS/butanol, solutions containing 0.01, 0.025, 0.05, 0.1 and 0.2 w/w% of trisilanol POSS. The corresponding pigment dispersions were dried and washed with THF (3 times) and the infrared spectra of the dry pigment pressed in KBr pellets were recorded. Closer inspection of the peak intensity of the ν_{as} (CH_3) band at 2953 cm^{-1} (Fig. 11A) indicated progressive occupation of accessible sites on the pigment surface (Fig. 11B). Because the modified pigment was thoroughly washed before spectra measurements, it can be conceived that, at lower concentrations, the trisilanol POSS molecules formed a discontinuous layer on the pigment surface. At the saturation limit (~10% nominal concentration of trisilanol POSS in hexane), complete coverage of the pigment surface was achieved, the mass of which was estimated from TG measurements (see below).

The use of infrared spectroscopy provides the simplest way of establishing the formation of siloxane (Si—O—$Ti_{surface}$) bonds. The corresponding stretching band has been observed at 910–960 cm^{-1} in the *in situ* prepared titania–silica composite [43]. The corresponding band is strong and clearly visible, in contrast to the case in which the titania pigment has been surface modified with aminopropyltrialkoxysilane [60] by ultrasonic treatment of titania pigment in corresponding precursor solution. The most direct evidence of the assignment of the Si—O—Ti vibrational band has been found in the infrared spectra of trisilanol POSS/$Ti(iOPr)_4$ prepared by end corner-capping reactions [18,67,68], showing Si—O—Ti vibrational bands at 920 and 935 cm^{-1}, which replace the single SiOH band of trisilanol POSS at 892 cm^{-1} (Fig. 9).

Inspection of the vibrational bands shown on Fig. 9B–D revealed weak bands at 971 and 913 cm^{-1}. The former did not have any counterpart in the infrared spectra of bare mTiA, in contrast to the band at 913 cm^{-1}, which also appeared as a very weak shoulder band in the spectra of mTiA. Accordingly, the band at 971 cm^{-1} was attributed to the (Si—O—$Ti_{surface}$) mode, which confirmed the establishment of covalent bonding between SiOH groups of dispersant and the surface of the mTiA pigment. Due to the presence of the (Si—O—$Ti_{surface}$) mode and the observed frequency shifts and band intensity changes of the Si—O—Si modes shown in Fig. 9, we concluded that the covalent and hydrogen bonding formed between the trisilanol POSS and the mTiA pigment surface.

3.3. TG measurements

TG analysis enables the amount of dispersant attached on the pigment surface [60] to be estimated and can provide additional information about the dispersant layers obtained either from elemental analysis or infrared spectra studies. Thermal degradation of POSS macromers have already been intensively studied in the past due to their flame retardancy [69,70] and as pre-ceramic materials, the thermochemistry of which is known due to the formation of SiO_xC_y chars and SiC ceramics [71,72]. The results showed, as in the case of our own results [18], that water was first released, followed by the degradation of isobutyl groups at 220 °C and decomposition of the —CH_2 and —CH_3 groups, starting at 230 and terminating at 250 °C. The main decomposition of the dispersant was terminated at 250 °C, when restructuring of the POSS cages started, leading to the formation of silica at ~530 °C, as also reported in [42].

In order to confirm the adsorption of trisilanol POSS on the mTiA surface, TG measurements (temperature range up to 600 °C) of bare mTiA pigment and washed mTiA/trisilanol POSS/butanol and mTiA/trisilanol POSS/hexane pigments equilibrated in trisilanol POSS/butanol and trisilanol POSS/hexane solutions were performed and the corresponding results compared with mass losses detected for the unwashed surface modified mTiA (Fig. 12) and trisilanol POSS alone.

Comparison of the mass losses (Δm in %) observed for the bare (un-modified) mTiA ($\Delta m = -11.65\%$) and unwashed mTiA/trisilanol POSS/butanol ($\Delta m = -14.37\%$) revealed that the amount of dispersant that, was adsorbed on the unwashed pigment surface equilibrated in trisilanol POSS/butanol solvent was $\Delta m = 2.72\%$. As expected, the amount of dispersant adsorbed on the surface of mTiA after washing with THF decreased to $\Delta m = -12.45\%$, indicating that more than half of the initially present dispersant

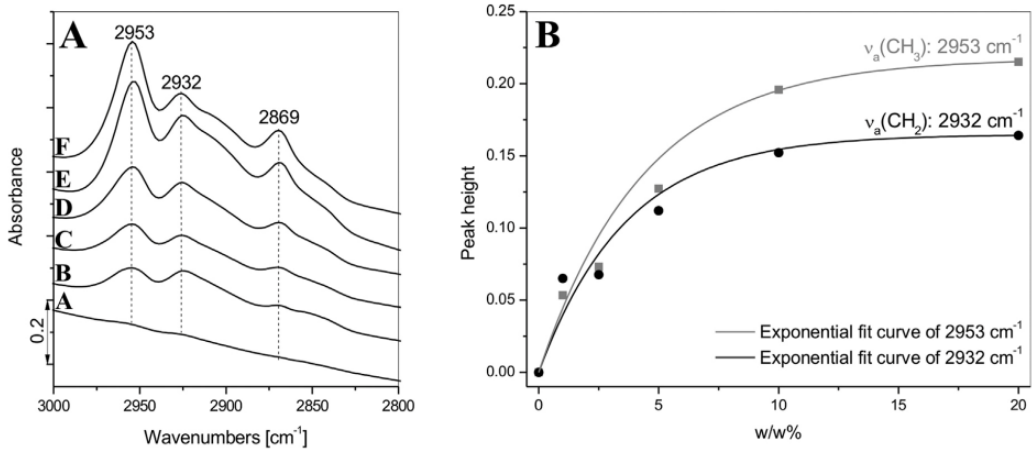


Fig. 11. Adsorption (A) and infrared spectra (B) of washed mTiA/trisilanol POSS dispersions obtained from the intensity band variations of C—H stretching modes after equilibrating mTiA in hexane/trisilanol POSS solutions with concentrations (A) base line, (B) 0.01, (C) 0.025, (D) 0.05, (E) 0.1 and (F) 0.2 w/w%.

was washed away and only 0.8% of the trisilanol POSS remained attached on the pigment surface.

TG results of mTiA/trisilanol POSS/hexane pigments showed similar trends, except that the amount of adsorbed dispersant was in this case higher, i.e., $\Delta m = -16.39\%$, indicating that the amount of dispersant that was adsorbed on the surface of mTiA from the hexane solution was nearly 2 times ($\Delta m = 4.74\%$) higher than that of mTiA equilibrated in butanol dispersant solutions. This was in agreement with the fact that adsorption was favoured from less polar (hexane) than from more polar (butanol) solvent.

Comparing these results with those reported for black spinel pigment [18] showed that bare mTiA in its as-prepared state contained more adsorbed species (Δm (mTiA) = 11.65%, vs. 2.5%) but the amounts of trisilanol POSS that remained on both mTiA and black spinel pigments after washing were close to each other, i.e., 4.74% (mTiA) vs. ~5% (black spinel pigment).

3.4. Morphology of coatings

3.4.1. AFM measurements

The average roughness expressed by the R_a parameter for the mTiA pigment coating was acquired from the AFM images. The

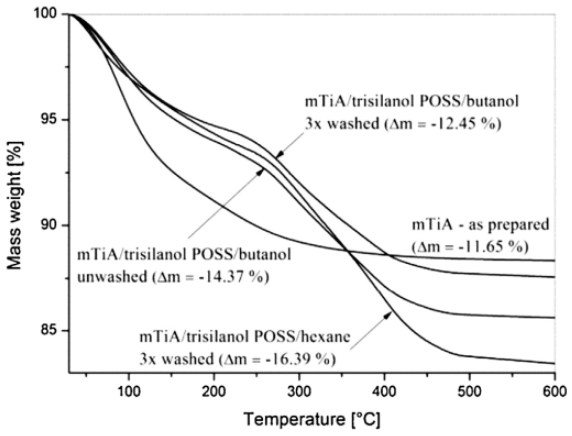


Fig. 12. TG measurements of bare (un-modified) mTiA, unwashed and washed mTiA/trisilanol POSS/butanol equilibrated in trisilanol POSS/butanol and washed mTiA/trisilanol POSS/hexane modified pigment equilibrated in hexane/trisilanol POSS mixture.

R_a (in nm) was taken over areas of $10 \times 10\,\mu m^2$ (not shown here) and $2 \times 2\,\mu m^2$ (Fig. 13). Two or three positions were analyzed on every mTiA01, mTiA02 and mTiA04 sample obtained from dispersions milled with zirconia beads of 0.1, 0.2 and 0.4 mm in size, respectively, and the average R_a values were then calculated. The corresponding R_a values did not monotonically increase with the particle size used for milling; the smallest, $R_a = 9.2$ nm, was obtained for the mTiA02 coating. As expected, $R_a = 21.7$ nm was the highest; while the R_a for coatings obtained from dispersions milled with the smallest beads (0.1 mm) was 16.3 nm. The estimated error was ±2.0 nm.

Examination of the AFM images (Fig. 13B) of mTiA02 clearly showed the presence of separate pigment particles, with a size from 50 to 70 nm, corroborating the size of aggregates obtained from TEM and DLS measurements (Fig. 4). Interestingly, the distribution of the particles and their packing was denser on the surface of the mTiA02 coatings than on the mTiA04 coatings, contrasting faint surface features with barely observable particles on the surface of the mTiA02 coatings. At least for the mTiA01 coatings, we could infer that the matrix, consisting of particle gravel formed due to the intensive milling with 0.1 mm zirconia beads, surrounded the larger (50–70 nm) pigment particles. We correlated this with the increased R_a values noted for the mTiA01 coatings ($R_a = 16.3$ nm), surpassing the R_a values of mTiA02 coatings ($R_a = 9.2$ nm) and nearly reaching the R_a values of the mTiA04 coatings ($R_a = 21.7$ nm). This meant that too intense milling with 0.1 mm beads led to a coating that consisted of almost fused smaller particles with embedded larger particles ousted from the surface of the coating. The optical properties, which are presented below, indirectly confirmed the correspondence between haze and the surface roughness of the coatings.

3.4.2. SEM micrographs

The surface texture of the pigment coatings made of mTiA/trisilanol POSS/butanol dispersions with added 10% of $Ti(iOPr)_4$ acting as binder and deposited on FTO glass was studied with SEM microscopy (Fig. 14). The samples were cut from larger pieces of the corresponding coatings, part of which also served for the AFM measurements, thickness measurements and determination of haze.

Examination of the SEM micrographs (Fig. 14) showed that the use of larger zirconia beads of 0.4 mm led to coatings consisting of coarser particles, agreeing with the AFM results (Fig. 13C), compared to the mTiA02 coating (Fig. 13B). The effect of added butanol

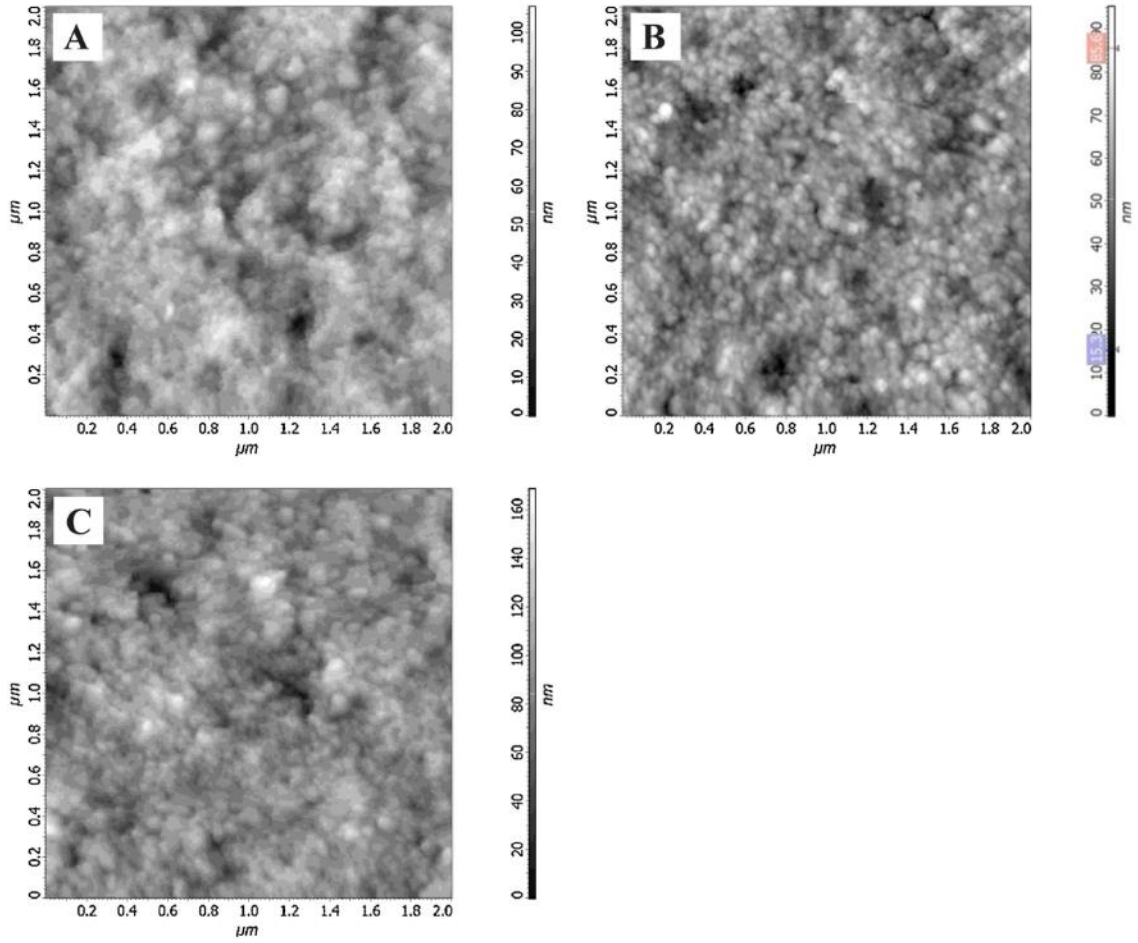


Fig. 13. AFM images obtained over an area of $2 \times 2\ \mu m^2$: (A) mTiA01 (R_a = 16.3 nm), (B) mTiA02 (R_a = 9.2 nm) and (C) mTiA04 (R_a = 21.7 nm).

to the mTiA/trisilanol POSS coating was deduced from Fig. 14A and B. While a homogeneous and compact, void-free coating formed from less diluted pigment dispersions, a certain extent of flocculation could be inferred for the coating deposited from dispersions with added butanol. This indicated that the pigment dispersions were more suitable for the deposition of coatings with high pigment loadings (~90%), which has been found to be important for electrochromic applications, as reported in [35] and as described below in more detail in relation to haze.

3.5. Optical properties and EC properties of pigment coatings

3.5.1. Optical properties of mTiA pigment coatings on FTO glass and ITO PET substrates

Knowledge of the optical properties (TT, DT and haze) of the pigment coatings was needed for assessment of their applications in electrochromic systems. In order to obtain information about clear sight through the mTiA pigment coatings and their high light transmission in a bleached state, total transmittance (TT), diffuse total transmittance (DT) and haze were determined from the corresponding spectral values (TT(λ), DT(λ)) and correlated with processing parameters, i.e., the size of zirconia beads used for milling dispersions, and with the corresponding SEM and AFM results.

Examination of the DT(λ) and TT(λ) spectra of mTiA01, mTiA02 and mTiA04 pigment coatings made with trisilanol POSS dispersant (Fig. 15) revealed that scattering was stronger for all coatings at shorter wavelengths than with the bare FTO glass. Haze values, as expected, strongly correlated with the surface roughness (R_a); coatings milled with beads of 0.2 mm (mTiA02) had the lowest haze (1.7%), agreeing with the smallest surface roughness (R_a = 9.7 nm) determined from AFM measurements (Fig. 13B) and they also showed the highest transmittance (TT = 82%).

As expected, the haze values of the pigment coatings (not shown here) also made with trisilanol POSS, that were deposited on ITO PET foils (~15%) greatly exceeded those of the same coatings (i.e., mTiA02 with 10% of the binder) on FTO glass. We attributed this to the higher haze of ITO PET foil compared to FTO glass (FTO glass: haze = 0.39%, TT = 83.47%, DT = 0.66% and ITO PET foil: haze = 1.09%, TT = 9.11%, DT = 1.26%) and also to the difference in the surface energy values of ITO PET foil and FTO glass, the former exhibiting a much smaller polar part and total values of surface energy (σ^{AB} = 7.05 mJ/m^2 and σ^{tot} = 46 mJ/m^2) than the latter (σ^{AB} = 1.66 mJ/m^2, σ^{tot} = 37 mJ/m^2 [17]), which provided better wetting of ITO PET foil compared to glass. Smaller haze values could

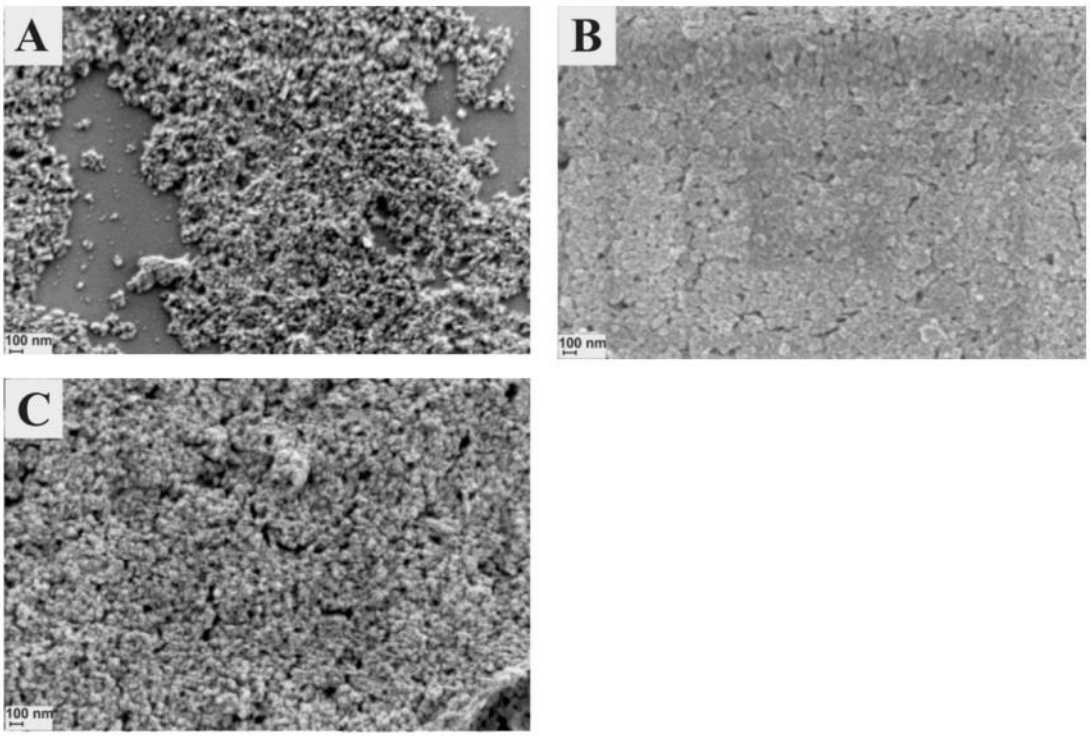


Fig. 14. Surface morphology of mTiA pigment coatings: (A) mTiA02 (diluted dispersion), (B) mTiA02, (C) mTiA04.

obviously be expected when a less polar binder is used instead of $Ti(iOPr)_4$, which we intend to do in the future.

The low haze and high TT and low DT values of pigment coatings made with trisilanol POSS dispersant could be explained by the absence of voids and holes, which are the main source of scattering (Fig. 14). This suggested that after the evaporation of butanol, mTiA particles collapsed without significant folding (Fig. 13) and dense coatings with high pigment-to-pigment particle contacts and pigment loading formed. High pigment loading facilitated electron transfer from the FTO glass or ITO PET electrode surface to the coating's interior but leaving sufficient space for diffusion of lithium ions, which beneficially affected EC properties, as shown below.

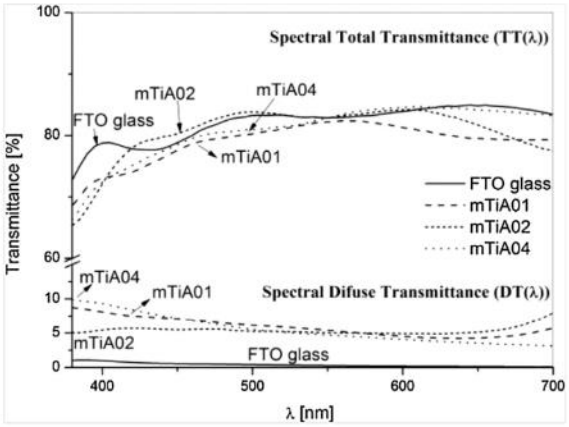


Fig. 15. Total (TT(λ)) and diffuse (DT(λ)) transmission spectra of mTiA coatings on FTO glass made of mTiA/trisilanol POSS dispersions after milling with various zirconia beads (0.1, 0.2 and 0.4 mm) and spin coated for 40 s at a rotation speed of 1500 s^{-1}.

3.5.2. *EC properties: in situ chronocoulometry (CC) spectroelectrochemical measurement of mTiA coatings*

In order to demonstrate that the electrochromic response of the mTiA pigment coatings depended on the trisilanol POSS dispersant and the size of the mTiA particle, two types of coating were examined; first, made with and without dispersant and second, by milling each of them with zirconia beads of different sizes, i.e., 0.4, 0.2 and 0.1 mm. The intensity of the electrochromic effect was evaluated from the *in situ* spectroelectrochemical chronocoulometric measurements (CC) providing correlations between the amount of charge expressed by ion storage capacity (in mC/cm^2) defined by the amount of lithium ions inserted per unit active area and the corresponding colouring/bleaching changes ($\Delta T = T_{colored} - T_{bleached}$). The mTiA pigment coatings (working electrode) were immersed in a 1 M $LiClO_4$/PC (liquid) electrolyte charged at potential 0 V and −1.7 V vs. Ag/AgCl reference electrode and the corresponding direct transmittance spectra ($T(\lambda)$) of coatings were recorded *in situ* every 4 s. The corresponding change of the spectral transmittance of the mTiA pigment coatings is presented on Fig. 16Aand B, showing the typical dark blue colour of the mTiA with Ti ions in the ~3+ oxidation state.

The advantage of using trisilanol POSS dispersant was inferred from inspecting the EC effect of various mTiA pigment coatings, as shown in Fig. 17. The effect of the dispersant was easily seen by comparing the transmittance curves ($T(\lambda)$) of the mTiA04 coatings made from dispersions milled with the largest beads (0.4 mm) with and without added dispersant (Fig. 17A). The mTiA04 with trisilanol POSS pigment coatings exhibited transmittance curves in bleached and coloured states that showed a steep rise of transmittance at shorter wavelengths, while $T(\lambda)_{bleached}$ and $T(\lambda)_{coloured}$ curves

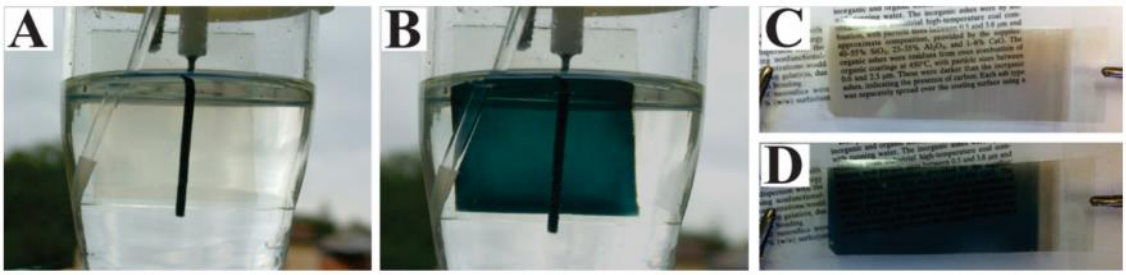


Fig. 16. Electrochromic changes of the mTiA pigment coatings mTiA01 (1× spin-coating) deposited on FTO glass in initial (A) and charged state (B) obtained after charging for 1 min at −1.7 V (see text). EC devices on ITO PET foils in bleached (C) and coloured (D) states are also presented (for details see text).

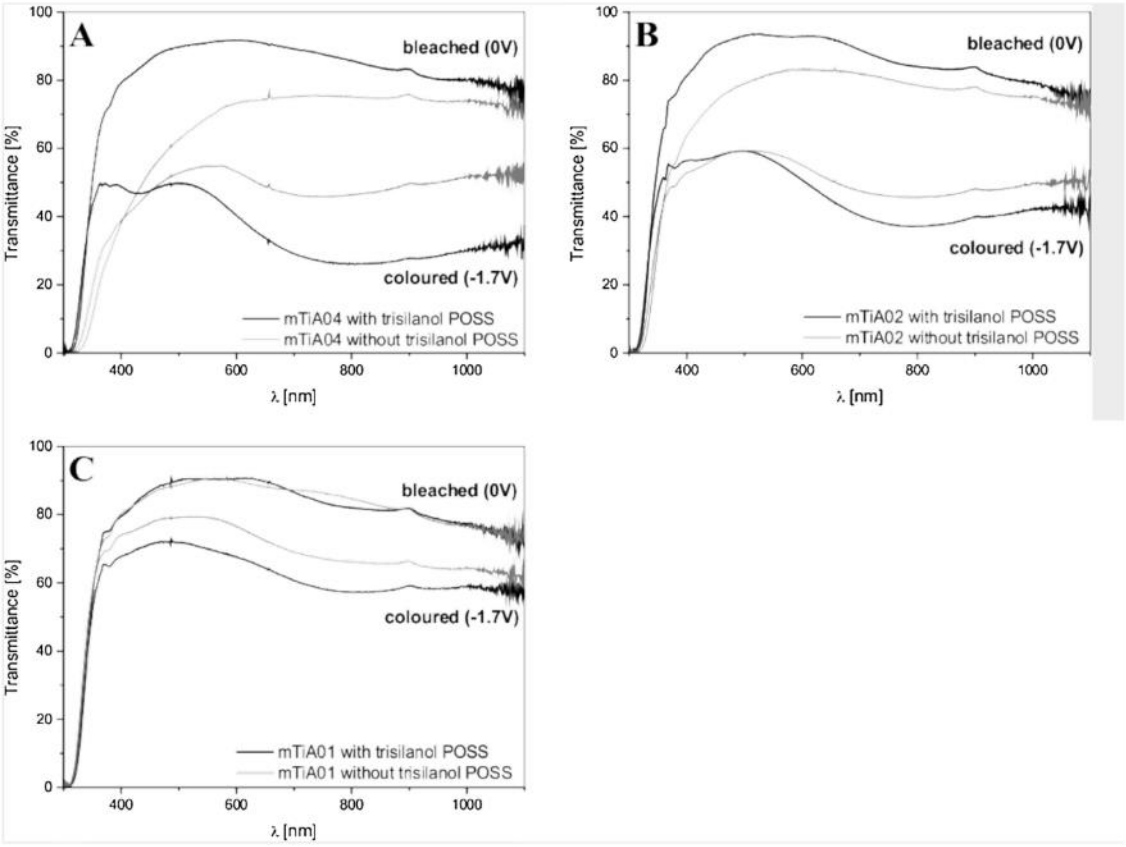


Fig. 17. *In situ* UV–vis spectroelectrochemical changes of mTiA04 (A) mTiA02 (B) and mTiA01 (C) pigment coatings with and without trisilanol POSS deposited by single spin-coating deposition on FTO glass, charged (coloured) at −1.7 V (60 s) and discharged (bleached) at 0 V (60 s). The monochromatic transmittance changes were obtained at λ = 634 nm (Table 1).

Table 1
Charge capacities (Q in mC/cm^2), transmittance of the mTiA based pigment coatings made with and without trisilanol POSS deposited by single spin-coating deposition on FTO glass in coloured (charged) at −1.7 V (60 s) and bleached (discharged) state at 0 V (60 s) at λ = 634 nm and the corresponding difference of transmittance (ΔT).

	Q (mC/cm^2)		TT (%)		ΔTT (%)	d (nm)
	Coloured	Bleached	Coloured	Bleached		
mTiA01	−5.4	4.0	90.4	65.5	24.9	86 ± 20
mTiA02	−20.9	15.9	92.7	46.6	46.1	155 ± 20
mTiA04	−32.1	24.6	91.3	35.6	55.7	300 ± 20
mTiA01 without trisilanol POSS	−21.1	15.1	88.6	73.8	14.8	100 ± 20
mTiA02 without trisilanol POSS	−16.7	11.3	82.9	51.9	31.0	175 ± 20
mTiA04 without trisilanol POSS	−15.6	9.8	94.2	48.0	46.2	270 ± 20

of the same coatings exhibited more suppressed transmittance curves. This was attributed to the effect of scattering stemming from larger particle aggregates present in the latter coatings. These results agreed with the AFM (Fig. 13) results and optical properties (Fig. 15), indirectly also confirming the influence of trisilanol POSS interactions with the mTiA particles, which was conceived from the infrared spectra studies. The observed EC effect was fairly large ($\Delta T = T_{bleached} - T_{coloured} = 55.7\%$, $\lambda = 634$ nm), agreeing with the high Q values (Table 1) attributed to the high coating thickness ($d = 300$ nm) that, originated from the milling of the pigment with the large size of zirconia beads (0.4 mm).

The influence of trisilanol POSS on the EC effect on the mTiA02 and mTiA01 pigment coatings was less pronounced, even though both pigment coatings showed a steeper transmittance increase (i.e., less scattering) than the coatings in which dispersant was not used (Fig. 17B). Accordingly, the EC effect was also smaller ($\Delta T = T_{bleached} - T_{coloured} = 46.10\%$, $\lambda = 634$ nm) because the dispersion consisted of smaller particles, which formed a thinner coating ($d = 155$ nm) after deposition (Table 1). The effect of dispersant on the EC effect was worst expressed for the thinnest ($d = 86$ nm) mTiA01 pigment coatings (Fig. 17C), which scattered to the smallest extent but exhibited also the smallest EC effect ($\Delta T = T_{bleached} - T_{coloured} = 25\%$, $\lambda = 634$ nm). To conclude, the EC effects of the mTiA/trisilanol POSS pigment coatings were similar to other titania thin films and coatings, as already reviewed by Sorar et al. [73].

The mTiA02 pigment coatings were used for the preparation of flexible EC device because of their small surface roughness (Fig. 13) and fairly high EC effect (Fig. 17B). The corresponding flexible EC device was assembled from the mTiA/trisilanol POSS pigment coatings with $Ni_{1-x}O$ [35,51] coatings, which were also prepared by a wet deposition (coil-coating) technique from $Ni_{1-x}O$ pigment dispersions, as described in detail in [51]. Since $Ni_{1-x}O$ is an anodic material and mTiA a cathodic one, in the corresponding EC device they coloured simultaneously at negative and bleached at positive potentials, which contributed to the enhanced electrochromic effect (Fig. 16C and D). The two coatings were glued together with semi-solid lithium conducting membrane type electrolyte with a conductivity of 5×10^{-4} S/cm, as described in [35,51]. The detailed electrochemical and electrochromic properties of the flexible EC device deserve special study, which will be published elsewhere.

4. Conclusions

The described procedure started from the preparation of metatitanic acid (mTiA) in the form of aggregates consisting of a mixture of anatase and rutile (15%) particles, which, in the next stage, was milled with zirconia beads of different sizes in a trisilanol POSS/butanol and trisilanol POSS/hexane mixture, until the particle aggregates reached a size of 50 nm. A small amount (10 wt%) of added $Ti(iOPr)_4$ serving as binder was enough to achieve the mechanical integrity of pigment coatings with haze below 5%.

Adsorption of trisilanol POSS on the surface of the mTiA pigment particles was determined from the infrared spectra measurements of mTiA, which was equilibrated in trisilanol POSS/butanol and trisilanol POSS/hexane solutions with different concentrations of dispersant. Vibrational bands of trisilanol POSS and trisilanol POSS adsorbed on mTiA pigment were examined and their changes ascribed to the H bond interactions of the SiOH groups of the POSS cages with the mTiA pigment, while the formation of covalent bonds between trisilanol POSS and the pigment surface was inferred from the presence of the ($Si{-}O{-}Ti_{surface}$) mode at 971 cm^{-1}. An adsorption curve was constructed from the intensity variations of vibrational bands attributed to the trisilanol POSS that remained attached on the mTiA surfaces after washing with THF.

Direct evidence of the formation of a dispersant layer on the pigment surface was obtained from TEM and EDAX measurements performed on mTiA pigment, also verified for rutile pigment. TG measurements also revealed that the amount of trisilanol POSS adsorbed on the mTiA surface was higher when the pigment was equilibrated in trisilanol POSS/hexane solutions than in a solution of trisilanol POSS in butanol. Most importantly, the mTiA pigment coatings made from dispersions containing trisilanol POSS dispersant exhibited much lower haze than coatings made without it. The method described in this study is fairly versatile, since it could be used for making many other inorganic electrochromic metal oxide electrochromic coatings and opens the possibility of deposition of electrochromic coatings on polymeric substrates.

Acknowledgement

The research leading to these results has received funding from the European Community's Seventh Framework Programme (FP7) under Grant Agreement no. 200431 (INNOSHADE) and from CO-NOT, Centre of Excellence for Low-Carbon Technologies (grant no. MVZT 3211-09-000641). We wish to thank Dr. Ivan Jerman for his help in preparation of pigment dispersions and SEM pictures and Dr. Dejan Verhovšek for TEM measurement.

References

[1] www.hybridplastics.com;1.
[2] D.A. Loy, K. Tahimian, in: H.S. Nalwa (Ed.), Handbook of Organic–Inorganic Hybrid Materials and Nanocomposites, American Scientific Publishers, Stevenson Ranch, Calif, 2003, pp. 125–163.
[3] P.G. Harrison, Silicate cages: precursors to new materials, J. Organomet. Chem. 542 (1997) 141–183.
[4] D.B. Cordes, P.D. Lickiss, F. Rataboul, Recent developments in the chemistry of cubic polyhedral oligosilsesquioxanes, Chem. Rev. 110 (2010) 2081–2173.
[5] P.D. Lickiss, F. Rataboul, Chapter 1 fully condensed polyhedral oligosilsesquioxanes (POSS): from synthesis to application, in: F.H. Anthony, J.F. Mark (Eds.), Advances in Organometallic Chemistry, Elsevier Academic Press Inc, San Diego, California, 2008, pp. 1–116.
[6] H.Z. Liu, S.X. Zheng, K.M. Nie, Morphology and thermomechanical properties of organic–inorganic hybrid composites involving epoxy resin and an incompletely condensed polyhedral oligomeric silsesquioxane, Macromolecules 38 (2005) 5088–5097.
[7] B.X. Fu, M. Namani, A. Lee, Influence of phenyl-trisilanol polyhedral silsesquioxane on properties of epoxy network glasses, Polymer 44 (2003) 7739–7747.
[8] M. Kozelj, B. Orel, Synthesis of polyhedral phenylsilsesquioxanes with KF as the source of the fluoride ion, Dalton Trans. (2008) 5072–5075.
[9] M. Kozelj, B. Orel, N-Heterocyclic carbenes-catalysts for the preparation of polyhedral silsesquioxanes, Dalton Trans. 42 (2013) 9432–9436.
[10] I. Jerman, B. Orel, A. Surca Vuk, M. Kozelj, J. Kovac, A structural and corrosion study of triethoxysilyl and perfluorooctyl functionalized polyhedral silsesquioxane nanocomposite films on AA 2024 alloy, Thin Solid Films 518 (2010) 2710–2721.
[11] I. Jerman, A. Šurca Vuk, M. Koželj, F. Švegl, B. Orel, Influence of amino functionalised POSS additive on the corrosion properties of (3-glycidoxypropyl)trimethoxysilane coatings on AA 2024 alloy, Prog. Org. Coat. 72 (2011) 334–342.
[12] I. Jerman, A. Surca Vuk, M. Kozelj, B. Orel, J. Kovac, A structural and corrosion study of triethoxysilyl functionalized POSS coatings on AA 2024 alloy, Langmuir 24 (2008) 5029–5037.
[13] S. Kraus-Ophir, I. Jerman, B. Orel, D. Mandler, Symmetrical thiol functionalized polyhedral oligomeric silsesquioxanes as building blocks for LB films, Soft Matter 7 (2011) 8862–8869.
[14] M. Colovic, I. Jerman, M. Gaberscek, B. Orel, POSS based ionic liquid as an electrolyte for hybrid electrochromic devices, Sol. Energy Mater. Sol. C 95 (2011) 3472–3481.
[15] E. Stathatos, V. Jovanovski, B. Orel, I. Jerman, P. Lianos, Dye-sensitized solar cells made by using a polysilsesquioxane polymeric ionic fluid as redox electrolyte, J. Phys. Chem. C 111 (2007) 6528–6532.
[16] I. Jerman, B. Tomšič, B. Simončič, B. Orel, Tailoring of cotton fabrics surface properties by silsesquioxane molecules, in: Proceedings of the 41st International Symposium on Novelties in Textiles and 5th International Symposium on Novelties in Graphics and 45th International Congress IFKT, Ljubljana, Slovenia, 27–29 May 2010, Ljubljana: Faculty of Natural Sciences and Engineering, Department of Textiles, 2010, pp. 96–103.

[17] I. Jerman, M. Kozelj, B. Orel, The effect of polyhedral oligomeric silsesquioxane dispersant and low surface energy additives on spectrally selective paint coatings with self-cleaning properties, Sol. Energy Mater Sol. C 94 (2010) 232–245.
[18] I. Jerman, M. Mihelcic, D. Verhovsek, J. Kovac, B. Orel, Polyhedral oligomeric silsesquioxane trisilanols as pigment surface modifiers for fluoropolymer based thickness sensitive spectrally selective (TSSS) paint coatings, Sol. Energy Mater. Sol. C 95 (2011) 423–431.
[19] O.P. Agnihotri, B.K. Gupta, Solar Selective Surfaces, Wiley, New York, 1981.
[20] I. Jerman, M. Koželj, L. Slemenik Perše, B. Orel, Paint coatings for polymeric solar absorbers and their applications, in: M. Köhl, M.G. Meir, P. Papillon, G.M. Wallner, S. Saile (Eds.), Polymeric Materials for Solar Thermal Applications, Wiley-VCH, Weinheim, 2012, pp. 167–186.
[21] I. Jerman, B. Orel, M. Koželj, Application of POSS compounds for modification of the wetting properties of TISS paint coatings, in: M. Köhl, M.G. Meir, P. Papillon, G.M. Wallner, S. Saile (Eds.), Polymeric Materials for Solar Thermal Applications, Wiley-VCH Verlag GmbH & Co, KGaA, 2012, pp. 267–286.
[22] J. Vince, A. Šurca Vuk, U.O. Krašovec, B. Orel, M. Köhl, M. Heck, Solar absorber coatings based on CoCuMnOx spinels prepared via the sol–gel process: structural and optical properties, Sol. Energy Mater. Sol. C 79 (2003) 313–330.
[23] L. Kaluža, B. Orel, G. Dražič, M. Kohl, Sol–gel derived CuCoMnOx spinel coatings for solar absorbers: structural and optical properties, Sol. Energy Mater. Sol. C 70 (2001) 187–201.
[24] M. Koželj, B. Orel, M. Steinbücher, I. Jerman, V. Vodlan, Aminosilane modified pigments for spectrally selective coatings, method for preparation and their use in coatings, patent: EP 2261288 A1, 2010.
[25] R. Kunič, M. Mihelčič, B. Orel, L. Slemenik Perše, B. Bizjak, J. Kovač, S. Brunold, Life expectancy prediction and application properties of novel polyurethane based thickness sensitive and thickness insensitive spectrally selective paint coatings for solar absorbers, Sol. Energy Mater. Sol. C 95 (2011) 2965–2975.
[26] I. Jerman, M. Mihelčič, M. Koželj, B. Orel, Sol–gel based spectrally selective solar absorber coatings and the process for producing said coatings, patent: WO 2013158049 A1, National institute of Chemistry, 2012.
[27] C.G. Granqvist, Handbook of Inorganic Electrochromic Materials, Elsevier, Amsterdam; New York, 1995.
[28] C.G. Granqvist, Oxide electrochromics: why, how, and whither, Sol. Energy Mater. Sol. C 92 (2008) 203–208.
[29] R. Baetens, B.P. Jelle, A. Gustavsen, Properties, requirements and possibilities of smart windows for dynamic daylight and solar energy control in buildings: a state-of-the-art review, Sol. Energy Mater. Sol. C 94 (2010) 87–105.
[30] M.C. Choi, Y. Kim, C.S. Ha, Polymers for flexible displays: from material selection to device applications, Prog. Polym. Sci. 33 (2008) 581–630.
[31] U. Opara Krasovec, A. Surca Vuk, B. Orel, IR Spectroscopic studies of charged-discharged crystalline WO_3 films, Electrochim. Acta 46 (2001) 1921–1929.
[32] B. Orel, M. Macek, J. Grdadolnik, A. Meden, In situ UV–vis and ex situ IR spectroelectrochemical investigations of amorphous and crystalline electrochromic Nb_2O_5 films in charged/discharged states, J Solid State Electr 2 (1998) 221–236.
[33] F. Švegl, B. Orel, I. Grabec-Švegl, V. Kaučič, Characterization of spinel Co_3O_4 and Li-doped Co_3O_4 thin film electrocatalysts prepared by the sol–gel route, Electrochim. Acta 45 (2000) 4359–4371.
[34] A. Surca, B. Orel, B. Pihlar, P. Bukovec, Optical, spectroelectrochemical and structural properties of sol–gel derived Ni-oxide electrochromic film, J. Electroanal. Chem. 408 (1996) 83–100.
[35] M. Mihelčič, I. Jerman, B. Orel, Preparation of electrochromic $Ni_{1-x}O$ and TiO_2 coatings from pigment dispersions and their application in electrochromic foil based devices, Prog. Org. Coat. 76 (2013) 1752–1755.
[36] M. Mihelčič, A. Šurca Vuk, I. Jerman, B. Orel, F. Švegl, H. Moulki, C. Faure, G. Campet, A. Rougier, Comparison of electrochromic properties of $Ni_{1-x}O$ in lithium and lithium-free aprotic electrolytes: from $Ni_{1-x}O$ pigment coatings to flexible electrochromic devices, Sol. Energy Mater. Sol. C 120 (Part A) (2014) 116–130.
[37] H. Moulki, C. Faure, M. Mihelcic, A. Surca Vuk, F. Svegl, B. Orel, G. Campet, M. Alfredsson, A.V. Chadwick, D. Gianolio, A. Rougier, Electrochromic performances of nonstoichiometric NiO thin films, Thin Solid Films 553 (2014) 63–66.
[38] U. Opara Krašovec, A. Surca Vuk, B. Orel, Comparative studies of all sol–gel electrochromic windows employing various counter-electrodes, Sol. Energy Mater. Sol. C 73 (2002) 21–37.
[39] E.J. Widjaja, G. Delporte, F. Vandevelde, B. Vanterwyngen, Progress toward roll-to-roll processing of inorganic monolithic electrochromic devices on polymeric substrates, Sol. Energy Mater. Sol. C 92 (2008) 97–100.
[40] C.M. Lampert, Large-area smart glass and integrated photovoltaics, Sol. Energy Mater. Sol. C 76 (2003) 489–499.
[41] C.M. Lampert, Welcome and introduction, Displays 25 (2004), 165–165.
[42] J. Godnjavec, B. Znoj, N. Veronovski, P. Venturini, Polyhedral oligomeric silsesquioxanes as titanium dioxide surface modifiers for transparent acrylic UV blocking hybrid coating, Prog. Org. Coat. 74 (2012) 654–659.
[43] Z. Li, B. Hou, Y. Xu, D. Wu, Y. Sun, W. Hu, F. Deng, Comparative study of sol–gel-hydrothermal and sol–gel synthesis of titania–silica composite nanoparticles, J. Solid State Chem. 178 (2005) 1395–1405.
[44] H.Z. Liu, S. Kondo, R. Tanaka, H. Oku, M. Unno, A spectroscopic investigation of incompletely condensed polyhedral oligomeric silsesquioxanes (POSS-monool, POSS-diol and POSS-triol): Hydrogen-bonded interaction and host–guest complex, J. Organomet. Chem. 693 (2008) 1301–1308.
[45] Y.R. Liu, Y.D. Huang, L. Liu, Influences of monosilanolisobutyl-POSS on thermal stability of polymethylsilxoane, J. Mater. Sci. 42 (2007) 5544–5550.
[46] D. Verhovšek, N. Veronovski, U. Lavrenčič Štangar, M. Kete, K. Žagar, M. Čeh, The synthesis of anatase nanoparticles and the preparation of photocatalytically active coatings based on wet chemical methods for self-cleaning applications, Int. J. Photoenergy 2012 (2012) 10pages.
[47] www.cinkarna.si.
[48] S. Sathyamoorthy, G.D. Moggridge, M.J. Hounslow, Controlling particle size during anatase precipitation, AIChe J. 47 (2001) 2012–2024.
[49] S. Sathyamoorthy, G.D. Moggridge, M.J. Hounslow, Particle formation during anatase precipitation of seeded titanyl sulfate solution, Cryst. Growth Des. 1 (2001) 123–129.
[50] S. Doeuff, C. Sanchez, Propriétés électrochromes de films de TiO2 anatase préparés parle procédé sol–gel, C. R. del'Acad. Sci., Série 2 309 (1989) 531–534.
[51] M. Mihelcic, I. Jerman, F. Svegl, A. Surca Vuk, L. Surca Perse, J. Kovac, B. Orel, U. Posset, Electrochromic $Ni_{1-x}O$ pigment coatings and plastic film-based $Ni_{1-x}O/TiO_2$ device with transmissive light modulation, Sol. Energy Mater. Sol. C 107 (2012) 175–187.
[52] H.L. Yu, C.C. Hsiao, W.C. Liu, New apparatus for haze measurement for transparent media, Meas. Sci. Technol. 17 (2006) N29–N36.
[53] X. Chen, S.S. Mao, Titanium dioxide nanomaterials: synthesis, properties, modifications, and applications, Chem. Rev. 107 (2007) 2891–2959.
[54] S. Kango, S. Kalia, A. Celli, J. Njuguna, Y. Habibi, R. Kumar, Surface modification of inorganic nanoparticles for development of organic–inorganic nanocomposites—A review, Prog. Polym. Sci. 38 (2013) 1232–1261.
[55] H. Zou, S.S. Wu, J. Shen, Polymer/silica nanocomposites: preparation, characterization, properties, and applications, Chem. Rev. 108 (2008) 3893–3957.
[56] P. Silberzan, L. Leger, D. Ausserre, J.J. Benattar, Silanation of silica surfaces—a new method of constructing pure or mixed monolayers, Langmuir 7 (1991) 1647–1651.
[57] W.D. Bascom, R.B. Timmons, Hydrolysis of triethylethoxysilane at silica–carbon tetrachloride interface, J. Phys. Chem. 76 (1972), 3192-&.
[58] A. Šurca Vuk, R. Ješe, M. Gaberšček, B. Orel, G. Dražič, Structural and spectroelectrochemical (UV–vis and IR) studies of nanocrystalline sol–gel derived TiO_2 films, Sol. Energy Mater. Sol. C 90 (2006) 452–468.
[59] J. Zhao, M. Milanova, M.M.C.G. Warmoeskerken, V. Dutschk, Surface modification of TiO_2 nanoparticles with silane coupling agents, Colloid Surf. A 413 (2012) 273–279.
[60] M. Sabzi, S.M. Mirabedini, J. Zohuriaan-Mehr, M. Atai, Surface modification of TiO_2 nano-particles with silane coupling agent and investigation of its effect on the properties of polyurethane composite coating, Prog. Org. Coat. 65 (2009) 222–228.
[61] E. Ukaji, T. Furusawa, M. Sato, N. Suzuki, The effect of surface modification with silane coupling agent on suppressing the photo-catalytic activity of fine TiO_2 particles as inorganic UV filter, Appl. Surf. Sci. 254 (2007) 563–569.
[62] V.C. Farmer, The Infrared Spectra of Minerals, Mineralogical Society, London, 1974.
[63] J.J. Deng, J.T. Polidan, J.R. Hottle, C.E. Farmer-Creely, B.D. Viers, A.R. Esker, Polyhedral oligomeric silsesquioxanes: a new class of amphiphiles at the air/water interface, J. Am. Chem. Soc. 124 (2002) 15194–15195.
[64] M.K. Ferguson-McPherson, E.R. Low, A.R. Esker, J.R. Morris, Corner capping of silsesquioxane cages by chemical warfare agent simulants, Langmuir 21 (2005) 11226–11231.
[65] S. Klein, S. Thorimbert, W.F. Maier, Amorphous microporous titania–silica mixed oxides: preparation, characterization, and catalytic redox properties, J. Catal. 163 (1996) 476–488.
[66] J. Wang, M.K. Kuimova, M. Poliakoff, G.A.D. Briggs, A.N. Khlobystov, Encapsulation and IR probing of cube-shaped octasilasesquioxane H8Si8O12 in carbon nanotubes, Angew. Chem. Int. Ed. 45 (2006) 5188–5191.
[67] F.J. Feher, D.A. Newman, J.F. Walzer, Silsesquioxanes as models for silica surfaces, J. Am. Chem. Soc. 111 (1989) 1741–1748.
[68] F.J. Feher, K.J. Weller, J.J. Schwab, Reactions of hydrosilsesquioxanes and chlorosilsesquioxanes with phosphoranes, Organometallics 14 (1995) 2009–2017.
[69] Y.R. Liu, Y.D. Huang, L. Liu, Thermal stability of POSS/methylsilicone nanocomposites, Compos. Sci. Technol. 67 (2007) 2864–2876.
[70] K. Wu, L. Song, Y. Hu, H. Lu, B.K. Kandola, E. Kandare, Synthesis and characterization of a functional polyhedral oligomeric silsesquioxane and its flame retardancy in epoxy resin, Prog. Org. Coat. 65 (2009) 490–497.
[71] R.A. Mantz, P.F. Jones, K.P. Chaffee, J.D. Lichtenhan, J.W. Gilman, I.M.K. Ismail, M.J. Burmeister, Thermolysis of polyhedral oligomeric silsesquioxane (POSS) macromers and POSS—siloxane copolymers, Chem. Mater. 8 (1996) 1250–1259.
[72] A. Fina, D. Tabuani, F. Carniato, A. Frache, E. Boccaleri, G. Camino, Polyhedral oligomeric silsesquioxanes (POSS) thermal degradation, Thermochim. Acta 440 (2006) 36–42.
[73] I. Sorar, E. Pehlivan, G.A. Niklasson, C.G. Granqvist, Electrochromism of DC magnetron sputtered TiO2 thin films: role of deposition parameters, Sol. Energy Mater. Sol. C 115 (2013) 172–180.

Chapter 6

Foil-Based TiO_2/Gel Electrolyte/$Ni_{1-x}O$ Electrochromic Device Made of Electrochromic Pigment Coatings

In the previous chapter, the interactions and EC behaviour of TiO_2 (mTiA) pigment modified with trisilanol POSS was presented. In this study, the focus was on a comparison of the optical and electrochromic response of three different commercially available TiO_2 pigments, which served for making EC coatings from the pigments. The TiO_2 pigments used were P25 from Degussa (i), nanocrystalline TiO_2 from Infarmat (TiInfr) (ii) and metatitanic acid (mTiA) obtained from Cinkarna Celje (iii). As-prepared pigment dispersions were deposited by spin coating on conductive glass (FTO) and conductive plastic substrate (ITO PET). The deposited TiO_2 pigment coatings were cured at 150 °C for 30 minutes, at which the conductive plastic ITO PET foil is still thermally stable.

Cyclic voltammetric (CV) measurements were performed in a three electrode cell, in which 1 M $LiClO_4$/PC electrolyte was used. The applied potential was between –1.7 V (colouration) and 0 V (bleaching) vs. the Ag/AgCl reference electrode (Figure 6.1).

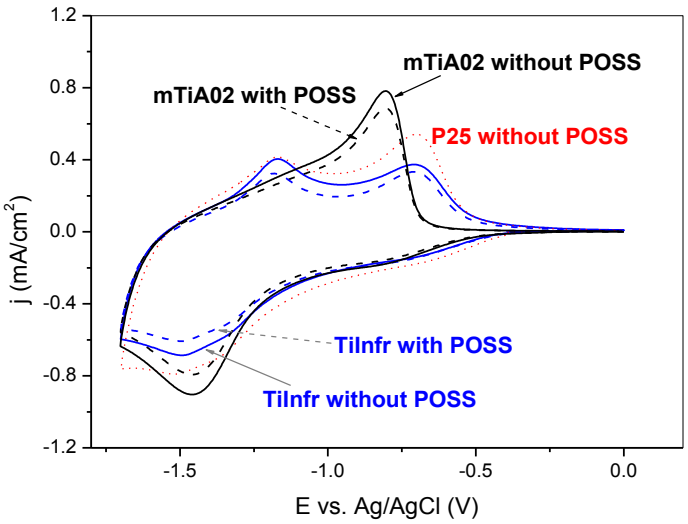


Figure 6.1: Cyclic voltammograms of mTiA, TiInfr (for both: with and without dispersant) and P25 pigment coatings without dispersant.

For the preparation of EC devices with the desired optical modulation of light ($\Delta T = T_{charged} - T_{discharged}$) and neutral colouration, i.e., so-called "neutral-tint devices", TiO_2 cathodically colouring coating was combined with a $Ni_{1-x}O$ anodically colouring coating. The neutral colouration of the EC device means a change of colouration from transparent to brown or grey. This was achieved because the strong absorption of TiO_2 at shorter wavelengths is compensated by the strong absorption of $Ni_{1-x}O$ in the lower wavelengths of the visible spectrum. Such EC devices are rare: TiO_2/NiO, WO_3/NiO, W/Ti oxide/NiO and Nb_2O_5/NiO. In all corresponding systems, the $Ni_{1-x}O$ was crucial for neutral colouration, because its broad absorption compensates the transmission of the anodic EC coatings (TiO_2, Nb_2O_5, and WO_3).

At the end of this study, a flexible EC device consisting of ITO PET/TiO_2 (mTiA)/sol-gel electrolyte/$Ni_{1-x}O$/ITO PET was assembled and its optical and EC properties were presented.

In Figure 6.2A, UV-Vis spectroscopic analysis of flexible EC device is shown and a change of transmission in colouration and bleaching state of 34.3% is demonstrated. The neutral tint colouration of the foil-based EC device was expressed by the colour coordinates in the L*a*b* colour space (Figure 6.2B).The preparation and characterisation of $Ni_{1-x}O$ pigment particles and EC coatings have already been described in our previous work [90].

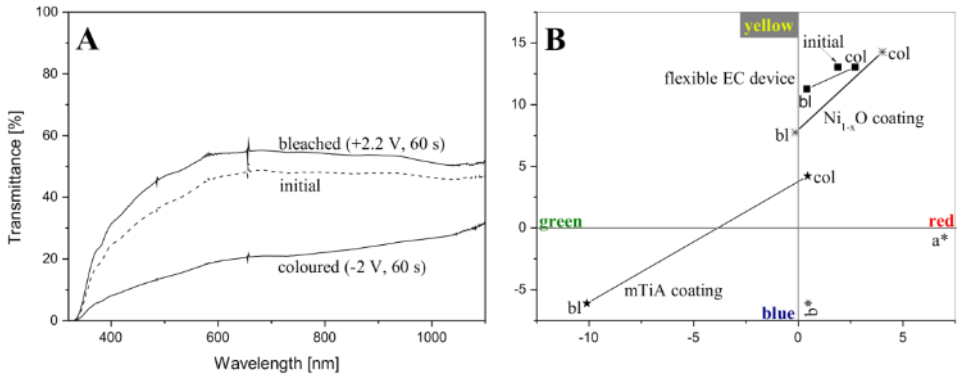


Figure 6.2: UV-Vis spectra of mTiA02/sol-gel electrolyte/$Ni_{1-x}O$ flexible EC device A) and a* and b* colour coordinates for single coatings and EC device B).

A practical result of this work was an award for second best innovation from the Public Agency of the Republic of Slovenia for Entrepreneurship and Foreign Investments (JAPTI), entitled: Preparation of EC coatings on flexible substrates. The National Institute of Chemistry Ljubljana and Amanova d.o.o. also received a special award for the most innovative business model [91].

My contribution consisted of sample and dispersion preparation, most of the measurements and part of the writing.

Acta Chim. Slov. **2014,** *61,* 517–529

Scientific paper

Foil-based TiO_2/gel Electrolyte/$Ni_{1-x}O$ Electrochromic Device Made of Electrochromic Pigment Coatings

Mohor Mihelčič,[1] Angela Šurca Vuk,[1,2] Dejan Vrhovšek,[3] Franc Švegl,[4] Metka Hajzeri[1] and Boris Orel[1,2,*]

[1] *National Institute of Chemistry, Hajdrihova 19, 1000 Ljubljana, Slovenia*

[2] *CO-NOT, Hajdrihova 19, Ljubljana, Slovenia*

[3] *Cinkarna d.d., Kidričeva 26, 3001 Celje, Slovenia*

[4] *Amanova Ltd., Tehnološki Park 18, 1000 Ljubljana, Slovenia*

** Corresponding author: E-mail: boris.orel@ki.si*
Phone: 00386-(0)1-4760-276; Fax: 00386-(0)1-4760-300

Received: 24-12-2013

Dedicated to the memory of Prof. Dr. Marija Kosec.

Abstract

Thin electrochromic coatings were obtained by co-grinding the mTiA particle aggregates (300 nm in size) with open-corner heptaisobutyl trisilanol POSS (T_8 IB_7 $(OH)_3$ POSS) acting as dispersant. After the addition of titanium tetraisopropoxide (3–5%) the mTiA pigment dispersion was deposited on FTO glass and plastic ITO PET foils and coatings were obtained by thermal treatment at 150 °C.

Optical transmittance and luminous haze from 2 to 6% of the coatings were determined from the corresponding UV-Vis spectra. The achieved electrochromic effect was evaluated by electrochemical charging/discharging in 1 M $LiClO_4$/PC electrolyte. Results revealed that the colouring/bleaching changes depended on the extent of grinding and the size of the milling zirconia beads, enabling to distinguish between the surface charging of the mTiA grains and the filling and emptying of the anatase density of states.

mTiA pigment coatings deposited on plastic foil were used in combination with $Ni_{1-x}O$ pigment coatings for construction of foil-based electrochromic device employing novel gel electrolyte with ionic liquid co-solvent.

Keywords: TiO_2, anatase, pigment coatings, electrochromics, flexible electrochromic device, gel electrolyte.

1. Introduction

Glass based electrochromic (EC) devices providing light transmittance modulation have been extensively studied in the past because of their potential for manufacturing "smart" windows for buildings.[1] Recently foil-based EC devices[2–6] attracted attention (Fig. 1), because they can be made from coatings deposited by highly efficient deposition techniques such as wet roll-to-roll (R2R) processing,[7] spray-coating, spin-coating, inkjet printing and vacuum based R2R deposition.[6,8] Among them roll-to-roll technique process having high potential for production of commercial "smart" windows at a price up to 10–50 times lower (~50 \$/m^2 for a whole EC stack[9]) as compared to the standard glass-based EC windows.[9,10] When suitable pigment dispersions (i.e. paints) are available, wet R2R (i.e. coil-coating) application technique enables mass production of many different functional coatings; spectrally selective paint coating based on black spinel pigments for aluminium-based solar absorbers[11–14] are typical solar energy related products. Large and commercially important field of application is inkjet printing enabling the fabrication of coatings used in many electronic devices and systems. Surface tension, rheological properties, stability of pigment dispersions and size of dispersed pigment particles, all of them should be known in details and taken into account in or-

der to deposit functional coatings by any of the mentioned wet deposition techniques.[15]

A simple and robust wet-deposition process similar to that used for paint production has been developed in our laboratory[16–19] and its efficacy has been demonstrated by deposition of electrochromic $Ni_{1-x}O$ coatings from dispersions made of pre-prepared $Ni_{1-x}O$ pigment dispersed with nickel oxyhydroxyde (NiO_xH_y). The appropriateness of $Ni_{1-x}O$ pigment dispersions coil-coating deposition has been demonstrated on coil-coating line in Coatema factory in Germany (www.coatema.de) in the frame of EU project INNOSHADE (www.innoshade.eu). This led us to transfer the knowledge[17,18] to the deposition of optically transparent TiO_2 pigment coatings based on metatitanic acid (anatase) powder (mTiA, for short)[20] on conductive foils.

Therefore, the goal of this study was to provide evidences that wet deposition of mTiA pigment dispersions (i.e. paint) could bring about pigment coatings with low scattering of visible light (i.e. low haze) and showing also strong EC effect. Namely, in our preliminary study,[21] commercial TiO_2 (anatase) pigment manufactured by Cinkarna Factory (SI) with ill-defined structure and composition was used. The metatitanic acid pigment dispersions were made by milling the pigment with the help of open-corner heptaisobutyl POSS-triol (T_8 IB_7 $(OH)_3$ POSS, trisilanol POSS, for short) dispersant, which enabled the deposition of pigment coatings having low haze (up to 6%). Among many commercial titania pigments, mTiA was selected because the EC properties of mTiA pigment coatings have not been reported yet and the material is easily made in a form of bare pigment particles, without any additional surface modifying layer.

We expected to get information about the EC effect inherent to the mTiA pigment coatings, and to compare it with other titania based EC coatings; compacted powders of anatase heat-treated at 750 °C,[22,23] mixed anatase and rutile coarse particle-like coatings made by anodic spark deposition technique reported by Reinhardt et al.,[24] sintered EC titania coatings deposited by doctor blade technique,[25] titania coatings used for reflective EC devices (usually with adsorbed viologens)[26,27] and many studies of titania coatings developed for dye-sensitized photoelectrochemical (DSPEC)[28] and photoelectrochromic (PEC) cells.[29]

It should be noted that TiO_2 pigment coatings for EC applications share certain common problems with those used for PEC and DSPEC devices, also consisting of pigment particles, but strongly differ in others. Good particle-to-particle and particle-to-substrate contacts should be attained already at low processing temperatures (i.e., ITO PET is stable up to T < 150 °C.[4]). Organic polymeric resin binders, which are usually employed for making sintered nanocrystalline TiO_2 photoanodes for PEC and DSPEC and fill the voids between particles therefore hindering the insertion of lithium ions into the particle based EC coatings, must be avoided. Thus, titainum tetraisopropoxide ($Ti(iOPr)_4$) was used as a binder (up to 20%) in order to assure mechanical integrity of the mTiA pigment coatings. $Ti(iOPr)_4$ was perfectly suitable as a binder because it forms compact films already at low temperatures and is compatible with the mTiA pigment. In general terms, mTiA electrochromic pigment coatings are basically sol-gel based coatings made of sol-gel pigment dispersion.

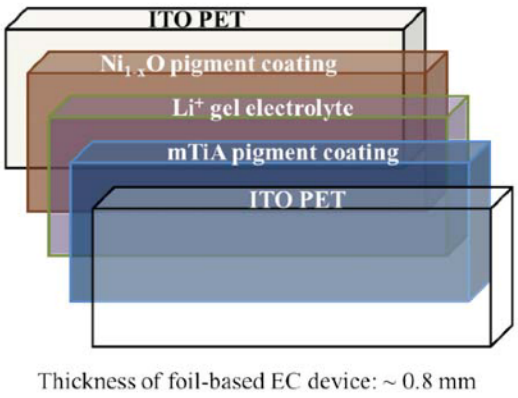


Fig. 1. Schematic presentation of foil-based EC device, consisting of $Ni_{1-x}O$ pigment coating/mTiA02 pigment coating, glued together with Li^+ gel (semi-solid) electrolyte.

Additional arguments substantiating more detailed studies of EC properties of mTiA are of general importance, originating from the fact that TiO_2 is not very popular EC material and during the last four decades nanoparticles of TiO_2 and thin films attracted only a sporadic interest in research devoted to electrochromism.[1] TiO_2 has been recognized as cathodically colouring material, which darkens under double insertion of ions and electrons, even though some studies have shown that TiO_2 can act also as non-colouring (i.e. optically passive) coating (for example, CeO_2/TiO_2 sol-gel films).[30–32] Thin TiO_2 film have been made with various techniques: evaporation,[33] sputtering and also with wet-deposition techniques such as anodization,[37] chemical bath deposition (CBT) technique[38] and sol-gel technique.[39,40] The latter techniques usually require heat-treatment of colloidal solutions at temperatures from 350–450 °C in order that anatase particles form *in-situ*. This means that wet deposition of coatings from pigment dispersions represent the most suitable approach for making pigment coatings for foil-based EC devices.

Electrochromic properties of titania coatings as reviewed by Sorar at al.[41] strongly depend on the preparation technique, which substantiated the assessment of EC properties also for the mTiA pigment coatings deposited from paints. For example, sputtered films show coloration efficiency η from 5 up to 37 cm^2/C,[35–36] while early works on sol-gel deposited films even claim TiO_2 films as grey colouring films.[42] Ozer et al.[43,44] were the first to demon-

strate that large η values could be achieved also with sol-gel technique. Gillet et al.[45] and Ivanova and Harizanova[46] have later shown that the η values for a dense sintered TiO_2 films dropped significantly, while samples comprising TiO_2 nanoparticles exhibit much higher η values. The large effective surface area of TiO_2 particles,[47] expected also to be present in pigment coatings reported in this study, provides a concomitant large number of adsorption sites for intercalation of ions, while the high surface-to-volume ratio ensures minimal diffusion path-lengths. This agrees with results reported by Nang Dinh et al.[25] who have shown that sintered TiO_2 particles deposited on FTO glass by doctor blade technique and consisting of porous and interconnected particles significantly increased ion storage capacity (~60 mC/cm^2 for 600 nm thick coatings), colouring/bleaching changes and stability of the EC effect (85% fading after 500 cycles), but decrease the speed of transmittance variations (few seconds).

It is clear that due to the controlled milling, the mTiA pigment coatings represent well-defined particle system, which was suitable for obtaining correlation between the effect of the size of the particle aggregates formed and the intercalation of lithium ions and concurrent EC effect. The haze of TiO_2 pigment coatings on FTO glass in initial state was determined in the range from 2 to 6%, depending on the coating thickness. On the basis of cyclic voltammograms and *in-situ* UV-Vis spectroelectrochemical measurements the coloration efficiency was assessed, while the onset of colouring and bleaching changes as a function of applied potential, shed light on the role of the pigment particle surface on the insertion/extraction reactions.

In the last part of this study, we demonstrated the EC effect of the mTiA pigment coatings by making EC device, which was constructed in combination with $Ni_{1-x}O$ pigmented coating[17,18] (Fig. 1). As stated by Granqvist et al.,[48] the use of gel or solid state electrolytes is important from many practical reasons, one of the most important ones is to present leakage. Herein, instead of PVC membrane based lithium electrolyte[21] we used an sol-gel electrolyte made of long-chain poly(ethyleneoxide) (M_w ~ 400, $(PEO)_n$ (n = 12)) terminated on both ends by trialkoxysilane groups linked via the uretano groups (urethanosil) to the PEO_{12} chains.[49,50] Lithium bis(trifluoromethanesulfonyl)imide (LiTFSI) served as a source for lithium ions. Haze, considered as one of the most relevant parameters of the pigment coatings, was determined also for EC device and correlated to the haze values shown by the individual pigment coatings.

2. Experimental

2. 1. Materials and Preparation of Coatings

Metatitanic acid powder (mTiA)). mTiA powder was prepared by the so-called "sulfate route"[20] and is currently used for its industrial manufacturing in the Cinkarna d.d. factory (www.cinkarna.si). In brief, white precipitate mTiA is obtained after dissolution of ilmenite in concentrated suphuric acid (98%, Cinkarna Celje), hydrolyzed in the presence of anatase seeds. The anatase seeds were prepared separately by hydrolyzing a titanyl sulphate solution at 80 °C and are added into dissolved ilmenite solution. By the variation of the amount of the solution (from 0.1–1.8%) different mTiA types are easily produced differing in the size of anatase powder.

From the XRD analysis of the mTiA powder milled in the presence of trisilanol POSS (Fig. 2) it was conceived that the pigment consisted of mixed rutile (~15%) and anatase phase.[20] The mTiA crystallites were composed of nanoparticles, which size was estimated from the various (hkl) peaks (A(101), A(004), A(200) and A(105)) to about 5–7 nm. They formed larger aggregates (up to 20–50 nm in size). Expectedly, the presence of trisilanol POSS was not observed. Such structure of the mTiA pigment aggregates was also obtained from TEM measurements (not shown here).

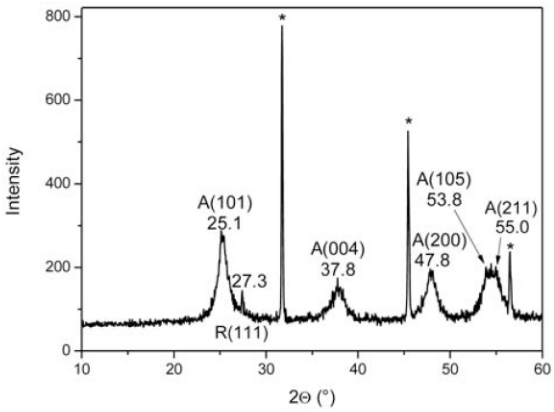


Fig. 2. XRD of trisilanol POSS/mTiA powder milled with zirconia beads (0.2 mm) with indicated (hkl) peaks and the corresponding 2Θ values. A corresponds to anatase and R to rutile phase; reflections of Al holder are indicated by *.

mTiA agglomerates (size up to few μm) consist of aggregates, the size of which is from 30–50 nm. The aggregates are formed of nanocrystallites (5–8 nm in size), determined from the XRD analysis of the mTiA powder (Fig. 2), strongly linked together via the crystalline bridges. In order to obtain dispersed aggregates of mTiA powder a small amount of barium chloride was added to the mTiA agglomerates.[20] Since barium has high affinity towards sulphate ions, the added barium salt drew together sulphate ions, which were removed from the mTiA by centrifugation, freeing agglomerates and forming separated aggregates. Before the as-prepared mTiA aggregates were used for making pigment dispersions, mTiA pigment

was thoroughly washed with distilled water and then dried at 100 °C. As-prepared dry mTiA powder aggregates were used for preparation of pigment dispersions.

Beside mTiA pigment, also commercial nanocrystalline TiO_2 obtained from Inframat (TiInfr, for short) and P25 anatase pigment (Degussa, DE) were used for making the pigment dispersions and pigment coatings deposition.

Preparation of pigment dispersion. 10 wt.% of as-prepared mTiA and TiInfr powders were first dispersed in n-butanol (Sigma-Aldrich) in the presence of trisilanol POSS dispersant (10 wt.% vs. powder), while P25 pigment dispersion was prepared by milling of the raw pigment in butanol without addition of any dispersant. The synthesis of trisilanol POSS was reported previously,[12,13] but could be obtained also commercially [www.hybrid plastics.com]. mTiA was milled with zirconia beads with dimensions of 0.4, 0.2 and 0.1 mm providing pigment dispersions mTiA04, mTiA02 and mTiA01, respectively. Since the mTiA02 coatings exhibited the smallest particle size, surface roughness and haze (Table 1), the TiInfr and P 25 pigments were milled only with the zirconia beads with diameter size of 0.2 mm. In order to improve the adhesion of the coatings onto the substrates, at the end of the milling process, $Ti(iOPr)_4$ was added together with glacial acetic acid ($AcOH_{gl}$), the latter enabling its hydrolysis and long-term stability.[39] As shown by dynamic light scattering (DLS), the mTiA particles in mTiA pigment dispersions have average particle size of about 50 nm (Fig. 3).

Deposition of pigment coatings. Coatings were deposited on FTO glass (Pilkington, 14 Ω/) and conductive polymeric substrate (Solaronix, ITO PET 175 μm thickness; 60 Ω/□) by spin-coating techniques. By repeating the number of spinning deposition cycles (one cycle: spinning frequency = 1000 RPM, t = 40 s) thickness of the deposited TiO_2 coatings was varied from 100 nm (1x spinning) up to 400 nm (4x spinning) (Table 1). Also dip-coating deposition technique was used giving reproducible results in terms of coating thickness, morphology and pigment particle distribution. As regards our experiences with the deposition of $Ni_{1-x}O$,[17,18] and sol-gel spectrally selective paint coatings,[11] the corresponding TiO_2 dispersions were suitable also for continuous deposition via the coil-coating technique.

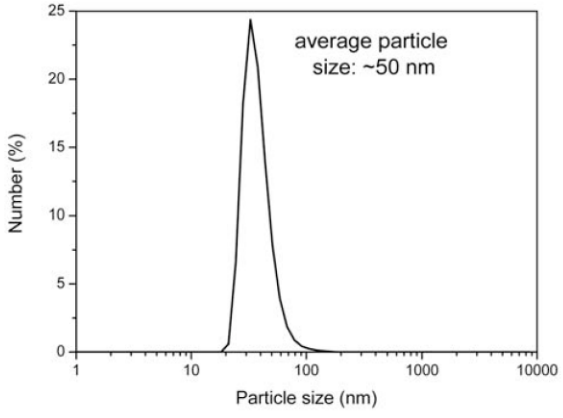


Fig. 3. Average particle size of particle aggregates in mTiA dispersion obtained from the DLS measurements was ~50 nm.

Table 1. Titania mTiA pigment coatings on FTO glass and ITO PET foil made from mTiA dispersions prepared with and without trisilanol-POSS dispersant and dispersions prepared from TiInfr and P25 TiO_2 powders. The size of milling beads was 0.1, 0.2 and 0.4 mm and the coatings were deposited various times (1 x, 2 x or 3 x).

TiO_2 coatings on FTO glass	**Haze (%)**	**TT (%)**	**DT (%)**
FTO glass	0.39	83.47	0.66
P25-02-1x[a]	5.11	80.92	4.59
TiInfr02-1x-P[b]	2.65	82.68	2.71
TiInfr02-02-1x	2.82	80.10	2.72
mTiA02-1x	2.76	83.52	2.83
mTiA02-2x	4.68	82.29	4.35
mTiA02-3x	5.93	81.40	5.30
mTiA01-1x-P	5.17	81.43	5.05
mTiA02-1x-P	1.68	83.36	5.01
mTiA04-1x-P	4.95	83.40	4.46
TiO_2 coatings on ITO PET plastic foil	**Haze (%)**	**TT (%)**	**DT (%)**
ITO PET	1.09	79.11	1.26
P25 - 2x	14.51	81.68	12.35
TiInfr02- 2x	12.80	81.69	10.99
TiInfr02-2x-P	14.26	81.22	12.19
mTiA02-2x	15.42	81.57	13.18
mTiA02-2x-P	16.83	82.96	14.57

[a,b] – Numbers 01, 02 and 04 in the names refers to the size of milling beads, letter P at the end of the name refers to the trisilanol POSS. 1x, 2x and 3x indicates the number of deposited layers.

Preparation of lithium conducting sol-gel electrolyte. An organic-inorganic hybrid on the basis of PEO chains and ethoxysilyl groups, classified as bis-end capped urethanosil (urethane -NH-C(=O)-O- bond instead of urea one), i.e. bis N-triethoxysilyl propylcarbamatoil PEO 400 (PEOCS)[49] was prepared by a reaction of 3-isocyanatopropyl-triethoxysilane with an equimolar amount of polyethylene glycol 400 (PEO 400) in tetrahydrofuran (THF). The reaction mixture was stirred together under reflux for 10 h. The THF was evaporated and the final product PEOCS was obtained. Glacial acetic acid ($AcOH_{gl}$) was chosen as the catalyst for the initiation of sol-gel processes, which inevitably leads to polycondensation of a bis end-capped alkoxysilane PEOCS precursor through a non-hydrolytic solvolysis route, liberating ester molecu-

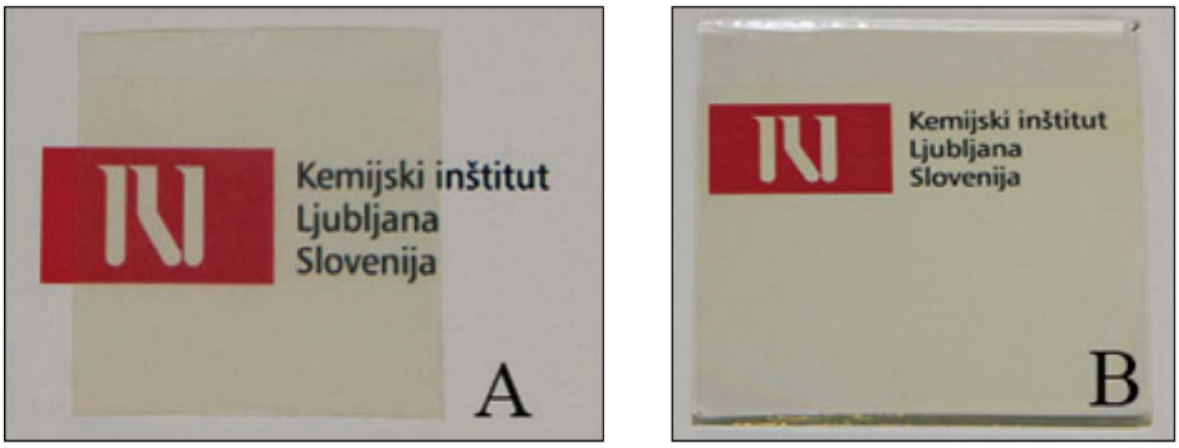


Fig. 4. mTiA02 pigment coatings obtained by 1x spin coating and thickness of about 150 nm deposited on ITO PET foil (A) and FTO glass (B) (for description see Table 1).

les.[51] In order to increase ionic conductivity, 3-methyl-1-(2,5,8,11,14,17,20,23,26,29,32-undecaoxypentatriacontan-35il)-1H imidazolium mesylate ($[PEO_{12}MeIm^+][OMs^-]$) ionic liquid was added in the sol-gel PEOCS network as co-solvent in molar ratio 1: 8 (PEOCS : ionic liquid). Addition of co-solvents has already been successfully suggested for electrolytes for lithium ion batteries.[52] The PEOCS hybrid and co-solvent were fully compatible and no segregation of phases was noted. The final electrolytes were obtained after dissolution of LiTFSI salt acting as a source of lithium ions.

Preparation of foil-based EC device. The EC device was made from mTiA02 and $Ni_{1-x}O$ pigment coatings combined with PEOCS/($[PEO_{12}MeIm^+][OMs^-]$)/LiTFSI/$AcOH_{gl}$ electrolyte. The electrolyte was spread on one of the electrodes (i.e. $Ni_{1-x}O$[17,18]) waited few minutes to dry and pressed together with another electrode (i.e. mTiA) until the electrolyte harden to a solid and transparent layer (~20 μm) gluing both halves of the EC device together. The performance of the foil-based EC device was evaluated by *in-situ* UV-Vis spectroelectrochemical measurements. The results showed moderate conductivity of electrolytes (approximately 10^{-4} S/cm) but the electrochemical window was quite large. The electrolytes exhibited excellent gluing properties. No sealing the flexible EC device was used.

2. 2. Instrumental

UV-Vis spectra of the pigment coatings on FTO glass and ITO PET foils were measured by a Perkin Elmer Lambda 900 UV-Vis spectrophotometer equipped with an integrating sphere. The optical quality of the coatings was estimated by determining transmission haze numbers (H in %), defined as the ratio of diffuse to total transmittance (DT/TT %) in the spectral range 380–780 nm following the ASTM test method D1003 as described previously.[17]

UV-Vis spectroelectrochemical properties of the coatings were characterized *in-situ* during potentiodynamic (cyclic voltammetry (CV) and chronocoulommetry (CC)) measurements on an Autolab PGSTAT 302N potentiostat-galvanostat. The coatings were examined in a 1 M $LiClO_4$/propylene carbonate (PC) electrolyte in a standard three electrode configuration consisting of the nanocrystalline TiO_2 coating on FTO glass (working electrode), a modified Ag/AgCl reference electrode and a platinum rod (counter electrode). The home-made spectroelectrochemical cell was mounted in an HP 8453A diode array spectrophotometer and the optical modulation of the coatings in the spectral range of 300 to 1100 nm recorded. CVs were measured between 0 and –1.7 V with a scan rate of 20 mV/s. CCs were used for coloration of coatings at –1.7 V (60 s) and bleaching at 0 V (60 s).

The specific conductivity of the sol-gel based electrolyte was measured on an Autolab PGSTAT 302N potentiostat-galvanostat with a FRA module in a Teflon cell between two Pt electrodes. The frequency range used for electrochemical impedance spectroscopy (EIS) was 10^5 to 0.01 Hz. The conductivity (σ in S/cm) was calculated according to the equation $\sigma = d/RA$, where R is the measured resistance obtained from the impedance plots, d the thickness and A the area of the sample between the Pt electrodes, respectively.

X-ray diffraction (XRD) analyses of surface modified mTiA powders were done by means of a Siemens 5000D X-ray powder diffractometer equipped with graphite monochromatized Cu-Kα radiation (λ = 1.54178 Å). The scan speed was 10°/min, with a scan step of 0.02° of 2Θ.

3. Results and Discussion

3. 1. Properties of Coatings

Properties of coatings are given in Table 1, providing information about total visible transmittance (TT in %), total diffuse transmittance (DT in %) and the corresponding haze values (in %). Spectral total transmittance (TT (λ)) of pigment coatings and their haze changed with the coatings' thickness; thicker coatings prepared by repetitive spin-coating deposition (1x, 3x, 5x) showed decreasing transmittance values (Table 1), but scattering did not change much, which could be conceived from Fig. 5B, showing the values of haze (up to 6.0%) as a function of the milling conditions. The thickness varied also with regard to the applied milling beads, namely, mTiA01, mTiA02 and mTiA04 pigment coatings (all 1x-P (with trisilanol POSS)) were about 70, 150 and 260 nm thick, respectively. Expectedly, pigment coatings made of dispersions milled with the largest beads (0.4 mm) scattered more in the range of shorter wavelengths (Fig. 6) compared to the (TT in%) values of the coatings, which were made from dispersions milled with 0.1 mm beads. Haze was found to be the smallest for the coatings milled with 0.2 mm beads, which could be correlated with the coating surface roughness ($R_s = 9.2 \pm 2.0$ nm),[21] which agreed also with surface topography of these pigment coatings showing homogeneously distributed particles. The size of the particles obtained was of about ~50 nm, which was also obtained from dynamic light scattering (DLS) (Fig. 3).

Inspection of results listed in Table 1 also revealed the influence of POSS dispersant on other titania coatings. Surprisingly, dispersant did not have pronounced effect on the haze of the TiInfr02 made with dispersant (TiInfr02-1x-P: 2.65%) and without it (TiInfr02-1x: 2.82%). P25 coating showed surprisingly high haze (5.11%), but the reasons for its high haze were not investigated further.

Haze values of the pigment coatings, which were deposited on ITO PET foils, drastically exceeded those determined for the same coatings on FTO glass (Table 1). We attributed this to the higher haze of ITO PET foil itself and also to the difference of the surface energy values of the foil and FTO glass, leading to different wetting and concurrently higher thickness of deposited coatings on foils compared to glass.

To conclude, mTiA pigment coatings did not show haze as low as noted for bare FTO glass and ITO PET substrates, but the clear sight through the coatings was not significantly hampered. The main part of scattering arose at shorter wavelengths, but was decreased significantly when the coatings were assembled in EC device (see below). Coatings exhibited interferences, which indicated that their properties closely resembled optical coatings.

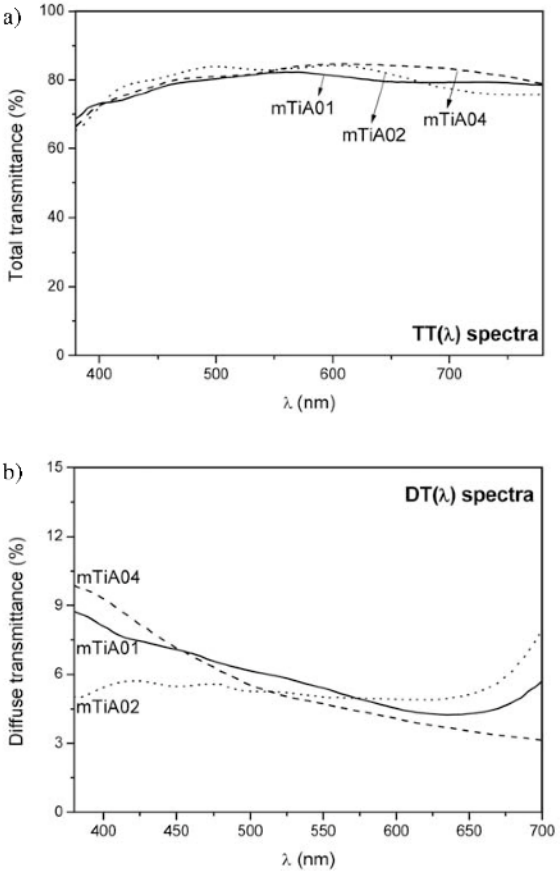


Fig. 5. Total (TT(λ)) (A) and diffuse (DT(λ)) (B) transmission spectra of mTiA01, mTiA02 and mTiA04 pigment coatings deposited on FTO glass and measured in air prepared under the same spin-coating conditions (all 1x-P (with trisilanol POSS)) (for description see Table 1).

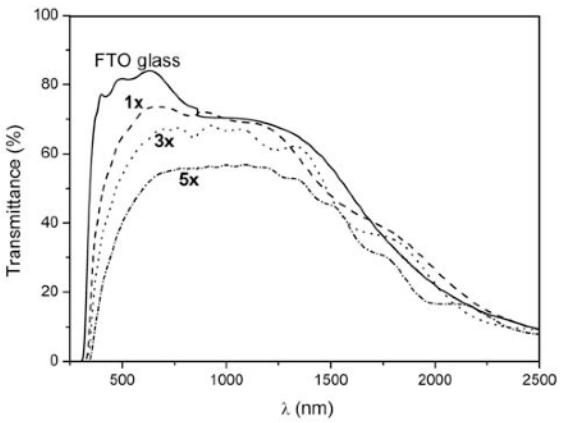


Fig. 6. Total transmittance (TT(λ)) spectra of mTiA pigment coatings prepared from trisilanol POSS/mTiA04 pigment dispersion milled with 0. 4 mm large zirconia beads deposited 1x, 3x and 5x by spin-coatings (for description see Table 1).

3. 2. Electrochemical Properties

3. 2. 1. Chronocoulometry (CC) and *in-situ* UV-Vis Spectroelectrochemical Measurement

Chronocoulometric (CC) and cyclic voltammetric (CV) measurements were carried out by immersing the mTiA pigment coatings (working electrode) in combination with a platinum counter electrode in a 1 M $LiClO_4$/PC electrolyte with an application of potential between 0 V and –1.7 V vs. Ag/AgCl reference electrode. The aim of the CV measurements was to determine the ability of the coatings to reversibly intercalate and deintercalate lithium ions, while the corresponding ion storage capacity (in mC/cm^2) was defined as the lithium ions inserted per unit active area of the coating using CC technique.

The CC measurements of the mTiA pigment coatings obtained by milling the pigment with different beads' size and with trisilanol POSS dispersant (all 1x-P in Fig. 7) revealed, that the ion storage capacity was higher for the mTiA04 than for other two pigment coatings (Fig. 7A). However, for all coatings, intercalation was higher than extraction (Fig. 7A), reaching for the mTiA04 coatings –32.1/+24.6 mC/cm^2. The corresponding ion storage capacity was higher than those of sol-gel amorphous or crystalline films by at least 2–3 times,[53] but still smaller compared to the heat-treated slip-casted coatings i.e., ~60 mC/cm.[25] Expectedly, colouring/bleaching changes increased with the coating thickness as a consequence of using different size of the milling beads, reaching up to ΔT 50% (λ = 800 nm) (Fig. 7B). Coloration efficiency (η in cm^2/C) varied accordingly, being the highest at larger wavelengths (Fig. 7B). Pigment coatings having different thicknesses, exhibited the same wavelength dependent η values suggesting that the insertion/extraction reactions proceeded throughout the whole coating thickness. Coloration efficiencies of pigment coatings were not exceptional for titania thin films and coatings as already reviewed by Sorar et al.[41]

EC effect was determined also for the pigment coatings, which were deposited on ITO PET substrate. The

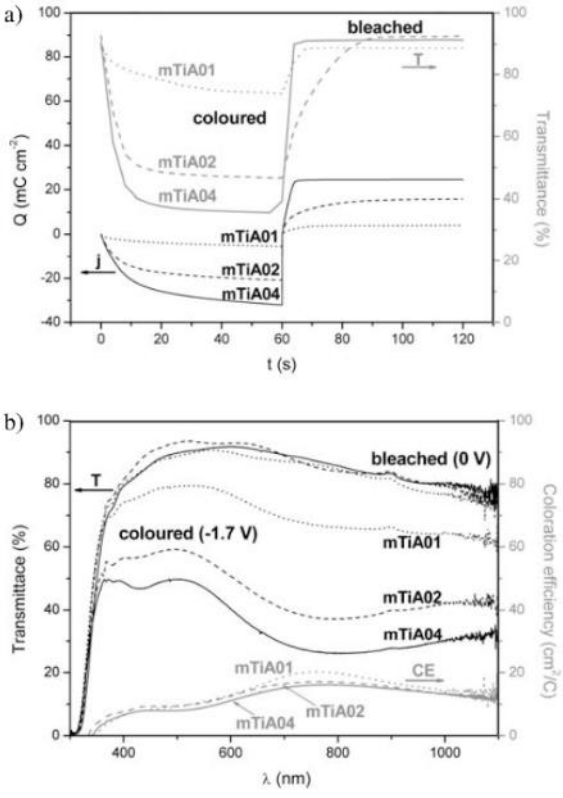


Fig. 7. *In-situ* UV-Vis spectroelectrochemical changes of mTiA01, mTiA02 and mTiA04 pigment coatings deposited by single spin-coating deposition on FTO glass, during CC colouring at –1.7 V (60 s) and bleaching at 0 V (60 s): A) CC curves and monochromatic transmittance changes at λ = 634 nm and B) UV-Vis spectra of coloured/bleached coatings with coloration efficiency as a function of wavelength (for description see Table 1).

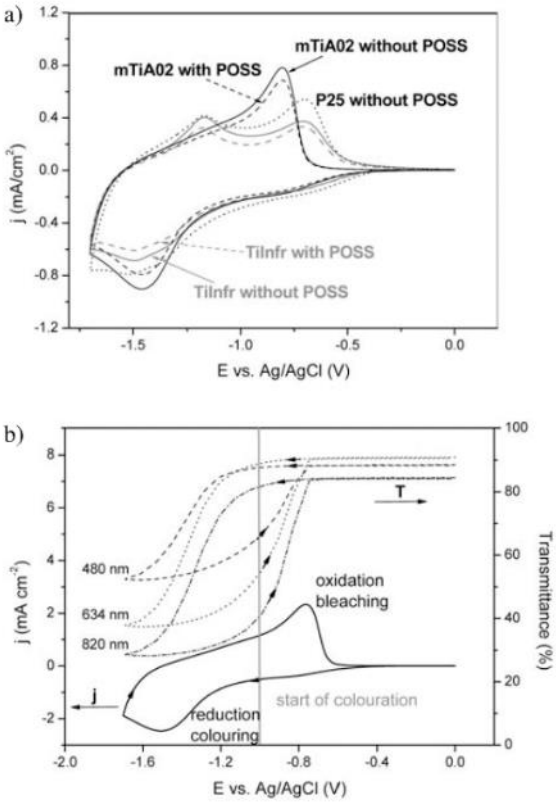


Fig. 8. *In-situ* UV-Vis spectroelectrochemical changes of mTiA02-2x-P pigment coating (see Table 1) deposited by two spinning cycles on ITO PET foil during CC colouring at –1.7 V (60 s) and bleaching at 0 V (60 s): A) CC curves and B) transmittance change during CC measurement.

mTiA02 pigment coatings were selected (Fig. 8) showing Q_{ins} ~ –47 mC/cm^2 and Q_{ext} ~ 38 mC/cm^2, inferring somewhat larger ion charging reversibility as noted for the same coatings deposited on FTO glass. EC effect was quite high reaching 70% at λ = 634 nm and dropped to 65% at λ = 480 nm, while the coloration efficiency was at the same wavelengths of about 10.7 cm^2/C, i.e. comparable to the values obtained for coatings deposited on FTO glass. Consequently, the haze of the pigment coatings on ITO PET was relatively high (16.83%), which was explained by different spreading of the pigment dispersion on both substrates. Pigment coatings did not show high speeds of colouring and bleaching, which was estimated to be ~1 min.

3. 2. 2. Cycling Voltammetry and *in-situ* Spectroelectrochemical Measurements

CVs provide information about potentials, at which oxidation and reduction reactions take place, enabling the distinction between the interacting sites of lithium ions and electrons as a function of materials' properties, i.e. size of crystallites, surface functionalization, porosity of coatings and their morphologies. In addition, from the variations of the current density of peaks obtained at various scan rates, information about the diffusion processes of intercalation species in the coatings can be obtained. The Randles-Sevčik equation is employed when the current peaks are proportional to the square root of the scan rate, but in the case that the current peaks show a linear dependence on the scan rate, the reactions are not diffusion-limited but rather surface reactions occur. This approach has been employed for confirmation of the surface charging of the $Ni_{1-x}O$ aggregates in the corresponding pigment coatings also prepared as "electrochromic paints".[17,18]

Effect of trisilanol POSS dispersant on CVs of the mTiA, TiInfr and P 25 pigment coatings, prepared with and without trisilanol POSS dispersant is shown in Fig. 9A. Inspections of the corresponding CVs revealed that dispersant did not have pronounced effect on the current densities of mTiA and TiInfr pigment coatings, but only slightly diminished the corresponding current density values. This was expected because trisilanol POSS interacted with the surface of the pigment aggregates screening the interacting sites and decreasing the extent of the insertion/extraction reactions.

The most apparent difference was observed in the shape of the CVs, which were quite different for the mTiA and TiInfr pigment coatings, the latter being nearly identical to the CV of the P25 pigment coatings, both also similar to the CV of the anodic spark-deposited pigment coatings.[24]. In the contrary, CVs of the TiInfr and P25 coatings resembled CVs of titania heat-treated thin films, deposited from colloidal solutions,[22,23,48,54–57]

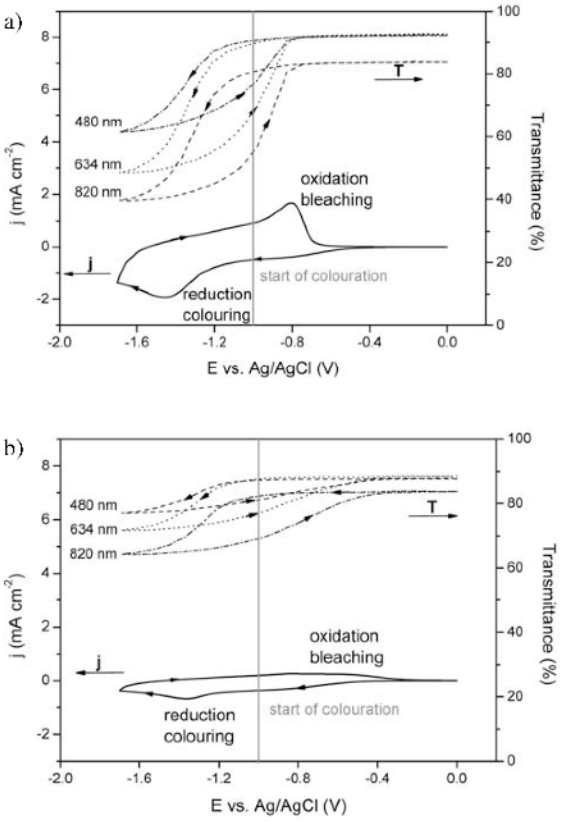


Fig. 9. A) Cyclic voltammograms of mTiA, TiInfr (for both: with and without dispersant) and P25 pigment coatings. *In-situ* UV-Vis spectroelectrochemical changes of the mTiA coatings: B) mTiA04, C) mTiA02 and D) mTiA01 (all 1x-P) (for description see Table 1). Start of colouration is indicated by grey vertical lines (see Figs. 9B-D).

heat-treated slip casted pigment coatings[25] and even titania thin films deposited with layer-by-layer deposition technique.[58]

The onset of colouring as function of applied potential was obtained from the *in-situ* UV-Vis spectroelectrochemical measurements, presented together with the CVs of the corresponding pigment coatings in Figs. 9B-D. Inspection of results revealed that CVs of the mTiA04, mTiA02 and mTiA01 pigment coatings were not the same, indicating the change of the interaction sites due to the size of the aggregates formed due to the different milling procedure. As expected, mTiA01 coatings (Fig. 9D) showed blurred peaks in the CVs, contrasting well-defined current density peaks in the CVs of the mTiA02 and mTiA04 pigment coatings (Fig. 9B, C). In this regards, the CVs of the mTiA01 coatings resembled CVs of the titania thin films prepared from the sol-gel precursor and heat-treated at 300 °C having also ill-defined crystallinity.[53] The same thin sol-gel films heat-treated at 560 °C have exhibited additional cathodic current peak at –0.86 V

vs. Ag/AgCl observed also as a weak and broad peak in CVs of the mTiA01 pigment coating (Fig. 8D). The corresponding cathodic peak has been attributed by Verma and Agnihotry,[53] to the presence of additional sites stemming from the crystallinity of the sintered sol-gel coatings. By analogy with the sol-gel sintered TiO_2 (anatase) thin films, the weak peak observed at –0.83 to –0.94 V was also attributed to the mTiA crystalline aggregates present in the pigment coatings (Fig. 8D).

In order to explain observed similarities between the mTiA01 and sol-gel amorphous and crystalline thin films[53], the mTiA02 pigment dispersion was milled 1 h more and the corresponding CVs were recorded (Fig. 10A). Comparison of CVs depicted in Fig. 9D and Fig. 10A showed, that the anodic peak at –0.83 to –0.94 V, which was seen in the CV of the mTiA01 coating (Fig. 9D) became observable also at ~0.94 V in the CV of the mTiA02 obtained by longer milling (Fig. 10A), mainly

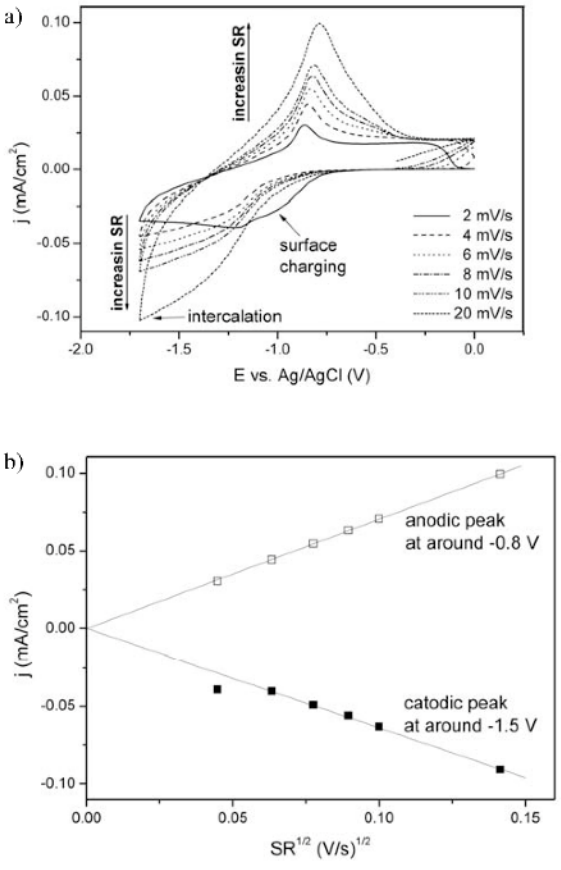


Fig. 10. Cyclic voltammograms of the mTiA02 coating made with 0.2 mm zirconia beads (longer time of milling, 2 h) and with trisilanol POSS dispersant at different scan rates: A) CVs, B) peak current densities vs. square root of scan rates. Current peaks (A) revealing surface charging (–0.83 to –0.94 V) and the start of the intercalation reactions (–1.5 V) are also indicated.

with low scan rates. Both described CVs showed smeared anodic current response between –0.6 V and –0.3 V (Fig. 9D, 10A).

Cathodic current peak at –0.83 to –0.94 V, observed also by Verma and Agnihotry,[53] for the crystalline sol-gel EC anatase films, we attributed to the electrochemical activity of the surface of mTiA aggregates. The corresponding cathodic peak was difficult to fit with sufficient reliability because its intensity was low and further lowered with increased scan rates, i.e. it vanished already at scan rates higher than 6 mV/s. On the contrary, cathodic peak at –1.5 V and its counterpart in a reverse scan at –0.8 V showed quite good linear dependence vs. square root of scan rates (Fig. 10B) albeit at low scan rates the deviation from the linearity was noticed. Fast vanishing of the cathodic current peak at –0.83 to –0.94 V strongly suggested the existence of some electrochemically active surface sites, contrasting start of coloration for the main cathodic current peak at ~1.5 V, which is in agreement with other reports.[22,23,25,48,55–59]

To conclude, according to expectations, the insertion/extraction of electrons and lithium ions represented the main mechanism of electrochromic effect of mTiA pigment coatings,[1] but their CV response reflected that the degree of the pigment aggregates was achieved for dispersions by variation of the milling procedures. Pigment coatings also showed quick saturation of specific sites of the crystalline aggregates, but the unquestionable confirmation of the statement that they were attributed to the low lying electron states, which are electrochromically deaf[24,59] was not obtained. EC effect also depended on the extent of milling indirectly through the coating thickness, being higher for coatings milled with larger zirconia beads.

3. 3. Flexible EC Device

Flexible EC device was assembled from mTiA02 and $Ni_{1-x}O$[17,18] pigment coatings deposited on ITO PET foils and produced as "electrochromic paint". $Ni_{1-x}O$ pigment coating was 500–600 nm thick and its haze was 10.8%, while the corresponding TT and DT values were 52.9 and 6.1%, respectively, and the inserted and extracted charge (Q_a/Q_c) was +15.2/–13.1 mC/cm^2. The coloration efficiency of the $Ni_{1-x}O$ pigmented coating was 54.6 cm^2/C (λ = 480 nm). Other details about the $Ni_{1-x}O$ pigmented coatings can be obtained from ref.[17,18] Since $Ni_{1-x}O$ is anodic material and mTiA cathodic one, in EC device they coloured simultaneously at negative and bleached at positive potentials, contributing to the enhanced electrochromic effect (Fig. 11). When charge capacities and coloration efficiencies match, the foil based EC device provides neutral colouring shown below.

The EC device was assembled by application of PEOCS/LiTFSI/$PEO_{12}MeIm^+OMs^-$/$AcOH_{gl}$ electrolyte, having the conductivity of 2×10^{-4} S/cm. Electrochemical

and optical response of the EC device was obtained when potential was swept from +2.2 to –2 V as shown in Fig. 11A. The variation of transmittance at λ = 634 nm with the chronocoulometric application of –2 V for colouring and 2.2 V for bleaching is shown in Fig. 11B, while the corresponding spectral response of EC foil-based device is depicted in Fig. 11C.

Inspection of results revealed, that the EC device showed the properties of both EC coatings, which we inferred from the presence of current peaks of mTiA02 at cathodic and $Ni_{1-x}O$ at anodic potentials (Fig. 11A). Moreover, the transmittance of device in its initial state was lower compared to the transmittance obtained when device was bleached. This we attributed to the substoichiometric $Ni_{1-x}O$ pigmented coating, which was not completely transparent in its initial state because of the presence of Ni^{+2}/Ni^{+3} redox couple.[17,18] Differences in the CVs attributed to the $Ni_{1-x}O$ at positive and mTiA02 at negative potentials indicated that the EC device was not perfectly balanced, which we attributed to the differences in the coating's thickness being 600 nm for $Ni_{1-x}O$ and 150 nm for mTiA pigment coatings affecting the inserted/extracted charges. EC device also showed fast bleaching (10–20 s) but the speed of colouring was rather small. It seemed that even after 1 min of charging the maximal colouring was not yet achieved (Fig. 11B).

Spectral response of transmitted light is important practical issue regarding construction of EC device with neutral-tint coloration. Coloration of foil-based EC device was expressed with the colour coordinates in L*a*b* colour space (Fig. 11D, Table 2).

It is evident that the blue coloration (negative b* values) of mTiA pigmented coating was overwhelmed with the brown coloration of $Ni_{1-x}O$ pigmented coating (positi-

Table 2. Lightness L* of the constructed foil-based EC device.

pigmented coating / EC device	L^*_{col}	L^*_{bl}
$Ni_{1-x}O$ on ITO PET	61.5	92.6
mTiA02 on ITO PET	61.7	96.2
flexible EC device	47.8	76.3

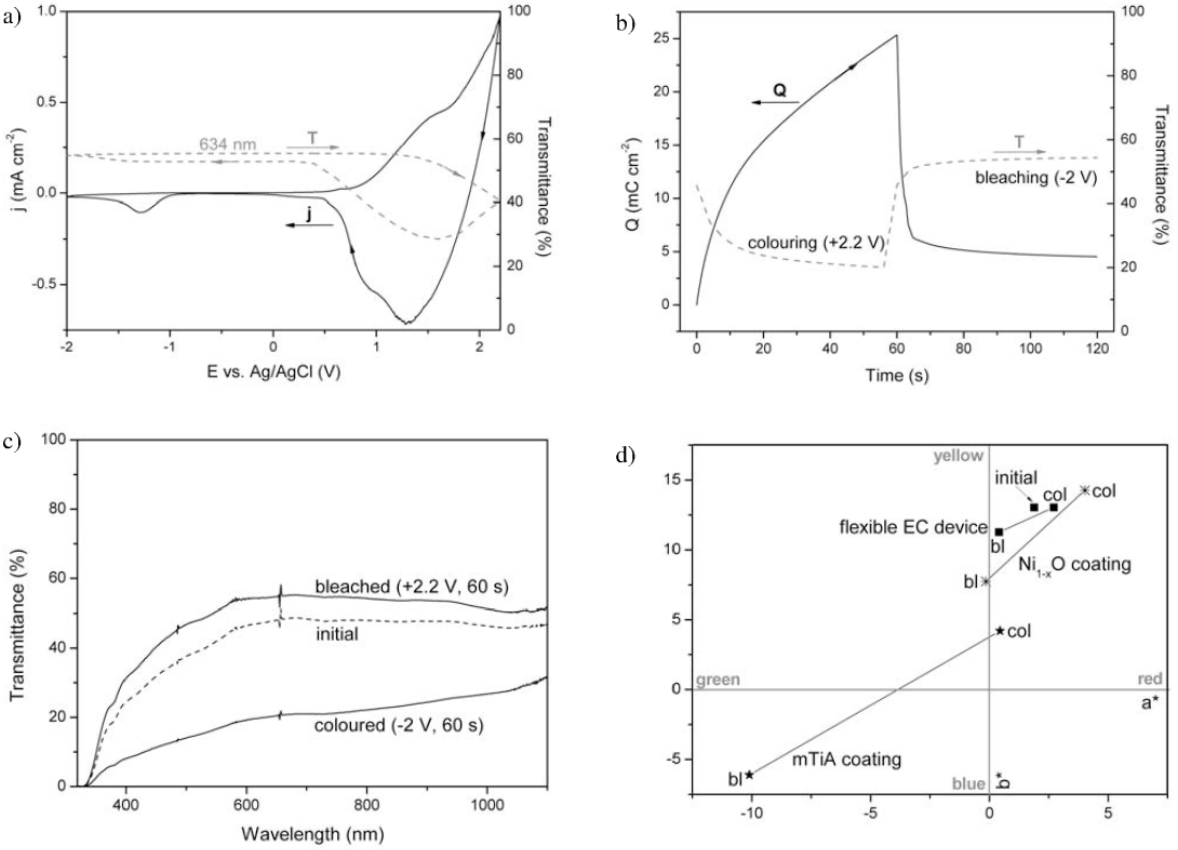


Fig. 11. *In-situ* UV-Vis spectroelectrochemical measurements of mTiA02/sol-gel electrolyte/$Ni_{1-x}O$ flexible EC device: A) CV curve with monochromatic transmittance response at 634 nm, B) CC curve with transmittance response at 634 nm, C) UV-Vis spectra and D) a* and b* colour coordinates.

ve a*, b* values). The EC device in bleached (a* = 0.4, b* = 11.3) and coloured (a* = 2.7, b* = 13.0) state revealed positive a* and b* values, the increase in a* during colouring of device indicating the tendency towards brown coloration. The initial colour of the foil-based EC device was closer to the a*,b* values of the device in coloured state, since the substoichiometric $Ni_{1-x}O$ was initially brownish as a consequence of the presence of Ni^{3+} ions.[17,18] Lightness L* increased from 47.8 (coloured) to 76.3 for the bleached state due to its higher transmittance. Contrary to mTiA/sol-gel electrolyte/$Ni_{1-x}O$ device the already reported flexible EC device with the same electrolyte and PEDOT and V-oxide electrodes[50] showed optical modulation from dark blue area (a* = 1.1, b* = –29.3) to the brighter blue area (a* = 8.8, b* = 7.4) due to the high thickness of blue-colouring PEDOT (800 nm). It seemed that by using inorganic EC materials, neutral-tint EC device is easier to be made compared to the EC device with mixed organic (PEDOT) and inorganic $Ni_{1-x}O$ EC coatings.

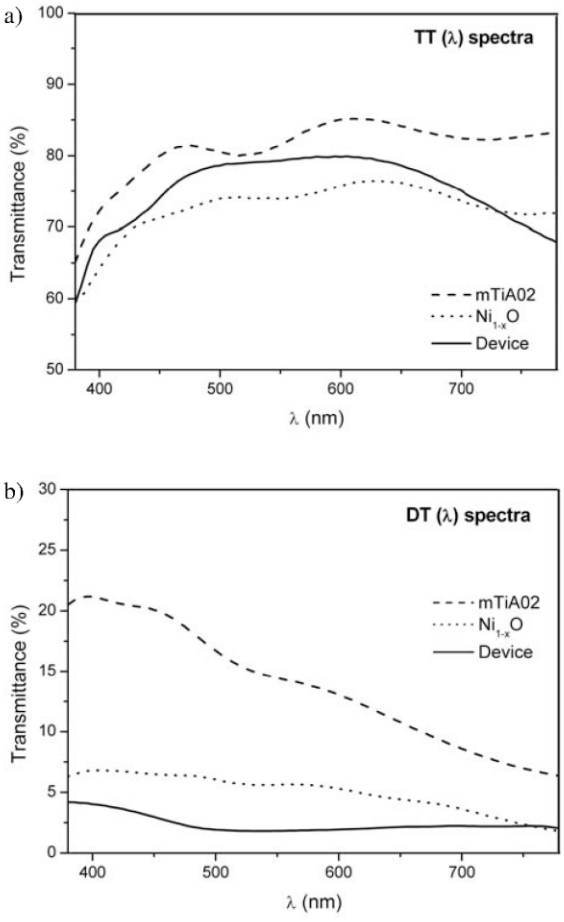


Fig. 12. Total (TT(λ)) (A) and diffuse (DT(λ)) (B) transmission spectra of mTiA02 and $Ni_{1-x}O$ pigment coatings and, mTiA02/sol-gel electrolyte/$Ni_{1-x}O$ flexible EC device.

Inspection of haze values revealed that even though the haze of the individual components was 10.8% ($Ni_{1-x}O$) and 16.8% (mTiA02), the haze value of the complete flexible EC device was just 6.3% (Fig. 12). This indicated positive effect of the semi-solid (or gel) electrolyte whose refractive index was much higher than air, which compensated the surface roughness of both EC pigmented coatings. Obviously, the electrolyte perfectly wetted the electrodes by entering within the surface pores of the coatings.

4. Conclusions

The main advantage of depositing electrochromic pigment coatings from pigment dispersions, i.e. "electrochromic paints", lies in the fact, that EC pigment coatings can be deposited at temperatures, which were compatible with temperature stability of plastic foils (~150 °C).

In addition, using this procedure, many different inorganic electrochromics,[1] which are otherwise difficult to be deposited in the form of thin films at low temperatures, can be used. Thus, the described procedure started from the synthesis of electrochromic pigment, which was in the next stage milled with zirconia beads of different size in the butanol/trisilanol POSS mixture, until the particle aggregates reached the size of 30–50 nm. A small amount of added $Ti(iOPr)_4$ served as binder, which contributed to the mechanical integrity of the pigment coatings.

Results confirmed our expectations that the optical quality of the coatings, i.e. haze, depended on the duration of milling and the size of the zirconia beads. The process allowed the deposition of coatings with about 5% of haze and electrochromic transmittance changes of up to 60%. Coil-coating (R2R) deposition technique on ITO PET foils is preferred.

Trisilanol POSS dispersant, which served for dispersing mTiA pigment in solvent, did not hamper electrochromic efficiency indicating sufficient porosity of the trisilanol POSS layer to allow the transfer of lithium ions across the dispersant layer.

The EC effect of cathodic mTiA electrochromic material is a multifaceted problem, which was affected by many variables: the chemical composition of pre-prepared EC pigment, its preparation route, the coatings' porosity and surface structure. It was shown, that the cyclic voltammetry peaks of mTiA coatings prepared from pigment dispersions milled with different zirconia beads and milling times can differ to some extent. The observed EC effect of the mTiA pigment coatings depended on the extent of milling; larger zirconia beads provided thicker coatings and correspondingly stronger colouring/bleaching changes. However, coloration efficiency remained equal for all three grades of mTiA pigment coatings, from which we inferred, that all three pigment coatings exhibited similar access for lithium ions throughout their physical thickness.

All mTiA pigment coatings showed electrochemical activation period. After few initial potential cycles, weak cathodic peak at –0.83 to –0.94 V disappeared, which we tentatively ascribed to the interactions with the electrochemically active surface sites. As expected, these sites did not bring about EC effect, which started at potential region where the strongest CV peak at –1.3 to –1.6 V was observed. mTiA pigment coatings behave as typical cathodic electrochromic material.

CVs response of TiInrf and P25 pigment coatings differed as regards the CVs of mTiA coatings, which was attributed to the presence of additional electrochemical sites.

Foil-based EC devices showed reversible and persistent EC effect (up to 200 cycles). As expected, haze of the EC devices was lower compared to the haze of the individual pigment coatings, which we attributed to the effect of the electrolyte, filling surface defects and surface roughness of the mTiA and $Ni_{1-x}O$ pigment coating electrodes.

5. Highlights

- Electrochromic pigment coatings were deposited from nanodispersions of anatase
- Trisilanol POSS was used as dispersant for anatase pigment dispersions
- Low temperature TiO_2 pigment coatings on conducting polymeric substrates
- Flexible EC device was constructed from TiO_2 and $Ni_{1-x}O$ pigment coatings

6. Acknowledgements

The research leading to these results has received funding from the European Community's Seventh Framework Programme (FP7) under Grant agreement no. 200431 (INNOSHADE), from CO-NOT, Centre of Excellence for Low-Carbon Technologies and Programme P1-0030 (Slovenian Research Agency). Acknowledgement to Dr. Marija Čolović for synthesis of electrolyte precursors and Doc. dr. Ivan Jerman for help in preparation of pigment dispersions.

7. References

1. C. G. Granqvist, Handbook of inorganic electrochromic materials, Elsevier, Amsterdam, **1995**, pp. 633.
2. C. G. Granqvist, *Sol. Energy Mater. Sol. Cells* **2008**, *92*, 203–208.
3. R. Baetens, B. P. Jelle, A. Gustavsen, *Sol. Energy Mater. Sol. Cells* **2010**, *94*, 87–105.
4. M. C. Choi, Y. Kim, C. S. Ha, *Prog. Polym. Sci.* **2008**, *33*, 581–630.
5. C. G. Granqvist, A. Azens, P. Heszier, L. B. Kish, L. Osterlund, *Sol. Energy Mater. Sol. Cells* **2007**, *91*, 355–365.
6. E. J. Widjaja, G. Delporte, F. Vandevelde, B. Vanterwyngen, *Sol. Energy Mater. Sol. Cells* **2008**, *92*, 97–100.
7. Skip Scriven, L.E., in: M. A. Galan, E. M. del Valle (Eds.), Chemical Engineering, John Wiley & Sons, Ltd., **2005**, Ch. 9, pp. 229–266.
8. C. Brigouleix, P. Topart, E. Bruneton, F. Sybary, G. Nouhant, G. Campet, *Electrochim. Acta* **2001**, *46*, 1931–1936.
9. C. M. Lampert, *Sol. Energy Mater. Sol. Cells* **2003**, *76*, 489–499.
10. C. M. Lampert, *Displays* **2004**, *25*, 165–165.
11. I. Jerman, M. Mihelčič, M. Koželj, B. Orel, Sol-gel based spectrally selective solar absorber coatings and the process for producing said coatings, WO patent number 2013158049 A1, date of patent October 24, **2013**.
12. I. Jerman, M. Koželj, B. Orel, *Sol. Energy Mater. Sol. Cells* **2010**, *94*, 232–245.
13. I. Jerman, M. Mihelčič, D. Verhovšek, J. Kovač, B. Orel, *Sol. Energy Mater. Sol. Cells* **2011**, *95*, 423–431.
14. R. Kunič, M. Mihelčič, B. Orel, L. Slemenik Perše, B. Bizjak, J. Kovač, S. Brunold, *Sol. Energy Mater. Sol. Cells* **2011**, *95*, 2965–2975.
15. K. Vojisavljević, B. Malič, M. Senna, S. Drnovšek, M. Kosec, *J. Eur. Ceram. Soc.* **2013**, *33*, 3231–3241.
16. F. Švegl, A. Šurca Vuk, M. Hajzeri, L. Slemenik Perše, B. Orel, *Sol. Energy Mater. Sol. Cells* **2012**, *99*, 14–25.
17. M. Mihelčič, I. Jerman, F. Švegl, A. Šurca Vuk, L. Slemenik Perše, J. Kovač, B. Orel, U. Posset, *Sol. Energy Mater. Sol. Cells* **2012**, *107*, 175–187.
18. M. Mihelčič, A. Šurca Vuk, I. Jerman, B. Orel, F. Švegl, H. Moulki, C. Faure, G. Campet, A. Rougier, *Sol. Energy Mater. Sol. Cells* **2014**, *120*, 116–130.
19. H. Moulki, C. Faure, M. Mihelčič, A. Šurca Vuk, F. Švegl, B. Orel, G. Campet, M. Alfredsson, A. V. Chadwick, D. Gianolio, A. Rougier, *Thin Solid Films* **2014**, *553*, 63–66.
20. D. Verhovšek, N. Veronovski, U. Lavrenčič Štangar, M. Kete, K. Žagar, M. Čeh, *Int. J. Photoenergy* **2012**, ID 329796, 10 pages.
21. M. Mihelčič, I. Jerman, B. Orel, *Prog. Org. Coat.* **2013**, *76*, 1752–1755.
22. T. Ohzuku, T. Hirai, *Electrochim. Acta* **1982**, *27*, 1263–1266.
23. T. Ohzuku, T. Kodama, T. Hirai, *J. Power Sources* **1985**, *14*, 153–166.
24. D. Reinhardt, S. Krieck, S. Meyer, *Electrochim. Acta* **2006**, *52*, 825–830.
25. N. Nang Dinh, N. M. Quyen, D. N. Chung, M. Yikova, V. V. Truong, *Sol. Energy Mater. Sol. Cells* **2011**, *95*, 618–623.
26. R. Cinnsealach, R. Boschloo, S. N. Rao, D. Fitzmaurice, *Sol. Energy Mater. Sol. Cells* **1998**, *55*, 215–223.
27. U. Bach, D. Corr, D. Lupo, F. Pichot, M. Ryan, *Adv. Mater.* **2002**, *14*, 845–848.
28. A. Hagfeldt, G. Boschloo, L. Sun, L. Kloo, H. Pettersson, *Chem. Rev.* **2010**, *110*, 6595–6663.
29. G. Leftheriotis, G. Syrrokostas, P. Yianoulis, *Sol. Energy Mater. Sol. Cells* **2010**, *94*, 2304–2313.

30. Baudry, P., A. C. M. Rodriguez, M. A. Aegerter, L. O. Bulhoes, J. Non-Cryst. Solids **1990**, *121*, 319–322.
31. U. Lavrenčič Štanger, B. Orel, I. Grabec Švegl, B. Ogorevc, K. Kalcher, *Sol. Energy Mater. Sol. Cells* **1993**, *31*, 171–185.
32. U. Lavrenčič Štanger, B. Orel, I. Grabec Švegl, B. Ogorevc, Acta Chim. Slov. **1994**, *41*, 39–64.
33. T. Seike, J. Nagai, *Sol. Energy Mater.* **1991**, *22*, 107–117.
34. S. F. Cogan, E. J. Anderson, T. D. Plante, R. D. Rauh, Materials and Devices In Electrochromic Window Development, in: Proceedings of SPIE – The International Society for Optical Engineering **1985**, *562*, 23–31.
35. M. Kitao, Y. Oshima, K. Urabe, *Jap. J. Appl. Phys.* **1997**, *36*, 4423–4426.
36. A. Gutarra, A. Azens, B. Stjerna, C. G. Granqvist, *Appl. Phys. Lett.* **1994**, *64*, 1604–1606.
37. K. Lee, D. Kim, S. Berger, R. Kirchgeorg, P. Schmuki, *J. Mater. Chem.* **2012**, *22*, 9821–9825.
38. T. J. Richardon, M. D. Rubin, *Electrochim. Acta* **2001**, *46*, 2119–2123.
39. S. Doeuff, C. Sanchez, *Comptes Rendus del'Academie des Sciences, Série 2*, **1989**, *309*, 531–534.
40. T. Ivanova, A. Harizanova, T. Koutzarova, N. Krins, B. Vertruyen, *Mater. Sci. Engin. B* **2009**, *165*, 212–216.
41. I. Sorar, E. Pehlivan, G. A. Niklasson, C. G. Granqvist, *Sol. Energy Mater. Sol. Cells* **2013**, *115*, 172–180.
42. J. Livage, D. Ganguli, *Sol. Energy Mater. Sol. Cells* **2001**, *68*, 365–381.
43. Ozer, N., *Thin Solid Films* **1992**, *214*, 17–24.
44. N. Ozer, F. Tepehan, N. Bozkurt, *Thin Solid Films* **1992**, *219*, 193–198.
45. P. A. Gillet, J. L. Fourquet, O. Bohnke, *Mater. Res. Bull.* **1992**, *27*, 1145–1152.
46. T. Ivanova, A. Harizanova, *Mater. Res. Bull.* **2005**, *40*, 411–419.
47. R. van de Krol, A. Goossens, J. Schoonman, *J. Phys. Chem. B* **1999**, *103*, 7151–7159.
48. I. B. Pehlivan, R. Marsal, E. Pehlivan, E. L. Runnerstrom, D. J. Milliron, C. G. Granqvist, G. A. Niklasson, *Sol. Energy Mater. Sol. Cells*, http://dx.doi.org/10.1016/j.solmat.2013.06.010.
49. V. de Zea Bermudez, L Alcácer, J. L Acosta, E Moraleset, *Solid State Ionics* **1999**, *116*, 197–209.
50. M. Hajzeri, A. Šurca Vuk, L. Slemenik Perše, M. Čolović, B. Herbig, U. Posset, M. Kržmanc, B. Orel, *Sol. Energy Mater. Sol. Cells* **2012**, *99*, 62–72.
51. B. Orel, R. Ješe, A. Vilčnik, U. Lavrenčič Štangar, *J. Sol-Gel Sci. Technol.* **2005**, *34*, 251–265.
52. Y. Matsuo, K. Fumita, T. Fukutsaka, Y. Sugie, H. Koyama, K. Inoue, *J. Power Sources* **2003**, *119–121*, 373–377.
53. A. Verma, S. A. Agnihotry, *Electrochim. Acta* **2007**, *52*, 2701–2709.
54. F. Cao, G. Oskam, P. C. Searson, J. M. Stipkala, T. A. Heimer, F. Farzad, G. J. Meyer, *J. Phys. Chem.* **1995**, *99*, 11974–11980.
55. M. Ottaviani, S. Panero, S. Morzilli, B. Scrosati, M. Lazzari, *Solid State Ionics* **1986**, *20*, 197–202.
56. G. Boschloo, D. Fitzmaurice, *J. Phys. Chem. B* **1999**, *103*, 7860–7868.
57. A. Hagfeldt, N. Vlachopoulos, M. Grätzel, *J. Electrochem. Soc.* **1994**, *141*, L82–L84.
58. T. Facci, F. Huguenin, *Langmuir* **2010**, *26*, 4489–4496.
59. M. Koelsch, S. Cassaignon, C. Ta Thank Minh, J.-F. Guillemoles, J.-P. Jolivet, *Thin Solid Films* **2004**, *451*, 86–92.

Povzetek

Tanke elektrokromne plasti smo naredili s sočasnim mletjem delcev mTiA agregatov (300 nm) s heptaizobutil trisilanol POSS (T_8 IB_7 $(OH)_3$ POSS), ki je deloval kot disperzant in dodatkom titanovega tetraizopropoksida (3–5 %) ter pigmentno disperzijo nanesli na FTO steklo in polimerne ITO PET folije in jih nato termično obdelali pri 150 °C.
Optično prepustnost in motnost prevlek smo določili na osnovi UV-Vis spektrov. Motnost prevlek na FTO steklu je znašala od 2 do 6 %, odvisno od debeline plasti. Elektrokromni učinek prevlek smo ocenili z elektrokemijsko interkalacijo/deinterkalacijo v 1 M LiClO4/PC elektrolitu. Rezultati so pokazali, da je optična modulacija odvisna od dolžine mletja in velikosti cirkonij-oksidnih kroglic, omogočili pa so tudi razlikovanje med površinskim nabijanjem mTiA delcev ter polnjenjem/praznenjem anataznih delcev.
mTiA pigmentne prevleke, ki smo jih nanesli na polimerne folije, smo uporabili v kombinaciji z $Ni_{1-x}O$ pigmentnimi prevlekami za izdelavo fleksibilnega elektrokromnega sklopa z novim gelskim elektrolitom in ionsko tekočino kot sotopilom.

Chapter 7

Comparison of the Electrochromic Properties of $Ni_{1-x}O$ in Lithium and Lithium-Free Aprotic Electrolytes: From $Ni_{1-x}O$ Pigment Coatings to Flexible Electrochromic Devices

The most important part of my Ph.D. thesis focused on a fundamental study of the EC effect of $Ni_{1-x}O$. The main aim was to establish the role of the surface charging of $Ni_{1-x}O$ in the EC anodic electrochromic effect, facilitated by the fact that the coating was porous and permeable for various ions but compact enough to allow transport of electrons. This was achieved by fabricating $Ni_{1-x}O$ pigment coatings using a similar approach as described in previous articles [90].

The first question that arose was to find an appropriate dispersant for $Ni_{1-x}O$ pigment particles, which should then be suitable for the deposition of an optically transparent EC coating. Trisilanol POSS dispersant, which has been extensively used for making spectrally selective coatings, was discarded since we aimed to deposit the $Ni_{1-x}O$ pigment coatings from water dispersions. One option was to use no dispersant and merely mill the $Ni_{1-x}O$ pigment in water, in line with the preparation of Prussian blue pigment dispersions [92]. Prussian blue pigment coatings are made by precipitation of iron(III) hexacyanoferrate(II) precursors, meaning that the as-prepared Prussian blue pigment particles in the corresponding dispersions are embedded in the corresponding precipitate, which prevents further aggregation of Prussian blue particles in water dispersions.

By analogy with the preparation of Prussian blue pigment particle dispersions, nickel oxyhydroxide (NiO_xH_y) was used for grinding $Ni_{1-x}O$ pigment particles. This decision was made mainly because NiO_xH_y itself exhibits an electrochromic effect, also being practically amorphous and, as such, used as a precursor for making electrochromic $Ni_{1-x}O$ coatings. Thus-prepared electrochromic $Ni_{1-x}O/NiO_xH_y$ coatings show a high electrochromic effect, and stabilization can be achieved by curing at 150 °C, which means that the dispersion is suitable for the deposition of coatings on conductive glass (FTO) and also flexible (ITO PET) substrate. For comparison, we prepared coatings without NiO_xH_y dispersant ($Ni_{1-x}O/H_2O$) thermally treated at 150 and 500 °C for half an hour.

Among the most significant findings was the fact that, because of the surface modification of the $Ni_{1-x}O$ pigment particle with the NiO_xH_y precursor, there is an

increase in the transport of lithium ions and the EC effect of $Ni_{1-x}O$ thin films prepared by this procedure was thus increased accordingly. A more substantial finding is that there is no need for lithium ions for the EC effect to become intercalated within the $Ni_{1-x}O$ particles. This was in agreement with the crystalline structure of $Ni_{1-x}O$ (cubic NaCl-type), which does not allow the insertion of lithium ions in the compact NaCl lattice. This assumption was confirmed by the use of different ionic liquid based electrolytes (in our study 0.1 M TBA^+ triflate/PC electrolyte was used), which consist of large ions that far surpass the dimensions of intercalation sites in the NaCl structure. The EC effect is basically driven by surface charging of the $Ni_{1-x}O$ particle; the charges established on the surface of the $Ni_{1-x}O$ pigment grains provided potential, which was sufficiently strong to move the electrons in the $Ni_{1-x}O$ electronic structure by partially emptying the valence band causing the colouring, while bleaching took place when the polarity was reversed. The driving force for the EC effect was the semi-conductivity of the $Ni_{1-x}O$, which enables electron transport also inside the $Ni_{1-x}O$ grains (Figure 7.1 and 7.2).

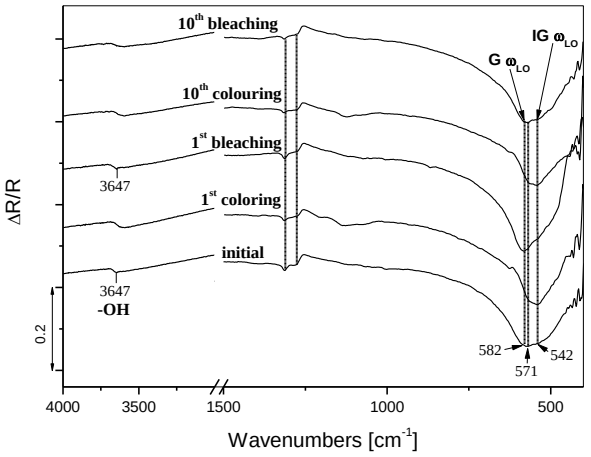


Figure 7.1: *Ex situ* IR RA spectroelectrochemical measurements of $Ni_{1-x}O/NiO_xH_y$ pigment coating (3x, 150 °C, 0.4 mm beads) in 1 M $LiClO_4$/PC electrolyte.

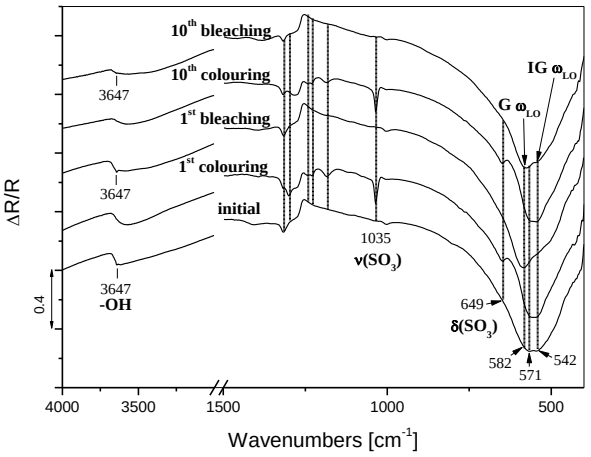


Figure 7.2: *Ex situ* IR RA spectroelectrochemical measurements of $Ni_{1-x}O/NiO_xH_y$ pigment coating (3x, 150 °C, 0.4 mm beads) in 0.1 M TBA^+ triflate/PC electrolyte.

Two items of supporting evidence should be mentioned: infrared spectroelectrochemical measurements proved that the $Ni_{1-x}O$ structure changed only at the $Ni_{1-x}O$ surface and that the $Ni_{1-x}O$ also charged/discharged in electrolytes that do not contain any lithium ions. The latter proof was achieved through collaborative work with the Laboratory of Bordeaux (CNRS, Universe Bordeaux, ICMCB). The observed effect opens up the potential use of pigment $Ni_{1-x}O$ dispersions for hybrid electrochromic systems, in which one of the electrochromic layers is an organic polymer (PEDOT). The electrolyte used can be an ionic liquid in liquid or semi-solid form [93].

As mentioned before, $Ni_{1-x}O/NiO_xH_y$ pigment coatings can also work in a lithium-free electrolyte, so different combinations of plastic based EC coatings were prepared (Figure 7.3). $Ni_{1-x}O/NiO_xH_y$ coatings were used as anode, and either self-standing PEDOT or WO_3 as cathodic coating. Either lithium-containing (LiTFSI-BMITFSI in PMMA) or lithium-free (BMITFSI in PMMA) electrolyte was used between the coatings.

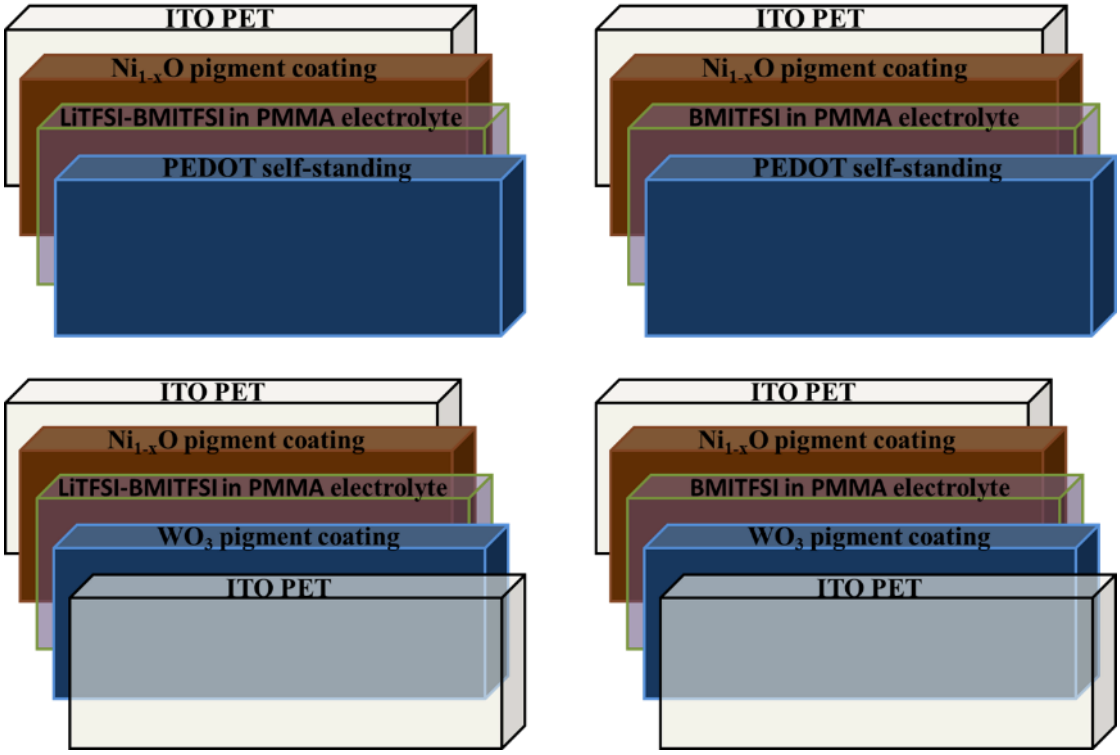


Figure 7.3: Schematic presentation of four different plastic based EC device compositions.

My contribution consisted of sample and dispersion preparation, most of the measurements and part of the writing.

Solar Energy Materials & Solar Cells 120 (2014) 116–130

Contents lists available at ScienceDirect

Solar Energy Materials & Solar Cells

journal homepage: www.elsevier.com/locate/solmat

Comparison of electrochromic properties of $Ni_{1-x}O$ in lithium and lithium-free aprotic electrolytes: From $Ni_{1-x}O$ pigment coatings to flexible electrochromic devices

Mohor Mihelčič [a], Angela Šurca Vuk [a], Ivan Jerman [a], Boris Orel [a,*], Franci Švegl [b], Hakim Moulki [c], Cyril Faure [c], Guy Campet [c], Aline Rougier [c,**]

[a] National Institute of Chemistry, Hajdrihova 19, SI-1000 Ljubljana, Slovenia
[b] Amanova Ltd., Tehnološki Park 18, SI-1000 Ljubljana, Slovenia
[c] CNRS, Université de Bordeaux, ICMCB, 87 avenue du Dr. A. Schweitzer, Pessac F-33608, France

ARTICLE INFO

Article history:
Received 12 February 2013
Received in revised form
4 July 2013
Accepted 21 August 2013
Available online 25 September 2013

Keywords:
Nickel oxide
ex situ IR spectroscopy
Pigment coatings
Surface reactions
Cycling in lithium-free aprotic electrolytes
Electrochromic device

ABSTRACT

Electrochromic nickel oxide ($Ni_{1-x}O$) pigment powder which was made from nickel acetate reacting with H_2O_2/urea solution followed by heat treatment of xerogels at 400 °C (24 h) was milled with zirconia beads in pure water or water with added nickel oxyhydroxy precipitate acting simultaneously as the dispersant and the coating binder. The corresponding pigment particle suspensions were spin coated on FTO glass and flexible ITO-PET foils, respectively, and cured at 150 °C. The optical properties of the deposited pigment coatings on FTO glass substrates were determined with an UV VIS spectrometer, providing total direct transmittance (TT), total diffuse transmittance (DT) and haze (in %). Haze increased with the coating thickness but did not exceed 4%. SEM micrographs of the deposited pigment coatings revealed that they consisted of agglomerated $Ni_{1-x}O$ pigment with voids.

Potential cycling of $Ni_{1-x}O$ pigment coatings and $Ni_{1-x}O$ thin films was performed in 1 M $LiClO_4$/PC and 0.1 M TBA^+ triflate/PC electrolytes, revealing that the pigment coatings exhibited electrochemical and electrochromic activity also in lithium free (aprotic) electrolyte, while variations of the oxidation and reduction reaction peaks at various scan rates confirmed the presence of surface electrochemical reactions. The near-grazing incidence angle reflection–absorption spectroscopic technique (IR RA) was employed for identifying surface and inner-grain Ni–O stretching modes, the former being responsible for observed electrochemical properties, which was also demonstrated from the *ex situ* IR RA measurements performed for coatings charged/discharged in 1 M $LiClO_4$/PC and 0.1 M TBA^+ triflate/PC electrolytes. The results disclosed in this study suggest that the electrochromic effect was not in direct correlation with the de-insertion/insertion of small ions into the NiO (bunsenite) grains but rather the pigment coatings behave similarly to nickel oxide electrochemical capacitors. The electrochromic response of a flexible EC devices made either of PEDOT (self-standing foil) or WO_3 and $Ni_{1-x}O$ pigment coatings glued with PMMA based electrolytes without and with lithium salt were recorded for the demonstration of the possible practical application of wet deposited $Ni_{1-x}O$ pigment coatings made as "electrochromic" paints.

© 2013 Elsevier B.V. All rights reserved.

1. Introduction

Nickel oxide (NiO) is a well-known electrochromic (EC) material [1], which shows optical transmittance modulation during electrochemical oxidation and reduction. NiO is a cheap and widely accessible EC anodic material, which, in the form of $Ni(OH)_2$, exhibits coloring on proton extraction; this makes it practically important as a counter electrode in EC devices, for example in combination with WO_3, using a hydrated Ta_2O_5 electrolyte [2]. The importance of anodic EC materials, such as colloidal prussian blue [3,4] and NiO, is expected to grow in the future due to the development of foil-based EC devices based on cathodic polymeric EC films such as poly(3,4-ethylene-dioxythiophene) (PEDOT) [5]. Polymeric EC materials are relatively easy to deposit via the wet (coil coating and roll-to-roll) deposition technique, providing cheap and mass production of foil-based EC devices.

The preparation of wet deposited $Ni_{1-x}O$ anodic EC pigment coatings based on pre-prepared $Ni_{1-x}O$ pigment particles has

* Corresponding author. Tel.: +386 1 4760 276; fax: +386 1 4760 300.
** Corresponding author. Tel.: +33 540006263; fax: +33 540002761.
E-mail addresses: boris.orel@ki.si (B. Orel), rougier@icmcb-bordeaux.cnrs.fr (A. Rougier).

0927-0248/$ - see front matter © 2013 Elsevier B.V. All rights reserved.
http://dx.doi.org/10.1016/j.solmat.2013.08.025

recently been reported [6]. The corresponding $Ni_{1-x}O$ pigment was synthesized via the sol–gel peroxo route [7] using a H_2O_2/urea mixture reacting with nickel(II) acetate salt, followed by heat treatment (400 °C, 24 h) of as-prepared xerogels. After milling the $Ni_{1-x}O$ pigment particles with zirconia beads, the corresponding pigment dispersions were used for coating deposition, consisting of $Ni_{1-x}O$ agglomerates (~80 nm) embedded within nickel oxyhydroxy precipitates (NiO_xH_y for short) acting simultaneously as both the dispersant and the coating binder. The $Ni_{1-x}O$ pigment coatings exhibit low haze (up to 7%) and were deposited on conductive foils via the coil coating deposition technique (Coatema, DE; www.coatema.de), enabling the construction of foil-based EC devices with nearly neutral tint coloration.

The same sol that was used for making $Ni_{1-x}O$ pigment powders was also used for the deposition of thin sol–gel $Ni_{1-x}O$ films [7]. The dark brown color of the films and their low electrical resistance (resistivity ~ 0.43 Ωcm) indicated that $Ni_{1-x}O$ is a p-type semiconductor with the cationic vacancies associated with the formation of Ni^{3+} [8] later also proven by XPS measurements [6]. The extra holes (e^+), which transfer from one Ni^{3+} to a neighboring Ni^{2+}, provide both optical absorption and conductivity. The corresponding electronic transitions are strongly coupled to the vibrational modes of the $Ni_{1-x}O$ clusters, which we decided to investigate with the help of the infrared reflection absorption (IR RA) technique performed on charged/discharged $Ni_{1-x}O$ pigment coatings prepared especially for this purpose (see below).

However, there were a number of other reasons for further detailed studies of the $Ni_{1-x}O$ pigment coatings. They exhibited an immediate and strong EC effect, also obtained when the pigment coatings were cycled in an aprotic electrolyte ($LiClO_4$/PC), contrasting with some vacuum-based dense NiO_x films, for which activation is needed in order to obtain the EC response [8]. The cycling ability of NiO films in aprotic electrolyte has been studied also in the past [9–13]. NiO (bunsenite) thin films prepared by the chemical bath deposition (CBD) technique [14] and NiO thin films made from aqueous N,N dimethylaminoethanol solution reported by Park et al. [15] exhibit an immediate electrochromic response on lithium based electrolytes, which was attributed to the films' porosity. The latter films exhibit two anodic/cathodic waves in their cyclic voltamogrammes, at potentials quite close to those reported for sol–gel $Ni_{1-x}O$ thin films [7] and $Ni_{1-x}O$ pigment coatings cycled in lithium-based electrolyte [6]. The influence of the porosity of NiO (bunsenite) coatings has been studied by Boschloo and Hagfeldt [16]. The corresponding particulate films, even though of poor optical quality, also exhibit two current anodic/cathodic waves (I and II in [16]), both of them showing linear dependency with the frequency of the potential sweep, which the authors used as proof of the existence of surface redox reactions. Moreover, the films also showed distinct current peaks when cycled in tetrabutylammonium triflate (TBA^+ triflate) dissolved in 3-methoxypropionitrile, which was attributed to the adsorption of TBA^+ cations replacing protons on the surface of the NiO (bunsenite) grains. Namely, the CVs of NiO cycled in 3-methoxypropionitrile containing either 0.2 M lithium triflate or 0.2 M lithium perchlorate was practically identical [16]. The presence of protons on the surface of the NiO (bunsenite) grains seems to be important because the OH groups spontaneously form on the [111] crystalline planes of the NiO (bunsenite) grains due to the catalytic activity of NiO when it is exposed to the humid environment of water [17].

The role of the p-type conductivity of "$Ni_{1-x}O$" on their electrochromic properties has also not often been considered, even though the semiconductivity of NiO has been thoroughly investigated in the past, mainly in relation to the catalytic properties of NiO [18–20]. However, Uplane et al. [21] pointed out in their studies of electrochromic NiO films that their p-type conductivity could explain the coloring and bleaching of the films without invoking proton insertion/extraction reactions, knowing that other ions than protons are reversibly inserted. Accordingly, by using cyclic voltammetry at different scan rates, we aimed here to study the role of surface of the $Ni_{1-x}O$ grains in pigment coatings and in $Ni_{1-x}O$ thin films with established p-type semiconductivity in the reactions with cations and anions from various electrolytes. Therefore, the $Ni_{1-x}O$ pigment coatings were deposited on FTO glass substrate from pre-prepared $Ni_{1-x}O$ pigment co-ground with nickel oxyhydroxyde dispersant, which also acted as a binder using a standard approach for making the paints [6,22,23]. This relatively simple and robust approach provided us with $Ni_{1-x}O$ pigment dispersions and coatings, in which the particle size of the $Ni_{1-x}O$ agglomerates could easily be varied and its effect on the electrochemical reactions and electrochromic properties was possible to determine in various lithium ions containing (1 M $LiClO_4$/PC) and lithium-free (TBA^+ triflate/PC and 1-butyl-3-methylimidazolium bis(trifluoromethylsulfonyl) imide (BMITFSI)) electrolytes.

It should be pointed out that the influence of p-type semiconductivity on the cycling of films in aprotic electrolytes was surmised by Moulki et al. [24] in their study of pulsed laser deposited Li–Ni–O films assumed to be highly p-type semiconducting due to the presence of lithium [20]. The corresponding Li–Ni–O films showed a good response in lithium based electrolytes but the observation of extra high capacity on the first oxidation as compared to that on the first reduction raises the question of whether this effect is related to the extra deinsertion of lithium ions originally present in the films or some other mechanisms, such as anion insertion from the electrolyte.

This led us to investigate the role of the electrochemical surface reactions by using the *ex situ* near grazing incidence angle reflection absorption (IR RA) spectra performed in P-polarized light. IR RA spectra provide the longitudinal optical (LO) phonon modes of the $Ni_{1-x}O$ grains and intergranular (i.e. surface) material [25] for $Ni_{1-x}O$ pigment coatings. Accordingly, the $Ni_{1-x}O$ pigment coatings were treated at different temperatures and charged/discharged in 1 M $LiClO_4$/PC and 0.1 M TBA^+ triflate/PC electrolytes, their LO spectra recorded and correlated to the recently reported phonon spectra of NiO (bunsenite) obtained from the reflectivity spectra of NiO monocrystals [26–28] and NiO microcrystalline powders pressed into pellets treated with Kramers–Kroening analysis, combined with the effective medium theoretical approach [25]. The experimentally obtained LO spectra of $Ni_{1-x}O$ pigment coatings were rationalized with respect to the LO modes, which had already been determined [25] as the vibrations of the Ni–O bonds in the structure of NiO grains and the vibrational modes of the surface NiO groups. The main aim of the *ex situ* IR RA spectroelectrochemical studies was the identification of the behavior of electrolyte ions (triflate, for example) during the coloring/bleaching of the $Ni_{1-x}O$ pigment coatings in lithium-free electrolyte. These measurements gave a direct evidence for the intercalation of anions within a porous structure of $Ni_{1-x}O$ pigmented coatings, while the lithium ions were not needed for obtaining an EC effect.

The final part of this study was devoted to the demonstration that flexible foil-based EC devices could be made with lithium-free electrolytes. In order to show this, the wet deposited $Ni_{1-x}O$ pigment coatings on plastic conducting foils (ITO-PET) were assembled with poly(3,4-ethylenedioxythiophene) (PEDOT) self-standing film developed in the frame of Innoshade EU project and WO_3 thin film made by sputtering technique [24] and glued together with either lithium-containing (LiTFSI-BMITFSI) or lithium-free (BMITFSI) PMMA based semi-solid electrolytes.

2. Experimental

2.1. Preparation of pigment coatings

$Ni_{1-x}O$ pigment coatings were prepared in a two-step procedure. First, $Ni_{1-x}O$ pigment was made using the peroxo route from nickel(II) acetate and hydrogen peroxide-urea powdered precursors as reported in Ref. [7]. The obtained dried xerogel was thermally treated at 400 °C for 24 h to obtain the substoichiometric $Ni_{1-x}O$ pigment. In the second step, two kinds of pigment dispersions were made for the preparation of pigment coatings: $Ni_{1-x}O$ pigment: H_2O: NiO_xH_y dispersant in molar ratio 1:9:0.3 ($Ni_{1-x}O/NiO_xH_y$) and $Ni_{1-x}O$ pigment dispersed in water in molar ratio 1:9 ($Ni_{1-x}O/H_2O$).

NiO_xH_y dispersant was prepared by precipitation of nickel(II) sulfate with sodium hypochlorite [6,29]. The precipitate was then washed with distilled water to remove sulfate anions and dried at 50 °C overnight. The paste-like material was then mixed with water and used as a dispersant and binder for milling of the above mentioned $Ni_{1-x}O$ pigment.

Both pigment dispersions ($Ni_{1-x}O/NiO_xH_y$ and $Ni_{1-x}O/H_2O$) were thoroughly milled with zirconia beads of 0.4 and 0.1 mm (Table 1) and deposited on FTO glass via two-step spin coating process using rotating speed of 500 rpm for 5 s, followed by 1000 rpm for 1 min. One ($1x$) to four ($4x$) two-step spin coating deposition cycles were repeated in order to vary the thickness of the coatings. The pigment coatings were finally thermally treated for half an hour at 150 and 500 °C. For particle size distribution determination, both kinds of dispersions, i.e. $Ni_{1-x}O/NiO_xH_y$ and $Ni_{1-x}O/H_2O$, were first milled with 0.4 mm zirconia beads for 2 h, then the final dispersions were further milled with zirconia beads having 0.1 mm in size for additional 2 h.

2.2. Preparation of EC device

Flexible EC devices were prepared by assembling $Ni_{1-x}O/NiO_xH_y$ pigment coatings (on ITO-PET) and either PEDOT (self-standing) or WO_3 (on ITO-PET) using hydrophobic ionic-liquid (IL) based polymer electrolyte membranes consisting of IL, namely BMITFSI blended with 50 wt% of poly(methyl methacrylate) (PMMA) purchased from the Solvionic company. The transparent viscous mixture of IL in PMMA (with or without LiTFSI) was spread under ambient atmosphere on the PEDOT (or WO_3) and $Ni_{1-x}O/NiO_xH_y$ pigment coatings using a syringe and dried for 2 h at 80 °C to remove butanone, leading to hydrophobic electrolyte membranes. The electrochromic films were then tightly attached together via a sticky membrane sandwiched between them, allowing the production of a solid-state EC device. Since the BMITSFI-PMMA and LiTFSI-BMITFSI in PMMA membranes solidify at ambient conditions in few hours, the EC devices did not need any sealing.

Table 1
Dependence of the size of the $Ni_{1-x}O$ agglomerates (in nm) obtained from DLS measurements after grinding the $Ni_{1-x}O$ pigment with NiO_xH_y dispersant ($Ni_{1-x}O/NiO_xH_y$) and in water ($Ni_{1-x}O/H_2O$), the percentage (%) of the particles with listed size as a function of the milling time and diameter of the zirconia beads used for grinding.

Sample	Size of beads (mm)	Time of milling (min)	Particle size (nm)	Particle distribution (%)
NiO_xH_y precipitate		0	779.5	98.7
$Ni_{1-x}O/NiO_xH_y$	0.4	15	191.7	94.1
		30	150.6	99.6
		60	**94.6**	**90.3**
		120	42.4	99.5
	0.1	15	43.1	99.7
		30	37.1	100
		60	**31.7**	**99.7**
		120	29.0	99.9
$Ni_{1-x}O/H_2O$	0.4	15	143.8	87.3
		30	102.6	80.3
		60	**89.4**	**93.5**
		120	58.4	99.3
	0.1	15	47.2	99.8
		30	34.3	99.6
		60	**30.4**	**99.7**
		120	30.8	99.7

2.3. Instrumental

The particle size distribution of the powder was measured by photon correlation spectroscopy (PCS) using a Malvern Zetasizer Nano ZS laser particle size analyzer. The instrument was equipped with a He–Ne laser source (λ=633 nm) at a scattering angle of 173°. The dispersion concentration was around 0.1 g/l. The suspension was prepared by dispersing the powder in distilled water and treating for 6 min in an ultrasonic bath to obtain a well-dispersed suspension.

SEM micrographs were recorded on a SUPRA 35VP scanning electron microscope. The thickness of the pigment coatings was determined using a Profilometer Taylor Hobson, Seria II. XRD patterns of $Ni_{1-x}O/H_2O$ powders were recorded on an X-ray diffractometer PANalytical X'Pert PRO equipped with monochromatized Cu-$K_{\alpha 1}$=1.5406 Å in the range from 5 to 60° of 2Θ.

UV–vis spectra of the pigment coatings were recorded on a Perkin Elmer Lambda 900 UV–vis spectrometer equipped with an integrating sphere. Pigment coatings deposited on FTO glass were placed in the sample compartment of the spectrometer and the total transmittance (TT (λ)) spectra measured (300–2500 nm range) with respect to air. The optical quality of the coatings was evaluated by determining the haze, defined as the ratio of diffuse (DT) to total transmittance (DT/TT %) in the 280–700 nm range, following the ASTM test method D1003. Measurements and calculations are described in more detail in Ref. [6].

The electrochromic properties of the pigment coatings were evaluated using in situ UV–vis spectroelectrochemical measurements on an Autolab PGSTAT302N. The pigment coating on FTO glass (1×4 cm^2) was mounted in a three-electrode home-made electrochemical cell as a working electrode, while a Pt rod and Ag/AgCl electrode (in a solution of 90 vol% of 1 M $LiClO_4$/PC and 10 vol% of 1 M LiCl/methanol) were used as reference and counter electrodes. The electrochemical cell was filled with 40 ml of either 1 M $LiClO_4$/PC or 0.1 M TBA^+ triflate/PC electrolyte and mounted in the sample compartment of the HP 8453 A diode array UV–vis spectrophotometer. The pigment coatings were first stabilised for 20 cycles; the optical modulation was then determined during chronocoulometric coloration at 1.7 V for 60 s and bleaching at −1 V for 60 s. Cyclovoltammetric measurements were thereafter performed using scan rates from 2 to 50 mV/s. Flexible EC devices were mounted via special holder in the same HP 8453 A diode array UV–vis spectrophotometer.

The infrared reflection–absorption (IR RA) spectra of the pigment coatings were recorded on a Bruker IFS66/S spectrometer using a Monolayer Grazing Angle Specular Reflectance Accessory at a near-grazing incidence angle (NGIA) of 80° and with P-polarized light. The pigment coatings were deposited on reflective FTO glass substrates of dimensions 2×5 cm^2. For *ex situ* measurements, these pigment coatings were chronocoulometrically colored (1.7 V)/bleached (−1 V) using an Autolab PGSTAT3 02N in an electrochemical cell filled with 100 ml of either 1 M $LiClO_4$/PC or 0.1 M TBA^+ triflate/PC electrolyte. After coloration/

bleaching, the sample was moved from the electrochemical cell, rinsed with ethanol, dried and placed in the NGIA accessory in the sample compartment of the IR spectrometer. The *ex situ* IR RA spectra were detected for the 1st and 10th coloring/bleaching cycle. An FTO glass was used for the background measurement.

3. Results and discussion

3.1. Properties of $Ni_{1-x}O$ pigment dispersions

Grinding $Ni_{1-x}O$ pigment consisting of microcrystalline agglomerates that are built up of nanosized $Ni_{1-x}O$ grains (5–7 nm) [6] is a very effective way of reducing the size of the pigment particle agglomerates, which could eventually lead to the formation of dispersions consisting of nanosized (a few tens of nm in size) agglomerates (see Fig. 9 in Ref. [6]). In our previous study [6], $Ni_{1-x}O$ pigment was co-ground with relatively large zirconia beads of 0.7 mm diameter in the presence of NiO_xH_y dispersant prepared from nickel(II) sulfate and sodium hypochlorite precipitate. This procedure has led to pigment coatings showing haze up to 7% depending on the thickness of coatings.

In this study, therefore, we aimed to improve the optical transmission of the $Ni_{1-x}O$ pigment coatings by decreasing their haze at least to below ~2%, by using smaller zirconia beads (i.e., 0.4 and 0.1 mm) for milling. The duration of milling was varied (up to 2 h) and the as-prepared dispersions analyzed with the DLS technique, which provided information about the size of the agglomerates formed. Two different pigment dispersions were made: $Ni_{1-x}O/NiO_xH_y$, again made by co-grinding $Ni_{1-x}O$ with NiO_xH_y precipitate [6] and $Ni_{1-x}O/H_2O$ dispersions, which were prepared by grinding the $Ni_{1-x}O$ pigment in pure water. The main reason for making $Ni_{1-x}O/H_2O$ dispersions was to avoid NiO_xH_y dispersant, which inevitably affected the particle-to-particle interactions and blurred the infrared spectra, making it difficult to differentiate between the Ni–O modes in the bulk of the NiO grains and at the surface. Surprisingly, good $Ni_{1-x}O/H_2O$ pigment coatings were deposited from dispersions obtained merely by milling the $Ni_{1-x}O$ pigment in water. Dispersions exhibited long-term stability (> 1 month), the sedimentation was small and the aged dispersions could be re-dispersed. The thickness of both pigment coatings was varied simply by increasing the number of spin-coating (1*x*, 3*x* and 4*x*) depositions. $Ni_{1-x}O/H_2O$ coatings were considered to be good model coatings for establishing the OH groups on the surface of the $Ni_{1-x}O$ particle agglomerates.

The results shown in Table 1 revealed that the initial (as-prepared) NiO_xH_y precipitate consisted of large particle agglomerates with dimensions of about 780 nm. The $Ni_{1-x}O/NiO_xH_y$ dispersion was next milled for 15 min and the particle size was determined from the DLS measurements to be 191.7 nm. The largest change was obtained after milling the corresponding dispersion for 60 min, when the particle size dropped from the initial 191.7 nm to 94.6 nm and additional grinding for 120 min resulted in a further drop to 42.4 nm. The $Ni_{1-x}O/NiO_xH_y$ pigment suspension obtained after 60 min of milling (marked bold in Table 1) was then further milled for 15 min with beads of diameter 0.1 mm, which led to dispersions with a particle size of about 43.1 nm. The latter dispersion was then milled again for 30, 60 and 120 min with beads of diameter 0.1 mm. Prolongation of the milling time led gradually to smaller agglomerates. Because the longest grinding time (120 min) provided only marginally smaller agglomerates (29.0 nm) than those obtained after 60 min of milling (31.7 nm), the pigment dispersions obtained after 60 min of milling time were used for the deposition of pigment coatings.

The same procedure was also applied for the preparation of the $Ni_{1-x}O/H_2O$ dispersions (Table 1). As expected, the starting size of the pigment agglomerates obtained after milling the pigment with larger beads (0.4 mm) for 15 min was smaller (143.8 nm) and then dropped to 102.6 nm after 30 min and to 89.4 nm after 60 min of milling. However, the size of the agglomerates obtained after 120 min of milling with milling beads of 0.4 mm was only 58.4 nm but not less, contrasting the smaller agglomerates when the $Ni_{1-x}O$ was milled in the presence of NiO_xH_y dispersant (i.e. 42.4 nm). Dispersions characterized with a size of agglomerate of 89.4 nm (marked bold in Table 1) (60 min of milling time, 0.4 milling beads), were further milled with smaller beads (i.e., 0.1 mm) for 60 min, giving particle agglomerates of about 30.4 nm. The results showed that prolongation of the milling time to 120 min did not have as pronounced effect on the size of the agglomerates as when 0.4 mm beads were used. However, the milling procedure for $Ni_{1-x}O/H_2O$ and $Ni_{1-x}O/NiO_xH_y$ dispersions was quite effective, resulting in an agglomerate size of about 30 nm, irrespective of the dispersant used and with the same duration of milling.

To sum up, a clear distinction in the size of agglomerates in $Ni_{1-x}O/H_2O$ and $Ni_{1-x}O/NiO_xH_y$ dispersions, which were milled for 1 h using 0.4 and 0.1 mm zirconia beads, made it possible to use the corresponding dispersions for the deposition of pigment coatings containing agglomerates that differed in size up to

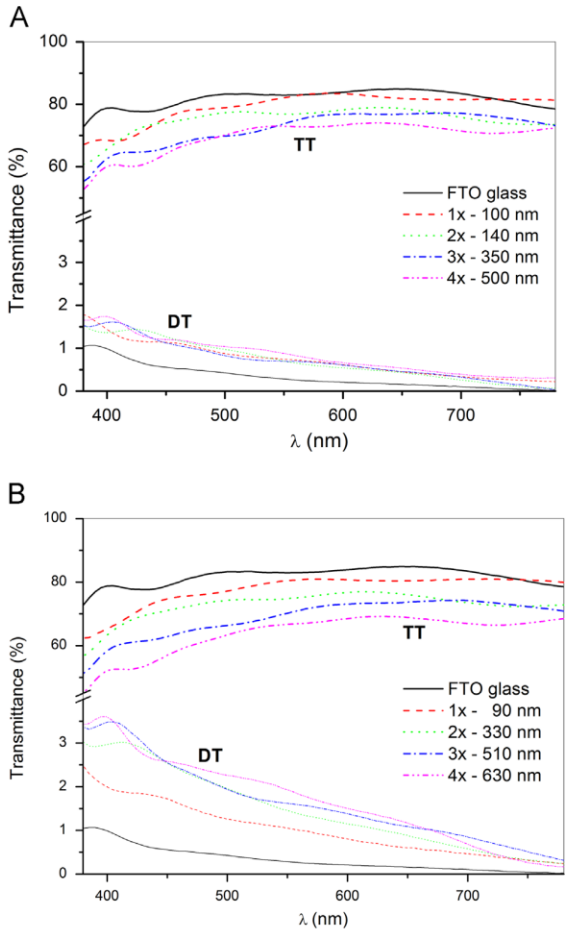


Fig. 1. DT_λ and TT_λ spectra (for haze values see Table 2) of the $Ni_{1-x}O/NiO_xH_y$ pigment coatings prepared from pigment dispersions using 60 min of milling time with various milling beads: (A) 0.1 mm and (B) 0.4 mm (see Table 1). Thermal treatment was performed at 150 °C.

Table 2
Thickness, haze (%), total transmittance (TT in %) and diffuse transmittance (DT in %) determined from the total hemispherical transmittance spectra of samples in the VIS spectral range (see Fig. 1) for various coatings made from $Ni_{1-x}O/NiO_xH_y$ dispersions milled with beads with diameters of 0.4 and 0.1 mm. Thermal treatment of the pigment coatings was performed at 150 °C.

$Ni_{1-x}O/NiO_xH_y$ pigment coatings	Deposition (No. of spin coatings)	*d* (nm)	Haze (%)	TT (%)	DT (%)
0.4 mm beads	1*x*	90	1.3	80.2	1.5
	2*x*	330	2.0	75.6	1.9
	3*x*	510	2.4	71.2	2.3
	4*x*	630	2.9	67.2	2.4
0.1 mm beads	1*x*	100	0.9	82.2	1.2
	2*x*	140	1.0	77.6	1.2
	3*x*	350	1.1	74.8	1.2
	4*x*	500	1.3	72.8	1.3

~60 nm (Table 1). Pigment coatings made from these dispersions (i.e., $Ni_{1-x}O/H_2O$ and $Ni_{1-x}O/NiO_xH_y$) provided suitable starting materials for further investigations of their electrochemical, electrochromic and structural properties.

3.2. Optical properties of pigment coatings

For any coatings that are intended for use in optical systems, their optical properties, i.e., total spectral transmittance (TT_λ), total spectral diffuse transmittance (DT_λ) and total transmittance (TT), total diffuse transmittance (DT) in the VIS spectral regions, together with the haze derived from these values (in %) (for details see [6]), should be known. These are basic and also decisive data about their applicability in corresponding optical systems.

Typical variations of the TT_λ and DT_λ spectra of the $Ni_{1-x}O/NiO_xH_y$ pigment coatings (0.1 and 0.4 mm milling beads) investigated as a function of thickness are shown in Fig. 1. As expected, haze increased with the coating thickness, i.e., number of spin coating cycles (Table 2), but the coatings deposited from pigment dispersions milled with smaller beads had smaller haze than those for which larger beads were used for milling. However, haze remained low for all coatings made by a single spin coating cycle, indicating that the size of agglomerates was well below 200 nm.

The effect of sintering on coating properties was next considered (Table 3). Even though we deliberately limited the heat treatment temperature to 150 °C in order to match the temperature stability of plastic foils, sintering at higher temperatures could beneficially increase the mechanical integrity of coatings. On the other hand, it could adversely affect their haze and—important for the present study—change the inherent transmittance of pigment coatings due to a diminution of the concentration of absorbing Ni^{3+} sites in the defect $Ni_{1-x}O$ bunsenite structure, leading to a loss of p-type semiconductivity.

Accordingly, the TT, DT and haze of the $Ni_{1-x}O/H_2O$ and $Ni_{1-x}O/NiO_xH_y$ coatings were determined and correlated to the coatings' thickness (Table 3). Coatings were prepared by using the same pigment dispersion procedure (milling beads 0.4 mm) and heat treated at 150 and 500 °C (30 min). The results revealed that sintering the $Ni_{1-x}O/H_2O$ and $Ni_{1-x}O/NiO_xH_y$ pigment coatings made by the same number of spin coating deposition cycles and heat-treated at 150 and 500 °C caused shrinkage of the coating layers and their densification but the haze remained practically unchanged. It seemed that sintering changed only the size of the particle grains, doubling their size from ~9.5 nm (150 °C) to ~16 nm (500 °C, 30 min) as revealed by XRD results (not reported herein), without affecting the larger pigment agglomerates, which could be responsible for scattering of light. Most interestingly, sintering caused bleaching of the coatings. Even though this could be attributed to the decrease of the coatings' thickness, bleaching caused by a decrease in the Ni^{3+} concentration seemed to be a genuine property of sintered coatings, as could be inferred from the corresponding A_λ/d values obtained by dividing the spectral absorbance (A_λ) by the coating thickness (*d*) (Table 3) (Fig. 2). This agreed with the similar bleaching of NiO thin films prepared by a chemical bath deposition technique reported by Xia et al. [30].

To sum up, $Ni_{1-x}O/H_2O$ and $Ni_{1-x}O/NiO_xH_y$ pigment coatings with good optical quality were reproducibly made from pigment particle dispersions, in which the size of the particle agglomerates was varied by varying the milling conditions. Even though all deposited pigment coatings exhibited a certain haze, it could easily be controlled by using smaller milling beads and prolonged milling times. Pigment particle dispersions provided reliable starting material for the deposition of structured $Ni_{1-x}O$ pigment coatings consisting of particle agglomerates with pre-selected size and well-defined surface and porosity on either FTO glass or ITO-PET flexible substrates, the latter being important for the deposition of pigment coatings via the coil coating deposition. In order to establish the surface morphology of the $Ni_{1-x}O$ pigment coatings, their SEM micrographs are shown below.

Table 3
Thickness (*d* in nm), haze (%), total transmittance (TT in %) and diffuse transmittance (DT in %) determined from the total hemispherical diffuse (DT_λ) and transmittance (TT_λ) spectra (see Fig. 2) of samples in the visible spectral range for various coatings made from $Ni_{1-x}O/NiO_xH_y$ and $Ni_{1-x}O/H_2O$ dispersions milled with beads of 0.4 mm diameter. Thermal treatment was performed at 150 °C and 500 °C.

Pigment coatings	Milling beads (mm)	Deposition (No. of spin coatings)	*T* (°C)	Haze (%)	TT (%)	DT (%)	*d* (nm)
$Ni_{1-x}O/NiO_xH_y$	0.4	1*x*	150	1.3	80.2	1.5	90[a]
		1*x*	500	1.5	84.2	2.0	80[a]
		3*x*	**150**	**2.4**	**71.2**	**2.3**	**510**[b]
		3*x*	**500**	**2.7**	**79.8**	**2.9**	**310**[b]
$Ni_{1-x}O/H_2O$	0.4	1*x*	150	2.1	79.5	2.2	140[a]
		1*x*	500	2.0	83.4	2.5	120[a]
		3*x*	**150**	**3.9**	**70.8**	**3.2**	**380**[b]
		3*x*	**500**	**4.5**	**79.7**	**4.3**	**300**[b]

[a] Indicates the pigment coatings used for determination of A_λ/d values shown in Fig. 2.
[b] Indicates the pigment coatings used for determination of electrochemical response (in bold).

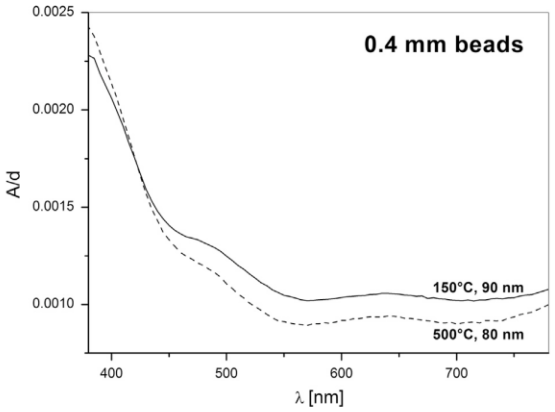


Fig. 2. Spectral absorbance divided by thickness of the coatings (A_λ/d) of $Ni_{1-x}O/NiO_xH_y$ pigment coatings (1*x*, 0.4 mm beads) heat treated at: (A) 150 °C (30 min) and (B) 500 °C (additional 30 min). The thickness of the coatings was 90 nm (150 °C) and 80 nm (500 °C) (see Table 3).

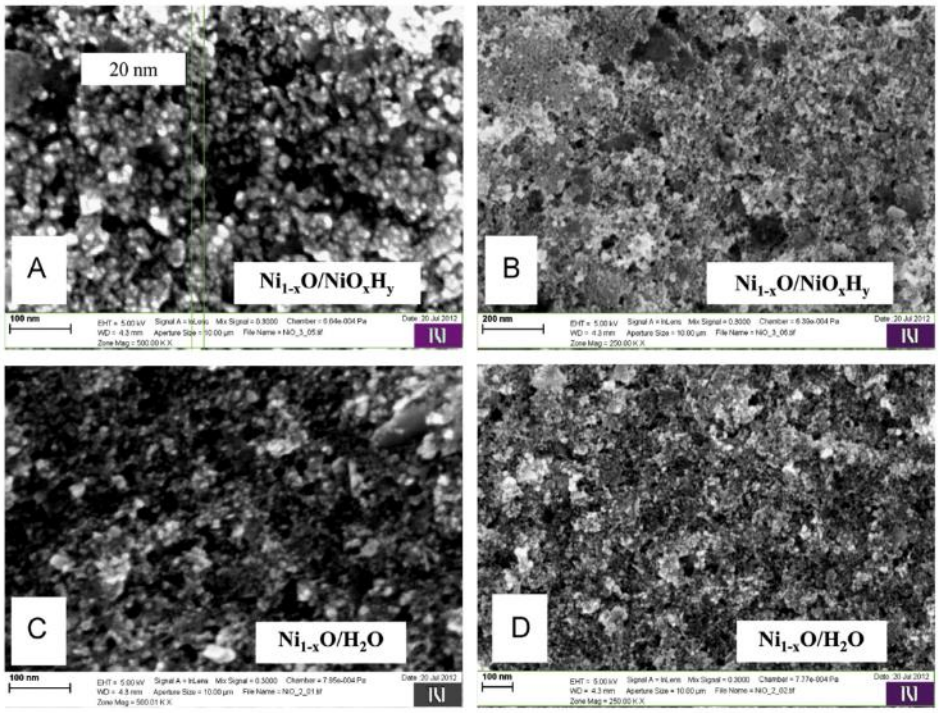


Fig. 3. SEM micrographs of pigment coatings prepared using 0.4 mm beads and heat treated at 150 °C for 30 min: (A, B) $Ni_{1-x}O/NiO_xH_y$ and (C, D) $Ni_{1-x}O/H_2O$.

3.3. SEM micrographs

For many EC films, the importance of their surface morphology and texture on their EC effect has already been addressed. NiO films made via the CBD technique [14,30] and NiO (bunsenite) particulate films prepared by Boschloo and Hagfeldt [16] are typical examples relevant also for this study. We focused here on SEM micrographs of $Ni_{1-x}O/H_2O$ and $Ni_{1-x}O/NiO_xH_y$ pigment coatings prepared from the corresponding pigment dispersions obtained under the same milling conditions (2 h, milling beads 0.4 mm), aiming to reveal their similarity, expected due to the coatings' similar haze and optical properties as described above.

The SEM micrographs of the pigment coatings (Fig. 3) revealed that both pigment coatings contained agglomerates of irregular shape, closely packed together with pores of similar size and prevalence. It seemed that when the pigment dispersion dried, the $Ni_{1-x}O$ agglomerates, which were separated in dispersions, collapsed to form a dense pigment layer with randomly interlinked particle agglomerates of a size fairly similar to the size in dispersions (Table 1). We expected that such a closely packed texture provided plenty of particle-to-particle contacts, allowing easy electron hole (e^+) transport between them and facilitating the EC effect. It seemed that the dispersant (i.e., NiO_xH_y or water) did not have a strong influence on the coatings' morphology, haze and optical properties. SEM micrographs of the corresponding pigment coatings heat treated at 500 °C showed a similar surface texture and are not shown here.

3.4. Electrochemical properties

Cyclic voltammetry, CV, is a fast and efficient technique for assessing electrochemical processes in EC films. In addition to basic information about the potentials at which the oxidation and reduction reactions take place, measuring the current densities of the corresponding peaks at various scan rates enables the establishment of diffusion processes of intercalation species within the films. The Randles–Sevčik equation can be used when the current peaks are proportional to the square root of the scan rate but, in the case that the current peaks show a linear dependence on the scan rate, the reactions are not diffusion-limited but rather a surface reaction occurs. Due to the high surface area of the pigment agglomerates, $Ni_{1-x}O/NiO_xH_y$ and $Ni_{1-x}O/H_2O$ pigment coatings were deposited from pigment dispersions obtained after milling the pigment with 0.4 mm milling beads followed by heat treatment of coatings at 150 and 500 °C. The thickness of the deposited coatings was adjusted by 1*x* and 3*x* spin coating cycles and their thickness was determined with a profilometer (Tables 1 and 2).

In our previous studies of $Ni_{1-x}O$ thin films [7] and $Ni_{1-x}O/NiO_xH_y$ pigment coatings prepared by milling with zirconia beads of 0.7 mm [6], two current peaks (peaks I and II) were noted in the corresponding CVs, similar in shape and appearing close to potentials reported for the NiO particulate films prepared by Boshloo and Hagfeldt [16] and Park et al. [15]. Boshloo and Hagfeldt [16] showed that both current peaks exhibit linear dependence on the scan rates in an aqueous electrolyte, suggesting surface redox reactions. Moreover, it has also been shown that nanostructured NiO particulate films also exhibit similar CVs when cycled in lithium or TBA^+ triflate in methoxypropionitrile electrolytes, even though peaks I and II were broader and less pronounced. From the change in the shape of peaks I and II and the onset of peak I, which shifted to a more positive potential (~0.6 V) in the lithium triflate electrolyte, they [16] assumed that H^+ ions, which are bound to $O_{surface}$ in aqueous electrolytes, were replaced in aprotic electrolytes either by Li^+ or TBA^+ ions, which are adsorbed on the $O_{surface}$. The oxidation redox process of the surface Ni^{2+} atoms was assumed to be coupled with cation desorption (Li^+ or TBA^+), the nature of which determines the positions of the peaks. This led them to conclude that the position and shape of peaks I and II do not simply correspond to oxidation

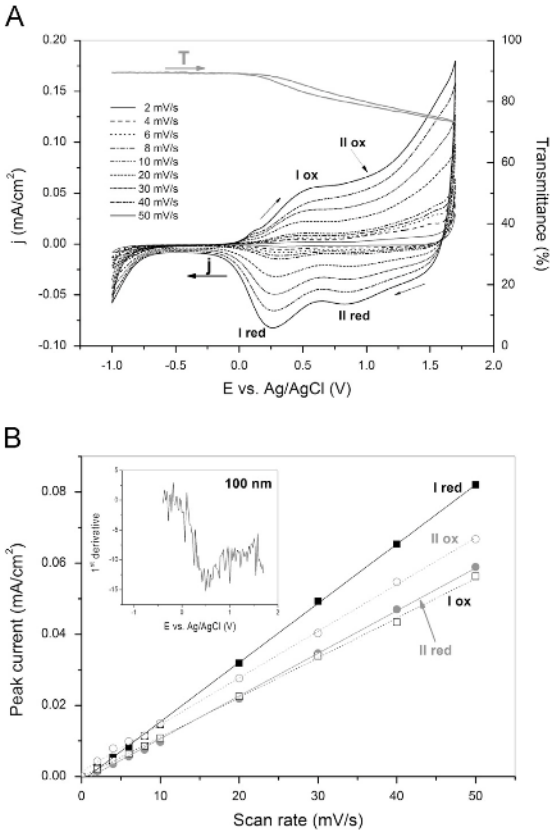


Fig. 4. Cyclic voltammograms of $Ni_{1-x}O/NiO_xH_y$ (1x, 150 °C, 0.4 mm beads) pigment coatings obtained with various scan rates in 1 M $LiClO_4$/PC electrolyte and (B) peak current density versus scan rate. Insert: 1st derivative of the transmittance response during anodic sweep from −0.04 to 1.7 V with a scan rate of 2 mV/s.

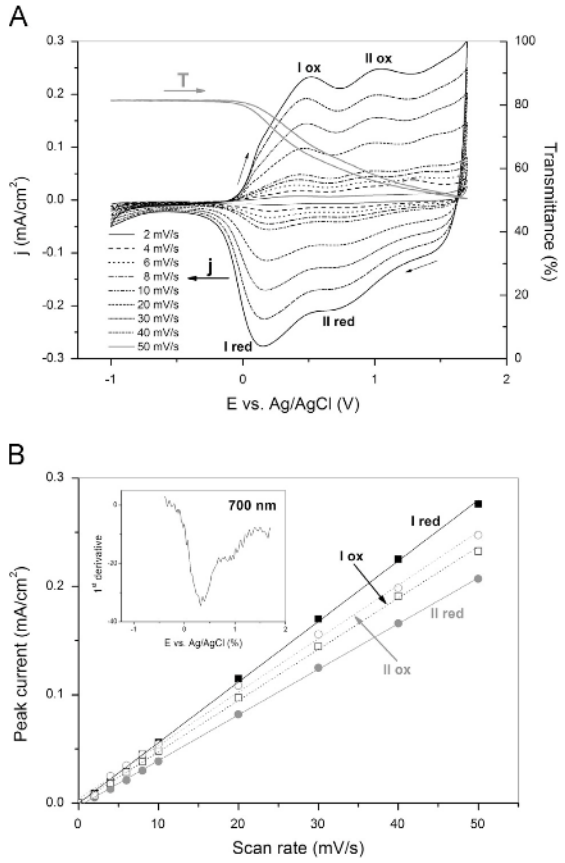


Fig. 5. Cyclic voltammograms of $Ni_{1-x}O/NiO_xH_y$ (3x, 150 °C, 0.4 mm beads) pigment coatings obtained with various scan rates in 1 M $LiClO_4$/PC electrolyte and (B) peak current density versus scan rate. Insert: 1st derivative of the transmittance response during anodic sweep from −0.04 to 1.7 V with a scan rate of 2 mV/s.

of Ni^{2-} to Ni^{3+} and Ni^{4+} and that anion adsorption does not seem to be important, since the CVs of the NiO films in 3-methoxypropioniltrile containing lithium triflate or lithium perchlorate are identical.

Accordingly, in order to establish the nature of redox reactions for peaks I and II, the $Ni_{1-x}O/NiO_xH_y$ (deposited 1x and 3x, 100 nm and 700 nm, 150 °C) and $Ni_{1-x}O/H_2O$ (3x, 290 nm, 500 °C) pigment coatings were deposited from pigment dispersions milled with 0.4 mm zirconia beads. The coatings were cycled in 1 M $LiClO_4$/PC and 0.1 M TBA^+ triflate/PC electrolyte. For the same pigment coatings, transmittance changes ($\Delta T_{480\ nm} = T_{bleached} - T_{colored}$) were obtained by performing in situ spectroelectrochemical measurements and presented as transmittance variations ($\Delta T_{480\ nm}$) as a function of potential. The first derivative of $\Delta T_{480\ nm}$ is depicted in order to correlate the electrochromic effect with the appearance of current peaks I and II.

As expected, the $Ni_{1-x}O/NiO_xH_y$ (1x, 150 °C, 0.4 mm beads) coatings cycled in 1 M $LiClO_4$/PC electrolyte (Fig. 4) exhibited weaker peaks I and II than the thicker $Ni_{1-x}O/NiO_xH_y$ (3x, 150 °C, 0.4 mm beads) pigment coatings (Fig. 5) but both showed a linear increase in the current peak densities (j in mA/cm^2) as the function of scan rate varied from 2 to 50 mV/s. While for the thinner (1x) pigment coatings $\Delta T_{480\ nm} = T_{bleached} - T_{colored} = 89\% - 73\% = 16\%$, the corresponding change in transmittance for the thicker coatings (3x) was $\Delta T_{480\ nm} = 81\% - 50\% = 31\%$ (Figs. 4 and 5A). Both pigment coatings exhibited typical linear dependence of the current densities of peaks I and II with the scan rate (Figs. 4 and 5B).

The situation did not change much for the $Ni_{1-x}O/H_2O$ (290 nm (3x), 500 °C, 0.4 mm beads) pigment coatings (Fig. 6) fired at 500 °C. The current peaks were less expressed and lower, due to the smaller thickness of these coatings compared to those prepared at 150 °C (Fig. 5), as well the electrochromic changes were smaller, indicating that the EC response became weaker.

More interesting was the behavior of the $Ni_{1-x}O/NiO_xH_y$ (700 nm (3x), 150 °C, 0.4 mm beads) pigment coatings when cycled in 0.1 M TBA^+ triflate/PC electrolyte (Fig. 7). The current peak CVs of the corresponding pigment coating showed a slower increase of peaks I and II with the scan rate, compared to that noted for the same $Ni_{1-x}O/NiO_xH_y$ (3x, 150 °C, 0.4 mm beads) (Fig. 5) pigment coatings cycled in 1 M $LiClO_4$/PC and the linearity at small scan rates was lost (Fig. 7B). However, the EC response ($\Delta T_{480\ nm} = T_{bleached} - T_{colored} = 77\% - 44\% = 33\%$) was comparable. Lower optical modulation ($\Delta T < 20\%$) was observed for $Ni_{1-x}O/H_2O$ pigment coatings (3x, 500 °C, 0.4 mm beads) tested in 0.1 M TBA^+ triflate/PC electrolyte (Fig. 8).

Finally, for comparison the sol–gel $Ni_{1-x}O$ thin films deposited by the dip-coating technique from the same sol as used for making $Ni_{1-x}O$ pigment [7] were cycled in 1 M $LiClO_4$/PC electrolyte and the corresponding current densities were recorded versus increasing scan rate (Fig. 9). The $Ni_{1-x}O$ thin films (Fig. 9) also showed two current peaks, the values of which increased fast (even 10 times) with an increasing scan rate compared to the pigment coatings (Figs. 4–8). The EC effect was strong ($\Delta T_{480\ nm} = T_{bleached} - T_{colored} = 86\% - 47\% = 39\%$),

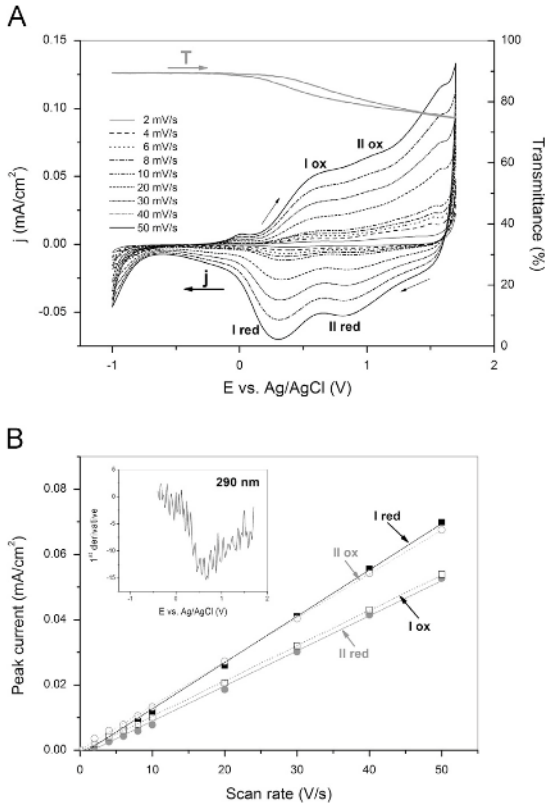


Fig. 6. Cyclic voltammograms of $Ni_{1-x}O/H_2O$ (3*x*, 500 °C, 0.4 mm beads) pigment coatings obtained with various scan rates in 1 M $LiClO_4$/PC electrolyte and (B) peak current density versus scan rate. Insert: 1st derivative of the transmittance response during anodic sweep from −0.04 to 1.7 V with a scan rate of 2 mV/s.

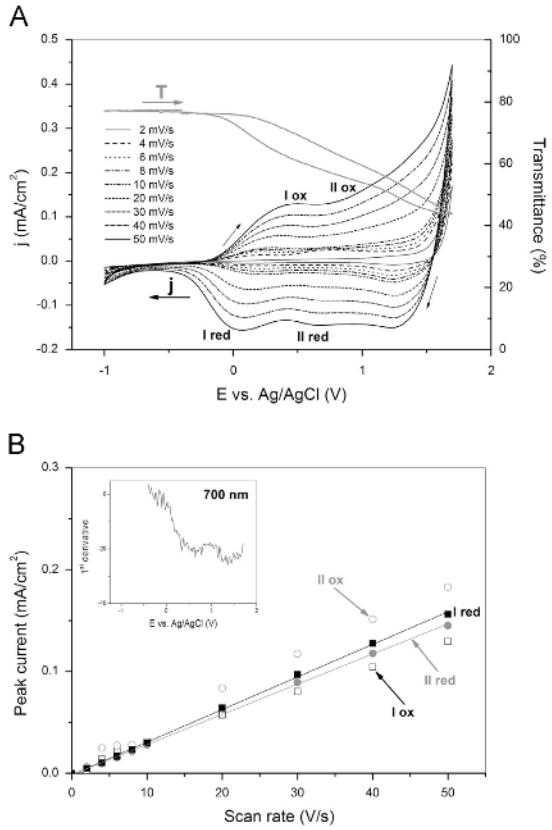


Fig. 7. Cyclic voltammograms of $Ni_{1-x}O/NiO_xH_y$ (3*x*, 150 °C, 0.4 mm beads) pigment coatings obtained with various scan rates in 1 M TBA^- triflate/PC electrolyte and (B) peak current density versus scan rate. Insert: 1st derivative of the transmittance response during anodic sweep from −0.04 to 1.7 V with a scan rate of 2 mV/s.

in fact stronger than that of the investigated pigment coatings (Figs. 4–8), even though the film thickness was 300 nm (Fig. 9). As expected, the strongest EC effect happened during the 1st anodic wave, resembling the behavior of the $Ni_{1-x}O$ pigment coatings (Figs. 4–8), indicating that a similar coloring/bleaching mechanism could also be attributed to thin $Ni_{1-x}O$ thin films (Fig. 9).

The similar electrochemical behavior of the $Ni_{1-x}O$ thin films (Fig. 9) and $Ni_{1-x}O$ pigment coatings (Figs. 4–8) was surprising because the surface reactions clearly seen for sol–gel thin films were not expected to be as pronounced as for the pigment coatings. Thin films definitely represent a more homogeneous system; their haze was negligibly small (<1%) [6], and larger pores inevitably present in pigment coatings could not be expected. However, thin films and pigment coatings shared a number of common properties; strong particle-to-particle contacts, the existence of holes (e^+) stemming from the presence of Ni^{+2}/Ni^{+3} redox couples and p-type semiconductivity, providing hole transport within the NiO grains. All this tends to indicate the existence of surface electrochemical reactions rather than lithium ions insertion/deinsertion reactions, suggesting that thin films and pigment coatings behave similarly to nickel oxide electrochemical capacitors, as reported by Srinivasan and Weidner [31].

To sum up, the CVs of the investigated pigment coatings in many aspects resembled those reported by Boschloo and Hagfeldt [16]; two anodic/cathodic peaks were observed, both exhibiting a linear increase with the scan rate, confirming the domination of redox processes, independent of the diffusion of ions in and out of the pigment coating. This suggests that redox processes were confined to the surface layer of the $Ni_{1-x}O$ grains, as also inferred from the results of electrochemical measurements in 0.1 M TBA^+ triflate/PC electrolyte. The results reported herein gave more information and a clearer picture about bleaching and coloring mechanisms than described in our previous studies of $Ni_{1-x}O$ films [6,7]. The highest coloring was noted for the first anodic peak, as inferred from the 1st derivatives of the corresponding monochromatic ($\Delta T_{480\ nm}$) transmittance changes. Moreover, pigment coatings cured at 150 °C exhibited higher current peaks than those of coatings fired at 500 °C. This could be ascribed to the larger size of the $Ni_{1-x}O$ grains in sintered coatings (Table 3). Furthermore, $Ni_{1-x}O/H_2O$ pigment coatings, in which only native OH groups existed on the surface of the $Ni_{1-x}O$ agglomerates, also exhibited an EC effect and similar electrochemical behavior in 1 M $LiClO_4$/PC and in lithium ions free 0.1 M TBA^+ triflate/PC electrolytes (Fig. 8). This indicates that, at least for our experimental conditions, the formation of OH surface groups on $Ni_{1-x}O$ grains (or agglomerates) cannot be avoided. They were generated per se due to the high catalytic activity of the NiO [32], stemming from native defects, such as the interstitial oxygen and nickel vacancies of the NiO (bunsenite).

3.5. Electrochromic properties

The electrochromic response of selected pigment coatings listed in Table 3 was next studied by performing in situ UV-vis spectroelectrochemical measurements. The pigment coatings were

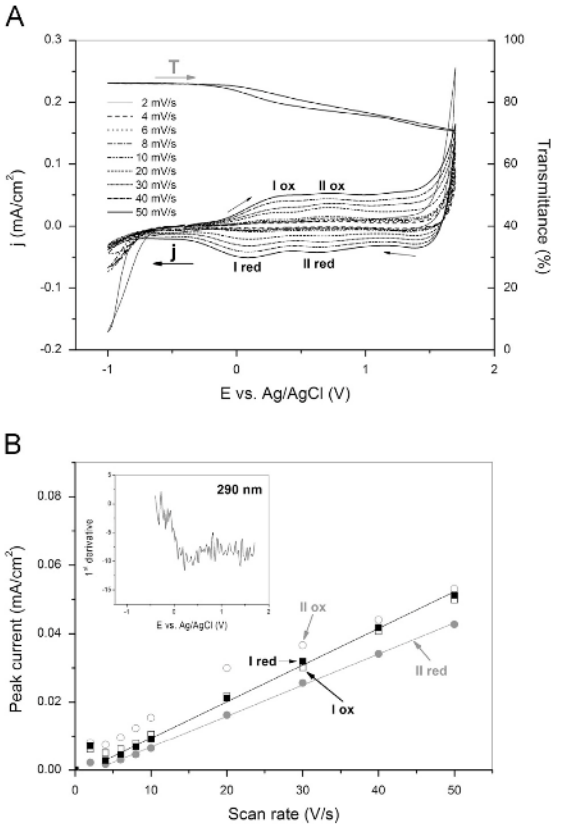


Fig. 8. Cyclic voltammograms of $Ni_{1-x}O/H_2O$ (3x, 500 °C, 0.4 mm beads) pigment coatings obtained with various scan rates in 0.1 M TBA^+ triflate/PC electrolyte and (B) peak current density versus scan rate. Insert: 1st derivative of the transmittance response during anodic sweep from −0.04 to 1.7 V with a scan rate of 2 mV/s.

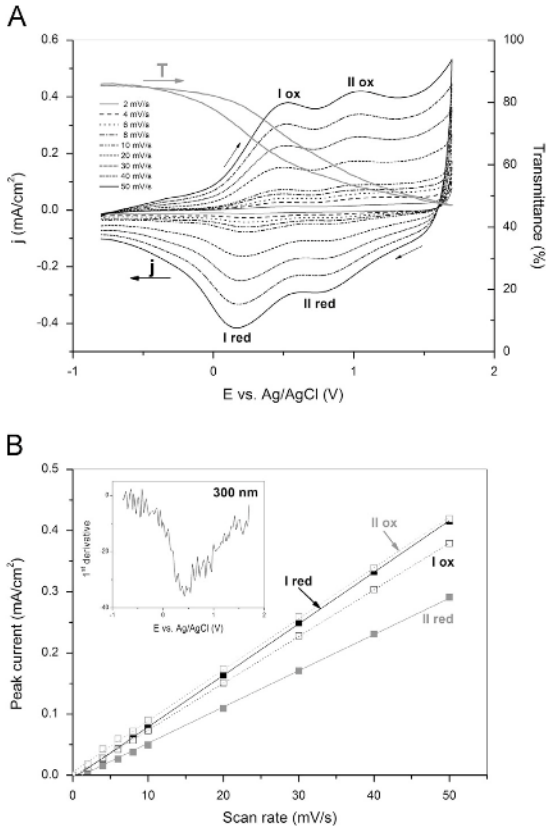


Fig. 9. Cyclic voltammograms of sol–gel $Ni_{1-x}O$ (4 dip-coated layers, 300 °C) thin films obtained with various scan rates in 1 M $LiClO_4$/PC electrolyte and (B) peak current density versus scan rate. Insert: 1st derivative of the transmittance response during anodic sweep from −0.04 to 1.7 V with a scan rate of 2 mV/s.

colored at 1.7 V and bleached at −1 V vs. Ag/AgCl in 1 M $LiClO_4$/PC and 0.1 M TBA^+ triflate/PC electrolytes (Fig. 10). Their EC response was difficult to compare quantitatively because the coatings had different thicknesses, as shown in Table 3.

The transmittance variations depicted in Fig. 10 showed that the transmittance of the initial (as-prepared) state was always between those of bleached and colored states. This confirmed the existence of Ni^{3+} states in the $Ni_{1-x}O$ pre-prepared pigment. Transmittance changes were always higher for pigment coatings that were heat treated at 150 °C but became weaker for those sintered at 500 °C (30 min), agreeing with smaller amount of Ni^{3+} in sintered coatings. The EC response only slightly depended on the electrolyte type, being similar for 0.1 M TBA^+ triflate/PC and 1 M $LiClO_4$/PC electrolytes. However, further measurements should be done for pigment coatings of the same thickness, in order to rationalize the EC response quantitatively. This is planned for the future. The stability of the pigment coatings was checked in a limited range of cycling (~250 cycles).

3.6. *Infrared spectra of pigment coatings*

The aim of the infrared spectra analysis was to establish the presence of the specific $Ni_{1-x}O$ surface sites responsible for the observed electrochemical behavior of the pigment coatings. At first sight, the problem seemed simple, because stoichiometric NiO with a bunsenite structure exhibits only one IR active transversal optical phonon mode (ω_{TO}) in the IR spectra, characterized by out-of-phase movement of nickel in opposition to the movement of the oxygen sublattice. The problem reduced to the identification of surface modes and distinguishing them from the Ni–O modes that stemmed from the bulk of the grains and/or agglomerates. In order to do that, IR spectra of pigment coatings made of $Ni_{1-x}O$ with and without dispersant ($Ni_{1-x}O/NiO_xH_y$ and $Ni_{1-x}O/H_2O$) exposed to different milling conditions (beads 0.1 and 0.4 mm) and heat treated at different temperatures (150 °C and 500 °C, 30 min) were measured and their spectra analyzed.

The infrared spectra of NiO (bunsenite) have not often been studied in relation to their electrochromic properties. Among various techniques, IR spectroscopy performed under near-grazing incidence angle (IR RA, for short) (80°) conditions and p-polarized light was chosen here [33–36]. The IR RA technique enables the measurement of thin films and coatings on metal or FTO glass substrates by providing the longitudinal optical mode (ω_{LO}) frequencies of coatings that correspond to the reflection minima ($\Delta R/R$) in the IR RA spectra. For bulk monocrystalline samples, LO modes correspond to the maxima $\mathrm{Im}(-1/\varepsilon(\omega))$ (frequency at which the real part (ε_1) of ε vanishes) of the complex dielectric permittivity function ($\varepsilon(\omega)$) of a material, while transversal optical (ω_{TO}) modes correspond to the maxima of the imaginary part of the $\varepsilon(\omega)$.

The $Ni_{1-x}O$ pigment coatings studied in this work were perfectly suitable for using the IR RA technique: they were thin enough, consisting of small $Ni_{1-x}O$ pigment particle agglomerates (Tables 1–3) and the pigment loading was at least 90% with anticipated voids (Fig. 3). Due to the particulate texture of the pigment coatings they could be described as air/$Ni_{1-x}O$

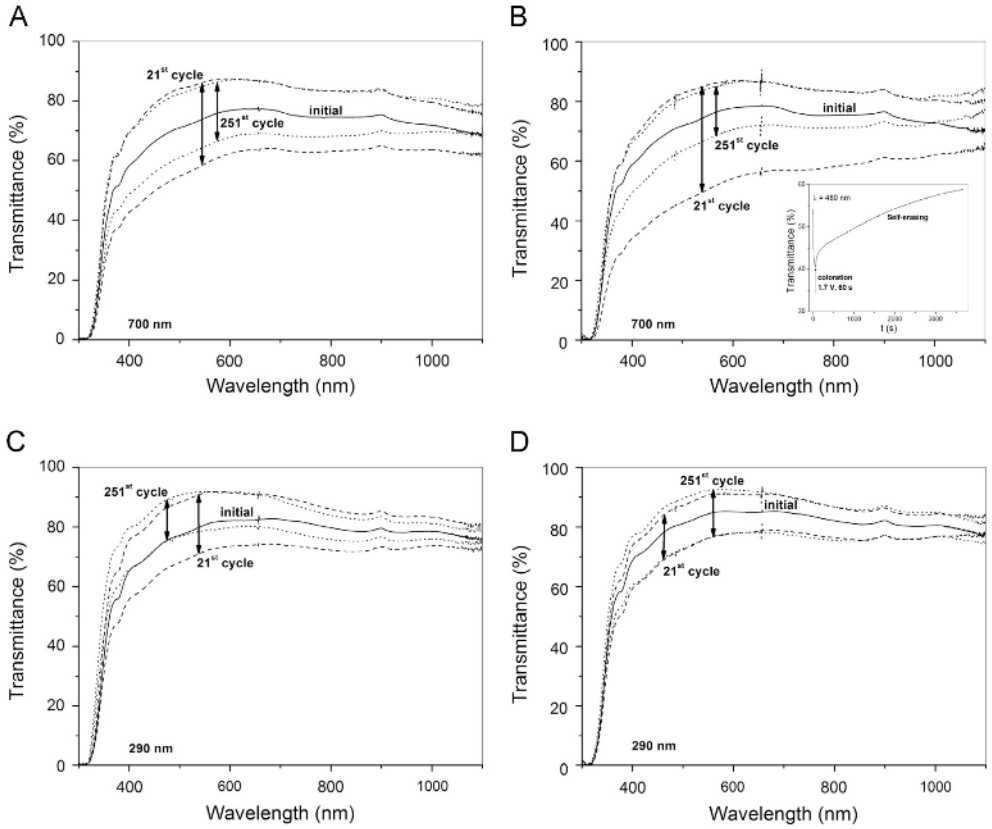


Fig. 10. Transmittance spectra of various coatings in initial, colored and bleached states for 21st and 251st cycles: (A) $Ni_{1-x}O/NiO_xH_y$ ($3x$, 150 °C) cycled in 1 M $LiClO_4$/PC, (B) $Ni_{1-x}O/NiO_xH_y$ ($3x$, 150 °C) cycled in 0.1 M TBA^+ triflate/PC electrolyte, (C) $Ni_{1-x}O/H_2O$ ($3x$, 500 °C) cycled in 1 M $LiClO_4$/PC and (D) $Ni_{1-x}O/H_2O$ ($3x$, 500 °C) cycled in 0.1 M TBA^+ triflate/PC electrolyte. Insert: Self erasing properties of the corresponding pigment coating in 0.1 M TBA^+ triflate/PC electrolyte.

nanocomposites consisting of grains and intergranular materials, the latter being specific for their surface. An effective-medium theoretical approach recently reported by Nikolić et al. [25] was used for the interpretation of the corresponding IR RA spectra.

The vibrational modes (ω_{TO}, ω_{LO}) of monocrystalline NiO (bunsenite) have already been reported [26,28,37] and were obtained by applying Kramers–Kroenig numerical analysis of the near-normal reflectivity spectra. Due to the difficulties of obtaining large enough high quality monocrystalline NiO samples, infrared spectra of NiO microcrystals pressed into the form of pellets have been studied and the vibrational modes of the corresponding NiO powders have been determined with the help of effective-medium theory (EMT). Pocharroman and Iglesias [38] treated a heterogeneous system of microcrystalline NiO (bunsenite) particles with modified effective-medium theory [39], showing that two phonon modes ($\omega_{TO1}\sim394\ cm^{-1}$ and $\omega_{TO2}\sim560\ cm^{-1}$) very well described the reflectivity curve of pressed pellets. However, the corresponding LO phonon modes have not been reported.

Nikolić et al. [25] interpreted the reflectivity spectra of pressed NiO microcrystals with the help of the four-parameter model of coupled oscillators introduced by Gervais and Piriou [40]. The calculation revealed that the spectra of NiO monocrystals reported by others [26,28] could be described very well with three oscillators; the first corresponds to those obtained for a single crystal at ω_{TO1} at 383–388 cm^{-1} and ω_{LO1} at 582–589 cm^{-1}, while the second phonon mode was found at ~560 cm^{-1} (ω_{TO2}) and 563 cm^{-1} (ω_{LO2}). For the third mode, the corresponding ω_{TO3} and ω_{LO3} were determined at 333–400 cm^{-1} and 369–407 cm^{-1}, respectively. The presence of two instead of just a single mode predicted for cubic NiO has been attributed to the expected substoichiometry of the investigated samples [41].

For the identification of vibrational modes attributed to Ni--O species at the surface of agglomerates and grains, we used a vibrational bands assignment based on the reflectivity spectra of microcrystalline NiO treated in terms of pores, NiO grains and intergranular material (with different filling factors) [25]. It has been shown that when microcrystalline NiO grains are modeled with one and intergranular material with two coupled oscillators, the corresponding ω_{TO} and ω_{LO} phonon modes of the NiO grains are described by $\omega_{TO\ grains}\sim385\ cm^{-1}$ and $\omega_{LO\ grains}\sim596\ cm^{-1}$ (G ω_{LO} mode, for short), while the phonon modes of the intergranular material appeared at $\omega_{TO\ intergranular1}\sim200–422\ cm^{-1}$ and $\omega_{LO\ intergranular1}\sim488–520\ cm^{-1}$ (IG ω_{LO} mode, for short), the latter depending on the sintering time, i.e., the porosity of the samples. An additional mode corresponding to the intergranular material was determined in the lower frequency range ($\omega_{TOintergranular2}$: 302–307 cm^{-1}, $\omega_{LO\ intergranular2}$: 373–435 cm^{-1}) (low frequency IG ω_{LO} mode). G ω_{LO} and IG ω_{LO} modes were adopted and used for the interpretation of our IR RA spectra of charged/discharged pigment coatings, as shown below.

3.6.1. *Identification of surface modes*

The IR RA spectra of $Ni_{1-x}O$ pigment coatings (Fig. 11) prepared under various conditions revealed a very consistent appearance of the LO modes, characterized by bands at 563–582 cm^{-1} and

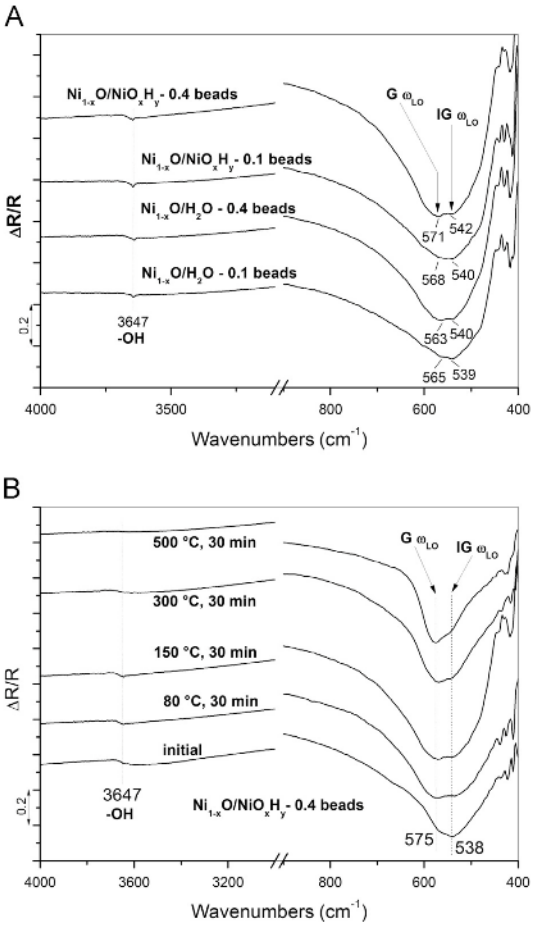


Fig. 11. IR RA spectra of $Ni_{1-x}O/NiO_xH_y$ pigment coatings: (A) prepared using milling beads of 0.1 and 0.4 mm and thermally treated at 150 °C 30 min and (B) prepared using milling beads of 0.4 mm and thermally treated at various temperatures.

538–542 cm^{-1}, which we attributed to the LO modes of the $Ni_{1-x}O$ grains (G ω_{LO}) and intergranular material (IG ω_{LO}) [25], the latter ascribed to the surface Ni–O modes. Neither band showed large frequency shifts but their relative intensity persistently changed with (i) particle size, varied by using different diameters of zirconia beads for milling, (ii) dispersant, which served for surface modifications of the $Ni_{1-x}O$ particles (NiO_xH_y precipitate or plain H_2O) and (iii) heat treatment (RT, 80, 150, 300 and 500 °C for 0.5 h), the last indirectly influencing the pigment coatings' porosity and the presence of voids. For example, the LO spectra of coatings prepared at 150 °C (Fig. 11A) from $Ni_{1-x}O$ dispersed in water ($Ni_{1-x}O/H_2O$) or with NiO_xH_y precipitate ($Ni_{1-x}O/NiO_xH_y$) exhibited stronger IG ω_{LO} at 539–542 cm^{-1} when smaller beads (0.1 mm) were used for milling, relative to the G ω_{LO} at 563–582 cm^{-1}.

In order to be sure that the G ω_{LO} at 563–582 cm^{-1} and IG ω_{LO} at 538–542 cm^{-1} bands were correctly assigned to grain and surface (intergranular) modes, the $Ni_{1-x}O/NiO_xH_y$ pigment coatings milled with 0.4 mm beads were fired at different temperatures (Fig. 11B). As expected, the corresponding G ω_{LO} and IG ω_{LO} bands remained in the spectra of the coatings heat treated up to 300 °C but when the same pigment coatings were fired at 500 °C, the IG ω_{LO} band considerably diminished in intensity. This agreed with the effect of sintering leading to an increase in the grain size.

In addition, the band at 3647 cm^{-1} disappeared at high temperatures, even though it was clearly seen in the spectra of $Ni_{1-x}O/NiO_xH_y$ and $Ni_{1-x}O/H_2O$ pigment coatings obtained at lower temperatures. These results demonstrated that the band at 3647 cm^{-1} can be ascribed to the surface OH^- groups. Their presence stemmed from the ability of the NiO to split water molecules, as reported by D. Cappus et al. [17]. Actually, NiO is already able to form OH^- groups readily by the interactions of the oxide surface with the residual gas atmosphere or by dosing water. In particular, the crystalline NiO(1 1 1) planes are essential for the formation of OH^- groups, because Ni atoms are exposed in these planes. It has also been noted [17] that the OH^- groups desorbed at 350 °C, agreeing with our results.

To conclude, the presence of the O–H bands, together with the stronger IG ω_{LO} mode at 538–542 cm^{-1} in the spectra of pigment coatings fired at 150 °C (Fig. 11A) and the absence of the former band and less intense IG ω_{LO} band in the spectra of pigment coatings fired at 500 °C, supported the assignment of the former band to the surface OH^- groups of the $Ni_{1-x}O$ grains and the latter to (surface) intergranular material around them. It seemed that the model calculations done by Nikolić et al. [25] reflected well the situation established in the measured LO spectra of porous nanocrystalline $Ni_{1-x}O$ pigment coatings.

3.6.2. *Ex situ IR RA spectra of electrochemically colored and bleached pigment coatings*

Assignment of the LO bands shown in Fig. 11 enabled us to rationalize the structural changes that accompanied coloring/bleaching of $Ni_{1-x}O$ pigment coatings providing the vibrational modes that took part in electrochemical processes. The $Ni_{1-x}O/NiO_xH_y$ pigment coatings obtained by spin coating (3*x*) dispersions milled with 0.4 mm beads and heat treated at 150 °C were selected, colored/bleached in 1 M $LiClO_4$/PC and 0.1 M TBA^+ triflate/PC electrolytes, respectively (Figs. 12 and 13) and their IR RA spectra recorded.

Coloring/bleaching of the $Ni_{1-x}O/NiO_xH_y$ (3*x*, 150 °C, 0.4 mm beads) pigment coating in the 1 M $LiClO_4$/PC electrolyte is shown in Fig. 12. The initial LO spectrum (Fig. 12) showed all the features typical of these coatings (Fig. 11A) but already after the first charging at −1.7 V, the colored pigment coating showed a red frequency shift of the G ω_{LO} mode from 582 to 571 cm^{-1}, while the IG ω_{LO} mode increased in intensity (Fig. 12). Bleaching caused a change of G ω_{LO} and IG ω_{LO} in the reversed manner and IG ω_{LO} blue shifted to 582 cm^{-1}, while the intensity of the IG ω_{LO} mode was considerably decreased. LO spectra of the pigment coatings

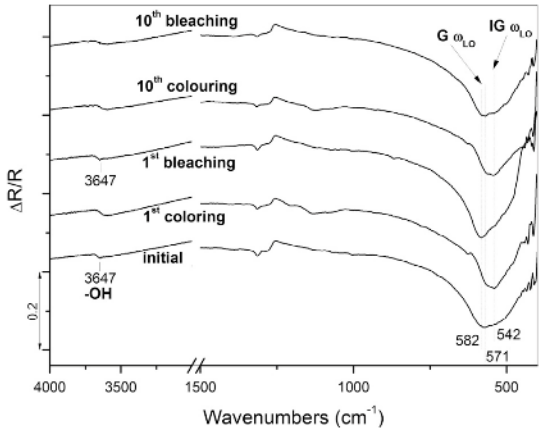


Fig. 12. *Ex situ* IR RA spectroelectrochemical measurements of $Ni_{1-x}O/NiO_xH_y$ pigment coating (3*x*, 150 °C, 0.4 mm beads) in 1 M $LiClO_4$/PC electrolyte.

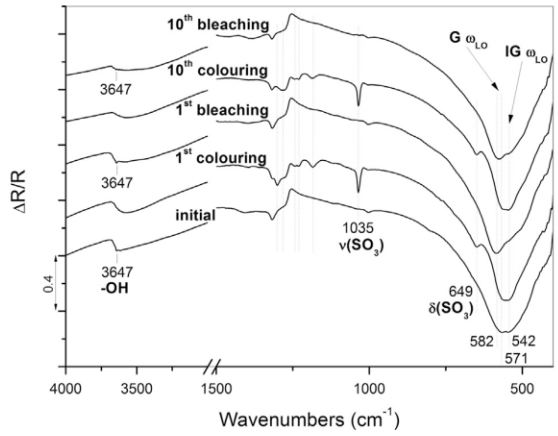


Fig. 13. *Ex situ* IR RA spectroelectrochemical measurements of $Ni_{1-x}O/NiO_xH_y$ pigment coating (3*x*, 150 °C, 0.4 mm beads) in 0.1 M TBA^+ triflate/PC electrolyte.

colored/bleached after the 10th repetitive cycle resembled the first colored/bleached LO spectra in all aspects.

In parallel with changes in the G ω_{LO} and IG ω_{LO} bands, a variation in the OH mode could be detected, despite the intensity of this band is being low (Fig. 12). While the initial spectra still showed a distinct band at 3647 cm^{-1}, this band was lost in the spectra of colored coatings and was replaced by a broader band, which will be commented later. For colored/bleached pigment coatings measured after the 10th cycle, the variations in the corresponding band could not be established because the thickness of the coatings became smaller due to cleaning the coatings before recording their spectra. Cleaning was necessary to get rid of any traces of the electrolyte that might have remained within the pores of the pigment coatings.

Finally, we measured the LO spectra of the $Ni_{1-x}O/NiO_xH_y$ (3*x*, 150 °C, 0.4 mm beads) pigment coatings in 0.1 M TBA^+ triflate/PC electrolyte, in which no lithium ions were present. The LO spectra shown in Fig. 13 showed that charging/discharging of the pigment coatings caused an analogous variation of the IG ω_{LO} and G ω_{LO} modes as shown for the same coating charged/discharged in 1 M $LiClO_4$/PC electrolyte (Fig. 12) but the changes of the band attributed to the OH^- groups were much better seen. The finding that charging/discharging in the lithium-containing and lithium-free electrolytes affected IG ω_{LO} and G ω_{LO} modes in the same way, enabled conclusion that the redox changes of the $Ni_{1-x}O$ could not be attributed to the insertion/deinsertion of lithium ions and the concurrent formation of Li–Ni–O bonds. IG ω_{LO} and G ω_{LO} modes merely reflected the changes in the Ni–O bond order stemming from the change of the oxidation state of nickel ions either on the surface or inside of the $Ni_{1-x}O$ grains.

Interestingly, in the LO spectra of $Ni_{1-x}O/NiO_xH_y$ pigment coatings colored (oxidized) in 0.1 M TBA^+ triflate/PC electrolyte (Fig. 13), a strong band at 1035 cm^{-1} together with weaker bands at 1185, 1230, 1242, 1282 and 1299 cm^{-1} and a band at 649 cm^{-1} appeared. Comparison of these bands with the bands of TBA^+ triflate [42–44] revealed that the triflate anions adsorbed on the surface of colored pigment coatings and could not be removed by washing. The sharpest and most intense band at 1035 cm^{-1} could be ascribed to the symmetric $\nu_s(SO_3)$ stretching mode of triflate anion. Simultaneously, the $\delta_s(SO_3)$ band at 649 cm^{-1} appeared in the spectra of colored pigment coatings. The additional TBA^+ triflate band corresponding to the $\delta_s(CF_3)$ mode reported from approximately 750–770 cm^{-1} in various PEO/PPO-alkali triflate systems [42–44] could hardly be seen in our IR RA spectra of colored pigment coatings (Fig. 13). We thus concluded that the consistent appearance of $\nu_s(SO_3)$ and $\delta_s(SO_3)$ bands in the colored coatings suggested that the triflate anions had become attached to the surface of the grains, filling the voids, and that the majority of them showed the corresponding dipole moment directions perpendicular to the surface of the FTO glass plane. Other bands, noted from 1299 to 1185 cm^{-1} could be assigned to the presence of $\nu_{as}(SO_3)$ and $\nu_s(CF_3)$ modes [43], but deserve separate study, which is planned for the future.

The observation of the triflate anion modes in the spectra of oxidized $Ni_{1-x}O$ pigment coatings was not expected. Namely, Boschloo and Hagfeldt [16] suggested that anions did not play any role in charging/discharging of NiO films in lithium aprotic electrolytes. In contrast to their observation, the CVs of our $Ni_{1-x}O$ pigment coatings were practically identical (see Section 3.4.). This led to the conclusion that the attached anions provided the necessary charge balance for transport of holes within the $Ni_{1-x}O$ grains, facilitated due to their p-type semiconducting properties, as was suggested by Uplane et al. [21].

To sum up, infrared spectra provided evidence of the existence of two NiO stretching modes, separated up to 20 cm^{-1}; the higher one was assigned to Ni–O vibrations inside the NiO grains (G ω_{LO}) and the lower frequency band as the surface Ni–O mode (IG ω_{LO}). The appropriate band assignment could be established without using the results of theoretical studies based on effective medium theories [25] because the G ω_{LO} mode remained practically unchanged, in contrast to the IG ω_{LO} mode, which showed intensity variations and was a function of temperature, size of agglomerates and coloring/bleaching. The OH stretching mode at 3647 cm^{-1}, also found in the spectra of hydrated NiO [29,33], characterized the spectra of the pigment coatings, being sensitive to temperature and the size of the agglomerates. The broad feature of this band when the cycling was done in protic electrolytes resembled that noted in the spectra of NiOOH. This suggested that the surface OH groups became reorganized. The most intriguing observation was the presence of the triflate anions, which became attached to the surface of the discharged coatings via the SO_3^- groups bonded perpendicularly on the surface of the agglomerates.

3.7. EC device properties

Encouraged with a distinct EC effect exhibited by the $Ni_{1-x}O/NiO_xH_y$ cycled in 0.1 M TBA^+ triflate/PC electrolyte (Fig. 10**B**) we assembled flexible EC devices glued together with lithium-free (i.e. BMITFSI in PMMA) and lithium-containing (i.e. LiTFSI-BMITFSI in PMMA) electrolytes with a semi-solid consistency. For all flexible EC devices $Ni_{1-x}O/NiO_xH_y$ pigment coating served as anodically coloring material, while as cathodic materials either PEDOT self-standing film or WO_3 thin film deposited via sputtering technique [24] were used. Two results were envisaged: at first, to get an additional evidence that the $Ni_{1-x}O/NiO_xH_y$ exhibited inherent ability to change color without assistance of lithium insertion/extraction reactions also when other than liquid TBA^+ triflate electrolyte was used and, secondly, to demonstrate that semi-solid EC flexible devices with a transmissive modulation of light can be made from WO_3 thin film and $Ni_{1-x}O/NiO_xH_y$ pigment coating only when combined with lithium-containing electrolyte. For the selected combinations of coatings and thin films in situ UV–vis spectra of the corresponding EC devices were recorded (Fig. 14), together with the values of exchanged charges (Fig. 15) serving to obtain speed of EC changes. All flexible EC devices were first charged at −1.5 V relative to counter electrode coating ($Ni_{1-x}O/NiO_xH_y$), while WO_3 or PEDOT were at positive potentials. Devices with lithium-containing electrolyte (Fig. 14A and C) became colored due to the insertion of lithium ions compensating electrons inserted within a structure of PEDOT or WO_3, while $Ni_{1-x}O/$

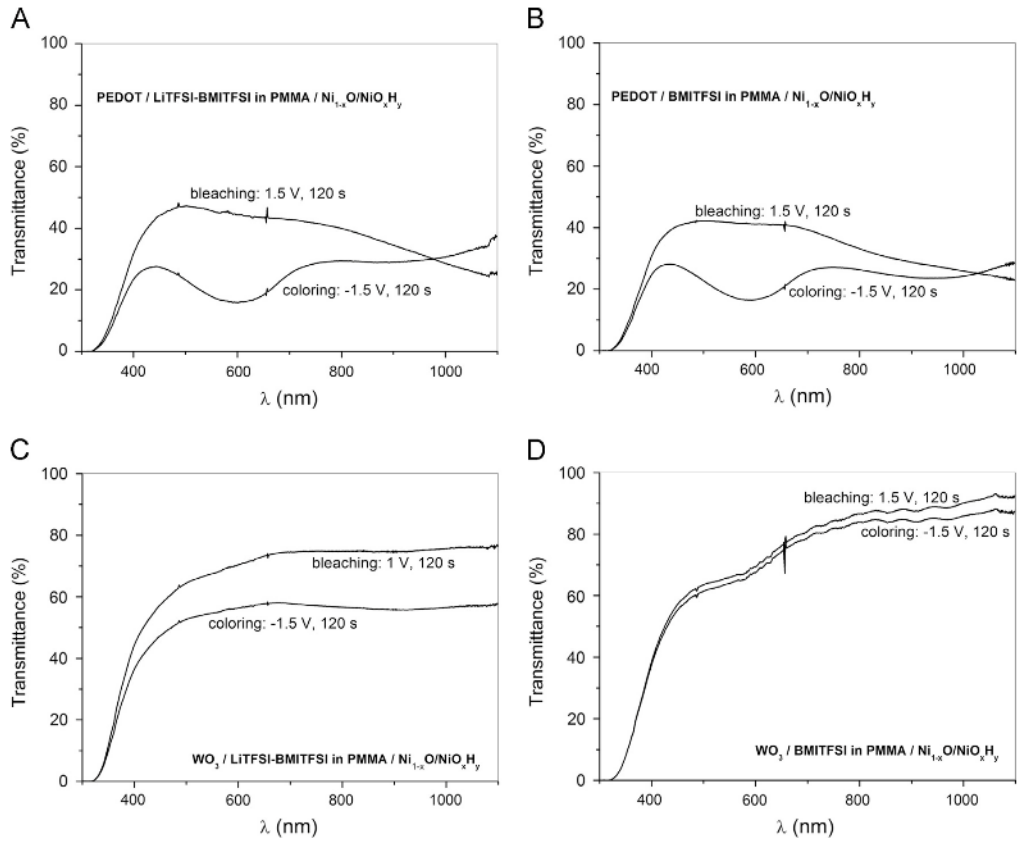


Fig. 14. In situ UV–vis spectra of flexible EC devices glued with a semi-solid PMMA based lithium and lithium-free electrolytes. (A) self-standing PEDOT film and $Ni_{1-x}O/NiO_xH_y$ pigment coating with LiTFSI-BMITFSI in PMMA electrolyte, (B) PEDOT and $Ni_{1-x}O/NiO_xH_y$ pigment coating with BMITFSI in PMMA electrolyte, (C) WO_3 thin film and $Ni_{1-x}O/NiO_xH_y$ pigment coating with LiTFSI-BMITFSI in PMMA electrolyte and (D) WO_3 thin film and $Ni_{1-x}O/NiO_xH_y$ pigment coating with BMITFSI in PMMA electrolyte.

NiO_xH_y changed its redox state from Ni^{2-} to Ni^{3+}. The reverse process happened when potentials were reversed. EC device constructed of PEDOT and $Ni_{1-x}O/NiO_xH_y$ pigment coating and lithium-free electrolyte (BMITFSI in PMMA) colored at negative potential due to the insertion of electrons filling the conjugated states in PEDOT, while $Ni_{1-x}O/NiO_xH_y$ colored due to the extraction of electrons changing nickel oxidation states from Ni^{-2} to Ni^{+3} stabilized by the adsorbed $TFSI^-$ ions, as shown for triflate anions with *ex situ* IR RA spectroelectrochemical measurements (Fig. 13). Both EC devices with lithium-containing electrolyte, i.e. PEDOT / LiTFSI-BMITFSI in PMMA/$Ni_{1-x}O/NiO_xH_y$ (Fig. 14A) and WO_3/LiTFSI-BMITFSI in PMMA/$Ni_{1-x}O/NiO_xH_y$ (Fig. 14C) showed expected coloration and bleaching changes in contrast to the WO_3/BMITFSI in PMMA/$Ni_{1-x}O/NiO_xH_y$ device (Fig. 14D), which was electrochromically deaf. In agreement with the observation of the EC effect of the $Ni_{1-x}O/NiO_xH_y$ cycled in 0.1 M TBA^+ triflate/PC electrolyte (Fig. 10B), EC flexible device made of PEDOT and $Ni_{1-x}O/NiO_xH_y$ glued together with the lithium-free BMITFSI in PMMA electrolyte exhibited characteristic EC effect of both coatings (Figs. 14 and 15B).

Coloring/bleaching speeds of devices were determined as time at which 95% of transmittance modulation was achieved (Fig. 15). Inspection of coloration times revealed that the WO_3/LiTFSI-BMITFSI in PMMA/$Ni_{1-x}O/NiO_xH_y$ device was colored in 70–78 s (21st cycle) outranging PEDOT/$Ni_{1-x}O/NiO_xH_y$ based devices made with LiTFSI-BMITFSI in PMMA (t_{col}=90–98 s in 21st cycle) and BMITFSI in PMMA (94 s in 21st cycle) electrolytes. Bleaching was the fastest for the WO_3/LiTFSI-BMITFSI in PMMA/$Ni_{1-x}O/NiO_xH_y$ (29–26 s), while PEDOT/LiTFSI-BMITFSI in PMMA/$Ni_{1-x}O/NiO_xH_y$ followed with 42–50 s (21st cycle). The PEDOT/BMITFSI in PMMA/$Ni_{1-x}O/NiO_xH_y$ showed values of about 36–38 s in 351th cycle. In was impossible to correlate coloring/bleaching speeds of EC devices as regards the ability of PEDOT, WO_3 and $Ni_{1-x}O/NiO_xH_y$ as individual coatings in lithium-free and lithium-containing electrolytes. Many variables could influence the speed of EC changes, among them the thickness and viscosity of the electrolytes seemed to be the most influencing ones.

4. Conclusions

The preparation of electrochromic paints was found to be useful not only for making flexible EC devices but—as shown here—$Ni_{1-x}O$ coatings made of the corresponding electrochromic pigment dispersions also provided excellent model coatings for studying the electrochemical and EC properties of NiO. The preparation method was borrowed from the technology of paint fabrication, enabling pigment dispersions to be made with a particle size below 50 nm. During deposition, when the water evaporated, the dispersion shrank and formed coatings consisting of closely packed agglomerates and of high optical quality, i.e., low haze. This process was spontaneous and was probably governed by strong particle-to-particle interactions, enabling also the formation of coatings from $Ni_{1-x}O/H_2O$ pigment dispersions, in which no specific dispersant was used.

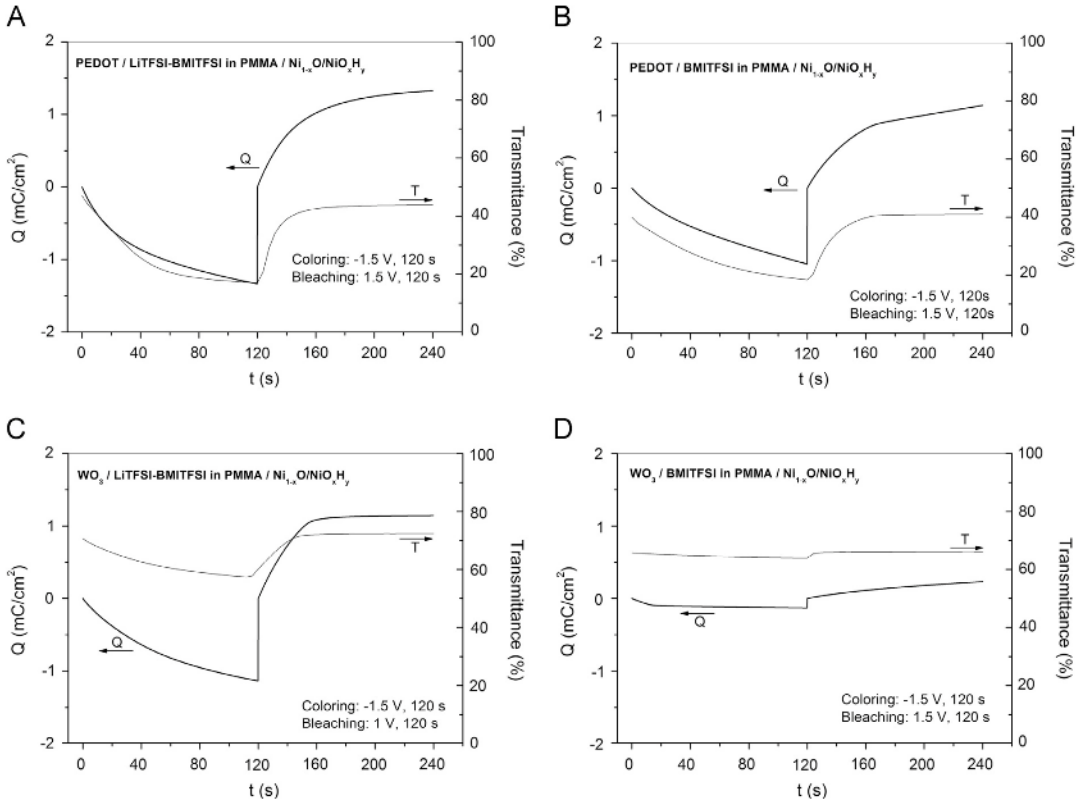


Fig. 15. EC changes (λ = 634 nm) of flexible EC devices glued with a semi-solid PMMA based lithium and lithium-free electrolytes charged at +1.5 and −1.5 V relative to counter-electrode film ($Ni_{1-x}O/NiO_xH_y$), while WO_3 and PEDOT were at positive potential: (A) self-standing PEDOT film and $Ni_{1-x}O/NiO_xH_y$ pigment coating with LiTFSI-BMITFSI in PMMA electrolyte, (B) PEDOT and $Ni_{1-x}O/NiO_xH_y$ pigment coating with BMITFSI in PMMA electrolyte, (C) WO_3 thin film and $Ni_{1-x}O/NiO_xH_y$ pigment coating with LiTFSI-BMITFSI in PMMA electrolyte and (D) WO_3 thin film and $Ni_{1-x}O/NiO_xH_y$ pigment coating with BMITFSI in PMMA electrolyte.

Electrochemical measurements performed on $Ni_{1-x}O$ pigment coatings revealed that coloring/bleaching reactions could be considered essentially as surface reactions facilitated by the small size of the agglomerates (from 30 to 50 nm) and $Ni_{1-x}O$ grains (from 5–8 nm). The most intense coloring appeared during the first anodic current wave for all pigment coatings, even those that were potentially cycled in TBA^+ triflate/PC electrolyte. Initial (as-prepared) pigment coatings exhibited transmittance that was between the transmittance of the colored and bleached states of the coatings. Pigment coatings showed an immediate electrochromic response in 0.1 M TBA^+ triflate/PC and 1 M $LiClO_4$/PC electrolytes.

The explanation for the electrochemical behavior of the pigment coatings was sought from the IR spectra, revealing the presence of two Ni–O stretching modes attributed to the Ni–O grains or NiO agglomerates (G ω_{LO}) and the surface Ni–O mode (IG ω_{LO}). One of the bands, i.e., the G ω_{LO} mode, remained practically unchanged in contrast to the IG ω_{LO} mode, which showed intensity variations with the temperature of curing and the size of the agglomerates. Accordingly, this band was assigned to the mode of the surface sites of the grains and/or agglomerates.

The presence of the native OH groups was established from the OH stretching mode at 3647 cm^{-1} found—as expected—in the spectra of $Ni_{1-x}O/NiO_xH_y$ and also in the spectra of $Ni_{1-x}O/H_2O$. Observation of the corresponding band in the latter coatings was especially persuasive for the existence of native OH groups on the surface of the $Ni_{1-x}O$ agglomerates. $OH_{surface}$ groups formed on the defect sites of the $Ni_{1-x}O$ surface, the origin of which was explained by the high catalytic activity of the substoichiometric nickel oxide.

The results revealed that it was not possible to attribute coloring/bleaching to the intercalation of cations within the $Ni_{1-x}O$ grains but only to adsorption/desorption on the surface of the grain agglomerates, independently confirmed for the $Ni_{1-x}O$ thin films cycled in TBA^+ triflate/PC lithium-free electrolyte. The coloring/bleaching process was accompanied by adsorption/desorption of triflate anions, identified in the IR spectra only for colored states, as SO_3 modes lying perpendicular to the coatings surface.

The attachment/de-attachment of perchlorate anions in the 1 M $LiClO_4$/PC electrolyte as a function of potential was not clearly detected. This can be understood as being due to the much stronger interactions (H-bond) of the SO_3 groups with hydroxyls on the surface of the $Ni_{1-x}O$ grains. The EC effect of the $Ni_{1-x}O$ pigment coatings is facile due to the inherent semiconductivity of the $Ni_{1-x}O$ pigment originating from the Ni^{+2}/Ni^{+3} sites in the structure of the of $Ni_{1-x}O$.

It is clear that the EC effect of NiO is a multifaceted problem, since it is affected by many variables: the chemical composition of the NiO (bunsenite) films depending on the preparation route used, the films' porosity and surface structure and p-type semiconductivity. NiO is an interesting electrochromic compound, which deserves more study in the future, especially in relation to its p-type semiconductivity and its role in obtaining an EC effect.

Acknowledgments

This work has received funding from the European Community's Seventh Framework Program (Grant Agreement No. 200431,

Innoshade) and the Slovenian Research Agency (Program P1-0030). The authors wish to thank Laura Bertus–Manceriu for helping in making electrochromic devices and fruitful discussion.

References

[1] C.G. Granqvist, Handbook of Inorganic Electrochromic Materials, Elsevier Science, Amsterdam (1995) 339–378.
[2] H.-J. Ahn, H.-S. Shim, Y.-S. Kim, C.-Y. Kim, T.-Y. Seong, Synthesis and characterization of NiO–Ta_2O_5 nanocomposite electrode for electrochromic devices, Electrochemistry Communications 7 (2005) 567–571.
[3] A. Gotoh, H. Uchida, M. Ishizaki, T. Satoh, S. Kaga, S. Okamoto, M. Ohta, M. Sakamoto, T. Kawamoto, H. Tanaka, M. Tokumoto, S. Hara, H. Shiozaki, M. Yamada, M. Miyake, M. Kurihara, Simple synthesis of three primary color nanoparticle inks of Prussian blue and its analogues, Nanotechnology 18 (2007) 345609, 1–6.
[4] S. Hara, H. Shiozaki, A. Omura, H. Tanaka, M. Tokumoto, T. Kawamoto, M. Tokumoto, M. Yamada, A. Gotoh, M. Kurihara, M. Sakamoto, Color-switchable glass and display devices fabricated by liquid processes with electrochromic nanoparticle ink, Applied Physics Express 1 (2008) 104002, 1–3.
[5] R. Ruffo, A. Celik-Cochet, U. Posset, C.M. Mari, G. Schottner, Mechanistic study of the redox process of an in situ oxidatively polymerised poly(3,4-ethylenedioxythiophene) film, Solar Energy Materials and Solar Cells 92 (2008) 140–145.
[6] M. Mihelčič, I. Jerman, F. Švegl, A. Šurca Vuk, L. Slemenik Perše, J. Kovač, B. Orel, U. Posset, Electrochromic $Ni_{1-x}O$ pigment coatings and plastic film-based $Ni_{1-x}O/TiO_2$ device with transmissive light modulation, Solar Energy Materials and Solar Cells 107 (2012) 175–187.
[7] F. Švegl, A. Šurca Vuk, M. Hajzeri, L. Slemenik Perše, B. Orel, Electrochromic properties of $Ni_{(1-x)}O$ and composite $Ni_{(1-x)}O$-polyaniline thin films prepared by the peroxo soft chemistry route, Solar Energy Materials and Solar Cells 99 (2012) 14–25.
[8] S. Green, J. Backholm, P. Georen, C.G. Granqvist, G.A. Niklasson, Electrochromism in nickel oxide and tungsten oxide thin films: Ion intercalation from different electrolytes, Solar Energy Materials and Solar Cells 93 (2009) 2050–2055.
[9] F. Decker, S. Passerini, R. Pileggi, B. Scrosati, The electrochromic process in non-stoichiometric nickel oxide thin film electrodes, Electrochimica Acta 37 (1992) 1033–1038.
[10] M. Li, A. Patra, Y. Sheynin, M. Bendikov, Hexyl-derivatized poly(3,4-ethylenedioxyselenophene): novel highly stable organic electrochromic material with high contrast ratio, high coloration efficiency and low-switching voltage, Advanced Materials 21 (2009) 1707–1711.
[11] A.C. Sonavane, A.I. Inamdar, E.S. Dalavi, H.P. Deshmukh, P.S. Patil, Simple and rapid synthesis of NiO/PPy thin films with improved electrochromic performance, Electrochimica Acta 55 (2010) 2344–2351.
[12] T. Kubo, Y. Nishikitani, Y. Sawai, H. Iwanaga, Y. Sato, Y. Shigesato, Electrochromic properties of LixNiyO films deposited by magnetron sputtering, Journal of the Electrochemical Society 156 (2009) H629–H633.
[13] S. Passerini, B. Scrosati, Characterization of non-stoichiometric nickel oxide thin film electrodes, Journal of the Electrochemical Society 141 (1994) 889–895.
[14] H. Huang, J. Tian, W.K. Zhang, Y.P. Gan, X.Y. Tao, X.H. Xia, J.P. Tu, Electrochromic properties of porous NiO thin film as a counter electrode for NiO/WO_3 complementary electrochromic window, Electrochimica Acta 56 (2011) 4281–4286.
[15] S.H. Park, J.W. Lim, S.J. Yoo, I.Y. Cha, Y.-E. Sung, The improving electrochromic performance of nickel oxide film using aqueous N,N-dimethylaminoethanol solution, Solar Energy Materials and Solar Cells 99 (2012) 31–37.
[16] G. Boschloo, A. Hagfeldt, Spectroelectrochemistry of nanostructured NiO, Journal of Physical Chemistry B 105 (2001) 3039–3044.
[17] D. Cappus, C. Xu, D. Erlich, B. Dillmann, C.A. Ventrice, K. Al Shamery, H. Kuhlenbeck, H.J. Freud, Hydroxyl groups on oxide surfaces—NiO(100), NiO (111) and CR2O3(111), Chemical Physics 177 (1993) 535–546.
[18] G.A. El-Shobaky, N.S. Petro, Effect of dopping on the electrical properties and surface characteristics of NiO catalyst, Surface Technology 9 (1979) 415–426.
[19] W.-L. Jang, Y.-M. Lu, W.-S. Hwang, W.-C. Chen, Electrical properties of Li-doped NiO films, Journal of the European Ceramic Society 30 (2010) 503–508.
[20] N. Giordano, E. Cavaterra, D. Zema, Semiconductivity and catalytic behavior of doped nickel oxides in the low-temperature oxidation of ammonia, Journal of Catalysis 5 (1966) 325–331.
[21] M.M. Uplane, S.H. Mujawar, A.I. Inamdar, P.S. Shinde, A.C. Sonavane, P.S. Patil, Structural, optical and electrochromic properties of nickel oxide thin films grown from electrodeposited nickel sulphide, Applied Surface Science 253 (2007) 9365–9371.
[22] I. Jerman, M. Koželj, B. Orel, The effect of polyhedral oligomeric silsesquioxane dispersant and low surface energy additives on spectrally selective paint coatings with self-cleaning properties, Solar Energy Materials and Solar Cells 94 (2010) 232–245.
[23] I. Jerman, M. Mihelčič, D. Verhovšek, J. Kovač, B. Orel, Polyhedral oligomeric silsesquioxane trisilanols as pigment surface modifiers for fluoropolymer based thickness sensitive spectrally selective (TSSS) paint coatings, Solar Energy Materials and Solar Cells 95 (2011) 423–431.
[24] H. Moulki, D.H. Park, B.-K. Min, H. Kwon, S.-J. Hwang, J.-H. Choy, T. Toupance, G. Campet, A. Rougier, Improved electrochromic performances of NiO based thin films by lithium addition: from single layers to devices, Electrochimica Acta 74 (2012) 46–52.
[25] M.V. Nikolić, V. Blagojević, K.M. Paraskevopoulos, T.T. Zorba, D. Vasiljević-Radović, P.M. Nikolić, M.M. Ristić, Far infrared properties of sintered NiO, Journal of the European Ceramic Society 27 (2007) 469–474.
[26] P.J. Gielisse, J.N. Plendl, L.C. Mansur, R. Marshall, S.S. Mitra, R. Mykolajewycz, A. Smakula, Infrared properties of NiO and CoO and their mixed crystals, Journal of Applied Physics 36 (1965) 2446–2450.
[27] I.G. Austin, B.D. Clay, C.E. Turner, Optical absorption of small polarons in semiconducting NiO and CoO in the near and far infra-red, Journal of Physics C 1 (1968) 1418–1434.
[28] S. Mochizuki, M. Satoh, Infrared spectra of single-crystal NiO at high temperatures, Physica Status Solidi b 106 (1981) 667–674.
[29] C. Faure, C. Delmas, M. Fouassier, Characterization of a turbostratic a-nickel hydroxide quantitatively obtained from an NiSO4 solution, Journal of Power Sources 35 (1991) 279–290.
[30] X.H. Xia, J.P. Tu, J. Zhang, X.L. Wang, W.K. Zhang, H. Huang, Electrochromic properties of porous NiO thin films prepared by a chemical bath deposition, Solar Energy Materials and Solar Cells 92 (2008) 628–633.
[31] V. Srinivasan, J.W. Weidner, An electrochemical route for making porous nickel oxide electrochemical capacitors, Journal of the Electrochemical Society 144 (1997) L210–L213.
[32] H. Sato, T. Minami, S. Takata, T. Yamada, Transparent conductive p-type NiO thin films prepared by magnetron sputtering, Thin Solid Films 236 (1993) 27–31.
[33] A. Šurca, B. Orel, B. Pihlar, P. Bukovec, Optical, spectroelectrochemical and structural properties of sol–gel derived Ni-oxide electrochromic film, Journal of Electroanalytical Chemistry 408 (1996) 83–100.
[34] A. Šurca, B. Orel, B. Pihlar, Sol–gel derived hydrated nickel oxide electrochromic films: optical, spectroelectrochemical and structural properties, Journal of Sol–Gel Science and Technology 8 (1997) 743–749.
[35] A. Šurca, B. Orel, R. Cerc Korošec, P. Bukovec, B. Pihlar, Structural and electrochromic properties of sol–gel derived Ni(Si)-oxide films, Journal of Electroanalytical Chemistry 433 (1997) 57–72.
[36] A. Šurca, B. Orel, B. Pihlar, Characterisation of redox states of Ni(La)-hydroxide films prepared via the sol-gel route by ex situ IR spectroscopy, Journal of Solid State Electrochemistry 2 (1998) 38–49.
[37] N.T. McDevitt, W.L. Baun, Infrared absorption study of metal oxides in the low frequency region (700–240 cm^{-1}), Spectrochimica Acta 20 (1964) 799–808.
[38] C. Pecharroman, J.E. Iglesias, A method for the determination of infrared optical constants from reflectance measurements on powdered samples, Journal of Physics: Condensed Matter 6 (1994) 7125–7141.
[39] C. Pecharroman, J.E. Iglesias, Effective dielectric properties of packed mixtures of insulator particles, Physical Review B 49 (1994) 7137–7147.
[40] F. Gervais, B. Piriou, Temperature dependence of transverse-optic and longitudinal-optic modes in TiO_2 (rutile), Physical Review B 10 (1974) 1642–1654.
[41] A.F. Wells, Structural Inorganic Chemistry, Oxford University Press, Oxford (1962) 454–479.
[42] B.L. Papke, M.A. Ratner, D.F. Shriver, Vibrational spectroscopic determination of structure and ion pairing in complexes of poly(ethylene oxide) with lithium salt, Journal of the Electrochemical Society 129 (1982) 1434–1438.
[43] W. Huang, R. Frech, R.A. Wheeler, Molecular structures and normal vibrations of CF_3SO_3- and its lithium ion pairs and aggregates, Journal of Physical Chemistry 98 (1994) 100–110.
[44] C.P. Rhodes, R. Frech, A symmetry-based analysis of Raman and infrared spectra of the compouds (poly(ethylene oxide))$_3$LiCF_3SO_3 and (poly(ethylene oxide))NaCF_3SO_3, Solid State Ionics 136–137 (2000) 1131–1137.

Chapter 8

Preparation of Photocatalytic Optically Transparent Coatings from Pigment Dispersions

The encouraging results with non-POSS dispersant described in the previous chapter led us to investigate alternative dispersants for the preparation of active nanopigmented coatings. P-25 (Degussa) was selected as the most commonly used photocatalytic TiO_2 pigment, which also exhibits a superhydrophilic effect. The idea behind this study was to prepare functional photocatalytic TiO_2 coatings from pigment particles in the limiting case even without dispersant (bare TiO_2 particles), because any dispersant present on the TiO_2 particles drastically hinders its photocatalytic properties.

In order to upgrade and follow research done on $Ni_{1-x}O$ coated with NiO_xH_y dispersant, P25 was milled in the presence of NiO_xH_y, while for keeping the pigment particles together, titanium (IV) isopropoxide (TiP) was used as adhesion promoter. Another reason for using NiO_xH_y as dispersant derived from the work of Yu et al. [94], showing that $Ni(OH)_2$ acted as a very efficient surface modifier of $TiO_2/Ni(OH)_2$ core–shell nanoparticles, imparting them 223x higher hydrogen production from water splitting. The primary mechanism is the reduction of Ni^{+2} to Ni^0, which occurs by irradiation with UV light, and the resulting core-shell nanoparticle changes the occupancy and recombination gaps with water, or the organic pollutants that are in contact with the surface of the TiO_2 pigment. In our study, we used NiO_xH_y instead of $Ni(OH)_2$ surface modifier for TiO_2 [90], thereby achieving a significantly higher photocatalytic effect.

P25, P25/TiP, P25/NiO_xH_y and P25/$Ni_{1-x}O$ pigment coatings were prepared in order to test photosuperhydrophilic (PSH) and photocatalytic (PCA) activities. PSH and PCA studies were performed in the Laboratory for Environmental Research in Nova Gorica.

All investigated coatings showed fairly fast conversion of the water contact angle (CA) from hydrophobic-to-hydrophilic (Figure 8.1). The CA value for P25 and P25/TIP coatings after 30 minutes of UV radiation was around 8°. P25/NiO_xH_y and P25/$Ni_{1-x}O$ coatings exhibited higher CA values: 13.5° and 16°, respectively. The CA for water of the compared reference material Pilkington Activ™ Glass was 36° after 240 min of UV irradiation[95].

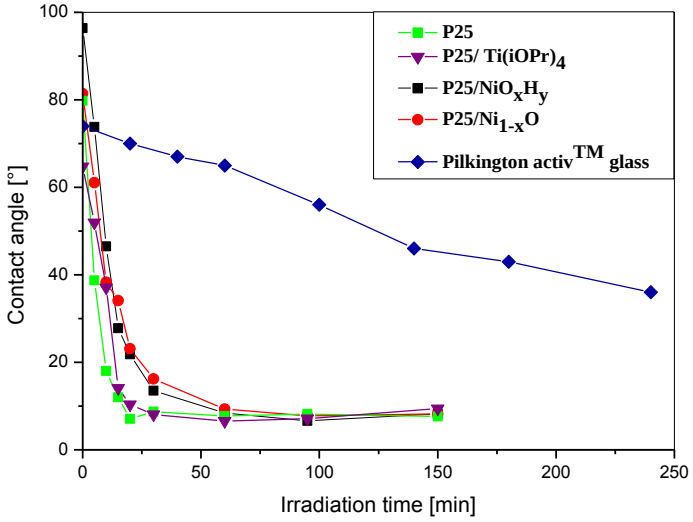


Figure 8.1: Water contact angles on the different coatings as a function of irradiation time. The reference used was Pilkington Activ^{TM} glass [95].

Calculations of k_1 values, which is the rate constant of formation of HTPA, revealed good photocatalytic activity for all tested coatings. PCA activity decreased in the order of P25 > P25/TiP > P25/NiOxHy > P25/NiO (Figure 8.2). The selected commercial sample, tested with the same procedure, serving as reference material, was Pilkington Activ^{TM} Glass, for which the k_1 value is 2.1× 10^{-9} M min^{-1} [95].

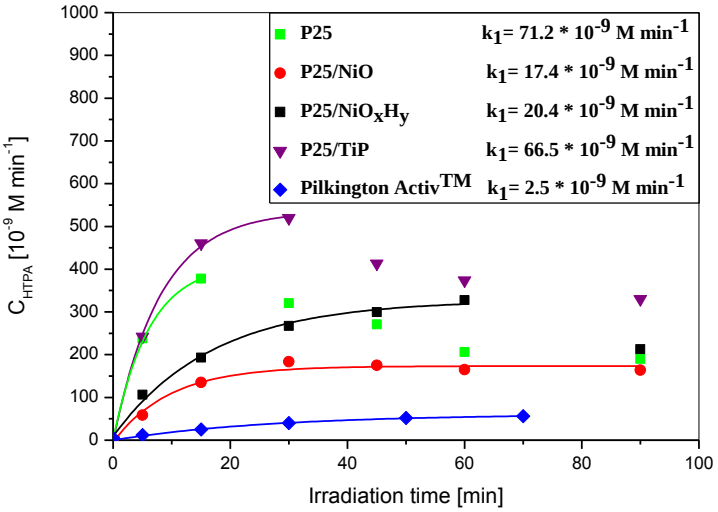


Figure 8.2: Evolution of the concentration of HTPA with irradiation time on the different coatings. Lines represent the fitting of the obtained data to the kinetic model; $k1$ values obtained from these fittings are included in the legend.

Similarly as shown for electrochromic TiO_2 layers, photocatalytic TiO_2 coatings negligibly scatter visible light, confirming the effectiveness of the process of grinding pigments. It is also important that the latter layers were made at 150 °C and calcination,

which is conventionally used in the manufacture of photocatalytic TiO_2 layers, was not necessary. Photocatalytic optically transparent coatings are a significant challenge due to adherence, scratch resistance and low haze, in addition to applicability on plastic substrates being difficult to achieve simultaneously.

My contribution consisted of sample and dispersion preparation and part of the writing.

Copyright © 2014 American Scientific Publishers
All rights reserved
Printed in the United States of America

Journal of
Surfaces and Interfaces of Materials
Vol. 2, 280–287, 2014

RESEARCH ARTICLE

Preparation of Photocatalytic Optically Transparent Coatings from Pigment Dispersions

M. Mihelčič[1], B. Orel[1,*], F. Fresno[2], U. Lavrenčič Štangar[2], and R. Kunič[3]

[1] National Institute of Chemistry, Hajdrihova Ljubljana, 19, 1000, Slovenia
[2] Laboratory for Environmental Research, University of Nova Gorica, Vipavska 13, 5001 Nova Gorica, Slovenia
[3] Faculty for Civil and Geodetic Engineering, Jamova 2, 1000 Ljubljana, Slovenia

A series of thin pigment particle coatings was prepared by milling titania pigment (P25, Evonik Degussa) with different zirconia beads in butanol providing pigment particle dispersions, which enabled the deposition of optical coatings with haze below 2%, obtained from the total diffuse and total transmittance (DT/TT%) values of the coatings in the visible spectral range. P25 was used uncombined and combined with $Ti(iOPr)_4$, nickel oxyhydroxide and NiO pigment, giving the P25, P25/TIP, P25/NiO_xH_y and P25/NiO coatings, respectively, which showed different photosuperhydrophylic (PSH) and photocatalytic (PCA) effects. PSH effect was determined from the contact angle (CA) measurements of water, which revealed that all the coatings showed a remarkable hydrophobic-to-hydrophilic conversion after 30 min of irradiation with UV light. PCA effect was studied using as model reaction the hydroxylation of terephthalic acid (TPA) to the highly fluorescent hydroxyterephthalic acid (HTPA), according to a procedure described. A simplified kinetic model that considers zero-order kinetics for the formation of HTPA from TPA revealed that the degradation rate constants (k_1) for the P25 and P25/TIP coatings were higher than for the P25/NiO_xH_y and P25/NiO coatings. All investigated coatings showed much stronger PSH and PCA effects compared to the Pilkington Activ™ Glass and only slightly higher haze.

Delivered by American Scientific Publishers

Keywords: P25, Photocatalytic Effect, Photosuperhydrophylic Effect, Pigment Particle Coatings, Optical Properties, Haze, Pilkington Activ™ Glass.

1. INTRODUCTION

Titanium dioxide (TiO_2) is one of the most extensively studied materials suitable for many industrial applications due to its non-toxicity, chemical stability and low cost. TiO_2 is used as heterogeneous catalyst (e.g., in mixed vanadia/titania catalyst for selective oxidation reactions) and photocatalyst, as gas sensor and in electric devices as varistor.[2] The most widely used application of TiO_2 is as white pigment in paints and as UV absorber in cosmetic products. Nanostructured TiO_2 in anatase form attracted attention in dye sensitized photoelectrochemical cells, Li-accumulators and also as electrochromic (EC) coating. TiO_2 shows strong cathodic electrochromism observed by the double injection of electrons and lithium ions into the film's interior, leading to the reduction of Ti^{4+} and formation of small polarons.[3]

Here, we report about a simple and robust wet process for making dispersion of anatase TiO_2 pigment particles, which enabled the deposition of photocatalytic TiO_2 coatings with distinguished photocatalytic (PCA, for short) and photosuperhydrophylic (PSH, for short) effect. We focused here on the deposition of transparent (no haze) TiO_2 coatings prepared at mild processing conditions (~150 °C) enabling the fabrication of PCA and PSH coatings on plastic foils and plastic glazing. Even though many nanocrystalline anatase powders are commercially available we deliberately chose here anatase-rutile made by Evonik Degussa (P25) due to its excellent and well established photocatalytic properties. The procedure used in this study has been developed in our previous investigations on NiO[4–6] and TiO_2[7,8] electrochromic coatings deposited on flexible foils and solar absorber coatings with high spectral selectivity, which are all characterized by homogeneous distribution of pigment particles[9] and are suitable for deposition with commercial coil-coating application techniques.

Low temperature processed TiO_2 pigmented coatings on plastic conductive foils are not new and have been made mainly for dye sensitized photelectrochemical cells

*Author to whom correspondence should be addressed.

 2164-7542/2014/2/280/008 doi:10.1166/jsim.2014.1070

(DSPEC) by pressing of oxide layers providing porous coatings (press method)[10,11] and by the lift-off process developed by Durr.[12] In the latter process, the TiO_2 layer is first applied to a thin gold layer on glass substrate. After sintering, the TiO_2 layer is removed from the glass by dissolving the gold layer. The TiO_2 layer is then transferred onto a transparent conductive oxide (TCO) coated polyethylene terephtalate (PET) film by application of high pressure. Low-temperature chemical sintering of suspensions based on nanocrystalline TiO_2, ethanol and HCl (1 M) has been reported recently, apparently giving good photoanodes for DSPEC cells.[13] Obviously, these approaches are not suitable for making PCA and PSH optical coatings on glass and flexible foils due to the too high haziness of the film-pressed titania particles.

The photocatalytic activity of TiO_2 has been extensively studied in the past. It has been already established that, when semiconductor particles are exposed to radiation with energy above the band gap energy, photoexcitation occurs which leads to the formation of excitons followed by charge separation and the creation of electron–hole pairs.[14,15] These photogenerated charges can be recombined either on the semiconductor particle surface or in bulk, but a certain part of them reaches the TiO_2 particle surface, where oxidation and reduction of adsorbed molecules take place (PCA effect). The most studied application of the PCA effect is the degradation of organic pollutants, in which the main oxidative species are hydroxyl radicals formed upon hole trapping by –OH groups and water molecules adsorbed onto the semiconductor surface. In a very related process, photoexcitation makes the surface of the TiO_2 particles superhydrophilic, which is known as photo-induced PSH effect and, in combination with PCA, endows TiO_2 with a wide range of applications related to anti-fogging, self-cleaning and self-sterilizing materials.[16] Many oxides based on Cd, Ce, Fe, Sb, Sn, W, and Zr exhibit PCA and/or PSH effect, TiO_2 being the most studied one[15–22] because it exhibits strong oxidizing power, cost effectiveness and long-term stability against photocorrosion and chemical corrosion.[23–27] In addition, it also shows activity for hydrogen production by photocatalytic water splitting.[14,16]

In order to enhance PCA, PSH and water splitting efficiency, TiO_2 has been modified by non-metal doping (N, C, etc.), dye sensitisation,[28] metal doping[18,29,30] and the deposition of platinum and other noble metals as co-catalysts.[31–34] With respect to the latter case, due to the high cost of Pt, numerous efforts have been undertaken to replace it with low-cost alternatives such as NiO and CuO,[28,35] which represents one of the motivations of the present study.

For example, enhanced photocatalytic H_2-production from methanol aqueous solutions has been obtained with nickel-intercalated titanate nanotubes[36] and with mesoporous TiO_2-supported NiO photocatalysts prepared by a single-step sol–gel process.[37,38] For our study, the most relevant is the work of Yu et al.,[39] who has reported an excellent H_2 production efficiency for $Ni(OH)_2$ cluster-modified TiO_2 ($Ni(OH)_2/TiO_2$) nanocomposite photocatalysts. The corresponding material has been prepared by a simple precipitation method using Degussa P25 TiO_2 powder (P25, for short) as support and $Ni(NO)_3$ as precursor, which changed to $Ni(OH)_2$ after the addition of NaOH to the dispersion of P25 and $Ni(NO)_3$ aqueous solution. The corresponding cluster-modified TiO_2 ($Ni(OH)_2/TiO_2$) nanocomposite exhibits H_2 production exceeding 223 times that of P25. The procedure was carried out at mild processing conditions (80 °C), which is important for the deposition of PCA coatings on flexible plastic foils, which was one of the aims of this study. It should be also noted that XRD spectra of the nanocomposite do not show changes in P25 structure, indicating that the deposited $Ni(OH)_2$ clusters do not incorporate into the lattice of TiO_2 and due to the low temperature processing the $Ni(OH)_2$ clusters on the surface of TiO_2 have no obvious influence on its crystallite size and morphology. Compared to the pure P25 no great change in the absorption edge of TiO_2 in the $Ni(OH)_2/TiO_2$ composites was observed, which further implies that $Ni(OH)_2$ was not incorporated into the lattice of TiO_2, but is only deposited on its surface, confirming the formation of core shell nanoparticles.

In the present work, two main modifications of the above-reported procedure were done: instead of the precipitation of $Ni(OH)_2$ onto the surface of P25 pigment, Ni oxohydroxide (NiO_xH_y)[4,5] was used being attached onto the pigment surface by ball milling. Two main benefits were expected regarding the physical properties of the final coatings: NiO_xH_y would act as dispersant and binder, while ball milling would provide fine dispersion with small P25 particles, thus enabling the deposition of coatings with low haze.

The use of NiO_xH_y as dispersant/binder for the pigment particle coating is not new.[4,5,40] This paste-like material made of small nanoparticles (Fig. 1) is of black colour due to the Ni^{+2}/Ni^{+3} species showing high efficacy for dispersing the NiO pigment, enabling the deposition of NiO/NiO_xH_y coatings with haze up to 7% (depending on thickness) and excellent electrochromic properties.[4] NiO_xH_y strongly bonds on the NiO pigment surface and also bonds together the NiO particles, which is a prerequisite for the deposition of the NiO electrochromic pigment coatings by one of the simple (spraying, dip coating) or more sophisticated (i.e., coil-coating, roll-to-roll) deposition techniques (Coatema, DE; www.coatema.de). Due to the excellent experiences with the NiO/NiO_xH_y coating, photocatalytic TiO_2 pigment particle coatings were prepared in this study.

From a functional point of view, it is possible to conceive that NiO_xH_y species may act, similarly to NiO and $Ni(OH)_2$ (*vide supra*), as an efficient co-catalyst for TiO_2,

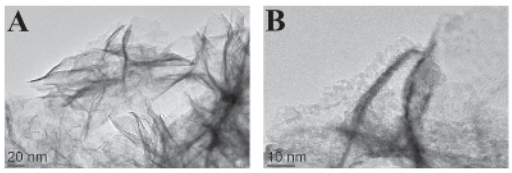


Fig. 1. TEM micrograph of NiO_xH_y (for details see Ref. [4]).

providing the system with improved photocatalytic activity with respect to bare titania coatings. Thus, the existence of Ni^{3+}/Ni^{2+} redox couples,[41] proven by XPS measurements on the $Ni_{1-x}O$ pigment,[4] close to the TiO_2 surface may provide visible-light absorption to the otherwise transparent titania coatings, and enhance charge separation and transfer between the TiO_2 pigment particles and adsorbed reactants.

In addition, by using NiO_xH_y we avoided the use of organics,[42] either polyhedral oligomeric silsesquioxanes, which have been found to be excellent dispersant for TiO_2[26,42] and black spinel solar-absorbing pigment,[9,43] or trialkyltrialkoxysilanes-based dispersants,[33,41] which are all well known dispersants for various pigments but hamper photoatalytic activity of P25 pigment. Beside the $P25/NiO_xH_y$ coating, additional photocatalytic P25 based coatings were prepared with the help of $Ti(iOPr)_4$ (TIP, for short) and the observed PCA and PSH effects compared to the photocatalytic efficiency of the bare P25 pigment milled in butanol, without any additional binder or surfactant. Even though the bare P25 coatings did not reach the mechanical consistency of the other coatings, the corresponding coating was used as a reference for the obtained photocatalytic activity of the other coatings.

This work is structured as follows. At first, the preparation route for making P25 dispersions is given followed by the description of the coating morphology inferred from the SEM micrographs and optical properties, providing information about the haze of the coatings. Photocatalytic and superhydrophylic properties, which represent the main focus of this study, are presented next.

2. EXPERIMENTAL DETAILS

2.1. Preparation of Pigment Dispersions

In order to prepare P25 dispersions, 10 wt% of as-received P25 (Evonik Degussa) powder was first dispersed in ultrasonic bath in butanol (Sigma-Aldrich). Then, the P25/butanol was ground with ZrO_2 pearls in a Dyno-mill Research Laboratory agitator bead mill (WAB, Willy A. Bachofen AG Maschinenfabrik) for 1 h at 3600 rpm, providing P25 (*coating* 1). P25/NiO (*coating* 2) pigment dispersions, used also for the deposition of the corresponding coatings, was prepared by adding the NiO (Inframat) (1 w/w% per P25) powder to the P25 pigment dispersion and co-ground with the P25 dispersion with ZrO_2 beads. $P25/NiO_xH_y$ pigment dispersions (*coating* 3) were made by dispersing first the P25 pigment in butanol with added NiO_xH_y (10 w/w% vs. powder) as reported in Ref. [4] and the corresponding mixture was then milled in a Dyno-mill using the zirconia bead having diameters of 0.4, 0.2 and 0.1 mm, providing dispersions with different particle size. The ratio between the zirconia beads and the modified P25 powder was 2:1 (in weight) for all dispersions. In order to improve the adhesion of the coatings to the substrates, at the end of the milling process $Ti(iOPr)_4$ was added together with glacial acetic acid ($AcOH_{gl}$) to the P25 pigment dispersion enabling the deposition of the $P25/Ti(iOPr)_4$ coating (*coating* 4).

2.2. Deposition of Pigment Coatings

Pigment coatings were deposited on FTO glass plates (Pilkington, 14 Ω/cm^2), fused quartz plates and conductive polymeric substrate by spin-coating techniques. By repeating the spinning deposition cycles (1 cycle: spinning frequency = 1000 RPM, time = 40 s), the thickness of the deposited coatings 1–4 was varied from 100 nm (1 × spinning) up to 400 nm (4 × spinning). A dip-coating deposition technique was also used, giving reproducible results in terms of coating thickness, morphology and pigment particle distribution. The samples were cut from larger pieces of the corresponding coatings, part of which also served for the thickness measurements and determination of haze. Based on our experience with the deposition of $Ni_{1-x}O$,[4–6] metatitanic acid powders[7] and copper manganese spinel sol–gel based pigment dispersions,[9] the corresponding P25 and NiO pigment dispersions are also suitable for continuous deposition via the coil-coating technique on flexible plastic foils. All coatings were heat treated for 1/2 h at 150 °C. Typical examples of the P25 coating deposited on FTO glass (A) and ITO PET flexible foil (B) (for description see Table I) by 1× spin coating cycle and thickness of about 150 nm are presented on Figure 2.

Ingenta: For Scientific Publishing Technology Only
IP: 91.67.1.20 On: Fri, 22 Feb 2013 13:13:10
Copyright: American Scientific Publishers

2.3. Measuring Techniques

UV-Vis spectra of the pigment coatings on FTO glass and ITO PET foils were measured by a Perkin Elmer

Table I. Haze (%), TT (%) and DT (%) values of various pigment particle coatings: P25 (this work), Inframat and metatitanic acid based coatings.[8] NiO[4] and black spinel solar absorber coating.[46]

Coating type	Haze (%)	TT (%)	DT (%)
P25	0.99	81.55	1.52
P25/NiO	0.91	82.83	1.47
$P25/NiO_xH_y$	1.30	81.73	1.80
P25/TIP	1.26	82.99	1.64
Inframat TiO_2	2.37	82.82	2.58
mTiA	2.76	83.52	2.83
NiO	0.94	74.8	0.99
Black spinel solar coating	4.88	62.53	3.42

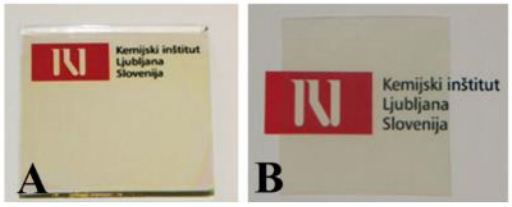


Fig. 2. P25 coating deposited on FTO glass (A) and ITO PET flexible foil (B) (for description see Table I) by 1× spin coating cycle and thickness of about 150 nm.

Lambda 900 UV-Vis spectrometer equipped with an integrating sphere, giving spectral total reflectance (R(λ)), spectral total transmittance (TT(λ)) and spectral diffuse transmittance (DT(λ)) spectra. The optical quality of the coatings was estimated by determining transmission haze numbers (H in%), defined as the ratio of diffuse to total transmittance (DT/TT%) of coatings in the spectral range 380–780 nm following the American Society for Testing and Materials (ASTM) test method D1003,[44] as described previously.[44]

SEM micrographs were obtained on a FE-SEM Supra 35 VP electron scanning microscope.

Coating thickness was determined by scratching the coating with a hard tip, in order to remove the coating from the FTO glass substrate, and the region was then used for Talystep measurements.

Water contact angle (CA) measurements were performed at room temperature using a horizontal microscope with a protractor eyepiece (contact angle meter CAM-100, KSV Instruments Ltd., Finland). Zero-time angles were determined after the specimens were stored in the dark for several days. Samples were subsequently irradiated in a chamber equipped with three UV lamps (Philips CLEO 20 W, broad maximum at 355 nm). The incident irradiance was 21.2 W m^{-2} in the interval 300–400 nm. On each sample, measurements were repeated twice at different irradiation times to obtain average water CA values.

Photocatalytic activities were studied using as model reaction the hydroxylation of terephthalic acid (TPA) to the highly fluorescent hydroxyterephthalic acid (HTPA) (Fig. 3), according to a procedure described in detail elsewhere.[1,29] Briefly, a TPA-containing film was deposited on the surface of each sample by dip-coating from a water/ethanol solution of sodium terephtalate and hydroxyethylcellulose. Specimens were subsequently

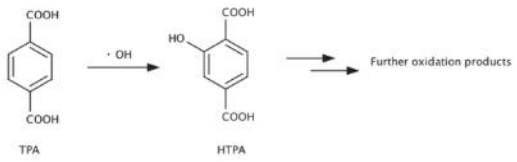


Fig. 3. Hydroxylation reaction of TPA to yield HTPA.

UV-irradiated under the same conditions adopted for water CA tests. At different irradiation times, samples of the reactive film were taken by washing the film away with 0.25 mL of a 1:1 water/ethanol mixture per each cm^2 of coated surface, using a specific sampling device.[29] HTPA concentration in the washates was finally determined by fluorimetry in a microplate reader Tecan Infinity F200, using 320 and 430 nm as excitation and emission wavelengths, respectively.

3. RESULTS AND DISCUSSION

3.1. Morphology of Coatings

3.1.1. SEM Micrographs

All samples showed surprisingly high adhesion to glass, FTO glass plates (Pilkington, 14 Ω/□), and ITO PET plastic foils (Solaronix, ITO PET 175 μm thickness; 60 Ω/□) indicating strong TiO_2 surface interactions. Adhesion of the P25 coatings seemed to be the worst. The surface texture of the P25, P25/NiO, P25/NiO_xH_y and P25/TIP pigment coatings made of the corresponding pigment dispersions and deposited on FTO glass was studied with SEM microscopy (Fig. 4). Examination of the SEM micrographs (Fig. 4) showed that the use of zirconia beads of 0.2 mm led to coatings consisting of close-packed and compact pigment particles. Obviously, at smaller magnifications all coatings looked homogeneous without any voids, which became visible at larger magnifications. Closer inspection of SEM micrographs revealed that all coatings exhibited a certain degree of porosity, stemming from the particulate nature of the pigment coatings. The most compact coating was obtained by co-grinding P25 with NiO pigment, while the less compact coatings were P25/TIP. This indicated that the addition of $Ti(iOPr)_4$ led to certain degree of flocculation, but the presence of NiO particles, having the average size of about 50 nm, filled the voids and pores present in the corresponding P25/NiO coatings. On larger scale, the P25/TIP coating exhibited

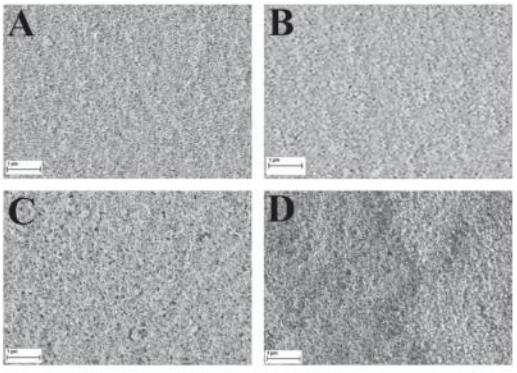


Fig. 4. SEM micrographs of surface morphology of P25 (A), P25/NiO (B), P25/NiO_xH_y (C) and P25/TIP (D) pigment coatings.

Delivered by Publishing Technology to:
IP: 93.91.26.12 On: Fri, 28 Feb 2014 13:19:01
Copyright: American Scientific Publishers

RESEARCH ARTICLE

non-homogeneity compared to other coatings, which we attributed to the partial flocculation originating from worse compatibility of P25 with ethanol solvent present due the addition of the $Ti(iOPr)_4$ serving as binder. This indicated that the pigment dispersions were more suitable for the deposition of coatings with high pigment loadings (~90%), as reported in Ref. [45] and as described below in more detail in relation to haze. The presence of NiO_xH_y used as dispersing phase in the P25/NiO_xH_y coatings seemed not to affect strongly the size and distribution of TiO_2 particles in the corresponding coatings.

3.2. Optical Properties of Coatings

For all coatings made of pigment particle dispersions prepared by standard grinding methods haze is inevitable, contrasting the coatings which are made by re-dispersing of colloidal solutions.[4,7] Haze is particularly high (10–20%) for standard paints containing TiO_2 pigment particles acting as UV absorbers, where scattering is beneficial in order to block the UV radiation. In the latter coatings the pigment loading is relatively low (up to 20%) and the pigment particles are in the form of larger aggregates (few 100 nm), which together with large difference between the refractive index of TiO_2 and the binder (usually organic resin) leads to strong scattering of UV and visible radiation.

Haze of the P25, P25/NiO, P25/NiO_xH_y and P25/TIP pigment particle coatings (Table I) were determined from the measured total (hemispherical) transmittance (TT(%)) and total diffuse transmittance values (DT(%)) obtained from the measured spectral total transmittance (TT(λ)) and diffuse spectral transmittance (DT(λ)) and is given in Table I and Figure 5.

Inspections of results shown in Figure 5 revealed that all coatings exhibited a certain degree of interferences indicating that the coatings actually behave as optical coatings. This made the evaluation of their total transmittance values TT(%) and diffuse transmittance DT(%) less accurate because the corresponding values were interrelated (Table I). Haze values did not differ significantly, being the smallest for the P25/NiO and P25 coatings (<1%) while the haze of the P25/$Ni(OH)_2$ and P25/TIP coatings were of about 1.30 and 1.26%, respectively.

To conclude, P25 pigment seemed to be the material of choice for making optical coatings from the pigment dispersion because as regards the optical properties it outranged titania coatings made of metatitanic acid (mTiA) pigment (Cinkarna, Celje, Slovenia) and Inframat TiO_2. The NiO pigment coatings made in our laboratory[4] (Table I and Fig. 6) seemed to have the highest haze. Haze strongly depends on the coating thickness and type of pigment, which could be inferred from Figure 6, showing DT(λ) and TT(λ) spectra of 300 nm thick coating of black spinel pigment particle layers used as solar absorber coatings on glass with antiglare properties. These coatings

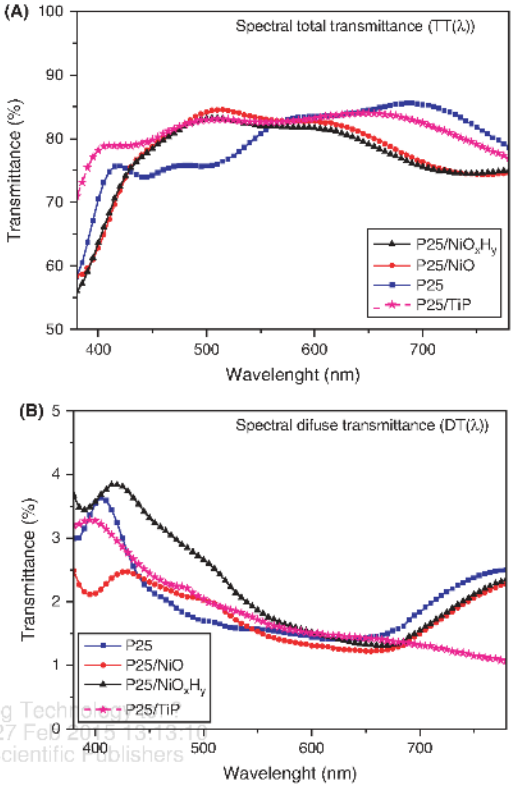


Fig. 5. Total (TT(λ)) (A) and diffuse (DT(λ)) (B) transmission spectra of the P25, P25/NiO, P25/NiO_xH_y and P25/TIP pigment coatings deposited on FTO glass and measured in air prepared under the same spin-coating conditions.

are highly absorbing (90%) at high thicknesses (>800 nm) but transmit light without high haze (~3–5%) at smaller coating thicknesses (Fig. 6).

3.3. PSII and PCA Properties

Figure 7 displays the evolution of the water contact angle on the different coatings with irradiation time. Upon UV

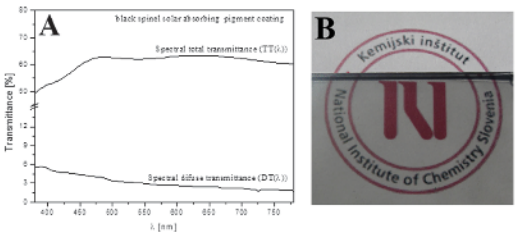


Fig. 6. Total (TT(λ)) and diffuse (DT(λ)) transmittance spectra of the black spinel solar absorbing pigment coating deposited on FTO glass[46] (A) and photograph of the correspondent coating (B).

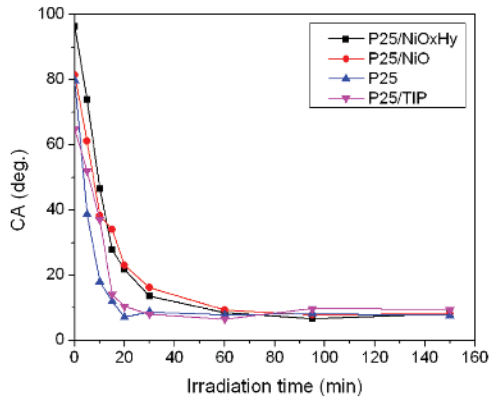


Fig. 7. Water contact angles on the different coatings as a function of irradiation time. Lines are guides to the eye only.

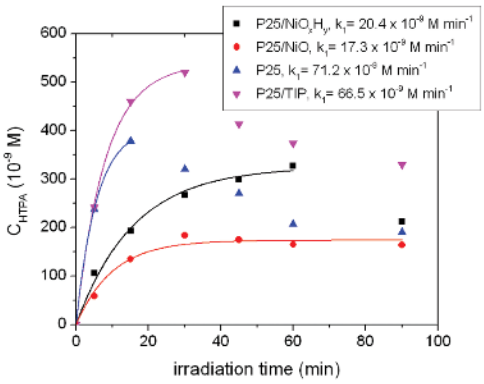


Fig. 8. Evolution of the concentration of HTPA with irradiation time on the different coatings. Lines represent the fitting of the obtained data to the kinetic model; k_1 values obtained from these fittings are included in the legend.

irradiation, all samples become superhydrophilic, reaching in all cases a constant CA of ca. 8° after 60 minutes. As can be seen in the Figure 7, the samples containing only TiO_2 in their composition, i.e., P25 and P25/TIP behave differently to those containing also NiO or NiO_xH_y. The former reach the lowest CA value in a shorter time, revealing a faster hydrophobic-to-hydrophilic conversion. The different behaviour of these two groups of samples is represented in Table II taking as reference the CA value reached after 30 minutes of irradiation, the time at which the CA values of P25 and P25/TIP becomes constant. For comparison, the value obtained with the reference material Pilkington Activ™ Glass[29] is included in Table II. All the coatings obtained in this work show a remarkably faster hydrophobic-to-hydrophilic conversion than this reference material.

The concentrations of HTPA as a function of irradiation time in the photocatalytic hydroxylation reaction of TPA on the different coatings are depicted in Figure 8, together with their fitting to the appropriate kinetic model. Given the intermediate nature of the HTPA molecule in the photocatalytic reaction, its concentration profile can be described, for the initial reaction times, by a simplified kinetic model that considers zero-order kinetics for the formation of HTPA from TPA in the first reaction step and first-order kinetics for the HTPA disappearance upon further oxidation:[1]

$$\frac{d[\mathrm{HTPA}]}{dt} = k_1 - k_2[\mathrm{HTPA}]$$

and therefore:

$$[\mathrm{HTPA}] = \frac{k_1}{k_2}(1 - e^{-k_2 t})$$

where k_1 and k_2 are the HTPA formation and degradation rate constants, respectively. The value of k_1 can be therefore used as indicative of photocatalytic activity for comparative purposes. The values of k_1 obtained with the different coatings are included in the legend of Figure 8.

The obtained k_1 values reveal in first place that all the tested coatings show to a superior photocatalytic activity with respect to the reference material Pilkington Activ™ Glass, for which a k_1 value of 2.1×10^{-9} M min^{-1} is obtained following the same procedure.[1] Together with the contact angle values, this confirms that the prepared coatings exhibit very promising self-cleaning properties. Regarding the relative activities of the different samples, they decrease in the order P25 > P25/TIP > $P25/NiO_xH_y$ > P25/NiO, with a considerable difference between the first two and the two following. That is, in line with that already observed in water contact angles, the presence of NiO-related species seems to be detrimental for the photocatalytic activity of TiO_2 coatings obtained by the present procedure. Interestingly, the considerably higher activity of the coatings composed only by TiO_2 species is in line with their higher porosity, as discussed in the SEM section. It seemed, that the added TIP did not disturbed the activity of the P25 particles, which is in agreement with the fact that amorphous titania also exhibits photocatalytic activity and superhydrophylic effect.[47] $P25/NiO_xH_y$ and P25/NiO coatings performed worse compared to the P25 and P25/TIP

Table II. Water contact angle values of coatings reached after 30 minutes of irradiation and for comparison water contact angle of reference material Pilkington Activ™ glass.

Coating type	CA after 30 min (°)	CA after 240 min (°)
$P25/NiO_xH_y$	13.51	
P25/NiO	16.18	
P25	8.71	
P25/TIP	8.05	
Pilkington activ™ glass[29]		36

Delivered by Publishing Technology to: Guest User, 27 Feb 2015 13:13:10
Copyright: American Scientific Publishers

RESEARCH ARTICLE

coatings. P25/NiO coating performed the worst, which could be conceived from SEM showing that the NiO pigment particles filled the pores in the mixed P25/NiO particle coating. The NiO_xH_y seemed to have disturbing effect on the P25 activity due to the blocking of the P25 surface, hindering the expected positive effect stemming from the presence of the $Ni(OH)_2$ phases as reported by Yu et al.[23] Detrimental effect of the NiO_xH_y phase in the P25/NiO_xH_y was compensated by excellent adhesion of the coatings on FTO glass and PET flexible foils even though adhesion was still slightly inferior compared to the P25/TIP coating.

4. CONCLUSION

We demonstrated in this study that it is possible to make titania coatings from pigment particle dispersions made of commercial titania pigments (Degussa, Inframat) and used them for the deposition of optical coatings with haze which did not exceed 2%. The main advantage of the presented deposition method could be conceived from high PSH and PCA effects exceeding substantially the activity of the Pilkington Activ™ glass. The P25/TIP coating was found particularly attractive because of excellent adherence on either FTO glass or flexible PET foil, the latter opening the possibility of the deposition of coatings via the coil coating deposition technique. Co-grinding of P25 with NiO particles deteriorates PSH and PCA activity, even though it was still superior compared to Pilkington Activ™ Glass. The use of NiO_xH_y was justified by the improved adherence and mechanical integrity of the P25/NiO_xH_y coating, yet the expected enhancement of the PCA effect, reported for the P25/$Ni(OH)_2$ core–shell nanoparticle coating for H_2 production,[23] was not confirmed. More detailed studies of the structural properties of the P25/NiO_xH_y coating are planned in the future in order to reveal the differences in the PCA mechanisms of the P25/$Ni(OH)_2$ and the P25/NiO_xH_y coatings.

Acknowledgment: This work has received funding from the Slovenian Research Agency (Program P1-0030). One of the authors (F. Fresno) additionally acknowledges EC for financial support from the SUNGREEN project (FP7-REGPOT-2011-1).

References and Notes

1. U. Černigoj, M. Kete, and U. L. Štangar, *Catal. Today* 151, 46 (**2010**).
2. U. Diebold, *Surf. Sci. Rep.* 48, 53 (**2003**).
3. C. G. Granqvist, Handbook of Inorganic Electrochromic Materials, Elsevier, Amsterdam, New York (**1995**).
4. M. Mihelčič, I. Jerman, F. Švegl, A. Š. Vuk, L. S. Perše, J. Kovač, B. Orel, and U. Posset, *Sol. Energ. Mat. Sol. C* 107, 175 (**2012**).
5. M. Mihelčič, A. Š. Vuk, I. Jerman, B. Orel, F. Švegl, H. Moulki, C. Faure, G. Campet, and A. Rougier, *Sol. Energ. Mat. Sol. C* 120, 116 (**2014**).
6. H. Moulki, C. Faure, M. Mihelčič, A. Š. Vuk, F. Švegl, B. Orel, G. Campet, M. Alfredsson, A. V. Chadwick, D. Gianolio, and A. Rougier, *Thin Solid Films* 553, 63 (**2014**).
7. M. Mihelčič, V. Francetič, P. Pori, H. Gradišar, J. Kovač, and B. Orel, *Appl. Surf. Sci.* 313, 484 (**2014**).
8. M. Mihelčič, A. Š. Vuk, D. Vrhovšek, F. Švegl, M. Hajzeri, and B. Orel, *Acta Chim. Slov.* 61, 517 (**2014**).
9. I. Jerman, M. Mihelčič, M. Koželj, and B. Orel, Sol–gel based spectrally selective solar absorber coatings and the process for producing said coatings. WO 2013158049 A1, April (**2012**).
10. A. Hagfeldt, G. Boschloo, L. C. Sun, L. Kloo, and H. Pettersson, *Chem. Rev.* 110, 6595 (**2010**).
11. H. Lindstrom, A. Holmberg, E. Magnusson, S. E. Lindquist, L. Malmqvist, and A. Hagfeldt, *Nano Lett.* 1, 97 (**2001**).
12. M. Durr, A. Schmid, M. Obermaier, S. Rosselli, A. Yasuda, and G. Nelles, *Nat. Mater.* 4, 607 (**2005**).
13. H. C. Weerasinghe, P. M. Sirimanne, G. V. Franks, G. P. Simon, and Y. B. Cheng, *J. Photochem. Photobiol. A* 213, 30 (**2010**).
14. X. Chen and S. S. Mao, *Chem. Rev.* 107, 2891 (**2007**).
15. A. L. Linsebigler, G. Q. Lu, and J. T. Yates, *Chem. Rev.* 95, 735 (**1995**).
16. A. Fujishima, X. Zhang, and D. A. Tryk, *Surf. Sci. Rep.* 63, 515 (**2008**).
17. R. Asahi, T. Morikawa, T. Ohwaki, K. Aoki, and Y. Taga, *Science* 293, 269 (**2001**).
18. W. Choi, A. Termin, and M. R. Hoffmann, *J. Phys. Chem.* 98, 13669 (**1994**).
19. M. Ksibi, S. Rossignol, J.-M. Tatibouët, and C. Trapalis, *Mater. Lett.* 62, 4204 (**2008**).
20. T. Lindgren, J. M. Mwabora, E. Avendaño, J. Jonsson, A. Hoel, C. G. Granqvist, and S. E. Lindquist, *J. Phys. Chem. B* 107, 5709 (**2003**).
21. G. R. Torres, T. Lindgren, J. Lu, C. G. Granqvist, and S. E. Lindquist, *J. Phys. Chem. B* 108, 5995 (**2004**).
22. J. M. Mwabora, T. Lindgren, E. Avendaño, T. F. Jaramillo, J. Lu, S. E. Lindquist, and C. G. Granqvist, *J. Phys. Chem. B* 108, 20193 (**2004**).
23. J. Yu, L. Qi, and M. Jaroniec, *J. Phys. Chem. C* 114, 13118 (**2010**).
24. M. Ksibi, S. Rossignol, J. M. Tatibouët, and C. Trapalis, *Mater. Lett.* 62, 4204 (**2008**).
25. M. Ni, M. K. H. Leung, D. Y. C. Leung, and K. Sumathy, *Renew. Sust. Energ. Rev.* 11, 401 (**2007**).
26. M. R. Hoffmann, S. T. Martin, W. Choi, and D. W. Bahnemann, *Chem. Rev.* 95, 69 (**1995**).
27. A. Fujishima, K. Hashimoto, and, T. Watanabe, TiO_2 photocatalysis: Fundamentals and Applications, BKC, Tokyo (**1999**).
28. Z. Jin, X. Zhang, Y. Li, S. Li, and G. Lu, *Catal. Commun.* 8, 1267 (**2007**).
29. J. Yu, Q. Xiang, and M. Zhou, *Appl. Catal. B* 90, 595 (**2009**).
30. K. Wilke and H. D. Breuer, *J. Photochem. Photobiol. A* 121, 49 (**1999**).
31. A. Galińska and J. Walendziewski, *Energ. Fuel.* 19, 1143 (**2005**).
32. S. Sakthivel, M. V. Shankar, M. Palanichamy, B. Arabindoo, D. W. Bahnemann, and V. Murugesan, *Water Res.* 38, 3001 (**2004**).
33. K. Sayama and H. Arakawa, *J. Chem. Soc. Faraday Trans.* 93, 1647 (**1997**).
34. T. Sreethawong and S. Yoshikawa, *Int. J. Hydrogen Energ.* 31, 786 (**2006**).
35. J. Bandara, C. P. K. Udawatta, and C. S. K. Rajapakse, *Photochem. Photobio. Sci.* 4, 857 (**2005**).
36. J. S. Jang, S. H. Choi, D. H. Kim, J. W. Jang, K. S. Lee, and J. S. Lee, *J. Phys. Chem. C* 113, 8990 (**2009**).
37. D. Jing, Y. Zhang, and L. Guo, *Chem. Phys. Lett.* 415, 74 (**2005**).
38. T. Sreethawong, Y. Suzuki, and S. Yoshikawa, *Int. J. Hydrogen Energ.* 30, 1053 (**2005**).
39. J. Yu, Y. Hai, and B. Cheng, *J. Phys. Chem. C* 115, 4953 (**2011**).
40. F. Švegl, A. Š. Vuk, M. Hajzeri, L. S. Perše, and B. Orel, *Sol. Energ. Mat. Sol. C* 99, 14 (**2012**).

Copyright © by Nishin... Fri, 27 ... American Scientific Publishers

41. D. A. Wruck and M. Rubin, *J. Electrochem. Soc.* 140, 1097 (**1993**).
42. Z. W. Wicks, Jr., F. N. Jones, S. P. Pappas, and D. A. Wicks, Organic Coatings: Science and Technology, 3rd edn., Wiley-Interscience, Hoboken, New York (**2007**).
43. L. S. Perše, M. Mihelčič, and B. Orel, edited by M. SjÖdqvist, Nordic Rheology Conference, (**2011**), June, Helsinki, Finland, Nordic Rheology Society 19, 253 (**2011**).
44. H. L. Yu, C. C. Hsiao, and W. C. Liu, *Meas. Sci. Technol.* 17, N29 (**2006**).
45. M. Mihelčič, I. Jerman, and B. Orel, *Prog. Org. Coat.* 76, 1752 (**2013**).
46. M. Mihelčič, V. Francetič, J. Kovač, A. Š. Vuk, B. Orel, and D. Peros, *Sol. Energ. Mat. Sol. C* (**2014**), submitted.
47. F. Piccinini, M. Levi, and S. Turri, *Prog. Org. Coat.* 76, 1265 (**2013**).

Received: 2 November 2014. Accepted: 8 December 2014.

RESEARCH ARTICLE

Delivered by Publishing Technology to: ?
IP: 93.91.26.12 On: Fri, 27 Feb 2015 13:13:10
Copyright: American Scientific Publishers

Chapter 9

Photocatalytic Cotton Modified with TiO_2 and TiO_2/APTES – Spectroscopic Analysis

The final challenge that was solved within the framework of this thesis, relates to textiles, particularly cotton. In the case of natural fibres such as cotton, modification of its surface is reasonable. Cotton is important in the textile industry since it is preferably used for clothing, in particular clothing in contact with the skin. In addition to a reduction in the absorption of water and mineral and organic oils, it is particularly important to achieve inhibition of the growth of algae and microorganisms. In most cases, this is achieved by impregnation of cotton fabrics with sol-gel precursors by dip coating deposition, followed by spinning, drying and processing at temperatures up to 150 °C. The processing of cotton fabrics with POSS and other silanes is known [96, 97].

Modification of the surface of textile fibres by depositing a nanocomposite consisting of titanium (IV) isopropoxide (TiP) and aminopropyltrialkoxy silane (APTES) is also presented in this thesis. The main purpose of this research was to confirm the usefulness of an infrared spectroscopy approach for the study of interactions between the absorbent and the substrate. This kind of basic research of cellulose fibres by infrared spectroscopy is relatively rare because most authors are more interested in technological processes and the properties of coated textiles, rather than the very nature of the interaction.

Our aim was also to make coatings that would be easy to prepare and which exhibit good coverage of the cotton fibres. Impregnation of the cotton was performed with three different nanosols, i.e., TiP, APTES and TiP/APTES. Cotton was immersed overnight in the precursor solutions at room temperature. The samples were then squeezed by a wet-pick up of 100%, dipped in boiling water for a few minutes and, at the end, air-dried. The presence of the various coatings on cotton was confirmed with SEM, EDX, XPS and ATR infrared spectroscopic measurements.

Infrared spectroscopy determined the interactions and structural changes of treated and untreated cotton. Changes of untreated cotton and cotton treated in absolute ethanol and boiling water are shown in Figure 9.1. The significant OH changes of inter- and intra- modes in cotton appear in the spectral region from 3700 to 2700 cm^{-1} and the attachment of ethanol on the cotton fibres in the region from 1200 to 900 cm^{-1}.

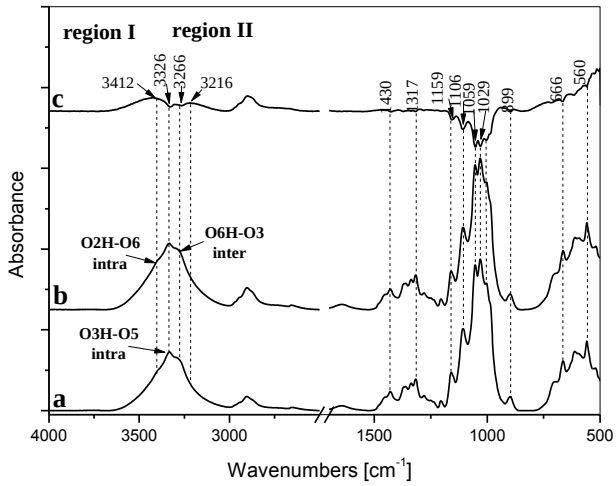


Figure 9.1: ATR spectra of cotton as-received (a), cotton treated in EtOH and boiling water (EtOH/cotton) and (b) the subtraction spectrum of (EtOH/cotton—cotton as-received) (c) in the spectral region from 4000 to 500 cm^{-1}.

The subtraction spectra of cotton fibres treated with either TiP or TiP/APTES hybrid gave strong positive bands at 978 and 903 cm^{-1} (Figure 9.2). These bands can be attributed to the Si–O–Si and Si–O–Ti modes, which confirmed the presence of the coating layer on top of the cotton fibres.

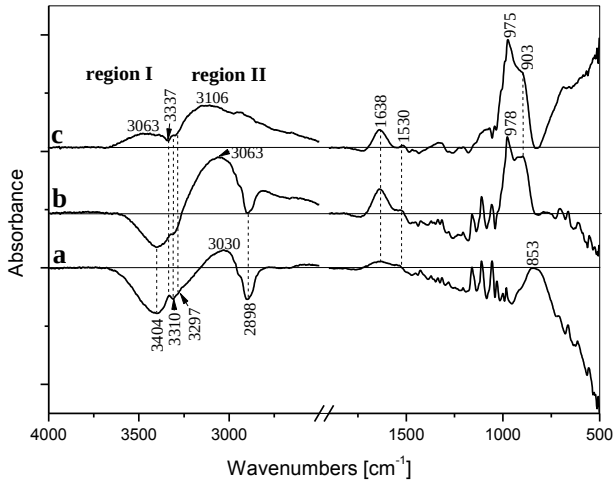


Figure 9.2: Subtraction spectra of TiP/cotton—EtOH/cotton (a), TiP/APTES/cotton—EtOH/cotton (b) and TiP/APTES/cotton—TiP/cotton (c) samples in the spectral region from 4000 to 500 cm^{-1}.

SEM analysis of the morphological change in the appearance of the cotton fibres after modification with TiP revealed that TiO_2 particles with a size of ~1 µm are clearly present on the surface of the cotton fibres (Figure 9.3A). The smooth surface of the TiP/APTES nanocomposites on the cotton fibres indicates a homogeneous layer without any detectable particles, suggesting an amorphous finish (Figure 9.3B).

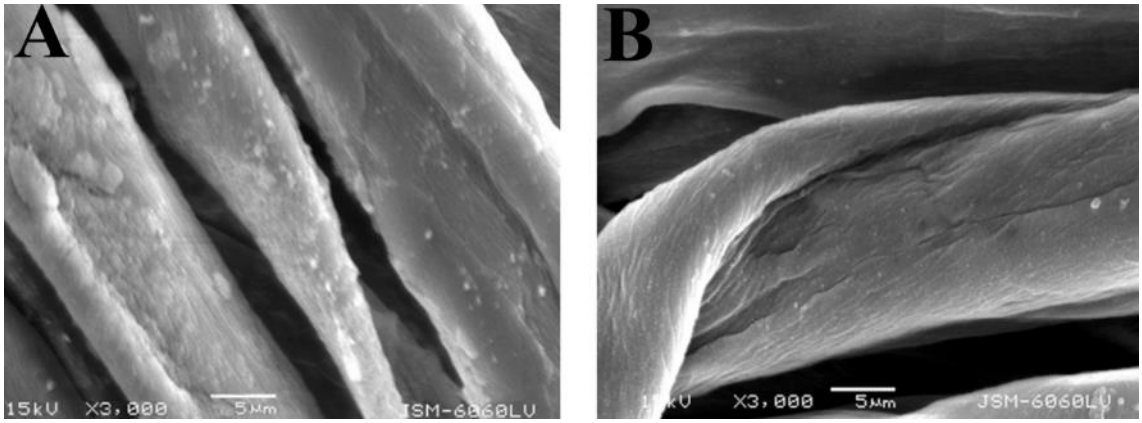


Figure 9.3: SEM images of TiP – coated cotton (A) and TiP/APTES coated cotton (B) fibres.

My contribution consisted of characterisation of samples by means of infrared spectroscopic analysis.

Cellulose
DOI 10.1007/s10570-015-0696-x

ORIGINAL PAPER

Bacteriostatic photocatalytic properties of cotton modified with TiO_2 and TiO_2/aminopropyltriethoxysilane

Brigita Tomšič · Vasko Jovanovski · Boris Orel · Mohor Mihelčič · Janez Kovač · Vojmir Francetič · Barbara Simončič

Received: 8 May 2015 / Accepted: 29 June 2015
© Springer Science+Business Media Dordrecht 2015

Abstract A new route for the functionalization of cotton fibres with organic–inorganic hybrid materials is proposed using titanium tetraisopropoxide (TiP) and aminopropyltriethoxysilane (APTES). The antimicrobial and photocatalytic activities of the new cotton finishes based on titania and mixed titania/amino-silica hybrids were tested by monitoring the growth of *Escherichia coli* (ATCC 25922) on the surfaces of functionalized fabrics under exposure to UV radiation and in the dark. Transmission electron microscopy revealed the amorphous nature of the hybrids and confirmed their similarity to other bactericidal aminofunctionalized polymers. Attenuated total reflection infrared spectra showed the protonated amino groups of the APTES in the TiP/APTES hybrid and the presence of Si–O–Ti bonding within the sol–gel hybrids between silica and titania by analogy with previous transmission and ATR infrared studies. Several analytical techniques were employed to establish the presence of the TiP and TiP/APTES modified cotton fibres. ATR measurements proved to be a very useful tool to study also the silane/–C–OH interactions between the hybrid materials and the cotton fibres, revealing the presence of covalent (i.e., –Si–O–C–) bonding with the OH functional group of cellulose. The advantages of the cotton finishes were demonstrated by the measured photocatalytic bacteriostatic effect, which persisted even after 15 washings; in contrast, the aminofunctionalized polymeric finishes, only showed a sufficient bacteriostatic effect. Furthermore, the TiP finishes were photocatalytically active, while the TiP/APTES finishes were not. The ultraviolet protective factor, degree of polymerization of the finished cotton samples were also investigated and revealed the suitability of the proposed method.

Keywords Cotton · Titania/silica hybrid coating · Antimicrobial properties · Photocatalytic properties · UV absorption · Washing fastness

B. Tomšič · B. Simončič (✉)
Department of Textiles, Faculty of Natural Sciences and Engineering, University of Ljubljana, Aškerčeva 12, 1000 Ljubljana, Slovenia
e-mail: barbara.simoncic@ntf.uni-lj.si

V. Jovanovski · B. Orel (✉) · M. Mihelčič
National Institute of Chemistry, Hajdrihova 19, 1000 Ljubljana, Slovenia
e-mail: boris.orel@ki.si

M. Mihelčič
Jozef Stefan International Postgraduate School, Jamova cesta 39, 1000 Ljubljana, Slovenia

J. Kovač
Institut Jožef Stefan, Jamova 39, 1000 Ljubljana, Slovenia

V. Francetič
Faculty of Chemistry and Chemical Technology, University of Ljubljana, Ljubljana, Slovenia

Introduction

The use of TiO_2 in textile finishes is attracting interest due to its relatively straightforward immobilization

Published online: 26 July 2015

onto cotton fabrics, enabling the fabrication of cotton fabrics with excellent protection against UV radiation, expressed in a high UV protection factor (UPF) (up to 50) (Saravanan 2007), and its photocatalytic bacteriostatic effects (Matsunaga et al. 1988; Saito et al. 1992; Linsebigler et al. 1995; Fujishima et al. 1999; Qi et al. 2006; Daoud et al. 2005; Wang et al. 2005; Li et al. 2008).

The photocatalytic antibacterial effect is not yet fully understood. According to Matsunaga et al. (Matsunaga et al. 1988), the presence of photogenerated holes on the surface of TiO_2 leads to electron transfer from coenzyme A (intracellular enzyme), inducing oxidation and the formation of dimeric coenzyme A, which decreases respiratory action and causes cell death. However, other mechanisms have also been proposed (Saito et al. 1992; Sunada et al. 1998, 2003; Kiwi and Nadtochenko 2005; Maness et al. 1999; Lu et al. 2003; Nadtochenko et al. 2008). It is now believed that photocatalytically reactive oxygen species (OH*, HO_2*, and O_2^-* radicals) further attack polyunsaturated phospholipids, causing the cell membrane breakdown and the failure of vital functions, such as the above-mentioned respiratory activity failure. As reported by Lu et al. (2003) in AFM and SEM studies (Liu et al. 2010), the photocatalytic action of TiO_2 significantly changes the surfaces of cells, modifying their shapes from rod-like to elliptical. The results show that the peroxidation of lipids also induces DNA damage and disruption of the cell membrane morphology due to the electron transport chain (Kumar et al. 2011).

One of the advantages of the TiO_2 nanoparticle coatings lies in the fact that they also kill the bacteria cells in the dark, and this action can be strongly influenced by the functionalization of the particle surfaces. For example, Thevenod et al. (2008) showed that the killing of the tumour cells is significantly enhanced when the TiO_2 nanoparticles were functionalized with organic molecules containing $-OH$, $-NH_2$ and $-COOH$ groups. $-NH_2$ groups are the most effective, in agreement with the findings of Li et al. (2005) and Nur (2006), who demonstrated the synergetic bactericidal effects of TiO_2 nanoparticles in the presence of aminosilanes. Similar effect was observed by Čepin et al. (2015) when nanocrystalline ZnO was modified with various amino-silanes and ionic liquid-silanes.

The antimicrobial effects of amino groups led to the development of antibacterial polymeric systems (Timofeeva and Kleshcheva 2011) with protonated primary or secondary/tertiary amine groups. Quaternary ammonium groups attached on various polymers (i.e., polymers of 3-(trimethoxysilyl)-propyldimethyloctadecyl ammonium chloride (Isquith et al. 1972; Tomšič et al. 2011; Simončič et al. 2012), copolymers of N-vinylpyrrolidone with (2-methacryloxyethyl)-triethylammonium halides (Panarin et al. 1971), poly(2-alkyl-1,3-oxazoline)s (alkyl = methyl, ethyl) with terminal quaternary ammonium groups (Waschinski and Tiller 2005) were the most efficient. Also relevant to this study is Milovic et al.'s (2005) demonstration that glass slides coated with aminopropyltriethoxysilane covalently derivatized with N-hexyl,methyl-polyethylenimine killed bacteria over the course of many successive generations. The killing effect of the corresponding coating has been attributed to the rupturing of bacterial cell membranes after contact with the amino functionalized polymeric chains.

Here, titanium tetraisopropoxide (TiP) precursor both alone and in combination with aminopropyltriethoxysilane (APTES) was selected and used for the preparation of TiO_2 and mixed TiP/APTES cotton fabric finishes. The sol–gel TiP/APTES hybrid finishes resemble aminofunctionalized polymeric systems in many aspects. Namely, TiP/APTES hybrids belong to a class of organic–inorganic hybrid materials that have been extensively studied in our laboratory in the past (Vince et al. 2006; Fir et al. 2007; Jerman et al. 2008; Vilčnik et al. 2009; Koželj et al. 2009; Čolović et al. 2011; Jerman et al. 2012; Simončič et al. 2014; Vasiljević et al. 2014). In the TiP/APTES hybrids studied here, the TiP and APTES acted as sol–gel network formers, while the amino groups of the APTES (the organic part of the hybrid) imparted the hybrid with bactericidal properties. To mimic the bactericidal aminofunctionalized polymeric systems as much as possible (Timofeeva and Kleshcheva 2011), the TiP/APTES hybrids were intentionally kept amorphous. To avoid the formation of crystalline titania within the TiP/APTES hybrid (Brooks and Moore 2000; Vuk et al. 2006; Moulder et al. 1995), favourably low processing temperatures ($\sim$100 °C) were used for the fabrication of the cotton finishes. In this way, the presence of TiO_2 particles

may lead to the loss of the Si–O–Ti inter phase bonds within the nanocomposite and between the titania nanoparticles and the cotton. Both of these interactions are important for the washing fastness of the functionalized cotton fabrics.

The aim was to produce amorphous coatings in a single step at temperatures below 100 °C by avoiding any post-deposition heat treatment. Inspection of the synthetic procedures revealed that the autoclaving of sol–gel or metal salt TiO_2 precursors at controlled water/ethanol pressures (Langlet et al. 2002, 2003) and the fabrication of TiO_2 suspensions at elevated temperatures from various acidic or basic aqueous solutions (Bacsa and Grätzel 1996; Kumar et al. 1994; Chemseddine and Moritz 1999; Yun et al. 2004) were not appropriate, leading us to focus on hot water treatment procedures (Kotani et al. 2000; Matsuda et al. 2000, 2003). The hot water treatment of cotton seemingly gives excellent results and enables the deposition of transparent anatase nanocomposite films on PET, PC, acrylic resin substrates and cotton fabrics. The corresponding finishes (Kotani et al. 2000; Matsuda et al. 2003) were mostly obtained by immersing cotton in hot water solutions of titania precursors followed by treatment at 90 °C to accelerate the condensation into nanocrystalline TiO_2. We simplified the titania formation process by soaking the cotton in the ethanolic solutions of TiP and TiP/APTES precursors and then immersing the soaked cotton fabrics in boiling water for several minutes. This procedure was not only faster, because of the elimination of the post-deposition treatment of cotton at 90 °C, but was also performed at neutral pH, avoiding the depolymerization of cotton fabrics that occurs at low pH values (Langlet et al. 2002; Mahltig et al. 2007). It should be noted that the application process is cost-effective and has practical potential because of cheap precursors, simplicity of the implementation process and the use of conventional equipment.

In addition to the main aim of this study, which is to demonstrate the bactericidal photocatalytic action of sol–gel TiP/APTES hybrid, the structural properties of these modifications were studied in detail. First, they were determined using attenuated total reflection (ATR) infrared spectroscopy and by focusing on the hydrolysis and condensation of the precursor solution under the same conditions as employed during the modification of the cotton fabric. Our main interest was to establish the presence of Si–O–Ti bonds within the sol–gel hybrids between silica and titania by analogy with previous infrared transmission (Schraml-Marth et al. 1992) and ATR studies (Aizawa et al. 1991) performed on silane coatings on titania particles (Puzenat and Pichat 2003; Mihelčič et al. 2014). In addition, the existence of SiOH bands and Si–O–Si bonds (Mihelčič et al. 2014; Brinker and Scherer 1990; Arkles and Larson 2004) in the hybrids and the presence of protonated amino groups in APTES (Bellamy 1954) were investigated using ATR. TEM micrographs were used to reveal the amorphous nature of the hybrids to confirm their similarity to other bactericidal aminofunctionalized polymeric systems (Timofeeva and Kleshcheva 2011).

The presence of TiP and TiP/APTES hybrids on cotton fibres was established by SEM, EDX, XPS and ATR infrared spectroscopic measurements. The latter technique has been extensively employed for the identification of vibrational modes of cellulose and its derivatives (Tsuboi 1957; Maréchal and Chanzy 2000; Chung et al. 2004; Hinterstoisser et al. 2001; Hinterstoisser and Salmén 1999) with different moisture contents (Hofstetter et al. 2006; Olsson and Salmén 2004; Tshabalala et al. 2003) and in the presence of various (mainly silane-based) coatings (Castellano et al. 2004; Xie et al. 2010; Abdelmouleh et al. 2002) and other coupling agents (Rasmussen et al. 2014a), providing a useful platform for investigations of adsorption (Abdelmouleh et al. 2002) and the silane/–C–OH interactions between the coatings and the cotton fibres (Castellano et al. 2004). Investigations oriented to reveal covalent bonding between silane with the OH functionality of cellulose (i.e., –Si–O–C– bonds) are rare (Radetić 2013), and most authors have preferred to focus on the effects of different finishes on the properties of the fabric (Daniels and Francis 1998; Ku et al. 2011) rather than the cellulose/silane interactions. The main emphasis has been to determine the type of bonding between the hybrids and the cotton and the identification of the hybrid anchoring sites on the cellulose via the formation of Si–O–C covalent bonds.

In addition to the structural studies of the cotton finishes, we devoted a great amount of effort to the investigation of the washing fastness of the cotton finishes by TG measurements, to establish the

correlation of the washing fastness with the changes of the UZF values and the degree of polymerization (DP). Finally, the antimicrobial photocatalytic activities of TiP- and TiP/APTES-modified cotton fabric were quantitatively determined by antimicrobial testing with and without UV illumination and correlated to the photocatalytic activities of the TiP and TiP/APTES cotton finishes.

Experimental

Materials

Titanium tetraisopropoxide, $Ti(iOPr)_4$ (TiP) (Aldrich), aminopropyltriethoxysilane (APTES) (ABCR) and absolute isopropanol (Aldrich) were used for the preparation of the nanosols.

Plain-woven 100 % cotton fabric with a mass of 162 g/m^2 was used in the experiments as the substrate. In the pre-treatment process, the fabric was bleached in an H_2O_2 bath, mercerized in NaOH solution and neutralized with dilute CH_3COOH.

Application of the nanosols

For the impregnation of the cotton, three different nanosols, i.e., TiP, APTES and TiP/APTES, were prepared at room temperature. The TiP sol was prepared by mixing $Ti(iOPr)_4$ in isopropanol to a concentration of 5 %. The same procedure was used for the preparation of the APTES sol, except that APTES was used instead of $Ti(iOPr)_4$. The TiP/APTES sol was prepared by mixing $Ti(iOPr)_4$ and APTES in isopropanol to a concentration of 10 %. The molar ratio of [$Ti(iOPr)_4$]:APTES was set to 1:2. Prior to use, the solutions were vigorously stirred for a few minutes. Impregnation of the cotton was achieved by overnight immersion in the precursor solutions at room temperature. The samples were then squeezed by a wet-pick up of 100 %, dipped in boiling water for a few minutes and air-dried.

For the spectrophotometric measurements, 10 % TiP/APTES sols were prepared using various $Ti(iOPr)_4$:APTES ratios (Ti:Si = 1:1, 3:4, 1:1.5, 1:2 and 1:2.5), applied to Si wafers using the dip coating technique and exposed to boiling water steam for specified durations to simulate hydrolysis and the conditions to which the cotton substrates were exposed during the application process. In addition, 5 % sols with one component (either TiP or APTES) were applied to Si wafers using the same procedure.

Washing procedure

The washing fastness of the cotton coatings was tested according to the ISO 105-C01:1989(E) standard method using a Launder-ometer. The samples were treated for 30 min at 40 °C in an ionic soap solution of ECE phosphate reference detergent (B) (SDC Enterprises Limited, United Kingdom) with a concentration of 5 g/l at pH 7, resulting in a liquor ratio of 1:50. The washing procedure was repeated for 20 cycles.

Measurement techniques

Transmission electron microscopy (TEM) micrographs were obtained on a JEOL JEM-2100 high-resolution transmission electron microscope (HR-TEM) operating at 200 keV.

Energy dispersive X-ray spectroscopy (EDX) measurements were performed on a JEOL JED-2300T EDS system with high energy resolution and high sensitivity.

Scanning electron microscopy (SEM) measurements were conducted on a Supra 35 VP FE-SEM (Carl Zeiss).

The presence of the hybrid modifications in the cotton fibres was assessed using a Perkin-Elmer System 2000 IR spectrophotometer equipped with an ATR cell (SpectraTech) with a diamond crystal (n = 2.0). The spectra were recorded over the range 4000–370 cm^{-1}.

X-ray photoelectron spectroscopy (XPS or ESCA) was applied to investigate the chemical statuses of the elements on the surface of the sol–gel coatings. The analysis was performed using a XPS spectrometer produced by Physical Electronics Inc., model TFA XPS. An Al K_α monochromatized X-ray source (200 W) was used. The energy of the X-ray beam was 1486.7 eV. The analysed area was 0.4 mm in diameter, and the signal during the XPS analysis corresponded to a depth of up to 6 nm from the surface layer. The sample charging during the XPS analysis was compensated by a low-energy electron gun-neutralizer. XPS method is sensitive for all elements except H and He can't be detected.

The UV blocking properties of the modified cotton fabric were measured according to the American standard method AATCC 183-2000 using a Varian Cary 1E UV–Vis spectrophotometer.

The antibacterial assessments of TiP, APTES and TiP/APTES-coated cotton samples washed 0, 1 and 10 times were performed using the bacterium *Escherichia coli* (ATCC 25922) according to the AATCC 100-1999 standard method. For the inoculation of the samples, a bacterial suspension with a concentration of 10^5 colony-forming units per ml (CFU/ml) was used. The bacterial growth reduction, R, which is a measure of the bactericidal activity of the studied samples, was determined according to the following equation:

$$R = \frac{B - A}{B} \times 100(\%) \quad (1)$$

where A denotes the number of CFUs that survived 24 h of contact with the studied sample and B denotes the number of CFUs at the beginning of the experiment. The values of A and B used in Eq. 1 were the averages of six counts according to the agar plate counting method. The experiments were performed with and without UV illumination. The UV black light (HQV 125, Osram), with the emission range of 300–400 nm and dimensions of 170 mm in length and 15 mm in diameter, was placed approximately 200 mm above the samples.

The fibre damage due to the photocatalytic activity of the TiP-based finishes was measured viscosimetrically using an Oswald shear dilution viscometer. In addition, the DP of the TiP-coated and uncoated samples was determined. Cuoxam, a solution of cupric hydroxide in aqueous ammonia, $[Cu(NH_3)_4](OH)_2$, was used as the solvent.

The photocatalytic activities of the TiP and TiP/APTES-coated cotton samples were assessed by monitoring the degradation of the colour marker and the dye bromophenol blue, (3′,3″,5′,5″-tetrabromophenolsulfonphthalein) (BPB), (Sigma Aldrich) after the exposure of the dyed fabric samples to artificial light at 65 ± 2 % relative humidity and 20 ± 1 °C using a Xenotest Alpha instrument (Atlas, USA) equipped with a xenon lamp with an adjustable radiation power region 0.8–2.5 kVA and an expanded range of radiation (300–400 nm). Each sample (60 mm × 40 mm) was dyed by 1-min immersion in 25 ml of a 0.04 % water solution of BPB dried at room temperature in the dark for 24 h. The dyed samples were placed in a sample holder and set in the exposure chamber in a vertical position for 30, 60, 90 and 120 min. After illumination, an assessment of the degradation of the dyestuff was performed using the reflectance measurements, R, of the studied samples on a Datacolor Spectraflash SF 600 spectrophotometer using D 65/10° light. For each sample, ten measurements of the R-value were obtained, and the corresponding K/S values were calculated according to the Kubelka–Munk equation (Zollinger 1991):

$$\frac{K}{S} = \frac{(1 - R)^2}{2R} \quad (2)$$

where K/S is the ratio of the coefficient of light absorption (K) to the coefficient of light scattering (S) and R is the reflectance at the maximum absorption wavelength determined at 610 nm. The mean K/S value was then determined.

Based on the K/S values, the dyestuff degradation was determined according to Colleoni (Colleoni et al. 2012):

$$\text{Dyestuff degradation} = \left(1 - \frac{\left(\frac{K}{S}\right)_i - \left(\frac{K}{S}\right)_{UD}}{\left(\frac{K}{S}\right)_0 - \left(\frac{K}{S}\right)_{UD}}\right) \cdot 100(\%) \quad (3)$$

where $(K/S)_{UD}$ is the K/S value of the undyed sample, $(K/S)_0$ is the K/S value of the dyed sample before illumination and $(K/S)_i$ is the K/S value of the sample after illumination for a given time.

Thermogravimetric analysis (TGA) was performed on a Mettler Toledo TGA/SDTA 851^e instrument. The TGA curves were measured from 30 to 800 °C in a nitrogen atmosphere at a heating rate of 10 °C/min.

Results and discussion

SEM, XPS and TEM measurements

SEM measurements

The morphological changes in the cotton fibres after the modification with TiP and TiP/APTES were studied using SEM (Fig. 1). Compared to the surfaces of the untreated cotton fibres, treatment with TiP caused the fibre surface to become rough, with barely detectable particles, suggesting their uneven

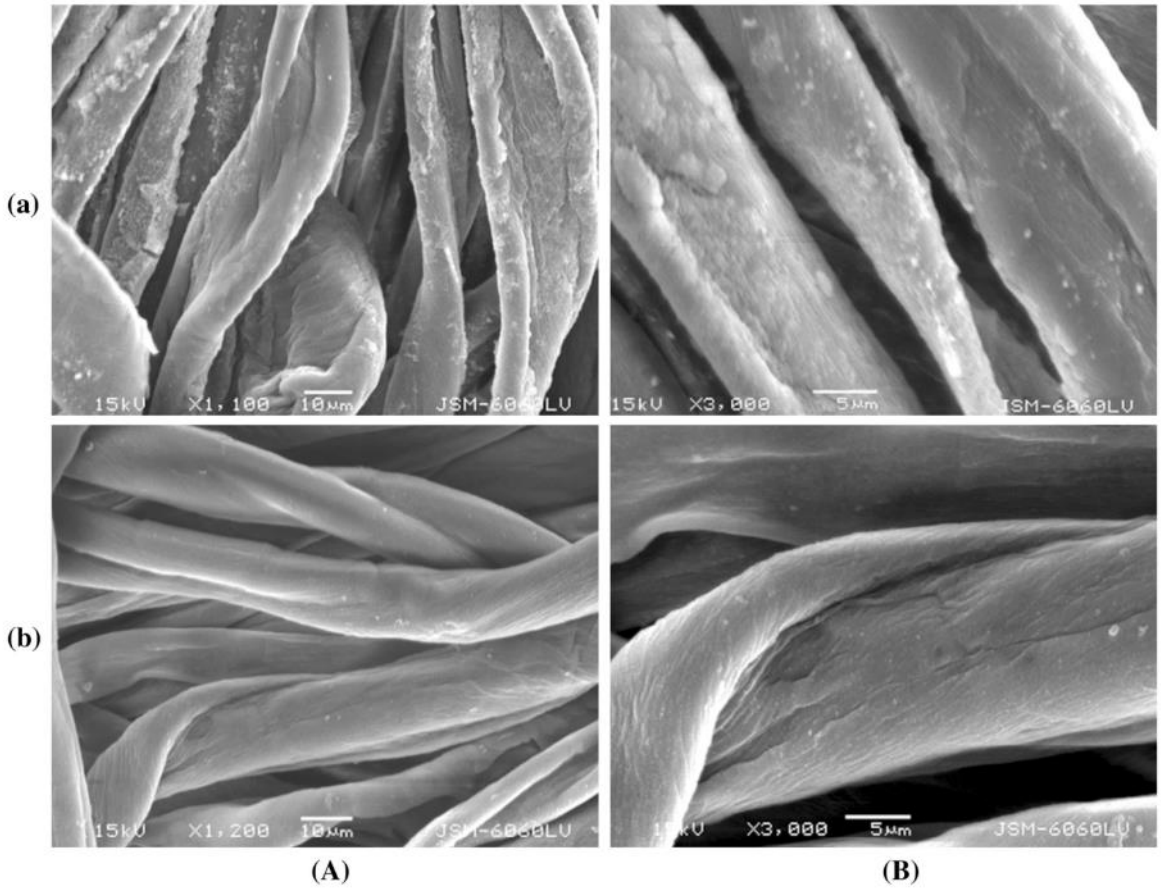
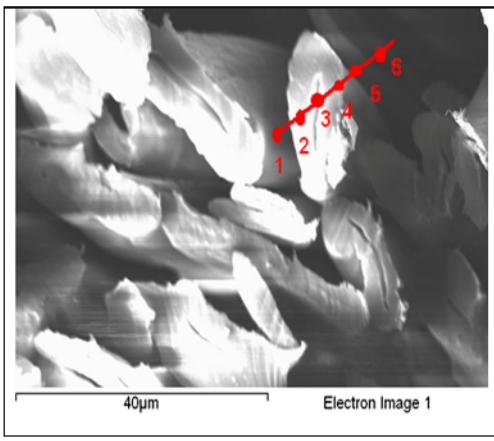


Fig. 1 SEM images of the TiP-coated cotton (**a**) and TiP/APTES-coated cotton (**b**) fibres taking at lower (**A**) and higher (**B**) magnification

distribution. In contrast, the surfaces of the TiP/APTES-treated cotton fibres were smooth, indicating a homogeneous layer without any detectable particles, suggesting an amorphous finish. The estimated size of the particles in the TP finishes was less than 1 μm. Cross-sectional SEM images of the TiP-coated fibres and the carbon, oxygen and titanium elemental contents were obtained. As expected, the results confirmed the presence of titanium on the fibre surface (points 1 and 6 in Fig. 2), but surprisingly, a greater amount of titanium was found in the inner part of the fibre (point 3 in Fig. 2), which clearly indicated that TiP deposition occurred not only on the surface of the fibres, as previously expected, but mainly in the bulk of the cotton fibres. Due to the penetration of the electron beam inside the cotton fibres, the cotton below the cross-cut visible in Fig. 1 could contribute to the observed EDX signal.

XPS measurements of cotton finishes

XPS analysis of the cotton fabrics with applied hybrids was performed to provide information about the surface compositions as well as the chemical environments and bonding of chemical species to the surface. The XPS spectrum of cellulose has been studied by Belgacem et al. (1995), while the XPS spectra of cotton fabrics with applied silane-based coatings have been studied by Mihailovic et al. (2011) and Abdelmouleh et al. (2002). Valades-Gonzales et al. (1999) studied henéquen fibres, which contain hemicellulose, lignin and waxes. The double peaks at 102 eV (Si 2p)



point	Elemental content (A%)		
	C	O	Ti
1	48.24	40.91	5.82
2	49.00	30.94	7.33
3	64.89	33.59	0.44
4	69.40	29.93	0.40
5	71.08	28.41	0.38
6	63.38	31.26	5.36

Fig. 2 Cross section of the TiP/cotton fibre and the elemental content of C, O and Ti at different measuring points

and 150 eV (Si 2s) indicated the presence of silicon atoms, while the C 1s peak at ~288 eV allowed the identification of the attachment of the silane coatings on the fibre surfaces. The C 1s peak splits into peaks at 288, 287 and 285.5 eV (Valadez-Gonzalez et al. 1999) indicating the presence of more than just one compound type bonding. The increase in the intensity of the peak at 285.5 eV relative to the peak at 288 eV (Abdelmouleh et al. 2002), which intensity increased due to the presence of methylene groups of silane, has been attributed to the C–O–Si bond on the cotton fibre surface. The variation in the C 1s peaks upon the application of silane is accompanied by a corresponding decrease in the surface O/C ratio.

Our XPS investigations (Fig. 3) showed that the chemical interaction of the TiP and TiP/APTES hybrids with the cellulose fibres decreased the C content, increased the O content, and led to the appearance of signals from Ti, Si, and N. The results revealed that the cellulose fibres treated with TiP and those treated with TiP/APTES contained Ti in significant amounts (9.7 and 7.0 %, respectively). Furthermore, TiP/APTES contained more N than TiP, and the latter contained a small amount of Si, which we attributed to impurities.

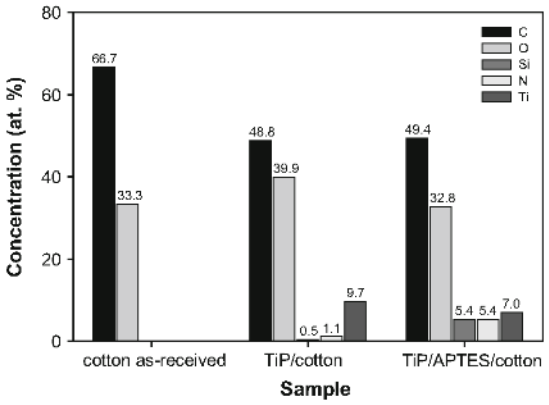


Fig. 3 Surface composition of cotton as-received and cotton treated with TiP and TiP/APTES hybrids

As shown in Fig. 4, two components could be identified in the XPS spectrum of O 1s (Fig. 4a). We attributed the peak at 530.0 eV to the oxygen lattice atoms in the TiO_2 structure, but the peak at 532.5 eV could be assigned to the OH, C–O, Si–O, and H_2O groups, all of which existed in the TiP/APTES cotton coatings and untreated cotton. Expectedly, the XPS spectrum of Ti (Fig. 4b) is a doublet structure consisting of Ti $2p_{3/2}$ and Ti $2p_{1/2}$ peaks separated by 5.5 eV. The Ti $2p_{3/2}$ peak is at ~458.7 eV and can be assigned to the Ti(4+) oxidation state in the TiO_2 structure.

Regarding the identification of the covalent Si–O–C bonds for the TiP/APTES hybrids with cotton, the O 1s spectra were less persuasive than the C 1s spectra obtained for the untreated samples (Fig. 4c) and the samples treated with TiP/APTES (Fig. 4d). For the untreated cotton, the C 1s spectrum consists of typical cellulose components, such as the C–OH peak at 286.4 eV, which is due to the characteristic C–OH bonds for cellulose; the peak at 285.0 eV, associated with the C–C/C–H bonds originating from either the lignin on the surface or adventitious carbon surface species; and the small peak at 288.1 eV, which is due to the C=O and O–C–O bonds in cellulose molecules (Fig. 4c).

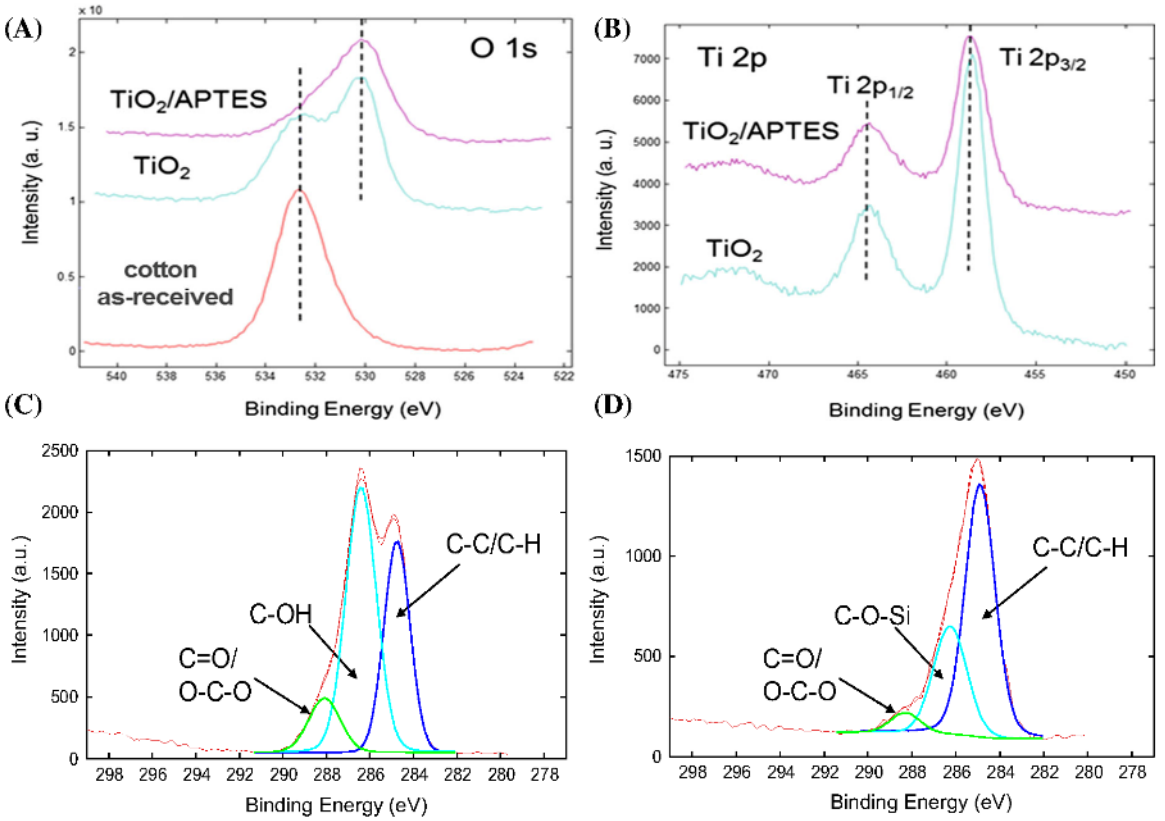


Fig. 4 The XPS O 1s (**a**) and Ti 2p (**b**) spectra of cotton as-received, TiP/cotton and TiP/APTES/cotton; and the XPS C 1s spectra of cotton as-received (**c**) and TiP/APTES/cotton (**d**)

The C 1s spectrum obtained after treating cotton with TiP/APTES (Fig. 4d) differed greatly from that of the untreated cotton. The main peak at 285.0 eV was due to the C–C/C–H bonds in the APTES structure, and the peak at 286.3 eV may be due to the C–O–Si bonds between the C atoms from the cellulose structure and the Si–O part of the silane molecule. There is also a small peak at 288.1 eV due to the C=O/O–C–O bonds. Because the signal during the XPS analyses is coming from the topmost 2–5 nm of the sample, the presence of the C–O–Si bonds in the XPS spectrum of the treated sample may indicate a reaction between the cellulose and the APTES molecules.

TEM and XRD measurements

Weakly expressed and barely observed TiO_2 particles on TiP/cotton fibres and the complete absence of any particles on the surfaces of the TiP/APTES cotton finishes motivated us to perform TEM measurement of TiP and TiP/APTES fine powders collected from the boiling water into which the precursor solutions were poured. The results revealed that the TiO_2 powder was highly agglomerated anatase with particle sizes of 5–10 nm, while the TiP/APTES powder was amorphous (Fig. 5). These results indicated that the TiP/APTES hybrids applied on cotton were likely to be amorphous and, in this respect, resemble the structures of the aminofunctionalized polymeric systems. As expected, the presence of TiP, despite its nanocrystalline form was not detected from the diffraction spectra of TiP/cotton samples (Fig. 6) because the amount of TiP was only 1.93 % w/w (Fig. 17a), which was too low compared to the detectable limit of small molecules (~8 %) that are crystalline and are mixed with cellulose. Even though the same argument could be applied also for TiP/APTES, the absence of this finis was directly consequence of its amorphous state.

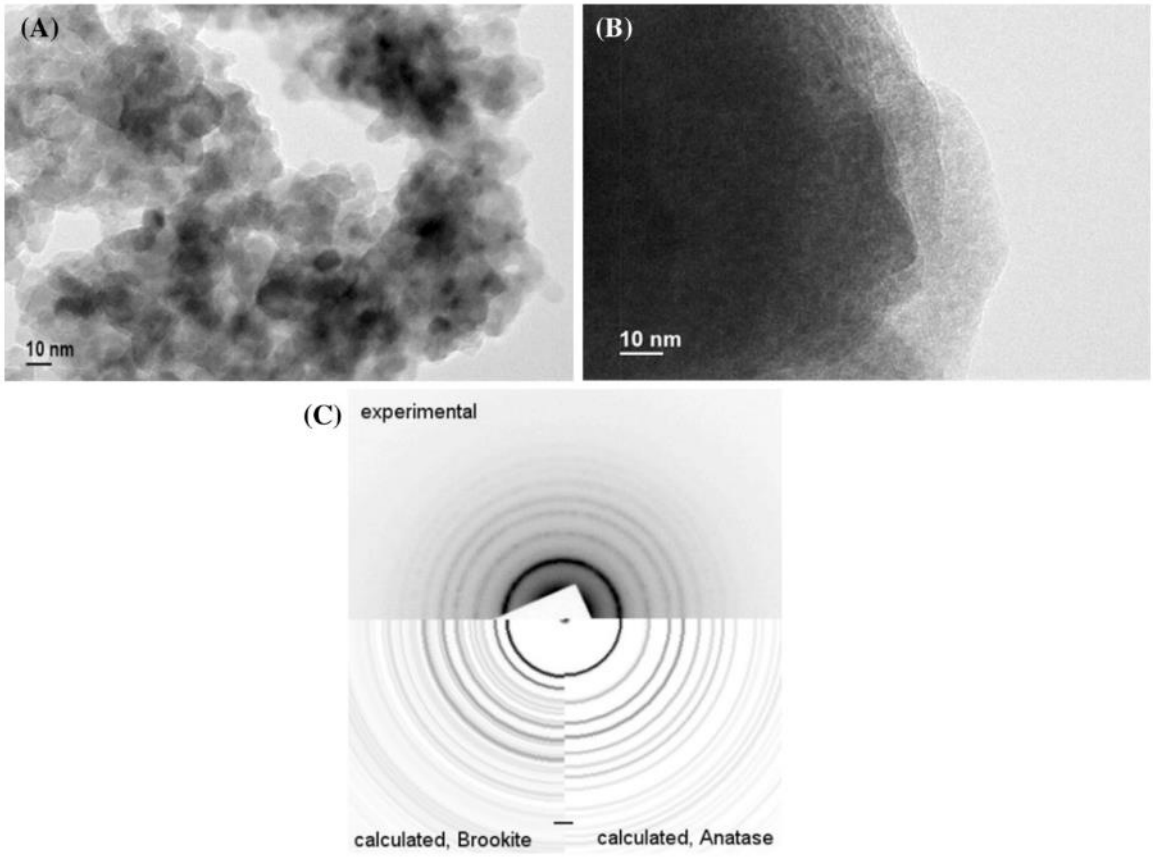


Fig. 5 TEM images of TiP (**a**) and TiP/APTES (**b**) powders obtained in the same way as used for the treatment of cotton and the corresponding interference fringes of anatase structure (**c**) of the TiP nanoparticles

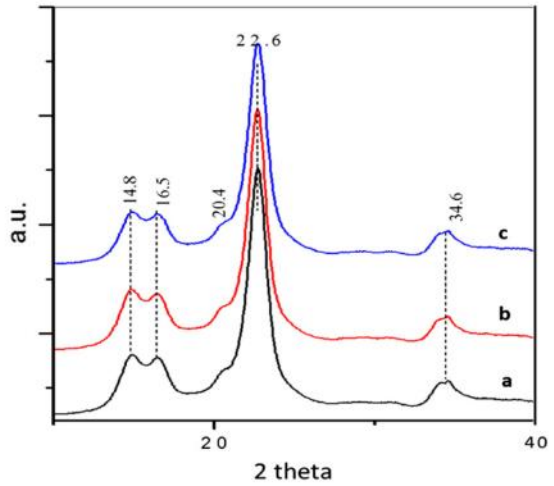


Fig. 6 XRD spectra of the studied cotton samples: cotton as-received (**a**), TiP/cotton (**b**) and APTES/TiP/cotton (**c**)

Properties of the finished cotton fabrics

UV absorption of the fabrics

The UV absorption study of the modified fabric samples (Table 1) revealed high UPFs, i.e., 31 for the TiP- and 18 for the TiP/APTES-coated samples, compared to a low UPF of 5 for untreated cotton. Lower UPF rating of the TiP/APTES-coated sample was attributed to the amorphous structure of the TiP/APTES hybrid coating in contrast to anatase TiP. The total hemispherical transmission of both coated samples was very low in the UV-A region but increased considerably in the UV-B region. This effect was attributed to the absorption of the TiP coating stemming from the anatase band gap energy of approximately $E_{gap/TiO2} \sim 3.2$ eV (Mahltig et al. 2005).

Table 1 Ultraviolet protective factor (UPF) and transmission in the UV-A and UV-B region of the studied samples before and after repeated washings

Sample	Washing cycles	UPF_{mean}	$T(UV\text{-}A)_{mean}$ (%)	$T(UV\text{-}B)_{mean}$ (%)
Cotton as-received	/	5.4	16.3	22.9
TiP/cotton	0	31.1	1.9	13.6
	1	35.8	1.6	12.4
	5	30.6	1.9	12.9
	10	30.0	2.0	12.9
	20	32.8	1.0	10.9
TiP/APTES/cotton	0	18.2	2.9	18.0
	1	20.5	2.4	16.5
	5	30.9	1.4	13.4
	10	28.4	1.6	13.4
	20	26.9	1.7	14.1

The increase of the UPF rating observed for both washed coated samples was hardly to explain, without assuming that during washings the cotton fibres formed lumps due to the shrinkage and compaction of the weft and warp yarns, which excessively scattered and absorbed light. However, the main reason for the retention high UV blocking capacity of finishes we attributed to the to the formation of covalent bonding resulting from a dehydration reaction between the hydroxyl groups of TiO_2 and SiO_2 and hydroxyl groups of cotton (Radetić 2013).

Figure 7a, b show hemispherical total reflection (TR) and hemispherical total transmission (TT) spectra of the untreated cotton sample, the untreated cotton sample soaked overnight in EtOH and then dipped in boiling water as well as the cotton samples coated with TiP and TiP/APTES. The absorption (A) spectra derived from the TR and TT spectra using the relation $[A = 1 - (TT + TR)]$ are shown in Fig. 7c. Inspection of the corresponding spectra revealed that the cotton sample treated in EtOH reflected (Fig. 7a) and transmitted (Fig. 7b) more UV radiation than the coated cotton samples, which proved its low absorption in the spectral region of $\lambda < 500$ nm (Fig. 7c). In contrast, the cotton samples coated with TiP and TiP/APTES strongly absorbed UV radiation up to 450 nm. These samples became non-absorbing in the 550–1200 nm spectral region, but their NIR absorption, which is interrupted by typical cotton absorptions, gradually increased. The TiP and TiP/APTES coatings were not exceptionally good UV absorbers compared to other cotton coatings in which TiO_2 forms a continuous layer on the fibre surface (Langlet et al. 2002).

Photocatalytic antimicrobial properties

The photocatalytic antimicrobial activity of cotton samples modified with TiP and TiP/APTES was quantitatively determined using an antimicrobial test performed in two different ways: with and without UV illumination. It is well known that several reactive oxygen species are generated by the photocatalytic reactions of TiO_2. These reactive species cause oxidation of the membrane lipids leading to the loss of cell viability and cell death (Sunada et al. 2003; Maness et al. 1999; Ibáñez et al. 2003; Hu et al. 2007). Moreover, Kikuchi et al. (1997) proposed that the actual lethal agent was hydrogen peroxide produced from hydroxyl radicals and superoxide anions. Therefore, it is not surprising that, under UV irradiation, the TiP coating showed a 60 % reduction in *E. coli*, which increased to 83 % after the addition of APTES due to the presence of amino groups (Table 2). APTES alone yielded a 52 % reduction in bacteria. The insignificant changes in bacteria growth on the untreated illuminated and not illuminated samples proved that UV irradiation did not add to the antimicrobial effect. The *E. coli* growth reduction of 60 % obtained for the TiP coating was very similar to that observed for TiO_2 powder (P25 Aeroxide, Degussa), which represents an anatase-brookite modification (Kowal et al. 2014), and nanocrystalline titania sol obtained by low-temperature sol–gel synthesis (Galkina et al. 2014). It should be noted that, despite being amorphous, the TiP/APTES hybrid finishes also showed a photocatalytic bacetriostatic effect, which is much more pronounced for crystalline anatase modification than for the

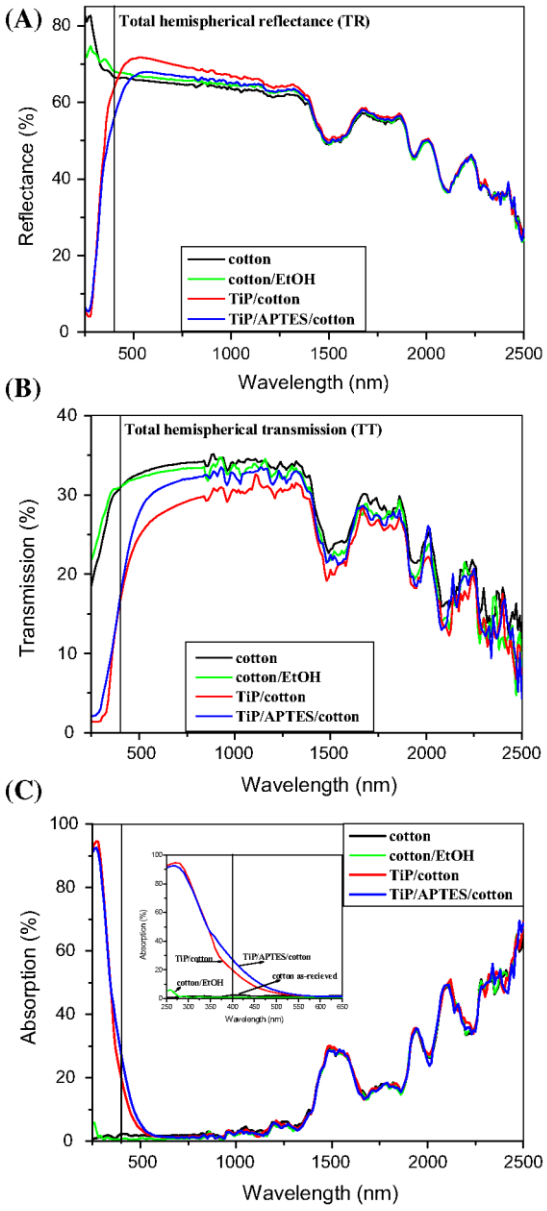


Fig. 7 Total hemispherical reflection (TR), total hemispherical transmission (TT) and absorption spectra of cotton as-received, cotton treated in EtOH (cotton/EtOH) and dipped in boiling water, TiP/cotton and TiP/APTES/cotton samples

amorphous noncrystalline titania coatings according to the literature (Radetic 2013).

The results gathered in Table 2 clearly indicate very good and durable bacteriostatic activities of the TiP and TiP/APTES coatings that were enhanced by UV irradiation. After repeated washings, the bacterial reduction for the TiP coating slightly increased. Meanwhile, the bacterial reduction for the TiP/APTES coating decreased by 10 % after the first washing and then did not change significantly after ten washings. At this point, it must be stressed that one washing in the Lauder-ometer is equivalent to five domestic washings. The APTES coating gave a negative bacterial reduction after the first washing, showing no washing durability, which could be attributed to the loss of the silane from the fibres or, more likely, blocking of the bacteriostatic effect of the amino groups. As expected, the bacterial activity of the TiP and TiP/APTES finishes strongly decreased under dark conditions (i.e., 18 and 51 %) due to the suppressed photocatalytic activity of TiO_2 in both examined coatings.

DP measurements

Photodegradation of the 1,4-β-glucosidic bond of cotton cellulose due to the photocatalytic activity of TiO_2 was studied by the measurement of the DP after different periods of UV illumination. It is well known that free radicals initiate the oxidative degradation of cellulose, which ruptures the (1 → 4) β glycosidic bonds of cellulose macromolecules and thus decreases the DP (Duan and Kasper 2011). Moreover, it has also been proven that, among the reactive species, the decrease in the DP is caused by free hydroxyl radicals, which abstract hydrogen atoms from cellulose molecules to form short-lived cellulose radical species, which then initiate further degradation processes (Fukatsu et al. 1999; Malešič et al. 2005). The results showed (Fig. 8) that, after 96 h of UV illumination, the DP of cellulose in the studied samples did not change significantly, indicating that the degradation process either did not occur to the extent that was measureable by the DP or did not occur at all. This result is in agreement with the poor photocatalytic efficacies of the TiP and TiP/APTES finishes.

Photocatalytic self-cleaning properties

Figure 9 shows the degradation of BPB deposited on the studied samples as a function of the UV exposure time, i.e., 30, 60, 90 and 120 min. Whereas the photodegradation of BPB on unwashed TiP/APTES/cotton and cotton as received as well as on 10 times washed TiP/APTES/cotton and TiP/cotton samples showed similar trend, the degree of the BPB

Table 2 Reduction (R) of bacteria *Escherichia coli* (ATCC 25922) according to the AATCC 100-1999 Standard Method of the studied samples before and after repeated washings, determined under UV illumination of the samples, R_{UV}, and without one, R_0

Sample	Washing cycles	R_{UV} (%)	R_0 (%)
TiP/cotton	0	59.6 ± 5.9	17.5 ± 5.9
	1	56.8 ± 6.3	/[b]
	10	63.1 ± 2.8	/[b]
APTES/cotton	0	51.9 ± 9.2	50.6 ± 1.7
	1	–[a]	/[b]
	10	–[a]	/[b]
TiP/APTES/cotton	0	82.8 ± 2.0	51.6 ± 3.2
	1	73.7 ± 5.1	/[b]
	10	72.2 ± 5.3	/[b]

[a] No reduction of bacteria

[b] Test was not performed

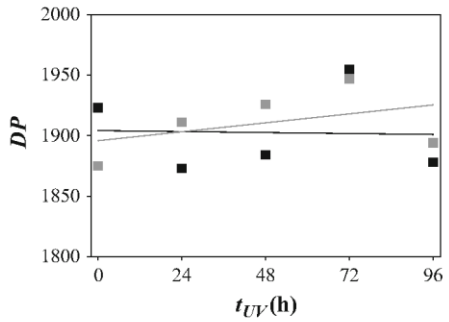


Fig. 8 Degree of polymerisation (DP) of the cotton as-received (*filled square box*) and TiP/cotton (*grey shaded square box*) samples after different time interval of UV illumination, t_{UV}

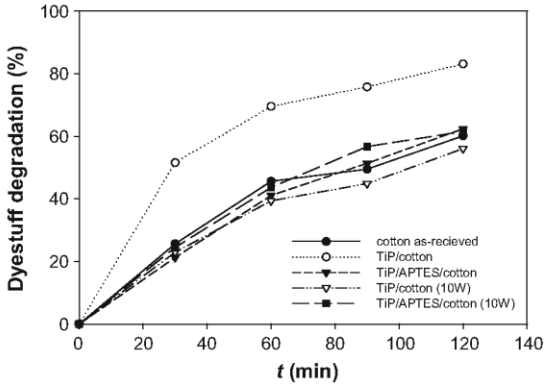


Fig. 9 Degradation of BPB on the cotton as-received, TiP/cotton and TiP/APTES/cotton samples before and after ten consecutive washings (10 W), obtained after different time interval, t, of illumination of the studied samples in Xenotest

photodegradation was significantly higher in the case of the unwashed TiP/cotton sample. BPB was selected deliberately due to the weak light stability stemming from the production of singlet and triplet radical species when illuminated (Subramanian et al. 2014) which after reaction with oxygen, form superoxide, peroxide and hydroxyl radicals (Reactive Oxygen Species) causing the BPB degradation and mineralisation. In the presence of TiP on the dyed cotton sample, the photocatalytic activity of TiO_2 anatase increased the concentration of ROS thus accelerating the BPB photodegradation and discoloration. Results revealed that, a 52 % degradation of BPB was obtained already after only 30 min of UV exposure. Expectedly, the self-cleaning effect became more pronounced by increasing the exposure time, with a 83 % degradation of the dyestuff observed at the end of the experiment. Consecutive washings of the TiP-coated sample caused a gradual decrease in the photocatalytic self-cleaning activity; specifically, the dyestuff degradation rate for the TiP-coated cotton sample washed ten times was equal to that obtained for the bare unfinished cotton. As shown in Fig. 9, the TiP/APTES-coated sample did not possess significant photocatalytic self-cleaning activity, which remained almost the same after ten washings. This lack of activity could be explained by the amorphous nature of the finish and that the amorphous TiO_2 surface was blocked by APTES moiety.

Structural studies: infrared spectral measurements

IR transmission spectra

In a first step, the IR transmission spectra of TiP, APTES and TiP/APTES finishes deposited on Si wafers (see "Experimental" section) were measured, and the vibrational bands signalling the hydrolysis and condensation reactions of the precursors (TiP and APTES) exposed to steam from boiling water were identified and assigned. From the spectra of the APTES coatings, the SiOH, OH···O and Si–O–Si vibrational bands were determined, and the changes attributed to the hydrolysis and condensation reactions were assessed, while the Si–O–Ti bands were assigned from the spectra of the TiP/APTES coatings with various TiP:APTES ratios (Ti:Si = 1:1, 1:2, 3:4, 1:1.5, 1:2.5).

The IR transmission spectra of the as-prepared TiP coatings (Fig. 10a) showed vibrational bands characteristic of TiO_2, which could be due to the increasing absorption below 800 cm^{-1} (Vuk et al. 2005, 2006). The APTES (Fig. 10a) spectra showed Si–O–Si bands at 1128 and 1024 cm^{-1}. The band at 930 cm^{-1} was attributed to SiOH (Orel et al. 2005a, b). After heat treatment at 200 °C (1/2 h), the SiOH vanished from the spectra (Fig. 10b), confirming the condensation reactions of APTES. N–H_2 stretching bands at 3656 and 3272 cm^{-1} and the corresponding deformational band at 1596 cm^{-1} were observed, while the mode belonging to the protonated amino groups expected at ~1550–1500 cm^{-1} was not observed because of the neutral pH conditions of the APTES sols (Bellamy 1954).

The IR spectra of various TiP/APTES coatings that were hydrolysed and condensed over water steam (Fig. 10a) and then heated at 200 °C (Fig. 10b) revealed the evolution of the bands attributed to the Si–O–Ti modes at 903 cm^{-1} (Schraml-Marth et al. 1992; Aizawa et al. 1991; Puzenat and Pichat 2003; Mihelčič et al. 2014). The position of the corresponding band at 903 cm^{-1} remained practically the same for all Ti:Si ratios (Fig. 10a, b), but the relative intensity of the Si–O–Ti band with respect to the Si–O–Si band at 1034 cm^{-1} was maximal for TiP/APTES when the Ti:Si ratio was equal to 1.33 (Fig. 10b). The strong Si–O–Ti band indicated highly interlinked silica and titania networks and the formation of a dense and compact hybrid (Schraml-Marth et al. 1992; Aizawa et al. 1991).

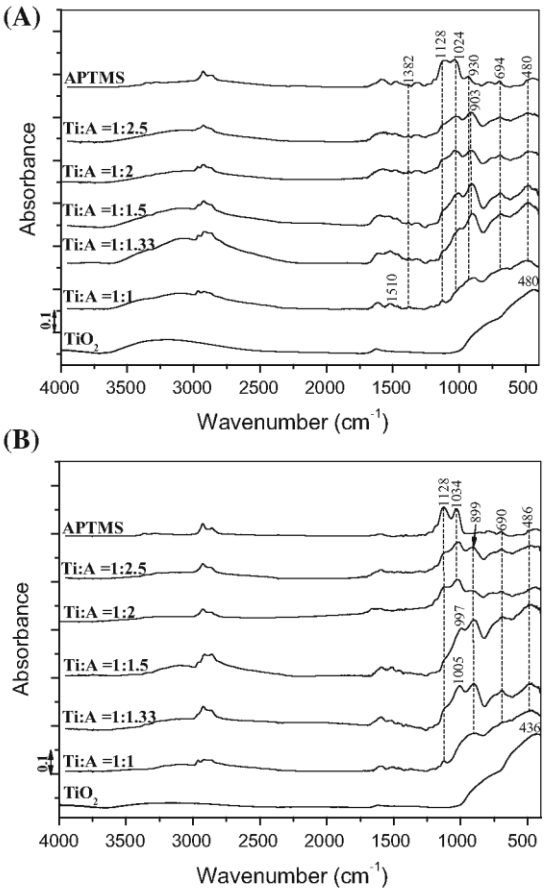


Fig. 10 IR spectra of TiO_2, APTES and various mixtures of TiP/APTES (Ti:A) deposited on a Si-wafer, hydrolysed and partially condensed over water steam (**a**) and then heated at 200 °C (**b**)

The transmission spectra of the TiP/APTES coatings showed a broad OH stretching band at 3051 cm^{-1}, indicating stronger H-bonding (intra and inter) than that found for cellulose (Maréchal and Chanzy 2000; Hinterstoisser and Salmén 1999; Hofstetter et al. 2006), which we inferred from the shift of this band to lower wavenumbers for inter (Hadzi and Orel 1973; Angeloni et al. 1974) and intra (Avbelj et al. 1985) H-bond systems. As expected, the OH stretching band showed a fine structure and redshifted slightly after the heat treatment (Fig. 10a, b).

Another important issue for this study was the establishment of the protonated amino groups, which were identified from the bands at 1550–1533 cm^{-1} and the C–N stretching band at 1275 cm^{-1} in the TiP/APTES spectra. The band at 1550–1500 cm^{-1} did not

appear in the APTES spectra, seemingly because TiP required acidic conditions for the formation of the protonated amino groups (Horner et al. 1992).

ATR IR spectra of the powders

To prevent the misinterpretation of the vibrational bands in the ATR spectra of the cotton finishes, the ATR spectra of the APTES and TiP/APTES powders (see "Experimental" section) (Fig. 11) were recorded and compared to the corresponding transmission spectra (Fig. 12). In the ATR spectra, the bands redshifted and exhibited band shape distortions due to the variable refractive index, which changes in the frequency range of the vibrational band (Vince et al. 2006). This effect is stronger for more intense bands (up to $\Delta\nu \sim -70$ cm^{-1} for the Si–O–Si bands, for example), while the weaker bands showed redshifts in the frequency of only a few cm^{-1} (the SiOH band, for example).

For the APTES powders, Si–O–Si bands appeared at 1070 and 997 cm^{-1} in the ATR spectrum (Fig. 11b) and at 1121 and 1031 cm^{-1} in the transmission spectrum (Fig. 12b). However, weaker SiOH bands were found in the transmission and ATR spectra at nearly the same frequencies i.e., at 929 and 922 cm^{-1}, respectively. As expected, for the TiP samples, the redshifts in the frequency were even greater; in the ATR spectrum (Fig. 11a), no distinct maximum attributed to the Ti–O stretching mode was observed,

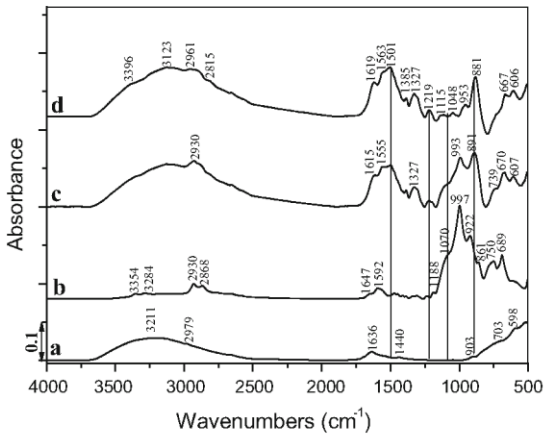


Fig. 11 ATR spectra of TiP (*a*), APTES (*b*) and TiP/APTES (*c*) powders and the subtraction spectrum of APTES from TiP/APTES (*d*)

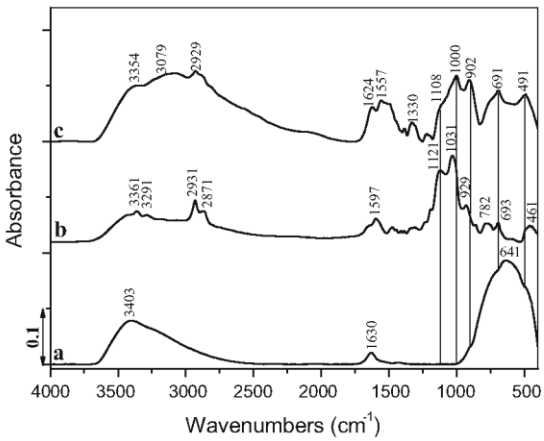


Fig. 12 Transmission spectra of TiP (*a*), APTES (*b*) and TiP/APTES (*c*) powders

but a maximum was clearly seen at 641 cm^{-1} in the transmission spectrum (Fig. 12a) (Vuk et al. 2005, 2006).

In the ATR spectrum of the TiP/APTES (Ti:Si = 1:1.33) powders (Fig. 11c), only one Si–O–Si band was observed at 993 cm^{-1}, while in the corresponding transmission spectrum, two Si–O–Si bands were assigned at 1108 and 1000 cm^{-1} (Fig. 12c). In these spectra, the SiOH and Si–O–Ti bands overlapped, showing only a single, relatively strong and broad band at 891 (ATR) and 902 cm^{-1} (transmission).

Although there was no doubt about the assignment of the Si–O–Ti mode at $\sim$891 cm^{-1} in the ATR spectra, the additional evidence about its mixed mode character was obtained from the (TiP/APTES–APTES) subtraction spectrum (Fig. 11d). The strong positive (881 cm^{-1}) and negative (800 cm^{-1}) bands indicated that the band at 891 cm^{-1} was the superposition of the Si–O–Ti (at 891–920 cm^{-1}) and SiOH bands, which also appeared in this region, as we inferred from the ATR spectrum of the APTES sample (at 922 cm^{-1} in Fig. 11b).

The strong OH stretching band centred at $\sim$3211 cm^{-1} in the ATR spectrum of TiP (Fig. 11a) and at 3123 cm^{-1} in the (TiP/APTES–APTES) subtraction spectrum (Fig. 11d) signalled the presence of a genuine OH-bond vibrational band formed due to the water steam treatment of the mixed TiP and APTES precursors. The establishment of the H bonding network was important because it enabled the bonding

of the sol–gel hybrid to the bound water molecules present in the non-crystalline region of cellulose (Hofstetter et al. 2006).

Finally, the ATR evidence of the protonation of the amino groups was sought because this protonation is responsible for the bactericidal properties. From the spectra shown in Figs. 11 and 12, in the transmission (Fig. 12b) and ATR (Fig. 11b) spectra of APTES, the NH_2 deformational band was found at 1597 cm^{-1}, while in the spectra of TiP/APTES, the band became broader and split into two bands in the 1550–1505 cm^{-1} spectral region (Figs. 11c, 12c), signalling the protonation of the amide groups (Bellamy 1954). The protonation of the APTES in the latter spectra could be explained by the presence of a more acidic TiP precursor. The protonation of APTES could be easily achieved, even when the APTES was deposited on a titanium metal surface (isoelectric point 6.0), while no protonated amine was observed when the APTES was deposited on a Ni metal surface (isoelectric point 10–12) (Horner et al. 1992). In summary, in the TiP/APTES hybrid, the TiP played the role of a hydroxylated acidic surface, which was necessary for realizing protonated APTES and imparting bactericidal properties to the hybrid nanocomposite.

ATR IR spectra of the cotton samples

ATR spectra of cotton: background selection We began investigations of the cotton finishes by measuring the ATR spectra of untreated cotton fabrics (cotton as-received) and fabrics stored overnight in an EtOH water solution, dipped in boiling water, and then dried (EtOH/cotton) (see "Experimental" section) (Fig. 13A, B). The latter spectra were required to obtain the subtraction spectra, which enable the characterization of the sol–gel hybrids on the cotton fabrics. The spectra were baseline corrected to 0 in the 4000–400 cm^{-1} region and normalized to 1 at 1160 cm^{-1}, the absorbance peak reflecting the carbohydrate backbone. The ATR spectra of both cotton samples showed typical bands attributed to the OH stretching mode of cellulose at 3412 cm^{-1} (O_2H–O_6, intra), 3326 cm^{-1} (O_3H–O_5, intra) and 3266 cm^{-1} (O_6H–O_3, intermolecular H bond) (Tsuboi 1957; Maréchal and Chanzy 2000; Chung et al. 2004; Hinterstoisser et al. 2001; Hinterstoisser and Salmén 1999).

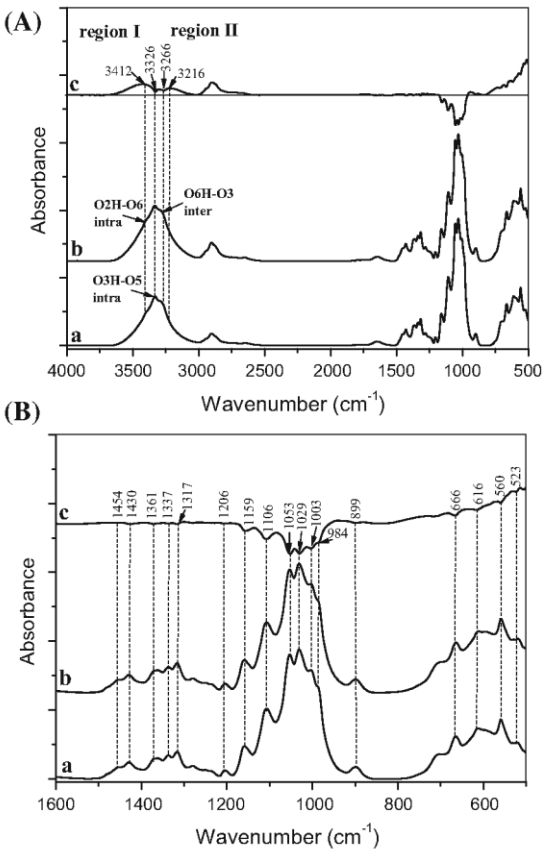


Fig. 13 ATR spectra of cotton as-received (*a*), cotton treated in EtOH and the boiling water (EtOH/cotton) (*b*) and the subtraction spectrum of (EtOH/cotton—cotton as-received) (*c*) in the spectral region from 4000 to 500 cm^{-1} (**A**) and in the spectral region from 1600 to 500 cm^{-1} (**B**)

The corresponding subtraction spectrum (EtOH/cotton—cotton as-received) (c in Fig. 13A) revealed that the OH–O band (3500–2700 cm^{-1}) gained intensity in the high (>3400 cm^{-1}, region I) and low (~3200 cm^{-1}, region II) frequency wings (as denoted in Fig. 13A) of the OH–O band. We attributed the intensity increase in region I to the presence of loosely bound water molecules ("free" water absorbs <3500 cm^{-1}), i.e., water indirectly bonded to the OH groups via another water molecule, while the presence of the 3200 cm^{-1} band (region II) was associated with strongly bound water (Walrafen and Klein 1987), i.e., water bound directly by hydrogen bonds to the OH groups of the cellulose (Olsson and Salmén 2004). Treatment of the cotton substrates with EtOH followed by dipping in boiling water strongly affected the

proportion of water that was more loosely versus strongly bonded to the cellulose. Changes were also observed in the fingerprint spectral region (1160–900 cm^{-1}), where the ring skeletal modes appear as negative bands, indicating that they were partially lost during the EtOH/boiling water treatment (Fig. 13B) (Maréchal and Chanzy 2000). However, all of the bands were negative, and they did not show frequency shifts or band shape changes. In contrast, Hinterstoisser and Salmen (1999) observed a small (few cm^{-1}) shift in the frequency of the 1,2-glucosid (–C–O–C–) band at 1158 cm^{-1} in the spectra of cellulose exposed to different humidity conditions. The most important observation was that the water uptake during the EtOH/boiling water treatment affected cotton selectively; more water was adsorbed on the easily accessible water sites (region I) than on sites with strongly absorbed water molecules (region II). This finding is not new and is in agreement with the moisture uptake study using dynamic IR and deuterium exchange performed by Hofstetter et al. (2006). Accordingly, to obtain the subtraction spectra, only the EtOH/cotton spectrum was used as the background.

ATR spectra of the coated cotton samples The ATR spectra of the TiP-coated cotton (TiP/cotton) and TiP/APTES-coated cotton (TiP/APTES/cotton) samples (Fig. 14) were examined to confirm the presence of hybrids on the cotton fabrics and, by inspecting the characteristic bands in the corresponding subtraction spectra (Fig. 15), to ascertain their interactions with the cotton fibres. The main challenge was to show the existence of the Si–O–C bonds known to form between the silanes and the OH groups of cellulose at elevated temperatures (Xie et al. 2010). To identify the corresponding modes in the ATR spectra, the TiP/cotton and TiP/APTES/cotton samples were exposed to heat treatment at 105 °C (24 h), and the corresponding subtraction spectra were examined (Fig. 16).

The ATR spectra of the TiP/cotton and TiP/APTES/cotton samples (Fig. 14) were very similar because the massive absorption of the cellulose bands blurred the vibrational bands of the applied finishes. This was not surprising as the amount of hybrids on the cotton was only a few percent. Nonetheless, the subtraction procedure gave reproducible spectra with good signals, as has been demonstrated in our previous

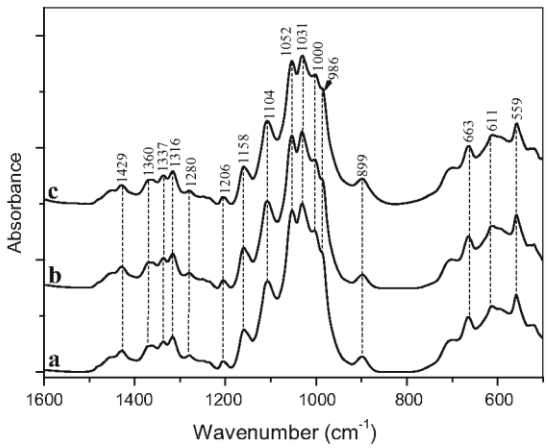


Fig. 14 ATR spectra of cotton as-received (*a*), TiP/cotton (*b*) and TiP/APTES/cotton (*c*) in the spectral region from 1600 to 500 cm^{-1}

studies of other finished cotton samples (Vilčnik et al. 2009; Vince et al. 2006).

A closer look at the subtraction spectra of (TiP/cotton—EtOH/cotton), (TiP/APTES/cotton—EtOH/cotton) and (TiP/APTES/cotton—TiP/cotton) samples (a, b and c in Fig. 15A) revealed expected changes in the spectral region from 3700 to 2700 cm^{-1}, where the OH stretching bands appeared. The broad OH···O stretching band was split into high (region I) and low frequency wings (region II), similar to the (EtOH/cotton—cotton as-received) subtraction spectrum (c in Fig. 13A). However, the intensity of the OH stretching band in region II was greater than that in region I, which suggested preferential occupation (bonding) of the TiP/APTES hybrid on the strongly bonded water molecules of cellulose or, even more likely, the presence and bonding of the hybrids on the fibres. The redshifted band maxima of the positive OH stretching band in the subtraction spectra (Fig. 15A) at 3030 cm^{-1} (a in Fig. 15A), 3060 cm^{-1} (b in Fig. 15A), and 3106 cm^{-1} (c in Fig. 15A) suggested that the strongest H-bonding occurred in the TiP/cotton finishes. In conclusion, at ambient temperatures, the hybrids bonded preferentially to the strongly the bonded water molecules of cellulose (Hinterstoisser and Salmén 1999).

The subtraction spectra (Fig. 15B) in the 1700–500 cm^{-1} spectral region did not confirm directly the existence of TiP hybrid on fibres because TiP did not show distinct band in this spectral region as

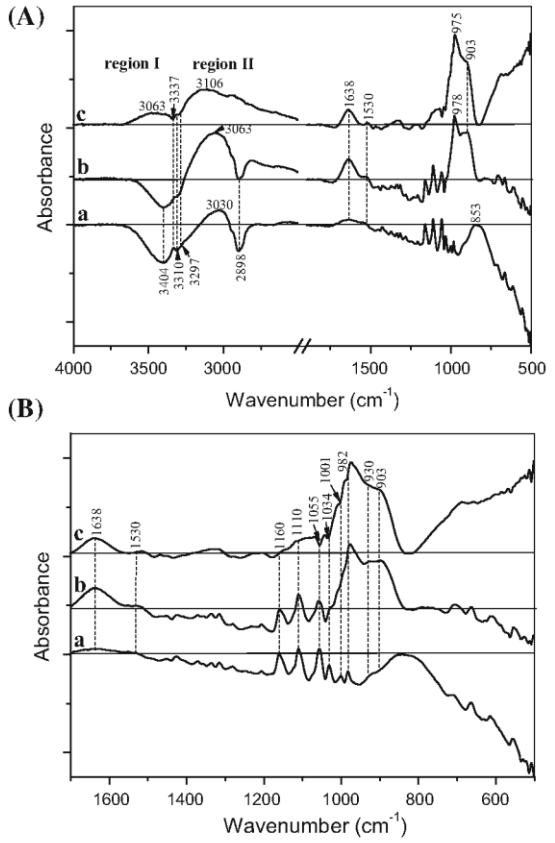


Fig. 15 Subtraction spectra of TiP/cotton—EtOH/cotton (*a*), TiP/APTES/cotton—EtOH/cotton (*b*) and TiP/APTES/cotton—TiP/cotton (*c*) samples in the spectral region from 4000 to 500 cm^{-1} (**A**) and in the spectral region from 1700 to 500 cm^{-1} (**B**)

silica. However, in the TiP/APTES spectrum, i.e., the (TiP/APTES/cotton—EtOH/cotton) subtraction spectrum (b in Fig. 15B), we observed strong positive bands at 978 and 903 cm^{-1}, which can be attributed to the Si–O–Si and Si–O–Ti modes. The latter mode corresponded nearly exactly to the Si–O–Ti band observed in the ATR spectra of the corresponding hybrid coatings prepared in the absence of cotton (c in Fig. 11). The redshift in the frequency of the Si–O–Si band ($\Delta\nu \sim -20$ cm^{-1}) suggested that the structure of the hybrid network was modified in the presence of cellulose, while the strong Si–O–Ti band, which indicated high extent of crosslinking between both precursors and their intimate mixing, did not change

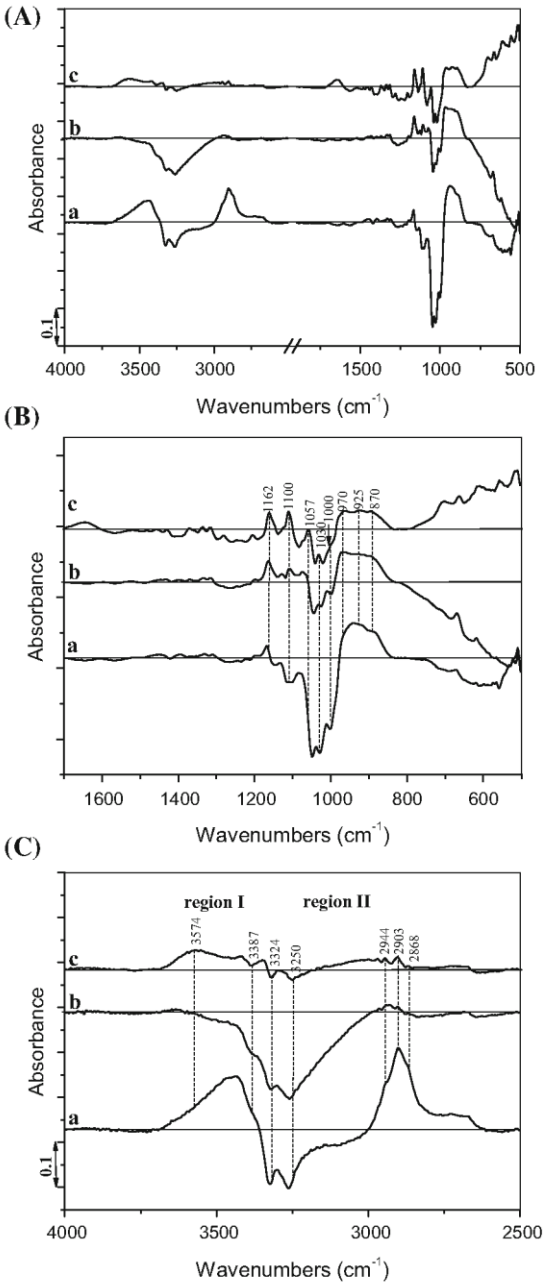


Fig. 16 Subtraction spectra of TiP/APTES/cotton (105 °C)—cotton-as received (*a*), TiP/APTES/cotton—EtOH/cotton (*b*) and TiP/APTES/cotton (105 °C)—cotton-as received (105 °C) (*c*) samples in the spectral region from 4000 to 500 cm^{-1} (**A**), in the spectral region from 1700 to 500 cm^{-1} (**B**) and in the spectral region from 4000 to 2500 cm^{-1} (**C**)

markedly. We attributed these results to the synthesis route; non-hydrolysed TiP and APTES precursors penetrated the fibres, where they were simultaneously subjected to hydrolysis in the boiling water for a very short time, which prevented the formation of separate silica and titania networks and the formation of nanoparticles (Schraml-Marth et al. 1992).

It is important to note that the skeletal modes of the cellulose (1158, 1104, 1052, 1031, 1000 and 986 cm^{-1}) (Fig. 14) changed slightly, indicating that they were not strongly affected by the application of the TiP/APTES and TiP hybrids. The interactions were rather weak, as suggested by the small frequency shifts in the cellulose skeletal bands at 1160, 1110, 1055, 1001 and 978 cm^{-1} in the (TiP/APTES/cotton—TiP/cotton) subtraction spectrum (b in Fig. 15B). But the bands at 1000 and 986 cm^{-1} diminished in intensity and became weaker compared to the other skeletal bands (1160, 1110, 1055 cm^{-1}), which suggested that they were preferentially consumed due to interactions with the Ti–OH groups in the TiP hybrid.

It should also be mentioned that the (TiP/APTES/cotton—EtOH/cotton) subtraction spectrum (b in Fig. 15B) confirmed that the protonation of the TiP/APTES reached completion. A strong band was observed at 1530 cm^{-1} (NH_3^+) in these spectrum, in contrast to the (TiP/cotton—EtOH/cotton) subtraction spectrum (a in Fig. 15B).

Although the positive bands at 978, 930 and 903 cm^{-1} (b in Fig. 15B) confirmed the presence of the TiP/APTES hybrid on cotton, they did not provide direct proof of the establishment of the Si–O–C bonds conceived from the XPS studies (Figs. 3, 4) that were expected to form due to the condensation reactions between the sol–gel hybrids and the OH groups of the cellulose. The formation of covalent Si–O–C bonds was proposed and anticipated by different authors (Xie et al. 2010; Abdelmouleh et al. 2002; Mihailović et al. 2011; Valadez-Gonzalez et al. 1999), but the OH groups of the cellulose, which may be involved in the formation of the covalent Si–O–Si bonds, have not yet been clearly identified from the ATR spectra. Because it has already been determined that, for heat treated cotton finishes, refluxing the fibres does not remove the finishes, we exposed the TiP/APTES/cotton, TiP/cotton and EtOH/cotton samples to heat treatment (105 °C, 24 h). The subtraction spectra of the [(TiP/APTES/cotton (105 °C)—cotton as-received), a in Fig. 16], [(TiP/APTES/cotton (105 °C)—EtOH/cotton), b in Fig. 16] and [(TiP/APTES/cotton (105 °C)—EtOH/cotton (105 °C), c in Fig. 16] samples were constructed and compared to the subtraction spectra of the non-heated cotton finishes (a, b in Fig. 14).

The corresponding subtraction spectra (Fig. 16) showed that the –C–OH bands, which were attributed to the primary and secondary alcohol groups of cellulose (Maréchal and Chanzy 2000; Hinterstoisser and Salmén 1999) at 1057, 1030 and 1000 cm^{-1} (c in Fig. 16B), were negative, which indicated that the primary and secondary alcohol groups (C–OH) were consumed when the TiP/APTES hybrid was applied to the cotton fabrics and then heated at 105 °C. Other skeletal bands at 1162, 1100 and 1057 cm^{-1} had slightly shifted frequencies, which indicated that they were also affected by the interactions with the silanol groups. However, more apparent was the negative absorption in the frequency window from 1150 to 1000 cm^{-1}, which was not observed in the subtraction spectra of the as-prepared, i.e., non-heated, TiP/APTES spectrum (b in Fig. 15B). The Si–O–Si and Si–O–Ti bands (970, 925 and 870 cm^{-1}) were clearly observed in both subtraction spectra.

The most intense negative bands were found in the (TiP/APTES/cotton—cotton as-received) subtraction spectrum (a in Fig. 16B), while the negative bands observed in the spectrum obtained by the subtraction of EtOH/cotton (b in Fig. 16B) and cotton as-received and heat treated at 105 °C (c in Fig. 16B) were less pronounced. It should be noted that the observed negative bands in the spectral region of the skeletal bands of cotton (1150–1000 cm^{-1}, Fig. 16B) were also reported by Valadez-Gonzales et al. (1999), but the authors did not attribute the corresponding negative absorption to the elimination of the skeletal bands in the cellulose [henéquen (*Agave fourcroydes*)] and thus to the interaction sites between the silane molecules and the cellulose. It seems that henéquen fibres are more susceptible to interactions with silanes, which we could attribute to the presence of lignin, which is known to interact strongly with silanes (Rasmussen et al. 2014b). Our cotton did not contain lignin.

The heat-treatment of the fabrics also changed the water content, as shown by the corresponding O–H···O bands (Fig. 16C). The subtraction of the as-received cotton heat treated at 105 °C from the TiP/

APTES/cotton heat treated at 105 °C showed relatively weak negative O–H bands in the spectral region 3600–2800 cm^{-1} corresponding to the $O_6H–O_3$ vibrational band at ~3250 cm^{-1}, the $O_5H–O_2$ intramolecular mode at ~3324 cm^{-1} and the $O_6H–O_2$ band at ~3387 cm^{-1} (c in Fig. 16C). This result indicated that the heat-treatment of the fabrics changed their water contents and suggested that some of the −OH groups were consumed by the silanol groups due to the condensation reactions. The condensation was not complete, as could be inferred from the presence of a positive band at 3574 cm^{-1}. This band indicated that some of the O–H groups were free of hydrogen bonding. We tentatively assigned the corresponding band to the "free" Si–OH groups of the TiP/APTES hybrids, although the assignment of this band to the C–OH stretching mode is also possible (Maréchal and Chanzy 2000).

Expectedly, the genuine intra and inter O–H···O bands of cotton were more intense and negative in the spectra obtained by the subtraction of the as-received cotton and the EtOH/cotton spectra from the TiP/APTES/cotton spectrum (105 °C) (b and c in Fig. 16C), indicating that more water (loosely and strongly bonded) existed in the corresponding cotton samples than in the heated samples. However, the positive band in region I (a in Fig. 16C) suggested that the TiP/APTES after the heat treatment preferentially bonded to the water molecules indirectly linked to the OH groups via another water molecule (Walrafen and Klein 1987) and not to the water bound directly by hydrogen bonds to the OH groups of the cellulose (Olsson and Salmén 2004), as occurred at ambient temperature (b in Fig. 15). This finding was consistent with the penetration of the TiP/APTES within the cotton fabrics and its bonding to the cellulose. Obviously, the interactions were not limited to the water system of cellulose; they also affected other molecular sites in cellulose, as shown by the characteristic bands at 1057, 1030 and 1000 cm^{-1} and described above (Fig. 16B).

TG measurements

TG analysis enables the estimation of the amount of the hybrid attached to the cotton fibre surface and can provide complementary information about the thermal behaviours of the hybrid coatings deduced from either elemental analysis or infrared spectroscopy. The TG analyses (Fig. 17) of the cotton fibres revealed that the pyrolysis of the cotton fibres included three stages: initial, main, and char decomposition (Zhu et al. 2004). In the initial stage below 300 °C, the weight loss is small and attributed to the loss of water. In the temperature range of 300–380 °C, the main pyrolysis stage occurs, and the weight loss was quite significant. It is known that the first stage involves changes in the amorphous part of the cellulose, while in the second stage, pyrolysis occurs in the crystalline regions of the cellulose fibres (Zhu et al. 2004). In the third stage, char is produced (T > 430 °C), and water and carbon dioxide form.

The results of the TG measurements of the TiP/APTES/cotton and TiP/cotton samples revealed that the mass losses of the cotton and finished cotton fibres were as expected. It should be noted that the mass that remained after heating the untreated cotton (i.e.,

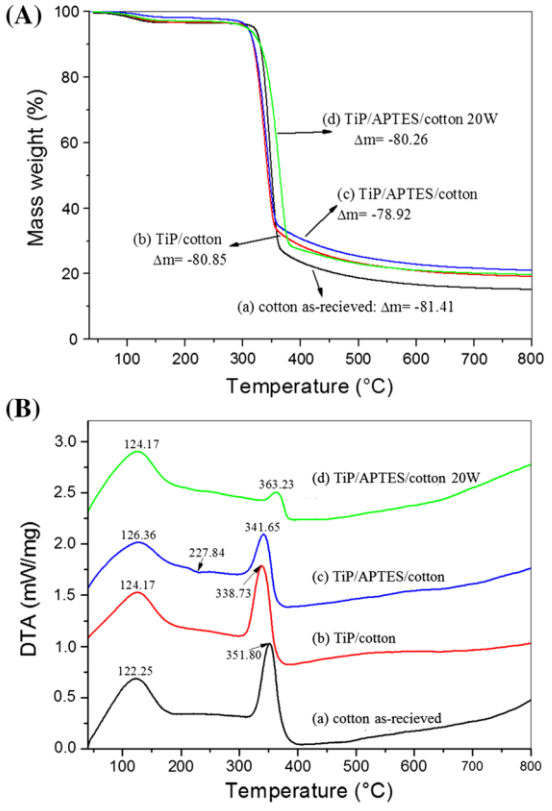


Fig. 17 TG (**A**) and DTA (**B**) graphs for cotton as-received (*a*), TiP/cotton (*b*) and TiP/APTES/cotton (*c*) and TiP/APTES/cotton after twenty consecutive washing (20 W) (*d*) samples analysed in a nitrogen atmosphere

18.59 %) in N_2 was a few percent higher than the mass losses obtained after heating the untreated cotton in air (Vasiljević et al. 2015; Xue et al. 2009). To avoid errors due to the complex pyrolysis mechanism, the measurements were repeated several times with increasing initial masses of the finished samples (up to 100 mg), i.e., up to 5–10 times. The as-received cotton sample (Fig. 17) showed a mass loss $\Delta m = -81.41$ %, exceeding the mass losses observed for the TiP/cotton ($\Delta m = -80.85$ %) and the TiP/APTES/cotton ($\Delta m = -78.92$ %) samples. The small mass losses were not surprising due to the short dipping times of the cotton fibres in the boiling water. Similarly, the shift in the maximal temperature of the mass change obtained from the dTG measurements was only few degrees (not shown here). The washed TiP/APTES/cotton sample had slightly higher mass losses than the untreated cotton ($\Delta m = -80.26$ %). In addition, TiP/APTES/cotton sample showed DTA curve which differed compared to the DTA curves of bare cotton and TiP/cotton samples. The heat changes in the temperature interval from 220 to 250 °C were attributed to the condensation reactions of the TiP/APTES hybrid competing with the loss of the amino groups of the APTES part of the hybrid. Unfortunately, we were not able to obtain Δm for the TiP/cotton sample; repetitive measurements gave scattered results ($\Delta m = \pm 0.5$ %), which indicated that the TiP coating was too small to provide reliable mass losses.

Conclusions

The soaking of cotton fabric in non-hydrolysed solutions of precursors followed by quick immersion in boiling water was an efficient method for the impregnation of cotton fabric with TiP/APTES, and to a lesser extent, with TiP hybrids, as shown in the SEM and EDX micrographs. Due to the short immersion time in the boiling water, the TiP/APTES hybrids were amorphous and resembled amino-functionalized polymers. The TiP hybrids were in the form of nanoparticles with sizes of 5–10 nm, as observed in the TEM images. These morphological differences caused differences in the photocatalytic activity; while TiP/APTES did not have any photocatalytic activity, TiP degraded BPB quite effectively. An additional advantage of low-temperature fibre processing, was the impregnation of the cotton fibres throughout their volume, contrasting surface coating depositions when other methods are applied. Infrared ATR measurements of the cotton hybrids revealed that the anchoring of the TiP/APTES hybrids at ambient temperatures occurred via the water bound directly by hydrogen bonds to the OH groups of the cellulose. Loosely bonded water also participated in bonding the hybrids to cellulose, but to a lesser extent. No covalent bonding of the hybrids to the OH groups of cellulose could be inferred from the ATR spectra; however, Si–O–C bonding was confirmed for the cotton heat treated at 105 °C.

The lack of covalent Si–O–C bonding was not detrimental to obtaining stable UPF and bacteriostatic properties because the interpenetrating H-bonding systems of cellulose and the hybrids as well as the presence of the hybrids inside the fabric provided sufficient mobility of the hybrid molecules or fragments and their expulsion to the fabric surface when the cotton fabrics were repetitively washed. This behaviour explained the stability of the bacteriostatic photocatalytic efficiency of the TiP/APTES hybrids, which dropped by ~10 %, and the variation in the UPF and bacteriostatic effects with washing and UV illumination observed for the TiP-coated cotton. We primarily ascribed the enhanced bacteriostatic effect of the TiP/APTES relative to the TiP-coated cotton samples to the presence of protonated amino groups. Further work is planned to apply the cotton finishes using heat treatment.

Acknowledgments Authors dedicate this article to doc. Dr. Vojmir Francetič who sadly passed away during the preparation of this work. This work was supported by the Slovenian Research Agency (Programmes P2-0213 and P2-0393). The authors would like to thank dr. Urban Novak from the National Institute of Chemistry for performing the IR spectroscopic measurements.

References

Abdelmouleh M, Boufi S, ben Salah A, Belgacem MN, Gandini A (2002) Interaction of silane coupling agents with cellulose. Langmuir 18:3203–3208

Aizawa M, Nosaka Y, Fujii N (1991) FT-IR Liquid attenuated total reflection study of TiO_2–SiO_2 sol–gel reaction. J Non-Cryst Solids 128:77–85

Angeloni L, Marzocch MP, Hadzi D, Orel B, Sbrana G (1974) Symmetric hydrogen bonding—infrared-absorption spectrum of potassium hydrogen succinate single-crystal. Chem Phys Lett 28:201–204

Arkles BC, Larson GL (2004) Silicon compounds: silanes and silicones: a survey of properties and chemistry. Gelest Inc, Morrisville

Avbelj F, Orel B, Klanjsek M, Hadzi D (1985) Vibrational-spectra of potassium hydrogen maleate crystal and solution. Spectrochim Acta A 41:75–87

Bacsa RR, Grätzel M (1996) Rutile formation in hydrothermally crystallized nanosized titania. J Am Ceram Soc 79:2185–2188

Belgacem MN, Czeremuszkin G, Sapieha S, Gandini A (1995) Surface characterization of cellulose fibres by XPS and inverse gas chromatography. Cellulose 2:145–157

Bellamy LJ (1954) The infra-red spectra of complex molecules. Methuen, London **(New York: Wiley)**

Brinker CJ, Scherer GW (1990) Sol–gel science: the physics and chemistry of sol–gel processing. Academic Press, Boston

Brooks RE, Moore SB (2000) Alkaline hydrogen peroxide bleaching of cellulose. Cellulose 7:263–286

Castellano M, Gandini A, Fabbri P, Belgacem MN (2004) Modification of cellulose fibres with organosilanes: Under what conditions does coupling occur? J Colloid Interface Sci 273:505–511

Čepin M, Jovanovski V, Podlogar M, Crnjak Orel Z (2015) Amino- and ionic liquid-functionalised nanocrystalline ZnO via silane anchoring—an antimicrobial synergy. J Mater Chem B 3:1059–1067

Chemseddine A, Moritz T (1999) Nanostructuring titania: Control over nanocrystal structure, size, shape, and organization. Eur J Inorg Chem 2:235–245

Chung C, Lee M, Choe EK (2004) Characterization of cotton fabric scouring by FT-IR ATR spectroscopy. Carbohydr Polym 58:417–420

Colleoni C, Massafra MR, Rosace G (2012) Photocatalytic properties and optical characterization of cotton fabric coated via sol–gel with non-crystalline TiO_2 modified with poly(ethylene glycol). Surf Coat Technol 2017:79–88

Čolović M, Jerman I, Gaberšček M, Orel B (2011) POSS based ionic liquid as an electrolyte for hybrid electrochromic devices. Sol Energy Mater Sol C 95:3472–3481

Daniels MW, Francis LF (1998) Silane adsorption behavior, microstructure, and properties of glycidoxypropyltrimethoxysilane-modified colloidal silica coatings. J Colloid Interface Sci 205:191–200

Daoud WA, Xin JH, Zhang YH (2005) Surface functionalization of cellulose fibers with titanium dioxide nanoparticles and their combined bactericidal activities. Surf Sci 599:69–75

Duan J, Kasper DL (2011) Oxidative depolymerization of polysaccharides by reactive oxygen/nitrogen species. Glycobiology 21:401–409

Fir M, Orel B, Vuk AS, Vilčnik A, Ješe R, Francetič V (2007) Corrosion studies and interfacial bonding of urea/poly(dimethylsiloxane) sol/gel hydrophobic coatings on AA 2024 aluminum alloy. Langmuir 23:5505–5514

Fujishima A, Hashimoto K, Watanabe T (1999) TiO_2 photocatalysis—fundamentals and applications. BKC Inc, Tokyo

Fukatsu K, Kokot S, Schweinsberg DP (1999) Bleaching of cotton fabric with electrogenerated oxygen—the role of hydroxyl and superoxide radicals. Text Res J 69:769–775

Galkina OL, Sycheva A, Blagodatskiy A, Kaptay G, Katanaev VL, Seisenbaeva GA, Kessler VG, Agafonov AV (2014) The sol–gel synthesis of cotton/TiO_2 composites and their antibacterial properties. Surf Coat Technol 253:171–179

Hadzi D, Orel B (1973) OH-stretching band of acid salts of carboxylic-acids and symmetry of hydrogen-bond. J Mol Struct 18:227–239

Hinterstoisser B, Salmén L (1999) Two-dimensional step-scan FT-IR: a tool to unravel the OH-valency-range of the spectrum of Cellulose I. Cellulose 6:251–263

Hinterstoisser B, Akerholm M, Salmén L (2001) Effect of fiber orientation in dynamic FT-IR study on native cellulose. Carbohydr Res 334:27–37

Hofstetter K, Hinterstoisser B, Salmén L (2006) Moisture uptake in native cellulose—the roles of different hydrogen bonds: a dynamic FT-IR study using Deuterium exchange. Cellulose 13:131–145

Horner MR, Boerio FJ, Clearfield HM (1992) An XPS investigation of the adsorption of aminosilanes onto metal substrates. J Adhes Sci Technol 6:1–22

Hu C, Guo J, Qu J, Hu X (2007) Photocatalytic degradation of pathogenic bacteria with AgI/TiO_2 under visible light irradiation. Langmuir 23:4982–4987

Ibáñez JA, Litter MI, Pizarro RA (2003) Photocatalytic bactericidal effect of TiO_2 on *Enterobacter cloacae*: comparative study with other Gram (−) bacteria. J Photochem Photobiol, A 15:81–85

Isquith AJ, Abbott EA, Walters PA (1972) Surface-bonded antimicrobial activity of an organosilicon quaternary ammonium chloride. Appl Microbiol 24:859–863

Jerman I, Vuk AU, Kozelj M, Orel B, Kovac J (2008) A structural and corrosion study of triethoxysilyl functionalized POSS coatings on AA 2024 alloy. Langmuir 24:5029–5037

Jerman I, Mihelčič M, Koželj M, Orel B (2012) Sol–gel based spectrally selective solar absorber coatings and the process for producing said coatings. WO 2013/158049

Kikuchi Y, Sunada K, Iyoda T, Hashimoto K, Fujishima A (1997) Photocatalytic bactericidal effect of TiO_2 thin films: dynamic view of the active oxygen species responsible for the effect. J Photochem Photobiol, A 106:51–56

Kiwi J, Nadtochenko V (2005) Evidence for the mechanism of photocatalytic degradation of the bacterial wall membrane at the TiO_2 interface by ATR-FTIR and laser kinetic spectroscopy. Langmuir 21:4631–4641

Kotani Y, Matsuda A, Tatsumisago M, Minami T, Umezawa T, Kogure T (2000) Formation of anatase nanocrystals in sol–gel derived TiO_2–SiO_2 thin films with hot water treatment. J Sol-Gel Sci Technol 19:585–588

Kowal K, Cronin P, Dworniczek E, Zeglinski J, Tiernan P, Wawrzynska M, Podbielska H, Tofail SAM (2014) Biocidal effect and durability of nano-TiO_2 coated textiles to combat hospital acquired infections. RSC Adv 4:19945–19952

Koželj M, Vuk AS, Jerman I, Orel B (2009) Corrosion protection of Sunselect, a spectrally selective solar absorber coating, by (3-mercaptopropyl)trimethoxysilane. Sol Energy Mater Sol C 93:1733–1742

Ku H, Wang H, Pattarachaiyakoop N, Trada M (2011) A review on the tensile properties of natural fiber reinforced polymer composites. Compos Part B Eng 4:856–873

Kumar K-NP, Kumar J, Keizer K (1994) Effect of Peptization on densification and phase-transformation behavior of sol–

gel-derived nanostructured titania. J Am Ceram Soc 77:1396–1400

Kumar A, Pandey AK, Singh SS, Shanker R, Dhawan A (2011) Engineered ZnO and TiO_2 nanoparticles induce oxidative stress and DNA damage leading to reduced viability of *Escherichia coli*. Free Radical Biol Med 51:1872–1881

Langlet M, Kim A, Audier M, Herrmann JM (2002) Sol–gel preparation of photocatalytic TiO_2 films on polymer substrates. J Sol-Gel Sci Technol 25:223–234

Langlet M, Kim A, Audier M, Guillard C, Herrmann JM (2003) Liquid phase processing and thin film deposition of titania nanocrystallites for photocatalytic applications on thermally sensitive substrates. J Mater Sci 38:3945–3953

Li Z, Hou B, Xu Y, Wu D, Sun Y (2005) Hydrothermal synthesis, characterization, and photocatalytic performance of silica-modified titanium dioxide nanoparticles. J Colloid Interface Sci 288:149–154

Li Q, Mahendra S, Lyon DY, Brunet L, Liga MV, Li D, Alvarez PJJ (2008) Antimicrobial nanomaterials for water disinfection and microbial control: potential applications and implications. Water Res 42:4591–4602

Linsebigler AL, Lu G, Zates JT (1995) Photocatalysis on TiO_2 surfaces—principles, mechanisms, and selected results. Chem Rev 95:745–758

Liu P, Duan W, Wang Q, Li X (2010) The damage of outer membrane of *Escherichia coli* in the presence of TiO_2 combined with UV light. Colloid Surface B 78:171–176

Lu Z-X, Zhou L, Zhang Z-L, Shi W-L, Xie Z-X, Xie H-Y, Pang D-W, Shen P (2003) Cell damage induced by photocatalysis of TiO_2 thin films. Langmuir 19:8765–8768

Mahltig B, Böttcher H, Rauch K, Dieckmann U, Nitsche R, Fritz T (2005) Optimized UV protective coatings by combination of organic and inorganic UV absorbers. Thin Solid Films 485:108–114

Mahltig B, Gutmann E, Meyer DC, Reibold M, Dresler B, Günther K, Faßler D, Böttcher H (2007) Solvothermal preparation of metallized titania sols for photocatalytic and antimicrobial coating. J Mater Chem 17:2367–2374

Malešič J, Kolar J, Strlič M, Kočar D, Fromageot D, Leamaire J, Haillant O (2005) Photo-induced degradation of cellulose. Polym Degrad Stab 89:64–69

Maness PC, Smolinski S, Blake DM, Huang Z, Wolfrum EJ, Jacoby WA (1999) Bactericidal activity of photocatalytic TiO_2 reaction: toward an understanding of its killing mechanism. Appl Environ Microbiol 65:4094–4098

Maréchal Y, Chanzy H (2000) The hydrogen bond network in Iβ cellulose as observed by infrared spectrometry. J Mol Struct 523:183–196

Matsuda A, Kotani Y, Kogure T, Tatsumisago M, Minami T (2000) Transparent anatase nanocomposite films by the sol–gel process at low temperatures. J Am Ceram Soc 83:229–231

Matsuda A, Matoda T, Kotani Y, Kogure T, Tatsumisago M, Minami T (2003) Evaluation of photocatalytic activity of transparent anatase nanocrystals-dispersed silica films prepared by the sol–gel process with hot water treatment. J Sol-Gel Sci Technol 26:517–521

Matsunaga T, Tomoda R, Nakajima T, Nakamura N, Komine T (1988) Continuous-sterilization system that uses photosemiconductor powders. Appl Environ Microbiol 54:1330–1333

Mihailović D, Šaponjić Z, Radoičić M, Lazović S, Baily CJ, Jovančić P, Nedeljković J, Radetić M (2011) Functionalization of cotton fabrics with corona/air RF plasma and colloidal TiO_2 nanoparticles. Cellulose 18:811–825

Mihelčič M, Francetič V, Pori P, Gradišar H, Kovač J, Orel B (2014) Electrochromic coatings made of surface modified rutile and anatase pigments: influence of trisilanol POSS dispersant on electrochromic effect. Appl Surf Sci 313:484–497

Milović NM, Wang J, Lewis K, Klibanov AM (2005) Immobilized N-alkylated polyethylenimine avidly kills bacteria by rupturing cell membranes with no resistance developed. Biotechnol Bioeng 90:715–722

Moulder JF, Stickle WF, Sobol PE, Bomben KD (1995) Handbook of X-ray photoelectron spectroscopy. Physical Electronics Inc., Eden Prairie

Nadtochenko VA, Sarkisov OM, Nikandrov VV, Chubukov PA, Denisov NN (2008) Inactivation of pathogenic microorganisms in the photocatalytic process on nanosized TiO_2 crystals. Russ J Phys Chem B 2:105–114

Nur H (2006) Modification of titanium surface species of titania by attachment of silica nanoparticles. Mater Sci Eng B Solid 133:49–54

Olsson AM, Salmén L (2004) The association of water to cellulose and hemicellulose in paper examined by FTIR spectroscopy. Carbohydr Res 339:813–818

Orel B, Ješe R, Stangar UL, Grdadolnik J, Puchberger M (2005a) Infrared attenuated total reflection spectroscopy studies of aprotic condensation of (EtO)(3)Si-R-Si(OEt)(3) and R-Si(OEt)(3) systems with carboxylic acids. J Non-Cryst Solids 351:530–549

Orel B, Ješe R, Vilčnik A, Stangar UL (2005b) Hydrolysis and solvolysis of methyltriethoxysilane catalyzed with HCl or trifluoroacetic acid: IR spectroscopic and surface energy studies. J Sol-Gel Sci Technol 34:251–265

Panarin EF, Solovskii MV, Ékzemplyarov ON (1971) Synthesis and antimicrobial properties of polymers containing quaternary ammonium groups. Pharm Chem J 5:406–408

Puzenat E, Pichat P (2003) Studying TiO_2 coatings on silica-covered glass by O_2 photosorption measurements and FTIR–ATR spectrometry: correlation with the self-cleaning efficacy. J Photochem Photobiol, A 160:127–133

Qi K, Daud WA, Xin JH, Mak CL, Tang W, Cheung WP (2006) Self-cleaning cotton. J Mater Chem 16:4567–4576

Radetić M (2013) Functionalization of textile materials with TiO_2 nanoparticles. J Photochem Photobiol, C 16:62–76

Rasmussen JS, Barsberg S, Felby C (2014a) Complex between lignin and a Ti-based coupling agent. Holzforschung 68:541–548

Rasmussen JS, Barsberg S, Venas TM, Felby C (2014b) Assessment of covalent bond formation between coupling agents and wood by FTIR spectroscopy and pull strength tests. Holzforschung 68:799–805

Saito T, Iwase T, Horie J, Morioka T (1992) Mode of photocatalytic bactericidal action of powdered semiconductor TiO_2 on mutans streptococci. J Photochem Photobiol, B 14:369–379

Saravanan D (2007) UV protection textile materials. AUTEX Res J 7:53–62

Schraml-Marth M, Walther KL, Wokaun A, Handy BE, Baiker A (1992) Porous silica gels and TiO_2/SiO_2 mixed oxides

prepared via the sol-gel process: characterization by spectroscopic techniques. J Non-Cryst Solids 143:93–111

Simončič B, Tomšič B, Černe L, Orel B, Jerman I, Kovač J, Žerjav M, Simončič A (2012) Multifunctional water and oil repellent ant antimicrobial properties of finished cotton: influence of sol–gel finishing procedure. J Sol-Gel Sci Technol 61:340–354

Simončič B, Hadžić S, Vasiljević J, Černe L, Tomšič B, Jerman I, Orel B, Medved J (2014) Tailoring of multifunctional cellulose fibres with "lotus effect" and flame retardant properties. Cellulose 21:595–605

Subramanian E, Subbulakshmi S, Murugan C (2014) Inter-relationship between nanostructures of conducting polyaniline and the photocatalytic methylene blue degradation efficiencies of its hybrid composites with anatase TiO_2. Mater Res Bull 51:128–135

Sunada K, Kikuchi Y, Hashimoto K, Fujishima A (1998) Bactericidal and detoxification effects of TiO_2 thin film photocatalysts. Environ Sci Technol 32:726–728

Sunada K, Watanabe T, Hashimoto K (2003) Studies on photokilling of bacteria on TiO_2 thin film. J Photochem Photobiol, A 156:227–233

Thevenot P, Cho J, Wavhal D, Timmons RB, Tang L (2008) Surface chemistry influences cancer killing effect of TiO_2 nanoparticles. Nanomed Nanotechnol 4:226–236

Timofeeva L, Kleshcheva N (2011) Antimicrobial polymers: mechanism of action, factors of activity, and applications. Appl Microbiol Biotechnol 89:475–492

Tomšič B, Klemenčič D, Simončič B, Orel B (2011) Influence of antimicrobial finishes on the biodeterioration of cotton and cotton/polyester fabrics: leaching versus bio-barrier formation. Polym Degrad Stab 96:1286–1296

Tshabalala MA, Kingshott P, VanLandingham MR, Plackett D (2003) Surface chemistry and moisture sorption properties of wood coated with multifunctional alkoxysilanes by sol-gel process. J Appl Polym Sci 88:2828–2841

Tsuboi M (1957) Infrared spectrum and crystal structure of cellulose. J Polym Sci 25:159–171

Valadez-Gonzalez A, Cervantes-Uc JM, Olayo R, Herrera-Franco PJ (1999) Chemical modification of henequén fibers with an organosilane coupling agent. Compos Part B Eng 30:321–331

Vasiljević J, Tomšič B, Jerman I, Orel B, Jakša G, Simončič B (2014) Novel multifunctional water- and oil-repellent, antibacterial, and flame-retardant cellulose fibres created by the sol–gel process. Cellulose 21:2611–2623

Vasiljević J, Jerman I, Jakša G, Alongi J, Malucelli G, Zorko M, Tomšič B, Simončič B (2015) Functionalization of cellulose fibres with DOPO-polysilsesquioxane flame retardant nanocoating. Cellulose. doi:10.1007/s10570-015-0599-x

Vilčnik A, Jerman I, Vuk AS, Koželj M, Orel B, Tomšič B, Simončič B, Kovač J (2009) Structural properties and antibacterial effects of hydrophobic and oleophobic sol–gel coatings for cotton fabrics. Langmuir 25:5869–5880

Vince J, Orel B, Vilčnik A, Fir M, Vuk AS, Jovanovski V, Simončič B (2006) Structural and water-repellent properties of a urea/poly(dimethylsiloxane) sol–gel hybrid and its bonding to cotton fabric. Langmuir 22:6489–6497

Vuk AS, Ješe R, Orel B, Dražič G (2005) The effect of surface hydroxyl groups on the adsorption properties of nanocrystalline TiO_2 films. Int J Photoenergy 7:163–168

Vuk AS, Ješe R, Gaberšček M, Orel B, Dražič G (2006) Structural and spectroelectrochemical (UV–Vis and IR) studies of nanocrystalline sol–gel derived TiO_2 films. Sol Energy Mater Sol C 90:452–468

Walrafen GE, Klein PH (1987) Infrared investigation of hydrogen-bonding on the surface of beryllium fluoride glass. J Chem Phys 86:6515–6522

Wang Z, Li G, Peng H, Zhang Z (2005) Study on novel antibacterial high-impact polystyrene/TiO_2 nanocomposites. J Mater Sci 40:6433–6438

Waschinski CJ, Tiller JC (2005) Poly(oxazoline)s with telechelic antimicrobial functions. Biomacromolecules 6:235–243

Xie YJ, Hill CAS, Xiao ZF, Militz H, Mai C (2010) Silane coupling agents used for natural fiber/polymer composites: a review. Compos Part A Appl Sci Manuf 41:806–819

Xue CH, Jia ST, Zhang J, Tian LQ (2009) Superhydrophobic surfaces on cotton textiles by complex coating of silica nanoparticles and hydrophobization. Thin Solid Films 517:4593–4598

Yun YJ, Chung JS, Kim S, Hahn SH, Kim EJ (2004) Low-temperature coating of sol–gel anatase thin films. Mater Lett 58:3703–3706

Zhu P, Sui SY, Wang B, Sun K, Sun G (2004) A study of pyrolysis and pyrolysis products of flame-retardant cotton fabrics by DSC, TGA, and PY-GC-MS. J Anal Appl Pyrolysis 71:645–655

Zollinger H (1991) Color chemistry: syntheses, properties and applications of organicdyes and pigments, 2nd edn. VCH Publisher, Weinheim/New York/Basel, Cambridge

Chapter 10

Conclusions

There is no doubt that solar energy will make an essential contribution to the future as a sustainable energy supply that does not depend on raw materials with limited availability. The main use of solar radiation will be the production of thermal energy over a broad range of temperatures. The basic technology for these applications has been developed in recent years and their application is still increasing; thermal energy costs, however, are still higher than for competing conventional technologies.

In chapters II and III, preparation and characterisation of thickness sensitive spectrally selective (TSSS) paint coatings based on fluorolymer resin (chapter II) and 3-glicidoxypropyltrimetoxy silane (chapter III) binder were presented. These coatings can be used for various solar collector systems, due to their good spectrally selective properties. High solar absorptance ((a_s) ≥ 0.90) and low thermal emittance ((e_T) < 0.2) can be achieved with TSSS paint coatings with a high PVC ratio and with POSS modified pigment. Thermal stability and high solar absorptance can be controlled by the type of the pendant groups attached to the POSS cage. It has been shown that thermal emittance is small if the thickness of the coating does not exceed 1μm.

There are many spectrally selective coatings, with a variety of binders and pigments, on the market today. An inappropriate binder can significantly degrade the optical properties of selective coatings, increasing the thermal emissivity of the coating and thus reducing the efficiency of the solar collectors. An alternative is binder, which could be synthesized by sol-gel route, with great potential to combine high spectral selectivity and long-term stability (including corrosion resistance) of the coating with cost effectiveness and an environmentally friendly synthesis process. Sol-gel based spectral selective coatings have been successfully deposited by the wet deposition technique (coil coating) with relatively high solar absorptance (a_S = 0.90) and low thermal emittance (e_T = 0.12). The selectivity of coatings can be improved by thermal heating to 400 °C, in order to get high power coatings (HIPO) with selectivity parameters a_s = 0.92 and e_T = 0.075.

In chapters IV and V, the procedure for preparation of electrochromic (EC) mTiA (metatitanic acid based anatase) modified with isobutyl trisilanol coatings was presented. The successful modification of mTiA with isobutyl trisilanol POSS was confirmed by EDAX, whereby the presence of silica originating from the trisilanol POSS molecule was noted. TEM measurements confirmed the presence of a thin layer (~2 nm) of trisilanol POSS dispersant on the mTiA pigment particles. DLS measurements revealed a particle size of ~50 nm. For comparison, mTiR (rutile) pigment was also modified with isobutyl trisilanol POSS, and similar modification efficacy of this dispersant was noted as found for the modification of anatase particles. Pigment dispersions with various concentrations of isobutyl trisilanol POSS equilibrated with mTiA pigment particles were prepared in

order to observe the adsorption of the dispersant on the surface of the mTiA particle. With the aid of IR spectroscopy, the intensity variations of the C-H vibrational bands at 2953 and 2932 cm^{-1}, attributed to the isobutyl trisilanol POSS dispersant, were monitored. Because the saturation limit of the mTiA pigment surface with isobutyl trisilanol POSS in hexane is not higher than ~10%, the attachment of 4.74% of isobutyl trisilanol POSS molecules to the pigment surface of mTiA, as determined from TG measurements, was quite high. IR spectroscopic analysis confirmed the formation of a siloxane (Si-O-$Ti_{surface}$) bond at 971 cm^{-1}.

Several important points should be mentioned. First of all, mTiA pigment coatings made from dispersions containing isobutyl trisilanol POSS dispersant exhibited lower haze than coatings without it. Secondly, the mTiA pigment coatings were thermally treated at 150 °C for 30 minutes, which made possible the deposition of the corresponding mTiA pigment dispersions on both conductive FTO glass and ITO PET flexible (plastic) foils, enabling the fabrication of flexible EC devices. The EC effect of mTiA was strong; by increasing the particle size, the thickness of the coatings was increased and thus the EC effect but, due to the finely grained pigment haze of the corresponding EC coatings, did not surpass the limit allowing clear sight through the device. The coloration efficiency remained nearly equal for all three grades of mTiA pigment coatings, with different particle sizes, which led us to conclude that all three pigment coatings (mTiA01, mTiA02 and mTiA04) exhibited similar access for lithium ions throughout their physical thickness. mTiA pigment coatings behave as typical cathodic electrochromic material. Cyclovoltametric studies showed a different response to that of commercially available TiO_2 powders (Inframat and P25), in which only one oxidation and reduction peak is observed instead of two. This could be attributed to the presence of additional electrochemical sites stemming from the particle nature of the coatings.

Finally, for demonstration of the efficiency of the presented approach for preparing pigment particle coatings, foil-based EC devices were assembled from the mTiA and $Ni_{1-x}O$ pigment coatings glued together with various electrolytes. The coatings deposited on ITO glass exhibited lower haze than the same pigment coatings deposited on the conductive ITO PET plastic substrate. The EC device showed a reversible EC effect and neutral colouration. We attributed the lower haze of the EC device to the effect of the electrolyte, which filled the surface defects and rough surface of electrodes.

In chapter VI, the preparation of $Ni_{1-x}O$ dispersed with NiO_xH_y and $Ni_{1-x}O$ dispersed only in water was presented. The influence of milling on the pigment particle size was determined by DLS measurements and the particle size of the milled pigment particles were compared with SEM micrographs. It was shown that milling had a large impact on particle size, leading to a reduction of the particle size from approximately 190 nm to 30 nm, in agreement with the results obtained from SEM and DLS measurements, the latter showing a size of about 50 nm. Particles formed aggregates consisting of grains with a diameter of about 7.7 nm, as seen from XRD measurements. The $Ni_{1-x}O$ pigment dispersions were deposited on the conductive substrate by spin coating but were also suitable for deposition on a larger roll-to-roll coating system (COATEMA, DE). The coatings deposited on flexible coils were used for assembling EC devices based on various electrolytes (lithium and lithium-free) and cathodic electrochromics (WO_3 and PEDOT).

The properties of $Ni_{1-x}O/NiO_xH_y$ pigment coatings deposited via the spin coating deposition technique on conductive FTO glass were examined in order to ascertain the influence of particle size, time of milling and diameter of the milling beads. It was found that, for example, coatings deposited from pigment dispersions milled with grinding beads of 0.4 mm size exhibited higher haze than coatings made of pigment dispersions

milled with 0.1 mm grinding beads. However, the haze of both types of coating remained small, not exceeding 5%.

The coatings were also tested for their EC properties. The results revealed that the EC effect of $Ni_{1-x}O$/ NiO_xH_y and $Ni_{1-x}O/H_2O$ pigment coatings was strong in 1 M $LiClO_4$/PC, as well as in 0.1 M TBA^+ triflate/PC electrolytes, indirectly confirming that the intercalation of small ions in the NiO structure did not greatly affect the EC effect. This was a surprising result, which has not previously been mentioned for anodic NiO coatings. In order to obtain a clearer picture of the "cation-free" intercalation of the deposited EC NiO coatings, various EC devices were assembled and their EC responses were determined. It was shown that the EC response of EC devices made of PEDOT cathodic EC coatings combined with $Ni_{1-x}O$, glued together with a lithium-free electrolyte, exhibited a strong EC effect. In contrast, when anodic NiO was combined with WO_3 and the same lithium-free electrolytes were used for gluing the gtwo electrodes together, the corresponding EC device did not show any EC response. As expected, both EC devices worked perfectly when the lithium electrolytes were used for their assembly.

In order to understand the colouring, i.e., insertion/extraction reaction of ions and electrons in the NiO coatings, an *ex situ* IR RA (reflection-absorption) technique was employed. The results revealed that the colouring/bleaching process was due to adsorption/desorption of the electrolyte species on the surface of the $Ni_{1-x}O$ grains but not to the intercalation of cations, which enter the $Ni_{1-x}O$ structure from the electrolyte. NiO exhibited an EC effect merely on account of the ions exchange that took place only on the surface of the NiO grains and did not rely on the insertion of small ions such as lithium. We attributed the colouring/bleaching mechanism mainly to the semi-conductivity of the NiO defect structure enabling transport of electrons under the applied potential.

In chapter VII, by analogy with chapter VI, NiO_xH_y was used as a dispersant for the modification of the P25 pigment dispersions from which coatings with photocatalytic and superhydrophilic properties were made. The role of the NiO_xH_y was to provide dispersion of the titania particles and also as a matrix former (binder), enabling the formation of the core shell TiO_2/NiO_xH_y particles with increased photocatalytic effect. Since the main focus was to make photocatalytic coatings, in addition to mTiA (custom-made titania) also P25 (Degussa) particles were used for making the photocatalytic pigment coatings. For the latter coatings, instead of the NiO_xH_y dispersant, $Ti(iOPr)_4$ was used as dispersant and binder. The coatings were intentionally made at a low processing temperature (150 °C for 1/2 h), and are thus appropriate for deposition on flexible foils. Special attention was devoted to determining their haze, which was up to 1.3 %, indicating that the coatings behave as optical coatings deposited either by vacuum deposition or by sol-gel, directly proving the efficacy of the deposition of coatings from pigment dispersions. The morphology of the coatings was assessed with SEM micrographs, which showed that all the coatings exhibited a certain degree of porosity, which beneficially affected their photocatalytic properties. The P25/NiO coating was the most compact, $P25/Ti(iOPr)_4$ coating was less compact, while $P25/NiO_xH_y$ was fairly porous, with some voids. The best photocatalytic effect was noted for the $P25/Ti(iOPr)_4$ coating. The coatings also exhibited excellent adhesion on glass and flexible foils. It should be mentioned that the photocatalytic properties were determined at University of Nova Gorica, and they confirmed that the photocatalytic efficiency of deposited pigmented coatings could compete with Pilkington Activ^{TM}, as revealed from the TPA oxidation rate constants, which were several times higher than commercial self-cleaning glass. The water contact angle after 1/2h of UV irradiation was highest for $P25/NiO_xH_y$ (13.51°) and lowest for the P25 coating (8.05°). The CA for commercial self-cleaning glass (Pilkington Activ^{TM} glass) after 240 min UV irradiation was 36°.

Chapter VIII was devoted to the modification of cotton fibres using organic inorganic nanocomposite sol-gel hybrid coatings based on titanium isopropoxide (TiP) and titanium isopropoxide/aminopropyltriethoxysilane (TiP/APTES) organic-inorganic hybrid precursors.

The main accent in this work was to show that infrared attenuated reflection spectroscopy, even though nearly half a century old, is able to provide an understanding of the binding of organic-inorganic hybrids on cellulose molecules. It was shown that hybrids interacted with the specific sites on the cellulose molecules, changing the H-bonding water system (intra- and intermolecular) and modifying the glycosidic bonds, enabling strong fastening of the hybrids on the cotton fibres. This was correlated with the washing fastness and other properties, such as antibacterial effect ascribed to amino groups and titania nanoparticles.

To sum up, we succeeded to confirm that the trisilanol POSS and its derivatives were suitable compounds for dispersing different pigments and manufacturing of paint dispersions which made possible the deposition of pigment coatings with optical properties (low haze, high and/or low transmittance), high abrasion resistance, temperature stability and adequate electrochromic response. In addition, we showed that trisilanol POSS molecules form adsorption layer on the surface of the titania pigment showing the electrochromic effect, but trisilanol POSS failed to make NiO pigment coatings electrochromically active. $Ni_{1-x}O$ electrochromics showed intriguing properties. The main novelty was the verification of our assumption, that the electrochromic effect was due to the p-type semiconductivity stemming from the substoichiommetric $Ni_{1-x}O$ pigment particles and because of the use of the NiO_xH_y dispersant enabling the fabrication of optically transparent (no haze), homogeneous pigment coatings with adequate porosity and particle-to-particle contacts providing the transfer of the electrons during the charging/discharging the $Ni_{1-x}O$ coating.

Also the practical aspect of this work should be mentioned finally. We demonstrated that the high quality optical coatings for solar thermal and electrochromic applications could be prepared on large scale with mass-deposition technique such as coil coating deposition. Especially for the solar thermal selective coatings it was found that the novel system trisilanol POSS/alcohol/3-glycidoxypropyltrimethoxy silane binder provided in combination with black manganese spinel pigment dispersions which were applied via the coil coating deposition and exhibited exceptionally high temperature long-term stability (400 °C, >1200h).

References

[1] S. W. Moore, "Solar-Absorber Selective Paint Research," *Solar Energy Materials,* vol. 12, pp. 435-447, 1985.

[2] M. Köhl, G. Jorgensen, and A. W. Czanderna, *Performance and Durability Assessment: Optical Materials for Solar Thermal Systems*, 1st ed. The Netherlands: Elsevier, 2004.

[3] T. H. Zvi, "Receiver for solar energy collectors," 1955

[4] C. G. Granqvist, "Solar energy materials," *Applied Physics A,* vol. 52, pp. 83-93, 1991.

[5] S. A. Kalogirou, "Solar thermal collectors and applications," *Progress in Energy and Combustion Science,* vol. 30, pp. 231-295, 2004.

[6] Available: http://solartribune.com/flat-plate-solar-system/. [Accessed 20 5 2015].

[7] I. Jerman, M. Mihelcic, D. Verhovsek, J. Kovac, and B. Orel, "Polyhedral oligomeric silsesquioxane trisilanols as pigment surface modifiers for fluoropolymer based Thickness Sensitive Spectrally Selective (TSSS) paint coatings," *Solar Energy Materials and Solar Cells,* vol. 95, pp. 423-431, 2011.

[8] M. Kozelj, B. Orel, M. Steinbuecher, I. Jerman, M. Vodlan, and D. Peros, "Coil-coated spectrally selective coatings on copper or aluminum with pigments modified by aminosilane," WO 2010133693, 2010.

[9] M. Kozelj, B. Orel, M. Steinbuecher, I. Jerman, and M. Vodlan, "Aminosilane modified pigments for spectrally selective coatings, method for preparation and their use in coatings," EP2261288 (A1), 2010.

[10] R. Kunič, M. Koželj, B. Orel, A. Šurca Vuk, A. Vilčnik, L. Slemenik Perše, D. Merlini, and S. Brunold, "Adhesion and thermal stability of thickness insensitive spectrally selective (TISS) polyurethane-based paint coatings on copper substrates," *Solar Energy Materials and Solar Cells,* vol. 93, pp. 630-640, 2009.

[11] B. Orel, H. Spreizer, A. S. Vuk, M. Fir, D. Merlini, M. Vodlan, and M. Kohl, "Selective paint coatings for coloured solar absorbers: Polyurethane thickness insensitive spectrally selective (TISS) paints (Part II)," *Solar Energy Materials and Solar Cells,* vol. 91, pp. 108-119, 2007.

[12] B. Orel, H. Spreizer, L. Slemenik Perše, M. Fir, A. Šurca Vuk, D. Merlini, M. Vodlan, and M. Köhl, "Silicone-based thickness insensitive spectrally selective (TISS) paints as selective paint coatings for coloured solar absorbers (Part I)," *Solar Energy Materials and Solar Cells,* vol. 91, pp. 93-107, 2007.

[13] R. D. McConnell and J. H. Vansant, "Glass heat pipe evacuated tube solar collector," US 4474170, 1984.

[14] A. Walker, F. Mahjouri, and R. Stiteler, *Evacuated-Tube Heat-Pipe Solar Collectors Applied to the Recirculation Loop in a Federal Building: Preprint*, 2004.

[15] Available: http://www.greenspec.co.uk/building-design/solar-collectors/. [Accessed 15 5 2014].

[16] Available: https://www.linkedin.com/pulse/pv-t-hybrid-solar-separating-fact-from-fiction-anthony-morgan. [Accessed 02 09 2015].

[17] S. Harrison and C. A. Cruickshank, "A review of strategies for the control of high temperature stagnation in solar collectors and systems," *Energy Procedia,* vol. 30, pp. 793-804, 2012.

[18] A. Serag Eldin, "New Developments in Large Scale Solar Energy Conversion," in *New Trends in Technologies*, B. Ramov, Ed., ed: InTech, 2010, pp. 109-132.

[19] Available: http://www.energynext.in. [Accessed 20 8 2014].

[20] N. Selvakumar and H. C. Barshilia, "Review of physical vapor deposited (PVD) spectrally selective coatings for mid- and high-temperature solar thermal applications," *Solar Energy Materials and Solar Cells,* vol. 98, pp. 1-23, 2012.

[21] C. K. Ho, A. R. Mahoney, A. Ambrosini, M. Bencomo, A. Hall, and T. N. Lambert, "Characterization of Pyromark 2500 Paint for High-Temperature Solar Receivers," *Journal of Solar Energy Engineering-Transactions of the Asme,* vol. 136, 2014.

[22] A. Ambrosini, T. N. Lambert, M. Bencomo, A. Hall, K. van Every, N. P. Siegel, and C. K. Ho, "Improved High Temperature Solar Absorbers for Use in Concentrating Solar Power Central Receiver Applications," in *Proceedings of the ASME 2011 5th International Conference on Energy Sustainability*, Washington, USA, 2011, pp. 587-594.

[23] J. Moon, T. K. Kim, B. VanSaders, C. Choi, Z. W. Liu, S. H. Jin, and R. K. Chen, "Black oxide nanoparticles as durable solar absorbing material for high-temperature concentrating solar power system," *Solar Energy Materials and Solar Cells,* vol. 134, pp. 417-424, 2015.

[24] Available: http://www.brightsourceenergy.com/. [Accessed 10 02 2014].

[25] V. Jain and A. Kokil, *Optical properties of functional polymers and nano engineering applications*: CRC Press, 2014.

[26] S. K. Deb, "A Novel Electrophotographic System," *Applied Optics,* vol. 8, pp. 192-195, 1969.

[27] S. K. Deb, "Optical and photoelectric properties and colour centres in thin films of tungsten oxide," *Philosophical Magazine,* vol. 27, pp. 801-822, 1973.

[28] C. G. Granqvist, *Handbook of inorganic electrochromic materials*. Amsterdam ; New York: Elsevier, 1995.

[29] J. S. E. M. Svensson and C. G. Granqvist, "Electrochromic coatings for “smart windows”," *Solar Energy Materials,* vol. 12, pp. 391-402, 1985.

[30] C. G. Granqvist, "Electrochromic tungsten oxide films: Review of progress 1993-

1998," *Solar Energy Materials and Solar Cells,* vol. 60, pp. 201-262, 2000.

[31] C. G. Granqvist, A. Azens, P. Heszler, L. B. Kish, and L. Osterlund, "Nanomaterials for benign indoor environments: Electrochromics for "smart windows", sensors for air quality, and photo-catalysts for air cleaning," *Solar Energy Materials and Solar Cells,* vol. 91, pp. 355-365, 2007.

[32] C. G. Granqvist, "Electrochromics for smart windows: Oxide-based thin films and devices," *Thin Solid Films,* vol. 564, pp. 1-38, 2014.

[33] R. J. Mortimer, "Organic electrochromic materials," *Electrochimica Acta,* vol. 44, pp. 2971-2981, 1999.

[34] G. Gunbas and L. Toppare, "Electrochromic conjugated polyheterocycles and derivatives-highlights from the last decade towards realization of long lived aspirations," *Chemical Communications,* vol. 48, pp. 1083-1101, 2012.

[35] J. M. Wang, X. W. Sun, and Z. H. Jiao, "Application of Nanostructures in Electrochromic Materials and Devices: Recent Progress," *Materials,* vol. 3, pp. 5029-5053, 2010.

[36] R. Baetens, B. P. Jelle, and A. Gustavsen, "Properties, requirements and possibilities of smart windows for dynamic daylight and solar energy control in buildings: A state-of-the-art review," *Solar Energy Materials and Solar Cells,* vol. 94, pp. 87-105, 2010.

[37] C. M. Lampert, "Chromogenic smart materials," *Materials Today,* vol. 7, pp. 28-35, 2004.

[38] P. R. Somani and S. Radhakrishnan, "Electrochromic materials and devices: present and future," *Materials Chemistry and Physics,* vol. 77, pp. 117-133, 2003.

[39] B. P. Jelle, A. Hynd, A. Gustavsen, D. Arasteh, H. Goudey, and R. Hart, "Fenestration of today and tomorrow: A state-of-the-art review and future research opportunities," *Solar Energy Materials and Solar Cells,* vol. 96, pp. 1-28, 2012.

[40] Available: www.gasimet.com. [Accessed 10 02 2014].

[41] A. Fujishima, T. N. Rao, and D. A. Tryk, "Titanium dioxide photocatalysis," *Journal of Photochemistry and Photobiology C: Photochemistry Reviews,* vol. 1, pp. 1-21, 2000.

[42] J. Schneider, M. Matsuoka, M. Takeuchi, J. L. Zhang, Y. Horiuchi, M. Anpo, and D. W. Bahnemann, "Understanding TiO_2 Photocatalysis: Mechanisms and Materials," *Chemical Reviews,* vol. 114, pp. 9919-9986, 2014.

[43] A. O. Ibhadon and P. Fitzpatrick, "Heterogeneous Photocatalysis: Recent Advances and Applications," *Catalysts,* vol. 3, pp. 189-218, 2013.

[44] M. A. Henderson, "A surface science perspective on TiO_2 photocatalysis," *Surface Science Reports,* vol. 66, pp. 185-297, 2011.

[45] B. Faure, G. Salazar-Alvarez, A. Ahniyaz, I. Villaluenga, G. Berriozabal, Y. R. De Miguel, and L. Bergstrom, "Dispersion and surface functionalization of oxide nanoparticles for transparent photocatalytic and UV-protecting coatings and sunscreens," *Science and Technology of Advanced Materials,* vol. 14, 2013.

[46] T. A. Kandiel, L. Robben, A. Alkaim, and D. Bahnemann, "Brookite versus anatase

TiO_2 photocatalysts: phase transformations and photocatalytic activities," *Photochemical & Photobiological Sciences,* vol. 12, pp. 602-609, 2013.

[47] A. Di Paola, G. Cufalo, M. Addamo, M. Bellardita, R. Campostrini, M. Ischia, R. Ceccato, and L. Palmisano, "Photocatalytic activity of nanocrystalline TiO_2 (brookite, rutile and brookite-based) powders prepared by thermohydrolysis of $TiCl_4$ in aqueous chloride solutions," *Colloids and Surfaces a-Physicochemical and Engineering Aspects,* vol. 317, pp. 366-376, 2008.

[48] A. Di Paola, M. Bellardita, and L. Palmisano, "Brookite, the Least Known TiO_2 Photocatalyst," *Catalysts,* vol. 3, pp. 36-73, 2013.

[49] G. Odling and N. Robertson, "Why is Anatase a Better Photocatalyst than Rutile? The Importance of Free Hydroxyl Radicals," *Chemsuschem,* vol. 8, pp. 1838-1840, 2015.

[50] T. Luttrell, S. Halpegamage, J. G. Tao, A. Kramer, E. Sutter, and M. Batzill, "Why is anatase a better photocatalyst than rutile? - Model studies on epitaxial TiO_2 films," *Scientific Reports,* vol. 4, 2014.

[51] U. Diebold, "The surface science of titanium dioxide," *Surface Science Reports,* vol. 48, pp. 53-229, 2003.

[52] A. Fujishima and K. Honda, "Electrochemical Photolysis of Water at a Semiconductor Electrode," *Nature,* vol. 238, pp. 37-+, 1972.

[53] Y. C. Lan, Y. L. Lu, and Z. F. Ren, "Mini review on photocatalysis of titanium dioxide nanoparticles and their solar applications," *Nano Energy,* vol. 2, pp. 1031-1045, 2013.

[54] N. J. Harrick, *Internal reflection spectroscopy.* New York,: Interscience Publishers, 1967.

[55] J. Fahrenfort, "Attenuated total reflection: A new principle for the production of useful infra-red reflection spectra of organic compounds," *Spectrochimica Acta,* vol. 17, pp. 698-709, 1961.

[56] T. Vo-Dinh and G. Gauglitz, *Handbook of spectroscopy.* Weinheim ; Cambridge: Wiley-VCH, 2003.

[57] P. Grosse, "Conventional and unconventional infrared spectrometry and their quantitative interpretation," *Vibrational Spectroscopy,* vol. 1, pp. 187-198, 1990.

[58] B. Harbecke, B. Heinz, and P. Grosse, "Optical-Properties of Thin-Films and the Berreman Effect," *Applied Physics a-Materials Science & Processing,* vol. 38, pp. 263-267, 1985.

[59] D. W. Berreman, "Infrared Absorption at Longitudinal Optic Frequency in Cubic Crystal Films," *Physical Review,* vol. 130, pp. 2193-2198, 1963.

[60] M. G. Hutchins, "Spectrally selective materials for efficient visible, solar and thermal radiation control," in *Solar thermal technologies for buildings: the state of the art* M. Santamouris, Ed., London: James & James (Science Publishers) Ltd., 2003.

[61] J. A. Duffie and W. A. Beckman, *Solar Engineering of Thermal Processes*, 4th ed. Hoboken, New Jersey: John Wiley & Sons, Inc., 2013.

[62] M. P. Diebold, *Application of Light Scattering to Coatings: A User's Guide.* New

York: Springer, 2014.

[63] G. Leftheriotis, G. Syrrokostas, and P. Yianoulis, "Development of photoelectrochromic devices for dynamic solar control in buildings," *Solar Energy Materials and Solar Cells,* vol. 94, pp. 2304-2313, 2010.

[64] H. L. Yu, C. C. Hsiao, and W. C. Liu, "New apparatus for haze measurement for transparent media," *Measurement Science & Technology,* vol. 17, pp. N29-N36, 2006.

[65] Available: http://www.astm.org/Standards/D1003.htm. [Accessed 10 11 2014].

[66] B. Gruska, S. Peters, and G. Dittmar, "Large Area Mapping of Thickness, Haze and Sheet Resistance of TCO Films on Glass," in *27th EU PVSEC*, Frankfurt 2012.

[67] W. E. Sumpner, "The Diffusion of Light," *Proceedings of the Physical Society of London,* vol. 12, p. 10, 1892.

[68] L. M. Hanssen and K. A. Snail, "Integrating Spheres for Mid- and Near-Infrared Reflection Spectroscopy," in *Handbook of Vibrational Spectroscopy*, J. M. Chalmers and G. P.R., Eds., ed Chichester: John Wiley & Sons, Ltd, 2006.

[69] C. J. Brinker and G. W. Scherer, *Sol-gel science: the physics and chemistry of sol-gel processing*. New York: Academic Press Inc., 1990.

[70] G. Carcano, M. Ceriani, and F. Soglio, "Spin Coating with High Viscosity Photoresist on Square Substrates - Applications in the Thin Film Hybrid Microwave Integrated Circuit Field," *Microelectronics International,* vol. 10, pp. 12-20, 1993.

[71] A. Münch, C. P. Please, and B. Wagner, "Spin coating of an evaporating polymer solution," *Physics of Fluids (1994-present),* vol. 23, p. 102101, 2011.

[72] Y. Chang, W. C. Wu, and W. C. Chen, "Theoretical analysis on spin coating of polyimide precursor solutions," *Journal of the Electrochemical Society,* vol. 148, pp. F77-F81, 2001.

[73] M. D. Tyona, "A theoritical study on spin coating technique," *Advances in Materials Research,* vol. 2, pp. 195-208, 2013.

[74] L. W. McKeen, *Flourinated Coating and Finishes handbook; The Definitive User's Guide and Databook*. New York: William Andrew Publishing, 2006.

[75] L. E. Scriven, "Physics and application of dip coating and spin coating," in *Better Ceramics Through Chemistry III*. vol. 121, C. J. Brinker, D. E. Clarke, and D. R. Ulrich, Eds., ed Pittsburg, PA,: Materials Research Society, 1988, pp. 717-728.

[76] C. J. Brinker, A. J. Hurd, P. R. Schunk, G. C. Frye, and C. S. Ashley, "Review of sol-gel thin film formation," *Journal of Non-Crystalline Solids,* vol. 147–148, pp. 424-436, 1992.

[77] A.-S. Jandel and B. Meuthen, *Coil Coating,Bandbeschichtung: Verfahren, Produkte und Märkte,* Wiesbaden: Springer Vieweg, 2013.

[78] Available: http://www.hklitong.com/js.html. [Accessed 20 08 2014].

[79] Y. M. Tan and M. R. Flynn, "Methods for estimating the transfer efficiency of a compressed air spray gun," *Applied Occupational and Environmental Hygiene,* vol. 17, pp. 39-46, 2002.

[80] Available: http://hybridplastics.com/. [Accessed 10 11 2014].

[81] J. F. Brown, "The Polycondensation of Phenylsilanetriol," *Journal of the American Chemical Society,* vol. 87, pp. 4317-4324, 1965.

[82] I. J. Bruce and T. Sen, "Surface modification of magnetic nanoparticles with alkoxysilanes and their application in magnetic bioseparations," *Langmuir,* vol. 21, pp. 7029-7035, 2005.

[83] I. Jerman, M. Kozelj, and B. Orel, "The effect of polyhedral oligomeric silsesquioxane dispersant and low surface energy additives on spectrally selective paint coatings with self-cleaning properties," *Solar Energy Materials and Solar Cells,* vol. 94, pp. 232-245, 2010.

[84] M. Nowacka, D. Ambrozewicz, and T. Jesionowski, "TiO_2-SiO_2/Ph-POSS Functional Hybrids: Preparation and Characterisation," *Journal of Nanomaterials,* 2013.

[85] S. Spoljaric and R. A. Shanks, "Novel elastomer dye-functionalised POSS nanocomposites: Enhanced colourimetric, thermomechanical and thermal properties," *Express Polymer Letters,* vol. 6, pp. 354-372, 2012.

[86] N. Willenbacher and K. Georgieva, "Rheology of Disperse Systems," in *Product Design and Engineering*, ed: Wiley-VCH Verlag GmbH & Co. KGaA, 2013, pp. 7-49.

[87] E. Kissa, *Dispersions: characterization, testing, and measurement.* New York: M. Dekker, 1999.

[88] I. Jerman, M. Mihelčič, M. Koželj, and B. Orel, "Sol-gel based spectrally selective solar absorber coatings and the process for producing said coatings," WO 2013/158049, 2012.

[89] A. Verma and S. A. Agnihotry, "Thermal treatment effect on nanostructured TiO_2 films deposited using diethanolamine stabilized precursor sol," *Electrochimica Acta,* vol. 52, pp. 2701-2709, 2007.

[90] M. Mihelcic, I. Jerman, F. Svegl, A. Šurca Vuk, L. Slemenik Perse, J. Kovac, B. Orel, and U. Posset, "Electrochromic $Ni_{1-x}O$ pigment coatings and plastic film-based $Ni_{1-x}O/TiO_2$ device with transmissive light modulation," *Solar Energy Materials and Solar Cells,* vol. 107, pp. 175-187, 2012.

[91] F. Švegl, B. Orel, M. Mihelčič, I. Jerman, and A. Šurca Vuk, "Tehnologija priprave "elektrokromnih barv" na fleksibilne substrate," in *Prava smer za prihodnost: [katalog inovacij]. Ljubljana: Javna agencija Republike Slovenije za podjetništvo in tuje investicije*, 2012.

[92] S. Hara, H. Tanaka, T. Kawamoto, M. Tokumoto, M. Yamada, A. Gotoh, H. Uchida, M. Kurihara, and M. Sakamoto, "Electrochromic thin film of Prussian blue nanoparticles fabricated using wet process," *Japanese Journal of Applied Physics Part 2-Letters & Express Letters,* vol. 46, pp. L945-L947, 2007.

[93] H. Moulki, C. Faure, M. Mihelčič, A. Šurca Vuk, F. Švegl, B. Orel, G. Campet, M. Alfredsson, A. V. Chadwick, D. Gianolio, and A. Rougier, "Electrochromic performances of nonstoichiometric NiO thin films," *Thin Solid Films,* vol. 553, pp. 63-66, 2014.

[94] J. Yu, Y. Hai, and B. Cheng, "Enhanced Photocatalytic H_2-Production Activity of TiO_2 by $Ni(OH)_2$ Cluster Modification," *The Journal of Physical Chemistry C,* vol. 115, pp. 4953-4958, 2011.

[95] D. Barreca, A. Gasparotto, C. Maccato, E. Tondello, U. L. Stanger, and S. R. Patil, "Photoinduced superhydrophilicity and photocatalytic properties of ZnO nanoplatelets," *Surface & Coatings Technology,* vol. 203, pp. 2041-2045, 2009.

[96] M. Abdelmouleh, S. Boufi, A. ben Salah, M. N. Belgacem, and A. Gandini, "Interaction of silane coupling agents with cellulose," *Langmuir,* vol. 18, pp. 3203-3208, 2002.

[97] B. Simončič, B. Tomšič, B. Orel, and I. Jerman, "Sol-gel technology for chemical modification textiles," in *6th Framework programe ADVANBIOTEX of the EU*, Enschede: University of Twente, pp. 17-34, 2010.

Bibliography

Publications Related to the Thesis

M. Mihelčič, V. Francetič, J. Kovač, A. Šurca Vuk, B. Orel, R. Kunič, and D. Peros, "Novel sol–gel based selective coatings: From coil absorber coating to high power coating," *Solar Energy Materials and Solar Cells,* vol. 140, pp. 232-248, 2015.

M. Mihelčič, V. Francetič, P. Pori, H. Gradišar, J. Kovač, and B. Orel, "Electrochromic coatings made of surface modified rutile and anatase pigments: Influence of trisilanol POSS dispersant on electrochromic effect," *Applied Surface Science,* vol. 313, pp. 484-497, 2014.

M. Mihelčič, B. Orel, F. Fresno, U. Štangar Lavrenčič, and R. Kunič, "Preparation of Photocatalytic Optically Transparent Coatings from Pigment Dispersions," *Journal of Surfaces and Interfaces of Materials,* vol. 2, pp. 280-287, 2014.

M. Mihelčič, A. Šurca Vuk, D. Vrhovšek, F. Švegl, M. Hajzeri, and B. Orel, "Foil-based TiO_2/gel electrolyte/$Ni_{1-x}O$ electrochromic device made of electrochromic pigment coatings," *Acta Chimica Slovenica*, vol. 61, pp. 517-529, 2014.

M. Mihelčič, A. Š. Vuk, I. Jerman, B. Orel, F. Švegl, H. Moulki, C. Faure, G. Campet, and A. Rougier, "Comparison of electrochromic properties of $Ni_{1-x}O$ in lithium and lithium-free aprotic electrolytes: From $Ni_{1-x}O$ pigment coatings to flexible electrochromic devices," *Solar Energy Materials and Solar Cells,* vol. 120, pp. 116-130, 2014.

L. Slemenik Perše, M. Mihelčič, and B. Orel, "Rheological and optical properties of solar absorbing paints with POSS-treated pigments," *Materials Chemistry and Physics,* vol. 149–150, pp. 368-377, 2015.

B. Tomšič, V. Jovanovski, B. Orel, M. Mihelčič, J. Kovač, V. Francetič, and B. Simončič, "Bacteriostatic photocatalytic properties of cotton modified with TiO_2 and TiO_2/aminopropyltriethoxysilane," *Cellulose,* vol. 22, pp. 3441-3463, 2015.

Journal Articles

I. Jerman, M. Mihelcic, D. Verhovsek, J. Kovac, and B. Orel, "Polyhedral oligomeric silsesquioxane trisilanols as pigment surface modifiers for fluoropolymer based Thickness Sensitive Spectrally Selective (TSSS) paint coatings," *Solar Energy Materials and Solar Cells,* vol. 95, pp. 423-431, 2011.

R. Kunič, M. Mihelčič, B. Orel, L. Slemenik Perše, B. Bizjak, J. Kovač, and S. Brunold, "Life expectancy prediction and application properties of novel polyurethane based thickness sensitive and thickness insensitive spectrally selective paint coatings for solar absorbers," *Solar Energy Materials and Solar Cells,* vol. 95, pp. 2965-2975, 2011.

M. Mihelčič, I. Jerman, F. Švegl, A. Šurca Vuk, L. Slemenik Perše, J. Kovač, B. Orel, and U. Posset, "Electrochromic $Ni_{1-x}O$ pigment coatings and plastic film-based Ni_{1-}

$_x$O /TiO_2 device with transmissive light modulation," *Solar Energy Materials and Solar Cells,* vol. 107, pp. 175-187, 2012.

M. Rodošek, L. Perše, M. Mihelčič, M. Koželj, B. Orel, B. Bengű, O. Sunetci, P. Pori, and A. Vuk, "Raman spectroscopy of fluoropolymer conformal coatings on electronic boards," *Electronic Materials Letters,* vol. 10, pp. 935-941, 2014.

H. Moulki, C. Faure, M. Mihelčič, A. Šurca Vuk, F. Švegl, B. Orel, G. Campet, M. Alfredsson, A. V. Chadwick, D. Gianolio, and A. Rougier, "Electrochromic performances of nonstoichiometric NiO thin films," *Thin Solid Films,* vol. 553, pp. 63-66, 2014.

F. Švegl, B. Orel, M. Mihelčič, I. Jerman, and A. Šurca Vuk, "Tehnologija priprave "elektrokromnih barv" na fleksibilne substrate.," in *Prava smer za prihodnost: [katalog inovacij]. Ljubljana: Javna agencija Republike Slovenije za podjetništvo in tuje investicije*, 2012.

Patent application

I. Jerman, M. Mihelčič, M. Koželj, and B. Orel, "Sol-gel based spectrally selective solar absorber coatings and the process for producing said coatings," WO 2013/158049, 2012.

Conference Paper

I. Jerman, M. Mihelčič, F. Švegl, A. Šurca Vuk, B. Orel, "Electrochromic plastic devices," in *10th IEA-SHC Task 39 Expert meeting*. Graz, pp. 4, 2010.

I. Jerman, M. Mihelčič, B. Orel, R. Kunič, "Cool materials for the built environment," in *10th IEA-SHC Task 39 Expert meeting*, Graz, 2010.

M. Hajzeri, F. Švegl, A. Šurca Vuk, M. Mihelčič, L. Slemenik Perše, B. Orel, "Low temperature preparation of electrochromic iron oxid based thin films using peroxo sol-gel route," in *The 16th International Sol-Gel Conference, Hangzhou, China, August 28th-September 2nd, 2011. Abstracts: Sol-Gel*. [Los Angeles]: International Sol-Gel Society, pp. 342, 2011.

M. Mihelcic, I. Jerman, A. Rauter, B. Orel, D. Peros, L. Slemenik Perše, "Novel sol-gel based selective coatings for flat plate absorbers made by coil-coating application," in *Coatings Science International 2014, 23 - 27 June 2014, Noordwijk, Netherlands. Book of abstracts*. Noordwijk, pp. 52-56, 2014.

M. Mihelcic, I. Jerman, and B. Orel, "Electrochromic TiO_2 pigment coating and plastic film-based NiO/TiO_2 device with transmissive light modulation," in *8th Coatings Science International 2012: COSI 2012 : book of abstracts: Hotels van Oranje Noordwijk, 25-29 June, 2012, The Netherlands*. Noordwijk: 2012, pp. 96-99, 2012.

M. Mihelcic, I. Jerman, and B. Orel, "Preparation of electrochromic $Ni_{1-x}O$ and TiO_2 coatings from pigment dispersions and their application in electrochromic foil based devices," *Coating Science International 2012, 25th to 29th June 2012, Noordwijk, the Netherlands,* vol. 76, pp. 1752-1755, 2013.

M. Mihelčič, B. Orel, U. Lavrenčič Štangar, and F. Fresno, "Structural and photocatalytic properties of TiO_2 coatings on plastic foils prepared from pigment dispersions," in *3rd European Symposium on Photocatalysis*, Portorož, Slovenia, pp. 6-2, 2013.

M. Mihelcic, A. Surca Vuk, and B. Orel, "Low-haze optically passive powdered coatings on the basis of cerium oxide," in E-MRS Spring Meeting, Lille, France, May 26th - 30th, 2014. *EMRS Spring Meeting 2014*, Strasbourg, pp.12, 2014.

M. Mihelčič, F. Švegl, A. Šurca Vuk, M. Hajzeri, L. Slemenik Perše, I. Jerman, J. Kovač, H. Moulki, A. Rougier, G. Campet, B. Orel, "Electrochromic NiO_x films prepared using modified peroxo sol-gel route," in *The 16th International Sol-Gel Conference*, Hangzhou, China, August 28th-September 2nd, 2011. *Abstracts: Sol-Gel.* [Los Angeles]: International Sol-Gel Society, pp. 340, 2011.

H. Moulki, M. Mihelčič, A. Šurca Vuk, F. Švegl, B.Orel, "Electrochromic performances of nonstoichiometric NiO thin films, " in *European Materials Research Society (E-MRS) Spring Meeting 2013 Symposium O: synthesis, processing and characterization of nanoscale multi functional oxide films IV, May 27-31, 2013, Strasbourg, France*, (Thin Solid Films, Vol. 553, 2014). Strasbourg: 2014, vol. 553, pp. 63-66, 2014.

L. Slemenik Perše and M. Mihelčič, "The influence of pigments on rheological properties and spectral selectivity of solar paints," in *Papers presented at the Nordic Rheology Conference, Reykjavik, Iceland, August 13-14, 2014,* pp. 95-101, 2014.

L. Slemenik Perse, M. Mihelcic, and B. Orel, "The influence of dispersing agents and their PVC ratio on rheological properties and spectral selectivity of paints for solar thermal application," in 8th Annual European Rheology Conference April 2-5, 2013, Leuven, Belgium. Annual European Rheology Conference 2013, Leuven, 2013.

L. Slemenik Perse, M. Mihelcic, and B. Orel, "The impact of POSS-treated pigments on rheological and optical properties of solar absorbing paints," in *10th Annual European Rheology Conference, Nantes, France, April 14-17, 2015*, pp. 109, 2015.

L. Slemenik Perse, M. Mihelcic, and B. Orel, "The influence of the PVC ratio of various dispersing agents on the rheological properties of specially selective paint coatings for solar thermal application," in *papers presented at the Nordic Rheology Conference, Helsinki, Finland, June 8-10, 2011: general papers and papers from the special session on Polymer solution, suspensions and melts*, (Annual transactions, vol. 19). Brabrand: Nordic Rheology Society, vol. 19, pp. 253-261, 2011.

P. Pori, A. Vilčnik, M. Mihelčič, A. Rauter, B. Orel, M. Petrič, "Light transparency of sol-gel films containing surface modified rutile or anatase nanoparticles," in *PRA's 9th international woodcoatings congress, Netherlands, 14-15 October 2014: Beauty, protection, sustainability.* [Amsterdam]: [Paint research association], pp. 1-8, 2014.

M. Rodosek, L. Slemenik Perse, M. Mihelcic, M. Kozelj, B. Orel, B. Bengu, O. Sunetci, P. Pori, and A. Surca Vuk, "Raman spectroscopy as a tool for investigation of fluoropolymer coatings on electronic boards," *Eurocorr 2014,* 2014.

A. Surca Vuk, M. Mihelcic, I. Jerman, A. Rougier, B. Orel, "Pigment particle based electrochromic coatings and devices. " in *E-MRS Spring Meeting, Lille, France, May 26th - 30th, 2014. EMRS Spring Meeting 2014*. Strasbourg, pp. 3-4, 2014.

Biography

Personal information

First name / Surname:	Mohor Mihelčič
Date of birth:	23 June 1985
Address:	Zali Log 26, 4228 Železniki
Nationality:	Slovenian

Work experience

15 October 2010-	Independent professional colleague Laboratory for Materials Chemistry, National Institute of Chemistry, Hajdrihova 19, 1001 Ljubljana
Field of research:	- Research on different inorganic materials which exhibit electrochromic behaviour (NiO, TiO_2, WO_3, CeO_2, V_2O_5). - development and characterisation of thickness dependant (TSSS) and thickness independent (TISS) spectral selective coatings used for solar absorbers - Participation in several EU projects: INNOSHADE, BONACO, NECSO, NANORESTART
1 May 2009-1 September 2010	Student work Laboratory for Spectroscopy of Materials, National Institute of Chemistry, Hajdrihova 19, 1000 Ljubljana
Field of research:	- development and characterisation of thickness dependent (TSSS) and thickness independent (TISS) spectral selective coatings
1 October 2008-1 May 2009	Work praxis Color d.d., Medvode Cesta komandanta staneta 4, 1215 Medvode

Education

2012-	Jožef Stefan International Postgraduate School, Ljubljana third-level study programme Programme: Nanosciences and Nanotechnologies Supervisor: Prof. Dr. Boris Orel

2010-2012	Jožef Stefan International Postgraduate School, Ljubljana second-level study programme Programme: Nanosciences and Nanotechnologies Title of qualification awarded: Master degree of nanoscience and nanotechnology 14 September 2012 - Defence of master thesis with title: Preparation and properties of thin electrochromic films based on nanoparticle dispersions. Supervisor: Prof. Dr. Boris Orel
2004-2010	Study at the Faculty of Chemistry and Chemical Technology, University of Ljubljana 23 September 2010 - Defence of degree with title: Polyhedral oligomeric silsesquioxane as a pigment modificator in preparation of spectrally selective coatings. Supervisor: Prof. Dr. Matjaž Krajnc Co-Supervisor: Prof. Dr. Boris Orel
2000-2004	High School Economic Gymnasium Kranj